UiT
NORGES
ARKTISKE
UNIVERSITET

Faculty of Science and Technology

Department of Geology

Carbonate concretions in an ice-contact delta, Skarmunken, Ullsfjord, northern Norway

Mats Amundsen

Master thesis in GEO-3900

March 2017

UNIVERSITETET I TROMSØ

Abstract

At Skarmunken, a small village south of Ullsfjord, northern Troms, Norway, an outcrop containing carbonate concretions have been investigated. From sedimentary logging, five facies (facies A-E) have been classified by their grading and composition. Depositional data from logs, maximum pebble size (MPS) and earlier investigations suggests an ice-contact delta. TOC/TS data have revealed a dominantly nonmarine depositional environment for the lower half of the outcrop, with one occurrence of marine environment.

The occurring carbonate concretions is indicated to have formed in two different processes, where the stratabound concretions are suggested to have formed by local buried carbon sources in the sediments and the carbonate concretions located in sand injections are suggested be the result of fluid migration. The precipitation processes of the carbonate concretions are indicated to be from both hydrocarbon oxidation and oxidation of buried carbon. Environmental data and the local geology suggest a biogenic carbon source for the precipitation of the carbonates.

Carbonate concretions samples revealed one main morphology, horizontal - vertical pipe concretions. Additional investigated morphologies were horizontal-subvertical intergrown pipes with plate surfaces, chimneys, blocky boulder and spherulites concretion. Thin section analyzes of the concretions suggests calcium carbonate cementation and a trend of channelized cementation paths. The carbonate concretions were commonly observed to accompany the extensive sand injections in the area, where the sand injections are indicated to be the result of fluidization of a fine-grained sand and mud sequence, caused by rapid sediment deposition and glacial compaction.

The occurrence of carbonate concretions inside the sand injections, thin section analysis and concretion morphologies indicate fluid migration control over the distribution of the carbonates and the concretion morphology. Observations of the sand injections and carbonate concretions behavior in the sediments, indicate that the heterogeneity of the seep sediments controls the pathway for the sand injections and subsequent also the morphology of the carbonate concretions. Spherulitic carbonate concretions appear to form from different processes than the other carbonate morphologies and may form due to special chemical conditions in the sediments.

Acknowledgement

First of all, I would like to thank my supervisor, Nils-Martin Hanken, for giving me the opportunity to work with this interesting project, and for great supervision both in the field and in my thesis. I am also very grateful to my co-supervisor Geoff Corner for guidance and constructive comments and feedback to improve my work. I would like to thank Martin Hovland for the financial support to the project and I would also like to thank the staff at the geo lab for teaching and helping me with the sample preparation, analysis and not yell at me when I forgot to clean up after myself.

I would like to thank everyone at the office and the red barrack for two wonderful years with unforgettable memories from fieldtrips and late hours at the university.

Special thanks go out to the people in barrack 17, for making my last year in Tromsø awesome.

Finally, I would like to thank my family and my friends for supporting me and encouraging me to do my best.

Contents

INTRODUCTION

1. INTRODUCTION

1.1 Objectives

The occurrence of carbonate concretions in the marine environment by gas seepage is widely recognized, where the formation of the concretions, geochemistry and morphology are much discussed topics (e.g. Claypool & Threlkeld, 1974; Gautier & Claypool, 1984; Hovland et al., 1987; Burton, 1993; Jørgensen, 1992; Peckmann et al., 2001; Luff et al.,2004; Martin Hovland et al., 2005). However, little is known about carbonate concretion behavior, morphology and placement in the soft-sediments. The aim for the research presented in this thesis is to attempt to improve the understanding of carbonate concretions and nodules behavior in soft-sediments, morphology and precipitation conditions for subaqueous environments

1.2 Study area

The study area is located in Skarmunken (Fig. 1BA, Fig. 2B and Fig. 6), in Troms county, Northern Norway. The area is located on the western side of Sørfjord, on the northern end, in the transition zone to Ullsfjord at the Tromsø-Lyngen moraine. The study location area is recognized as a raised coarse – grained, ice- contact delta (Andersen, 1968; Lønne, 1993) stretching from Skarmunken to Hjellneset (Fig. 1, B and Fig. 2, A. The Skarmunken part of the ice-contact delta consists of a 40m high and 900m long exposed hillside next to the shore (Fig.2, B). The area was deglaciated during 13-10 ^{14}C ka BP, which is also the age of the Skarpnes and Tromsø-Lyngen moraines (Plassen & Vorren, 2003b). The marine limit (ML) in the area is documented to be at 65-66m (Fig. 6) (Andersen, 1968; Lønne, 1993; Bakke et al., 2005).

Fig. 1. (A) The map over Norway were the study area is indicated by red dot. (B) Map over Troms county where the study location in Skarmunken is indicated by a black square Fig. 2. Figure A is a modified satellite image from Google Earth (2016) and figure B is a modified map from Norgeskart, Kartverket (2016).

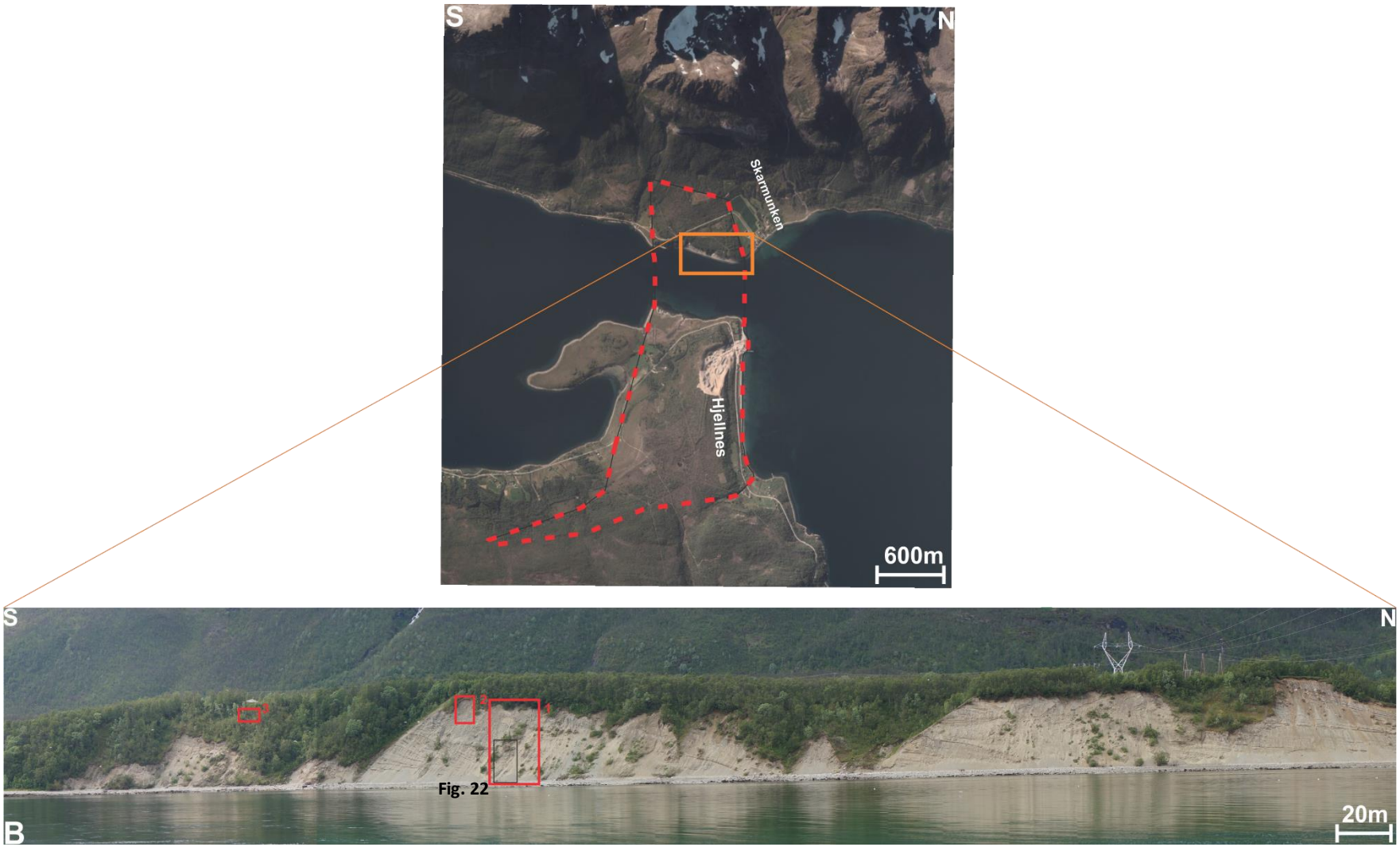

Fig. 2. (A) Air photo of the Skarmunken and the Hjellneset section, where the red dotted line represents the Tromsø-Lyngen moraine. The orange rectangle represents figure 2B, which is the exposed section at Skarmunken. (B) Panorama photo of the exposed Skarmunken section. The red rectangles 1 and 2 represent the study location and rectangle 3 represent the investigated fossiliferous unit by Andersen (1968). The rectangle 1 shows the position of vertical profile shown in Fig. 22 up to 28m, rectangle 2 shows the rest of the upper section of the vertical profile. The black rectangle indicates the position of Fig. 13 displaying the lower part of the excavated sections. Figure A is modified after Norgeskart, kartverket (2016) and the picture in figure B is taken from Hjellneset (2016).

2 GEOLOGICAL SETTINGS

2.1 Northern Norway

Northern Norway constitutes of mainly two types of rock, the Caledonian nappes and Precambrian rocks (Fig. 3 A). Most of northern Norway consist of Caledonian nappes, which overlie Precambrian, Archaean and Palaeoproterozoic crust. This crust underlies a large part of the NE part of the Fennoscandian Shield in Kola, Finland and northern Sweden. Dominant parts of the exposed Precambrian rocks are located west of the Caledonian nappes (Fig. 3 A) , represented by the West Troms Basement Complex (Bergh et al., 2010) and the basement suit of Lofoten – Vesterålen area (Griffin et al., 1978; Corfu, 2004a). From regional correlation of ductile shear zones, greenstone belts and Precambrian basement windows within the Caledonides, it is highly likely that these rocks are of the same origin as the Karelian, Belmorian and Kola-Norwegian/Murmansk provinces of the Fennoscandian Shield (Bergh et al., 2014).

2.1.1 Local geology

The Ullsfjord area of Nortern Troms (Fig. 3, B and C) consist of rocks from two allochthons: 1) a fragmented ophiolite complex and non- conformably overlying fossiliferous (Upper Ordovician – Lower Silurian) metasedimentary rocks (Balfjord group) of the Lyngen Nappe Complex. 2) Exotically derived metasedimentary and meta-igneous rocks of the overlying Tromsø Nappe complex (Coker-dewey et al., 2000).

The nappe sequence preserved in the Ullsfjord area, from bottom to top, includes the Nordmannvik Nappe (Fig. 3, B and C) and the Lyngen Nappe complex (Fig. 3, B and C) of the upper Allochthon and the Tromsø Nappe complex (Fig. 3, B and C) of the uppermost Allochthon (Arild Andresen & Steltenpohl, 1994). The nappes are regionally metamorphosed and show evidence of multiple deformations. The uppermost units of the Lyngen Nappe complex, the Balsfjord group (Fig. 3, B and C) (Bergh & Andresen, 1985), locally exhibits an abrupt (<1km), inverted metamorphic gradient, where the highest temperature occur immediately below the structurally overlying Tromsø Nappe complex (Binns, 1978; Krogh et al., 1990).

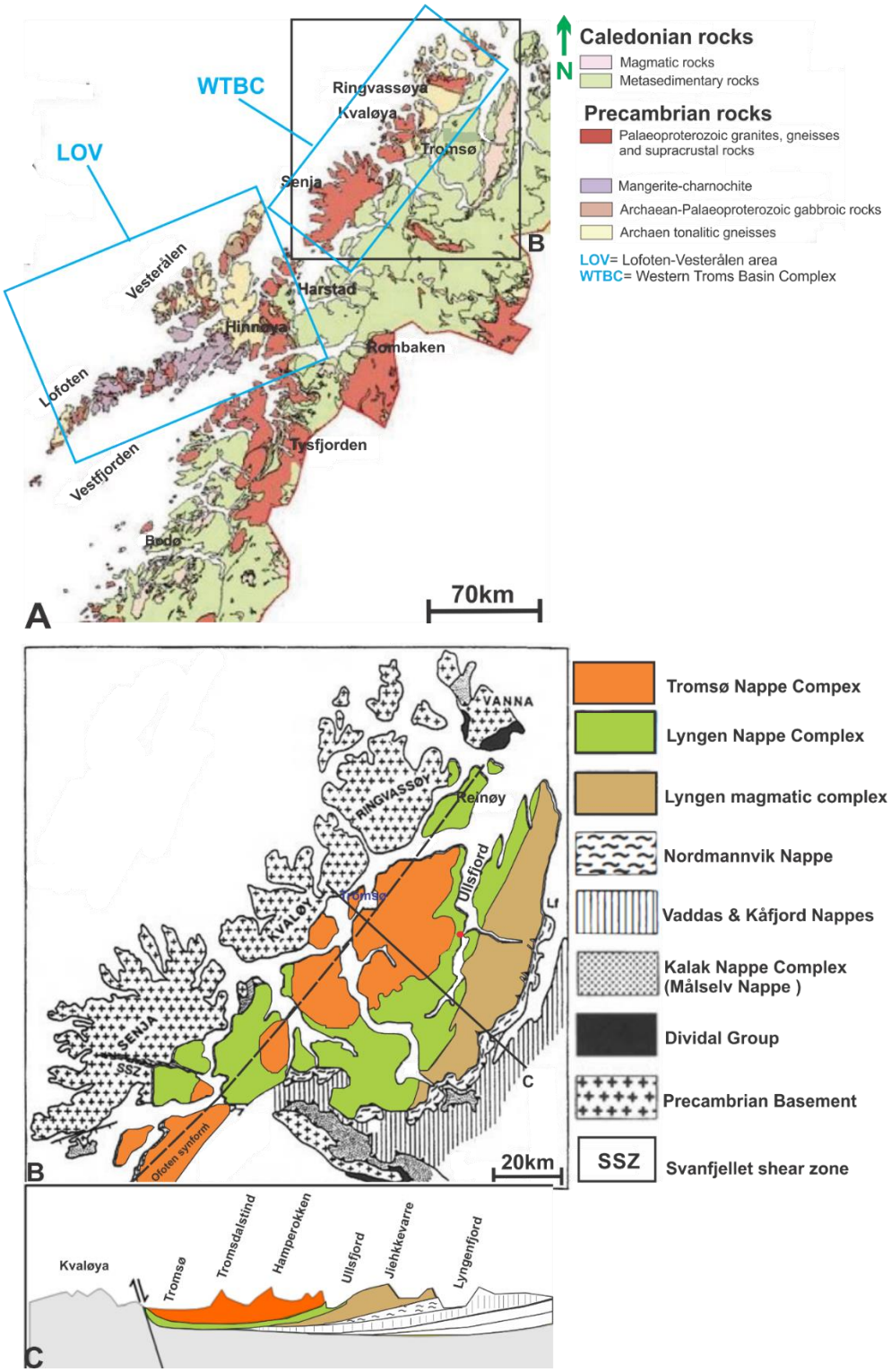

Fig. 3. (A) Geological map over Troms displaying the distribution of the Precambrian rocks and the Caledonian nappes, where the black square represent figure B. The blue rectangles represent the Western Troms Basin Complex and the Lofoten-Veståreln area. (B) More detailed geological map Troms, where the Tromsø Nappe, Lyngen Nappe and Lyngen magmatic complex is colored. The red dot indicates the study location, the black dotted line represents the Ofoten synform and the black line C represent the geological profile in figure C. (C) The geological profile of the black line on figure B. The Tromsø Nappe, Lyngen Nappe and Lyngen magmatic complex are highlighted in the same colors as in figure B. Figure A is modified after Ramberg et al.(2006)*, figure B is modified after Binns (1978) and Krogh (1992) and figure C is modified after* Janák et al. (2012)*.*

2.1.1.1 The Lyngen Nappe complex

The Lyngen nappe complex (Fig. 3, B and C) contains the Lyngen Magmatic complex (Fig. 3, B and C) and unconformably overlying Balsfjord Group metasedimentary rocks (Fig. 3, B and C) (Coker-Dewey et al., 2000). The Balsfjord Group metasedimentary rocks include a basal conglomerate, thick (-400m) calcite and dolomite marbles sequences, mica schist, quartzite, and carbonates pebble diamictite, which are interpreted to reflect on marginal marine shelf depositional environment (Steltenpohl et al., 1990). The Balsfjord Group provides important constraints on orogenic timing in northern Scandinavia because Late Ordovician to Early Silurian fossils are preserved that provide a maximum on the time of Scandian metamorphism (Bjørglykke & Olaussen, 1981; Andresen & Bergh, 1985; Steltenpohl et al., 1990)

2.1.1.2 Balsfjord Group, metasedimentary rocks

The Balsfjord group (Fig. 3, B and C) in the western Ullsfjord from bottom to top consists of the Sjurnsens phyllite, Skognesdalen quartzite, Stordalvatn phyllite, Breivikeidet marbles and Nakkefjell metasiltstone (Coker-dewey et al., 2000)

2.1.1.2.1 Sjursnes phyllites

The lowermost unit of the Balsfjord Group and the lowest exposed unit in the study area. It consists of at least 855m interlayer graphite and chlorite phyllite, calcite phyllite, rare thin micaceous marble, and massive greenstone with local pillowed metabasalts and metachert (Coker-Dewey et al., 2000).

2.1.1.2.2 Skognesdalen quartzite

The unit is interlayered with the Sjursnes phyllite and consists of five quartzite units with thickness ranging from <1m to 70m (Coker-Dewey et al., 2000).

2.1.1.2.3 Stordalvatn phyllite

The unit consists of magnetite bearing phyllite with quartz layers and minor greenstone lenses. It is structurally above the Sjursnes phyllite, where the unit is thickest (100m) in the southeast of Ullsfjord, thinning towards north (Coker-Dewey et al., 2000).

2.1.1.2.4 Breivikeidet marbles

The unit is structurally above the Stordalvatn phyllite and consists of 200m of calcite marbles with sparse layers of chloritic schist and massive tremolite – actinolite rich layers (Coker-Dewey et al.,

2000). Succeeding the calcite marbles are a 150m thick pure dolomite layer (Coker-Dewey et al., 2000).

2.1.1.2.5 Nakkefjell metasiltstone

The Nakkefjell metasiltstone is the uppermost unit of the Balsfjord Group and consists of a 300m thick sequence of banded metasiltstone and metasandstone (Coker-Dewey et al., 2000). The unit is characterized by interbedded graded beds with sharp contacts at the base of psammic layers where the beds grade upwards into fine-grained politic bands (Coker-Dewey et al., 2000). The unit contains numerous trondhjemite sills or dikes (Coker-Dewey et al., 2000).

2.1.1.3 Tromsø Nappe Complex

The Tromsø Nappe complex (Fig. 3, B and C is located structurally on top of the Balsfjord Group. The complex is divided into three main units: 1) the lower tectonic unit, 2) the middle unit and 3) the upper unit (Coker-Dewey et al., 2000).

The lower tectonic unit consist of migmatized, upper-amphibolite facies, felsic gneiss, amphibolite, schist and meta-igneous rock. The middle unit consist of the Skattørna Gneiss, comprises of banded migmatized amphibolite and amphibole gneiss cut by numerous dioritic to anorthositic dikes. The upper units consist of the Tromsdalstind complex, consisting of schists, gneisses, marbles, and eclogites. Variably serpentinized ultramafic rocks occur locally (Coker-Dewey et al., 2000).

2.2 Quaternary Geology

2.2.1 General setting

During the last 2,5-3 myr, the Scandinavian and the Nordic countries have experienced multiple glaciations. The ice sheets covering these areas are known as the Eurasian ice sheets. Due to cycles of glacial erosion and reworking in each glacial and interglacial events, most of the glacial imprints before Last Glacial Maximum (LGM) are poorly documented (Wohlfarth et al., 2007).

Fig. 4. Map over northern Eurasia, displaying the maximum extent of ice cover during the LGM. The white lines represent the ice cover margins. Trough and mouth fans for the continental shelf edge is marked with orange. SBKIS= Svalbard-Barents-Kara ice sheet, SIS = Scandinavian Ice Sheet, BIIS= British-Irish Ice Sheet. The map is taken from Hughes et al. (2016) .

2.3 Glacial history of Northern Troms

The Scandian ice sheet (SIS) is indicated to have covered most the northern Troms from approximate 28-15 ka ^{14}C yr BP (Hughes et al., 2016). However, work by Alm (1993) indicate that the northern parts of Andøya was deglaciated around 22.0 ka^{14}C yr BP, where previous work by Vorren et al. (1988) and Møller et al. (1992) supports an early deglaciation of the northern Andøya (Vorren & Plassen, 2002). Records indicate that Andøya commenced in a warm period between 16-15 ka^{14}C yr BP, before a cold phase commenced (Vorren, 1978; Vorren et al., 1988; Alm, 1993) during 13.8-13 ka^{14}C yr BP, causing glacial readvance (Vorren & Plassen, 2002).

The deglaciation of the SIS commenced during 14-12 ka^{14}C yr BP, during the Allerød Interstatial (Hughes et al., 2016), where records on Andøya indicate that the melting phase started during 13.2-12.2 ka ^{14}C yr BP, leading to the deglaciation of the whole Vågsfjord basin and an ice cap on Senja Island was separated from the continental ice sheet (Vorren & Plassen, 2002). During 12.2 ka ^{14}C yr BP (Eilertsen et al., 2005) the Skarpnes event commenced, depositing moraines throughout the northern Troms (BILDE?).

The following Younger Dryas period is characterized by a cold period, which lead to re-advancement of the SIS. This readvancement is known as the Tromsø-Lyngen event (10.7-10.3 ka^{14}C yr BP) (Vorren & Plassen, 2002), which formed an extensive moraine sets in northern Troms (BILDE?). The period after the Tromsø-Lyngen event marks the start of the glacial retreat and the final deglaciation of the fjord and valleys. Based on records from Andøya and Balsfjord, the period after the Tromsø-Lyngen event, during 10.4-9,8 ka ^{14}C yr BP, the glaciers are indicated to have retreated from the Tromsø-Lyngen moraines (Forwick & Vorren, 2002; Vorren & Plassen,2002). Records show that the final deglaciation of the Balsfjord and the Lyngen fjord occurred from 9.6-9.1 ka^{14}C yr BP (Corner, 1980; Forwick & Vorren, 2002).

2.3.1 Glacial history of Skarmunken

The glacial remnants from the SIS are located in the southern part of Ullsfjord and the in the transition zone between Ullsfjord and Sørfjord. In the southern part of Ullsfjord the Skarpnes moraine is located (Fig. 7A) (Plassen & Vorren, 2003b), indicating deposition during 12.2 ka ^{14}C yr BP (Eilertsen et al., 2005). The Skarpnes moraine consist of an approximate 80m deep and 500m broad incision, where the internal pattern of the moraine occurs as chaotic, weakly inclined and subhorizontal (Ballantyne, 1990).

The Tromsø-Lyngen moraine is located in the transition between Ullsfjord and Sørfjord (Fig. 2A), suggested to be deposited during 10 300 ka ^{14}C yr BP (Corner & Haugane, 1993). The moraine crosses the fjord SW-NE direction and is controlled by the bathymetry (Ballantyne, 1990). Andersen (1968) mapped the moraine over <10km on land, east of the fjord. The Lyngen Main shoreline, the elevation and inferred age of the shoreline correlate with the Tromsø-Lyngen moraines, where the shoreline displacement curve for Lyngen (Fig. 5) (Corner & Haugane, 1993) indicates the sea level at Skarmunken was around 50-51m a.s.l. (Fig. 5) under the Tromsø- Lyngen event and subsequent the formation of the ice-contact glaciomarine system.

Both moraines record the former presence of large glaciers that occupied much of Ullfjord and Lyngsfjord (Andersen, 1965; Andersen, 1968). Corner (1980) suggests tree advances or stillstands, interrupted by ice- sheet retreat around 9900-9800 BP, 9600-9500 BP and 9400BP, where the inner fjord valleys deglaciated by c. 9100 BP (Ballantyne, 1990). Thes ice-sheet retreat suggested by Corner (1980) correlate with the records from Andøya and Balsfjord (2.3), where the final deglaciation of the Balsfjord and the Lyngen fjord correlate with the work by Ballantyne (2.3)

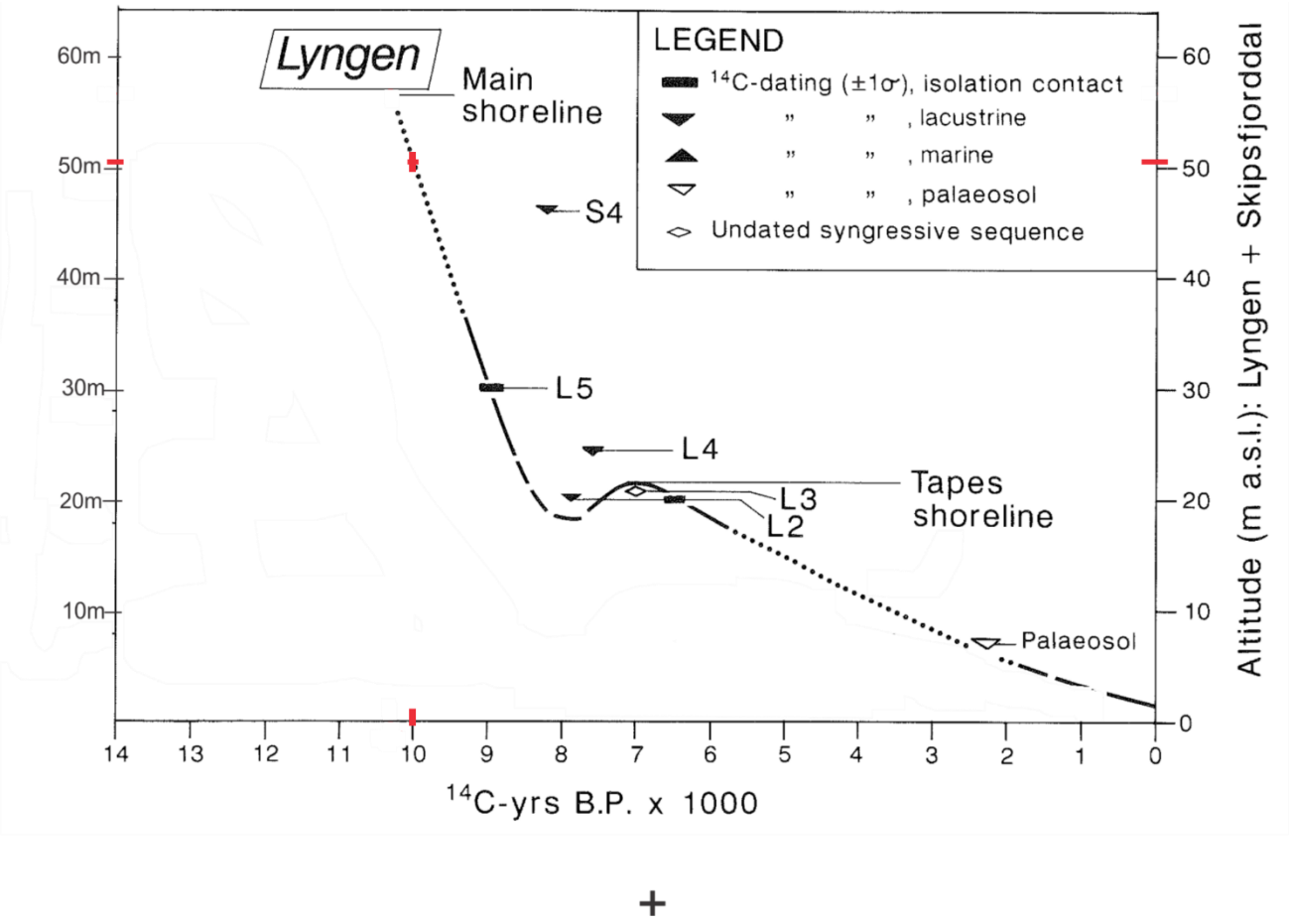

Fig. 5. The Lyngen shoreline displacement curves. The curve refers to high-tide level, where the dashed and continuous lines of the curve indicate relative degree of uncertainty. The dotted lines are interpolated or based on region data. The red marks represent the approximate timing (10 ka c. BP) of formation of the Tromsø-Lyngen event and the shoreline level (50-51m) at that point. The figure is modified after Corner & Haugane (1993).

2.4 Previous work

This subchapter focus on the previous work, interpretations and suggestions, done in the Skarmunken and Hjellneset area and the adjacent Ullsfjord area. The main themes in the previous work done in Ullsfjord focuses on sedimentary deposition related to Skarmunken and Hjellneset and fluid migration investigation.

2.4.1 Glacial Geology of Western Troms

Andersen (1968) investigated the ice-contact delta at Skarmunken in Ullsfjord (Fig. 1 and Fig. 2). Two parallel moraine ridges were located on the eastern moraine segments surface with clear traces of marine erosion below the 65-66m altitude. Andersen (1968) suggests that the exposed area at between Skarmunken (Fig. 2, A and B) and the fjord side to comprise of a fanshaped outwash delta.

The delta plain is documented to be very bouldery and steep near the apex, reaching 66-67m asl. (Andersen, 1968). Several marine terraces and shore bars is located on the steep front slope of the delta. The highest observed shore bare is located on the delta front, 65-66m a.s.l. This indicates that the marine limit was located around 65-66m a.s.l. Most of the exposed beds dip varies from 20-25° northwest, where most of the sediments are well sorted, varying from sand to cobbles.

Broken and unbroken bivalves from *Macoma calcarea, Hiatella (Saxicava) arctica, Mya truncata* and *Similipecten greenlandica (Pecten groenlandicus)* were located in the upper parts of a gully on the proximal part of the sea buff (Fig. 2) in a 4m thick laminated clay-silt unit. The documented proximal deposition of the clay-silt unit indicates a retreat of the glacier terminus at this time interval, where the deformation of the unit indicates a glacier terminus advance subsequent to the fossiliferous silt and clay unit. The clay-silt unit is documented to truncate the foreset sequence, indicating a clearly younger age. The shells were radiocarbon dated to $10{,}390^{+}_{-}$ 200 years BP (Andersen, 1968), where calculations by Stuiver & Reimer (1993)(version 7.0) gives c. 10616 cal BP – 10007 cal BP (Hughen et al., 2004.).

2.4.2 The Skarmunken- Hjellneset ice- contact delta

Lønne (1993) investigated the ice- contact delta and the different foreset facies at Skarmunken and Hjellneset (Fig. 2 and Fig. 6). The forming of the delta is proposed in two different ways: progradation of the depocenter during glacier terminus stagnation, or glacier advance. From mapping and observation of the Skarmunken, the thick wedges of the ice-contact deposits are evidence for glacier advance setting. Five different facies were recognized at the Skarmunken location by Lønne (1993), whereas only three facies were exposed at Skarmunken and the remaining two facies were schematically drawn. Due to repeated facies in the Skarmunken sequence, Lønne (1993) suggest a “generalized flow- parallel section of an ice- contact delta”. It is suggested that a progadational foreset sequence at Skarmunken most likely formed due to glacier advance with minor halts, were the bedded foreset sequence displayed closely resemblance clinoformal seismic facies (Lønne, 1993).

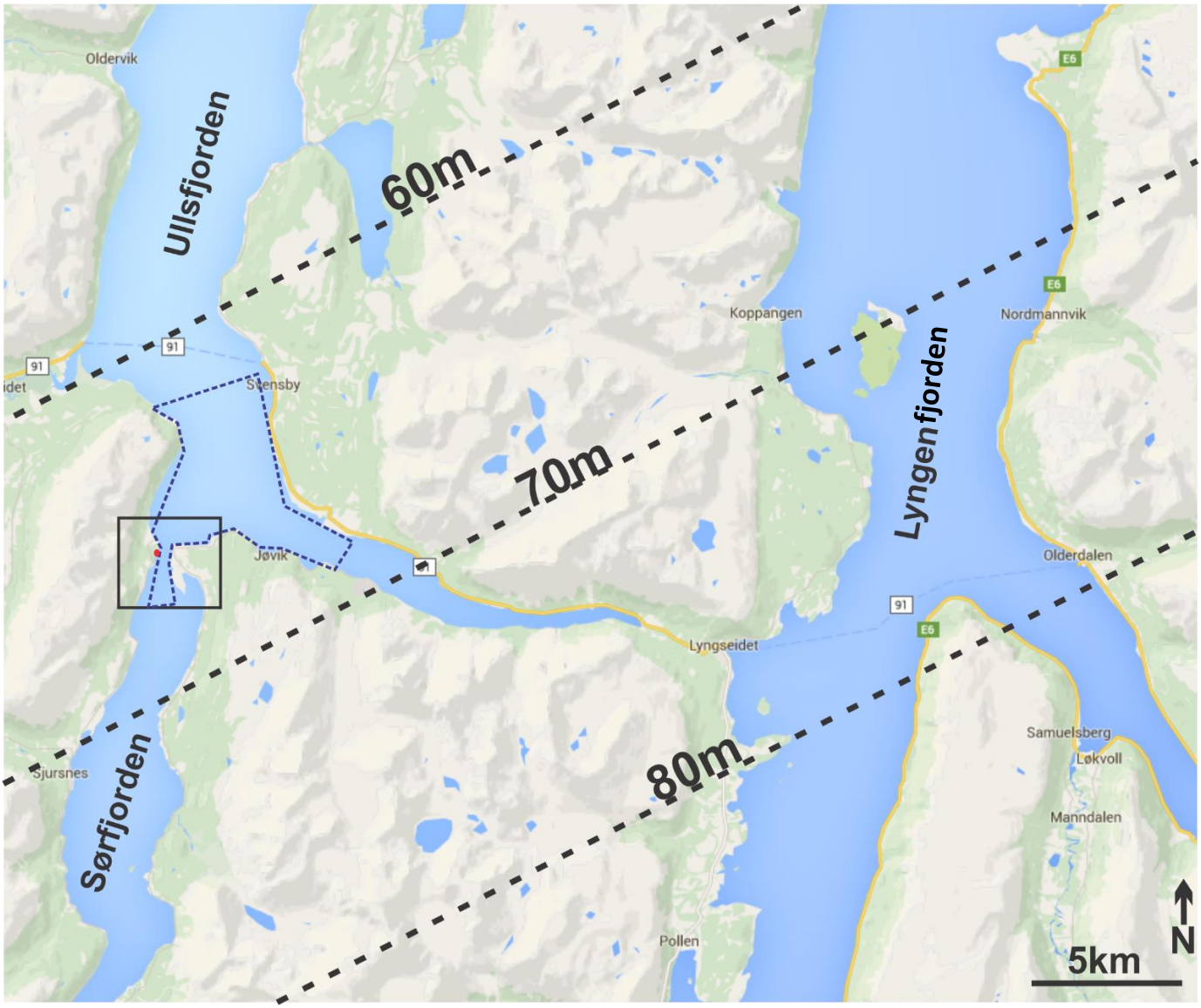

Fig. 6. Map over the Ullsfjord, Sørfjord and Lyngen area with a simplified display of the isobases for the extended S_0 marked with big black dotted lines. The map is taken from NorgesKart, Kartverket (2016) and the isobases is based on work by (Corner, 1980). *The black square represents the work area for Lønne (1993), the red dot represents the study area in this thesis, and the blue dotted area marks the area covered by Plassen and Vorren (2003b).*

2.4.3 Fluid flow features in fjord- fill deposits, Ullsfjord, North Norway

Previous work by Hovland & Judd (1988) documents several pockmarks and seabed doming features in Ullsfjord. Plassen & Vorren (2003a) has further developed the previous work where morphology, distribution and origin of the fluid flow related features were investigated. The investigated area starts from southern half of Ullsfjord to the northern end of Sørfjord (Fig. 7 A and B). For the investigation boomer, side scan sonar and sediment cores was used (Fig. 7 B and C). The pockmarks and dome structures are mainly located in the northern part of investigated area, on the Skarpnes moraine and in close proximity (Fig. 7 B).

Hovland and Judd (1988) suggests the biogenic gas to be the source of the fluid migration features, where factors of high mountains, glaciers, lakes and stream borders is proposed to play roles in formation of gas and groundwater-related processes in the seabed. Hovland and Judd (1988) disbanded the suggestion of thermogenic gas due to the crystalline bedrock in Ullsfjord.

Plassen and Vorren (2003a) recognize the pockmarks to lack infilling, indicating that fluid escape may occur frequently. The present glacigenic muddy sediments are suggested to act as a trap for the ascending gas and fluids (Plassen & Vorren, 2003a). The general trend in the investigated area is the lack of organic matter in the glacimarine sediments. As the investigated area is located in an area influenced by postglacial neotectonic activity (Dehls et al., 2000), Plasssen and Vorren (2003a) suggest the source for the pockmarks to possibly be thermogenic deep earth gas migrating to the surface. It is therefore suggested to be thermogenic gas and possibly ground water seepage that is responsible for the recognized seafloor features (Plassen & Vorren, 2003a).

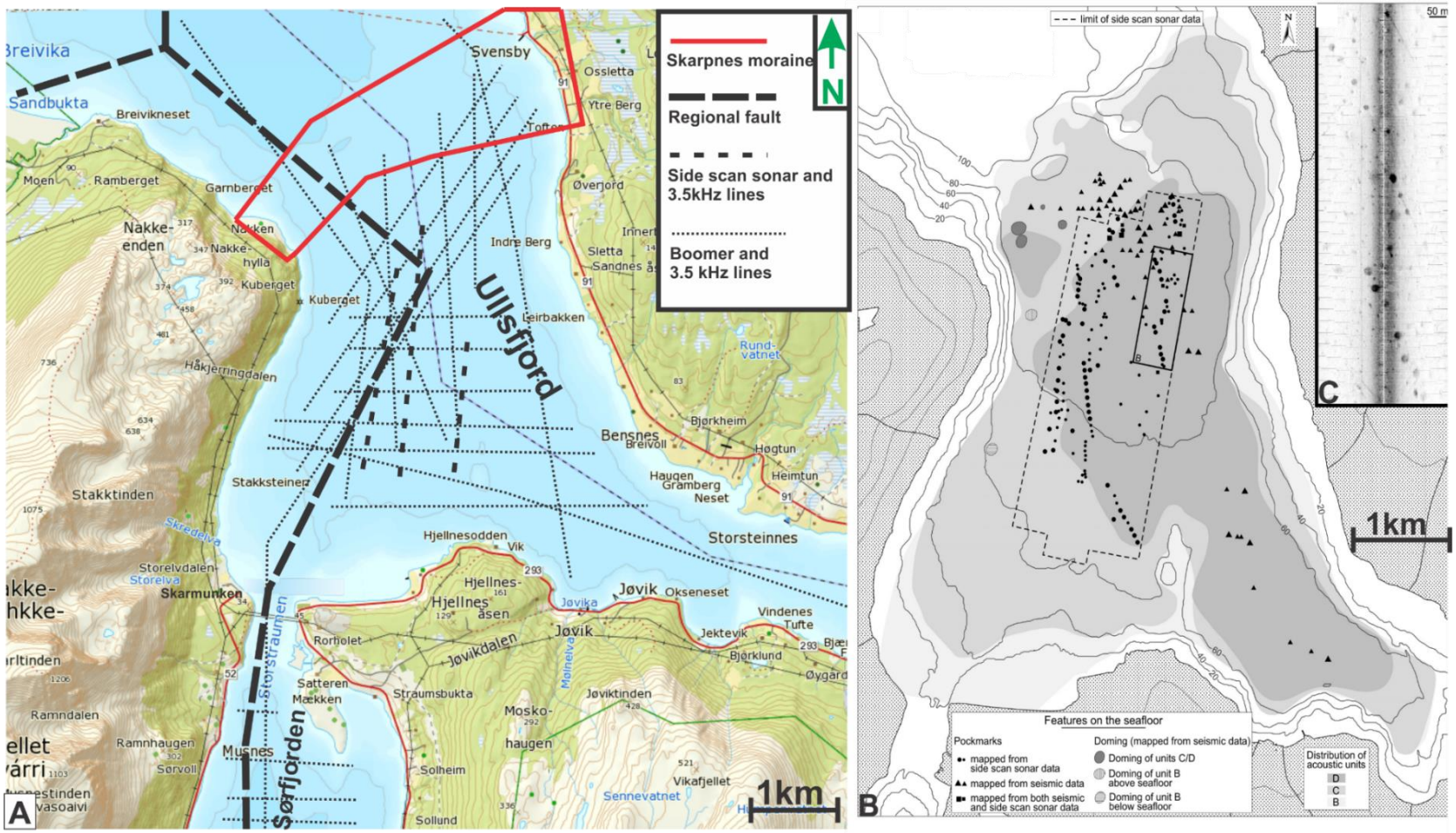

Fig. 7. (A) Map over the northern end of Sørfjord, Skarmunken, and the southern part of Ullsfjord with location of high-resolution acoustic data, side scan sonar, Boomer and 3.5kHz lines are indicated by black dotted lines. The enclosed area by red thick lines represent the Skarpnes moraine and the largest dotted line represent a regional fault going through Skarmunken and Ullsfjord. (B) Map over the southern part of Ullsfjord with pockmarks and doming structures indicated with respective signs. The enclosed area by dotted line represent the limit of the side scan sonar data and the black rectangle represent figure C. (C) Side scan sonar image displaying high reflecting areas, suggested to represent pockmarks. The map in figure A is taken from Norgeskart, Kartverket (2016) and modified after Plassen and Vorren (2003b). Figure B and C are modified after Plassen & Vorren (2003b).

2.4.4 Ullsfjord, sedimentary processes and the environment during deglaciation

Plassen & Vorren (2003b) studied the sedimentary processes and the environment during the deglaciation of Ullsfjord (Fig. 7 A and Fig. 8). The bedrock of the investigated basin, Ullsfjord, consist of quartz- biotite schist to the west and mica schist and phyllite, with bands of quartzite, to the south and east (Plassen & Vorren, 2003b). From the acoustic analysis, the basin between the Skarpnes and the Tromsø- Lyngen moraine consist of glacimarine and marine sediment, where at the Skarmunken-Hjellnesetet area in the threshold between Ullsfjord and Sørfjord, the minimum depth to the crystalline bedrock is approximate 100m (Fig. 8) (Neeb, 1981; Lønne, 1993)

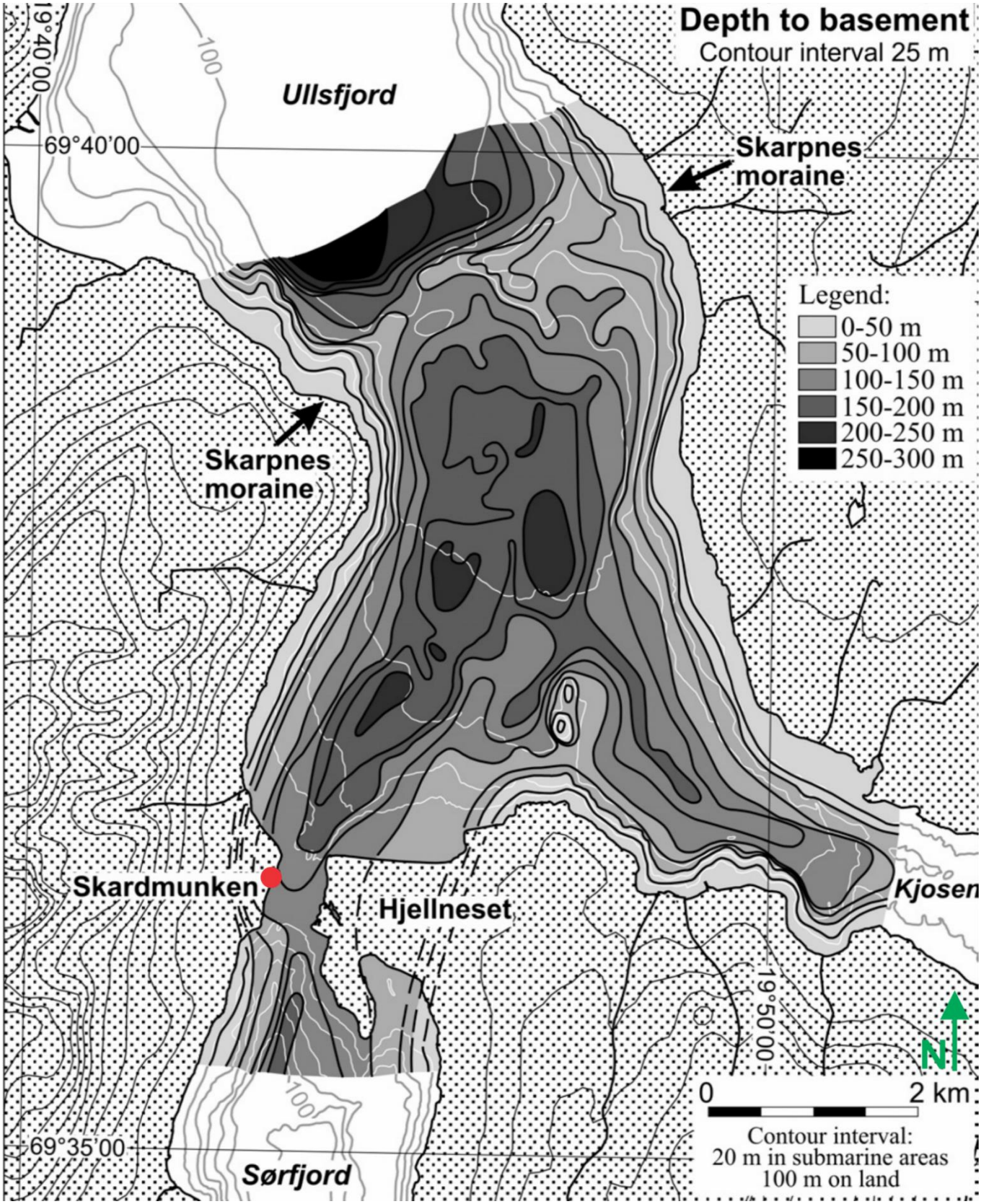

Fig. 8. Structure-contour map of the northern end of Sørfjord and southern end of Ullsfjord displaying the depth to acoustic basement. The acoustic basement represents the glacial deposits comprising the Skarpnes moraine, and crystalline bedrock further southwards. The red dot represents the study location and the white broken lines represent seafloor contours. The map modified after Plassen and Vorren (2003b).

2.4.5 Ice- contact glaciomarine systems

From previous work (Andresen, 1968; Lønne, 1993; Plassen & Vorren, 2003b), the Skarmunken and the Hjellneset area represent a product of an ice- contact glaciomarine system. Therefore, a definition of ice-contact glaciomarine systems is important.

Ice- contact glaciomarine systems are coarse-grained depositional systems associated with glacial termini and marine influence. Characteristics for the systems are highly variable facies and depositional architecture. The factors, which distinguishes the systems from other deltaic systems, are the depositional processes, the manner of sediment supply, and the influence of active, synsedimentary glacio-tectonic deformation (Lønne, 1995)

2.4.5.1 Mode of sediment supply

The glaciomarine systems have two main sediment sources: 1) Outwash material from meltwater outflow, incorporating subglacial, supraglacial, englacial and proglacial transportation. The outwash sediments consist of coarse-grained bedload material and fine-grained material from the buoyant meltwater plume (Lønne, 1995). The plume consists of fine sand and silt, which rises from the outlet of a subglacial or englacial channel (Powell & Molnia, 1989; Syvitski, 1989; Powell, 1990). 2) Basal till, or unsorted subglacial diamictic material squeezes and pushed to the base of the glacier terminus (Lønne, 1995).

The deposition of the ice-contact glaciomarine sediments takes place mainly or completely beneath the storm wave base, which is shallow in fjord basins. Ice-contact glaciomarine systems situated in fjords have an exceptional high sedimentation rate. In these systems, the glacier ice is the main contributor, where the reworking and redistribution of the waves are negligible (Lønne, 1995). However if the systems are situated near fjord mouths, over shallow marine sills, on open storm influenced shelves or is proglacial, the roles of the waves are considered influential (Elverhoi et al., 1980; Elverhøi & Solheim, 1983; Eyles, 1988; Powell & Molnia, 1989; Syvitski, 1989; Vorren, et al., 1989). Due to the high sedimentation rate and its character, a steep, prograding depositional slope form, regardless if the system is total subaqueous. The architecture of the slope exposes it to very strong resedimentation by gravitational processes (Lønne, 1995). The processes include debris flow, debris fall, turbidity currents, sediment slides and slums, small-scale gravitational winnowing (Nemec et al., 1984) and most likely slow sedimentary creep (Nemec, 1990).

High turbidity activity accompanied with the high sedimentation rate and low temperature inhibits fauna growth, causing it to be scarce or non-existent (Lønne, 1995). This leads to a low- insignificant bioturbation in the ice-proximal section of the glaciomarine systems (Syvitski et al., 1989)

2.4.5.2 Depositional processes

The ice-contact glaciomarine depositional consists of three categories, where two are relevant for the Skarmunken: 1) ice-contact subaqueous fans (Fig. 9), 2) ice- contact deltas (Fig. 10) (Lønne, 1995).

2.4.5.2.1 Ice- contact submarine fans

Ice-contact subaqueous fans (Fig. 9) are completely subaqueous systems. In cases of an ice-sheet front or in a front of tidewater glaciers in wide fjords, the fans can coalesce, creating broad aprons. The fan slope is commonly 20-30®, consisting of a submarine clastic wedged of coarse-grained sediments, containing well-bedded foreset and bottomset deposited in completely subaqueously at the grounding line of a tidewater glacier. The glacier can contain a partly floating glacier terminus (Lønne, 1995).

Numerous ice-contact fans display linear form normal to the direction of the sediment input. This is due to localized sediment input along a major part of the ice terminus (Lønne, 1995).

The ice-contact subaqueous fan is very sensitive to changes in glacier-terminus conditions, where the front of the tidewater glacier tend to be very unstable. The glacier terminus is often prone to iceberg calving, fluctuations in water and sediment discharges, switching of meltwater outlets, and short-term frontal oscillations, including glacier surges (Lønne, 1995).

The ice-contact subaqueous fan forms by resedimentation of subglacial diamictic material, outwash material from meltwater outflow and remolded sediments accreted from the substrate by the glacier, which is fused with ice-rafted debris (IRD) deposits. Syndepositional glacio-tectonic deformation is play a big role in the subaqueous fan system, controlling the architecture of the fan, the supply and dispersal of sediment. Sediment gravity-flow deposition dominates the ice-contact submarine fans. Based on facies composition, geometry, development of foreset and bottomset, the fans resemble the Gilbert-type deltas in relatively deep coastal water. The ice-contact fan forms at the glaciers underwater grounding line, below and slightly above, and represents the progradational accretion of a glacier-derived sediment on the lee slope of a local, pre-existing seafloor topography (Lønne, 1995).

From the outlet of the subglacial or englacial channel, a buoyant meltwater plume (Fig. 9) carries out fine-grained outwash material, which ascends abruptly to the free water surface shedding abundant fine sand, silt and mud on the fan slope (Lønne, 1995). In ice-contact submarine fans, the plume often sheds most of its sediment load rapidly over a narrow axial zone within a few hundred meters from the outlet (Elverhøi et al., 1980; Mackiewicz et al., 1984)

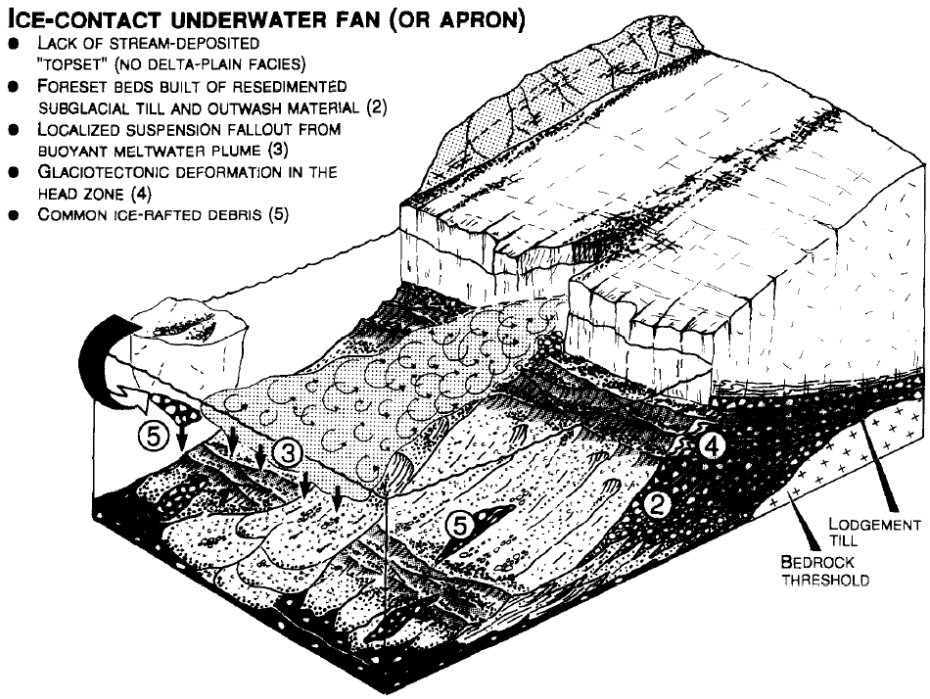

Fig. 9. Schematic figure of an ice-contact submarine fan. The different deposits are numbered and is explained in the upper leftt corner. Figure from Lønne (1995).

2.4.5.2.2 Ice-contact deltas

An ice-contact delta (Fig. 10 and Fig. 12, I) is much like the ice-contact submarine fans, distinguished by the deltas short subaerial distributary plain, developed at the top of the wedge. The characterizing feature of the ice-contact deltas are the tripartite structures of bottomset, foreset and topset deposits. Morphology wise, it compromises of a special, relatively short Gilber-type delta, formed directly at the glacier front (Lønne, 1995).

The ice-contact delta wedge consists of glacier outwash sediments. The sediments can contain stream derived distinguishable components of less well-sorted material from the glacier front till. The streams transporting the sediments are outwash streams running across the distributary plain to the delta front. As the sediments reach the delta front, reworking shoreline processes may occur

and further transports it subaqueously by gravitational processes further down the steep delta slope, below the effective storm wave base (Lønne, 1995).

An important diagnostic feature of ice-contact deltas is the presence of syndepositional glaciotectonic deformation caused by ice-front oscillations, but the delta itself is unaffected by glaciotectonics. Resedimented diamictic material are lacking in the submarine parts of the ice-contact delta due to sorting by fluvial streams along the delta plain. In an ice-contact delta, the location of glacier terminus is on the back-edge of the delta plain. Therefore, no deposition of IRD occurs on the subaqueous delta slope, except for IRD drifting from other adjacent tidewater glaciers or sea ice. The buoyant meltwater plume (Fig. 10) in the ice-contact delta tends to be relatively wide in contrast to the narrow axial zone in the submarine fans, feeding from the braided, multichannel delta plain and tends to be relatively wide. This causes a transportation and deposition in suspension over a much larger zone of the delta slope (Lønne, 1995).

The ice-contact subaqueous fan can evolve to an ice-contact delta by building up to the sea level during deglaciation. With increasing distance from the glacier terminus and the prograding delta, the ice- contact delta transforms into proglacial glaciofluvial delta. This makes the ice-contact delta a transitional stage between the ice-contact subaqueous fan and the proglacial glacifluvial delta, where in a long-term evolution of proglacial depositional conditions the ice-contact delta can appear as relatively short lived (Lønne, 1995).

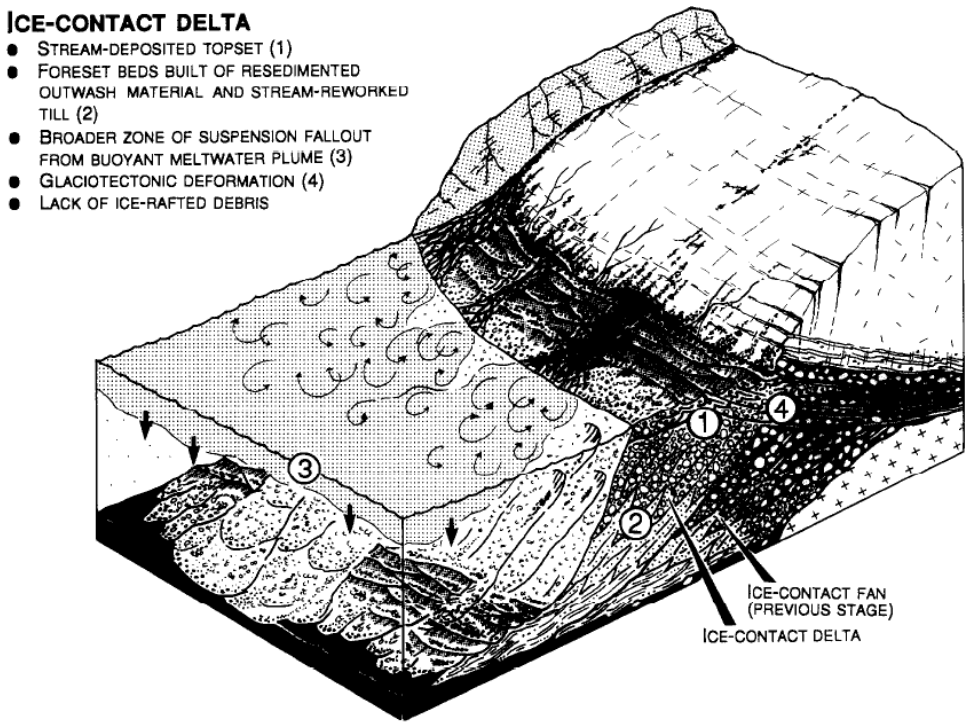

Fig. 10. Schematic ice-contact delta figure. The different kinds of deposits are numbered and is explained in the upper left corner. Figure from Lønne (1995)

2.4.5.2.3 Conceptual model for ice-contact glaciomarine systems

A suggested model for the classification of the ice-contact glaciomarine systems are the allostratigraphic conceptual model (Fig. 11) (Lønne, 1995). The concept of allostratigraphy (Walker, 1990; Walker & James, 1992; Walker, 1992) is the stratigraphic record divided by bounding discontinuities into mapable sedimentary bodies, allostratigraphic units. The division of stratigraphic record lay weight on the origin of the bounding surfaces and the geometrical relationships between the surfaces and the strata they separate. The allostratigraphic units can consist of a single lithofacies (monogenic, Fig. 12, A and B) or by an assemblage of different but genetically related lithofacies (heterogenic, Fig. 12, D-G and I- L) (Lønne, 1995).

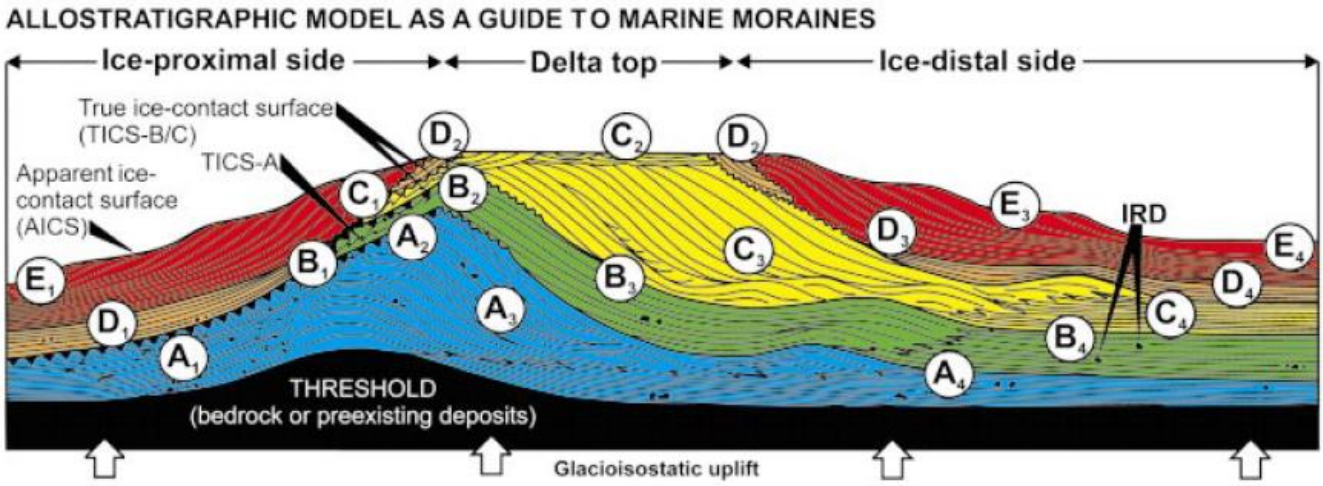

Fig. 11. Schematic figure of the allostratigraphic model with the main units are represented by A-E and the subunits 1-4. The black lines indicate true ice-contact surfaces, the apparent ice-contact surfaces and IRD deposits. Figure after Lønne (2001)

The model proposes a cycle of four phases for the systems: 1) ice-advance, 2) stillstand, 3) retreat and 4) glacio-isostatic uplift of the depositional area. The complete cycle is defined by 5 distinctive allostratigraphic units, labeled unit A-E. The unit's characteristics are their bounding discontinuities, internal facies associations, 3D shapes and bedding geometries and /or variable signs of glaciotectonic deformation (Lønne, 1995).

2.4.5.2.3.1 Unit A

Unit A is an ice-contact facies, formed during glacier advance and consists of four subunits, A1-A4 (Fig. 11). It represents the progradation of an ice-contact submarine fan contemporaneous with advance of the ice front. The unit consists of clinoformal foresets deposits, generally inverse graded and dipping away from the glacier. The foresets (subunit A3) passes downwards into subhorizontally bottomsets facies. The bottomsets (subunit A4) consists of silty mud intercalated with fine-grained turbiditic sand. Subglacial process, deposition of basal till, sorted debris and/or deformation, occur during deposition of units A3-A4, the ice proximal slope and in some cases at the fan top. These processes forms subunits A1-A2, with generally low preservation potential due meltwater flow and advancing glacier erosion (Lønne, 1995).

The glacier advance signatures on unit A can include both deposition, erosion and/or deformation. During glacier advance, the deformation can progressively change from proglacial to subglacial mode of deformation (Croot, 1988b). The switch to subglacial mode of deformation can lead to subglacial shear movement when the glacier is advancing over the fan top, creating a well-developed subhorizontal subunit A2. The subunit can be mistaken for subunit C2 (Fig. 11), the

glaciofluvial topset. Steeply inclined foresets with basinwards progradation of ice contact facies (Lønne, 1995) or boulder-rich foresets (Landvik et al., 1992), or subgacial facies includes in the depositional features. During stillstand of the glacier, the forming bedding pattern will usually dip less upwards (Lønne, 1995).

In complex ice-contact submarine fans, unit A usually makes up the lower core part (Fig. 11), whereas some fans can either consist of only unit A and/or unit Ad (Fig. 12, A and B), or comprise of several superimposed units of this type (Lønne, 1995).

2.4.5.2.3.2 Unit B

Unit B (Fig. 11) is an ice-contact facies, which forms during glacier stillstand or retreat and consists of ice-contact deposits formed during these stages. The unit consists of foreset beds (Fig. 11), generally dipping away from the glacier, where the upper part can display synsedimentary glaciotectonic deformation. The facies can be similar to unit A and as in unit A, some fans can comprise of only unit B sediments (Powell, 1981; Lønne, 1995) or as a transition from unit A to B. Foresets without any clear signs of synsedimentary ice-front advance is recognized as a characteristic for unit B (Lønne, 1995).

Unit B lay unconformably on unit A, where it is erosive in the upper fan zone. From the upper fan zone, down to the fan-toe zone, the boundary transforms from erosive to coeval concordance. In the fan-toe zone the bottomset, subunit B4, can merge conformably with subunit A4 (Fig. 11) (Lønne, 1995).

Subunit B1 (Fig. 11) forms in the ice-proximal slope (Fig. 12, K), formed by subglacial deposits, erosion and/or deformation. During glacier retreat the sedimentation can gradually change from the fan ‘s frontal slope to its ice-proximal backslope (Powell, 1990). When this occurs, a younger unit B will backlap on the previous one or deposit as foresets dipping towards the glacier. In both cases the deposits are coarse grained and from tractional currents. The switching of deposition creates an apparent topset of subhorizontal beds (subunit B2), and can be mistaken for a glaciofluvial deltaic topset (Lønne, 1995).

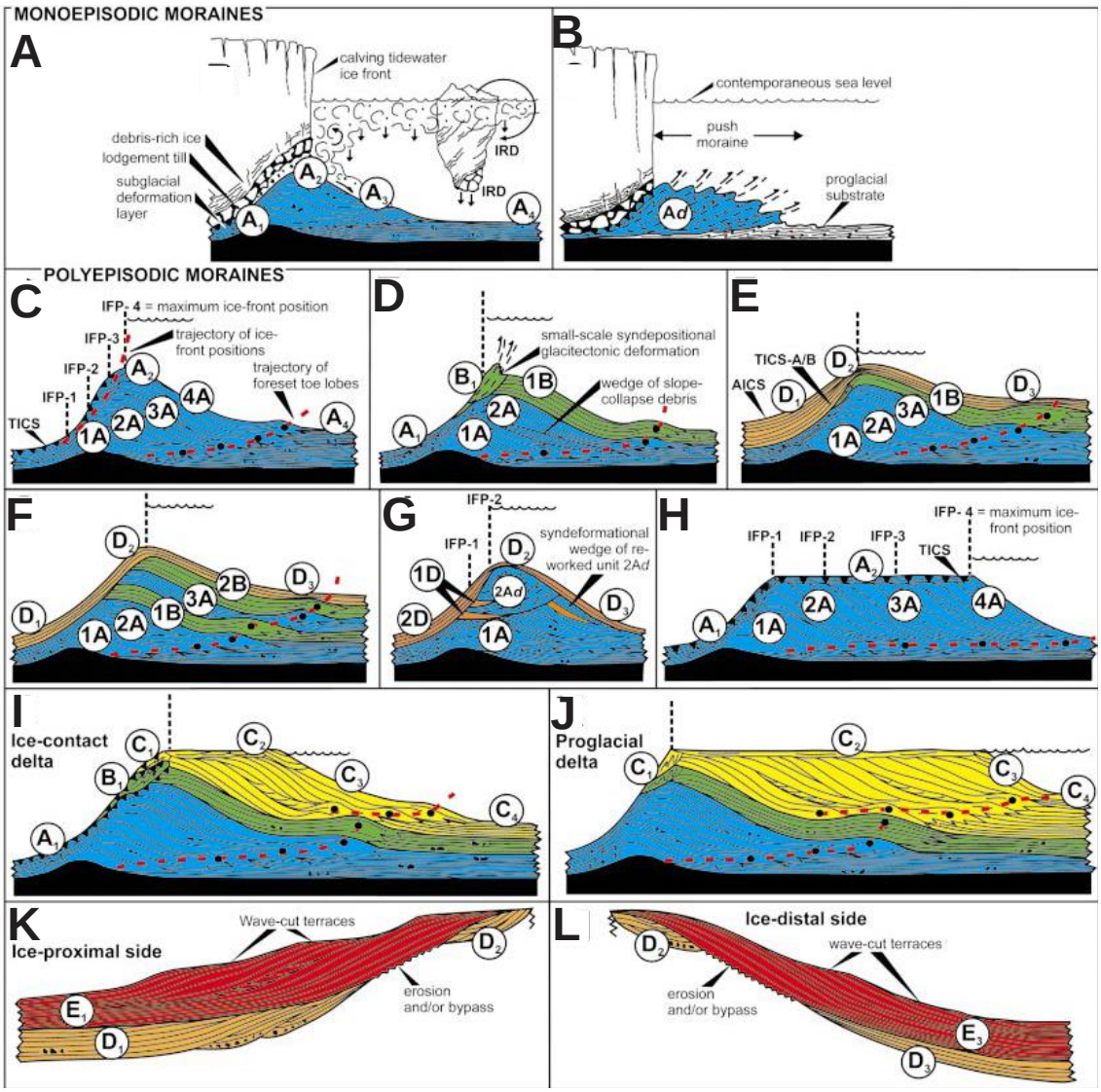

Fig. 12. Schematic model of mono-episodic (B-C), poly-episodic (D- I) moraine formation, ice-contact delta deposits (J), Proglacial delta deposits (K) and descriptive terms of different related slopes (L and M). The figure is modified after Lønne, (2001).

2.4.5.2.3.3 Unit C

Unit C (Fig. 11) is a glaciofluvial facies consisting of glaciofluvial deposits, which represents a short, proglacial and subaerial distributary plain termed the ice-contact delta plain. The unit forms the topset, subunit C_2, in the ice-contact delta and consists of subhorizontal mainly gravelly braided-stream deposits with recognizable channel lags and bars. Subunit C_1 is the ice-proximal equivalent of C_2. It consists of basal till or debris, erosion and /or deformation. Subunit C_3 is the foreset equivalent, consisting of subaqueously resedimented stream-derived material in form of turbidites and debris flow deposits on the delta slope (Thomas, 1984; McCabe & Eyles, 1988). C_3 is inverse graded and generally thinning in the dip direction, where it transforms into a bottomset. Here, the buoyant meltwater plume sheds suspension deposits on the bottomset (C_4), ranging from mud-

silty fine mud. Unit C can display iceberg related features in the ice-proximal part of C_2 and from adjacent tidewater glaciers, but usually lack this kind of features. Unit C lower boundary starts at the top, C_2, as an erosional discordance boundary, caused by the effect of the stream erosion coupled with the wave action at the delta front. Downwards at the delta slope and on the bottomset, C_3 and C_4, the boundary changes into a concordant discontinuity (Lønne, 1995).

The only criterion to recognize unit C of an ice-contact delta, is the subglacial derived diamiction and contemporaneous glacitectonic deformation. In the ice-proximal part of unit C or the entire unit C_2, the glacitectonic deformation can be more distinct. During major glacier advance, strong deformation and significant overthrusting occur in the sediments, labelled unit Ad (Fig. 11B) (Lønne, 1995).

2.4.5.2.3.4 Unit D

The unit D (Fig. 11) is an ice-distal facies, formed during glacier retreat. The unit commonly contain a highly heterogeneous facies assemblage with intraformational mud clasts and inverted textures. Deposition occur during retreat, mainly by the buoyant meltwater plume, drifting icebergs and contemporaneous gravitational winnowing from the fan surface. Synsedimentary glacitectonic deformation in the facies is only visible if readvancement occur. D_3 deposits commonly drape on the distal ice slope, the top and the proximal ice slope (Lønne, 1995).

The unit D usually displays fining graded deposits. However, the unit sedimentary facies are highly varied, often in the ice-proximal part (D_1) and the ice-distal part (D_3 and D_4, see Fig. 11 and Fig. 12, L). D_1 and D_3 are rich in slump beds and various debris-flow deposits. D_4 consists of mobile debris flow deposits, represented by more organized gravelly beds. The subunit can also be richer in turbidities than D_1 and D_3. D_2 consists of suspension fallout deposits represented by fine-grained sediments. D_2 can also display contemporaneous slump scar features, iceberg grounding and reworking of marine processes (Lønne, 1995).

Unit D is usually thickest on the ice-proximal slope (See D_1, Fig. 11 and Fig. 12, K). However, the unit will be thin if a rapid retreat occurs, where calving and abrupt cutoff of feeder channels to the fan affect the thickness. Another case is if the fan crest is steep and narrow. Cessation of coarse-grained sediments marks the Unit D lower boundary is regularly conformable with the underlying strata in the fan crest zone, towards the slope base and in the basin-plain zone. The lower boundary is disconformable in the upper- and middle-slope (Lønne, 1995 .

2.4.5.2.3.5 Unit E

The unit E (Fig. 11) forms during fan uplift. It is a non-glacial facies with no signs of contemporaneous glacitectonic deformation, varying from depositional –erosional and can resemble a glacofluvial topset (C_2). A hiatus (Fig. 11) marks the lower boundary of unit E, representing the uplift and erosion accompanied by resedimentation. Subarial erosion is a process often included (Lønne, 1995).

Unit E is generally inverse graded and forms by resedimentation and reworking of the fan deposits. When emerging, the shoreline facies can form on the former ice-distal flank (E_3 and E_4, see Fig. 11 and Fig. 12, L) and the ice-proximal flank (E_1) (Lønne, 1995). In the fan-crest zone, subunit E_2 can form if the zone is relatively wide and long and deposition occurs chiefly in storm wash over troughs and tidal channels, or inlets (Martini, 1990).

E_1 and E_3 are generally comparable in thickness. However, if exposure is too strong and basinal processes exceeds the ice-proximal processes, it will cause subunit E_3 to become thicker. Emergence and evolvement of the fan in a narrow fjord or surrounding high wave energy sea, replacement of unit E with raised beaches can occur (Lønne, 1995).

3 METHODICAL AND ANALYTICAL PROCEDURE

3.1 Fieldwork and sampling

The fieldwork was conducted from July – November 2015. 80 samples were collected for grains size distribution and 45 samples of carbonate concretions were collected for thin sections and classification. The samples were extracted from approximate 0,75m wide excavated sections. The uppermost surface of the sampled carbonate concretions was marked with an arrow.

3.1.1 Sampling strategy

3.1.1.1 Excavated sections

Sections were excavated from the bottom of the slope to the top, 20cm a.s.l. during middle high tide. The excavation was done to make a vertical profile of the deposited sediments in the slope.

The definition of a section in this thesis is a sub vertical area cut into the slope at the locality. The sections start at the bottom of the slope and continuous to the top. The starting point of the excavated sections were decided from the groundwater level. From the excavated sections, a stair was created, representing the vertical profile (Fig. 13) for the study area.

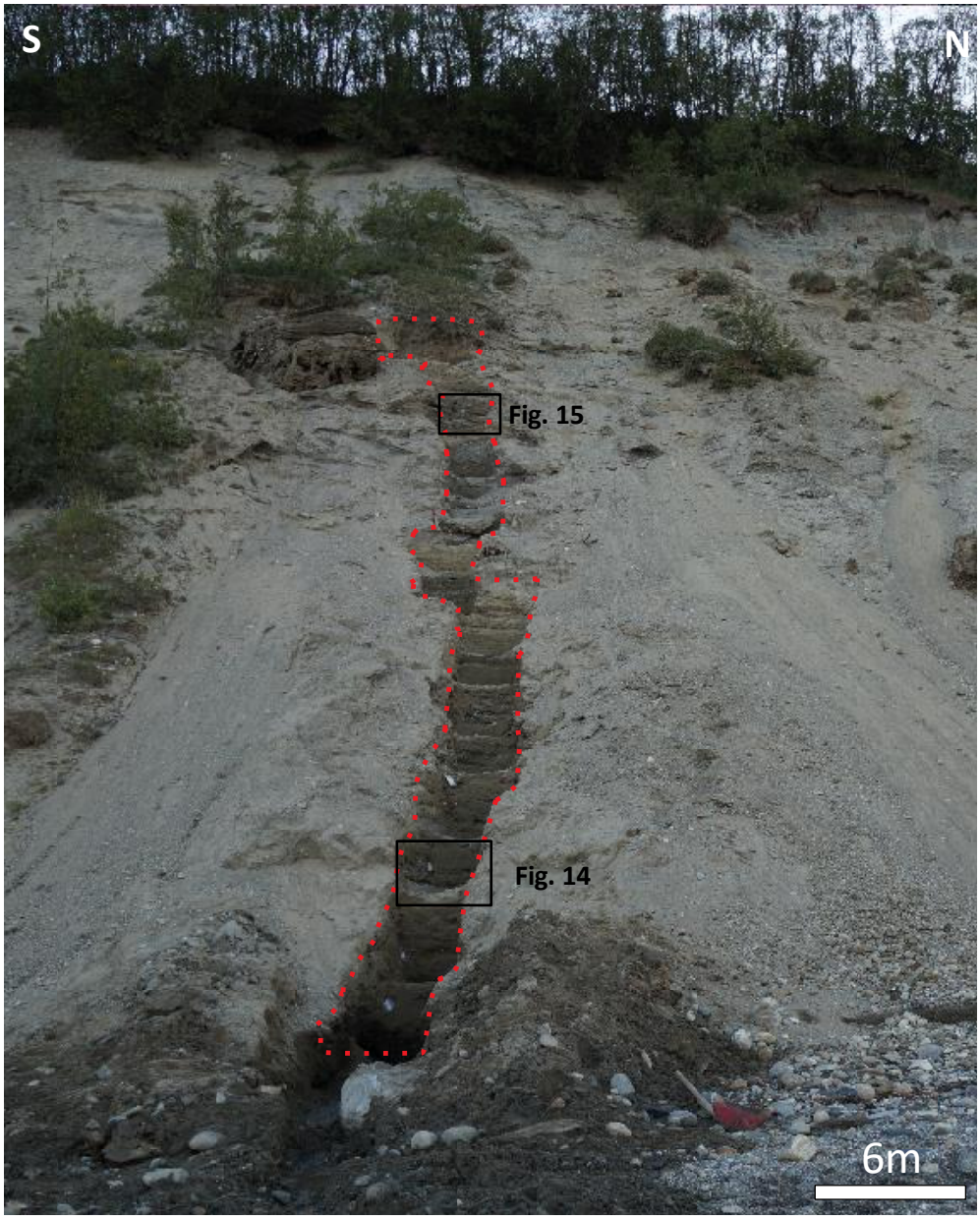

Fig. 13. The subvertical stair marked with stapled red line, representing the excavated sections and the lower part vertical profile. The location of the subvertical stair is indicated on Fig. 2. The vertical profile was measured by leveling from the highest tide erosional boundary during middle high tide up to top of the slope. The section was dug enough to reach into undisturbed layers, with a variation of 60-150cm in section width. The black rectangles represent the excavated sections in Fig. 14 and Fig. 15. The photo is taken from Skarmunken (2016).

The excavated sections were first formed roughly by shovel, where the height varied from 0,2m to > 1m. The sections were dug into undisturbed layers, both at the sub vertical surface and at the sides of the section (Fig. 14). These sides stand approximate 90 degrees to the sub vertical surface and display the dip direction of the bedding. The width of the sections in the vertical profile were decided by the depositional structures occurring in each section, where the width varied from 60-150cm.

Fig. 14. Excavated section at 2m in the vertical profile. The plastic bag in the upper left corner marks the 2m mark. The layers are displayed in both the subvertical surface (the middle section) and the sides standing 90 degrees to the subvertical. Surface. The photo is taken from Skarmunken (2016).

Three brushes of different coarseness were used to expose the depositional textural more readily, making it easier to distinguish layers and structures occurring in the sections.

Fig. 15. Excavated section at 12m in the vertical profile. The plastic bag represents the 12m mark and the black rectangles represent were the samples were extracted from. Each sample was extracted along the layers. Photo is taken from Skarmunken (2016).

3.1.1.2 Grain size distribution

The sampling strategy for the grain size distribution was to sample the most representative layer of each excavated section (Fig. 15), where the grain size was decided by grain size ruler. The size of the extracted samples is based on guidelines from the diagram by G. Coates (Fig.16), which bases itself on the mean grain size of the samples.

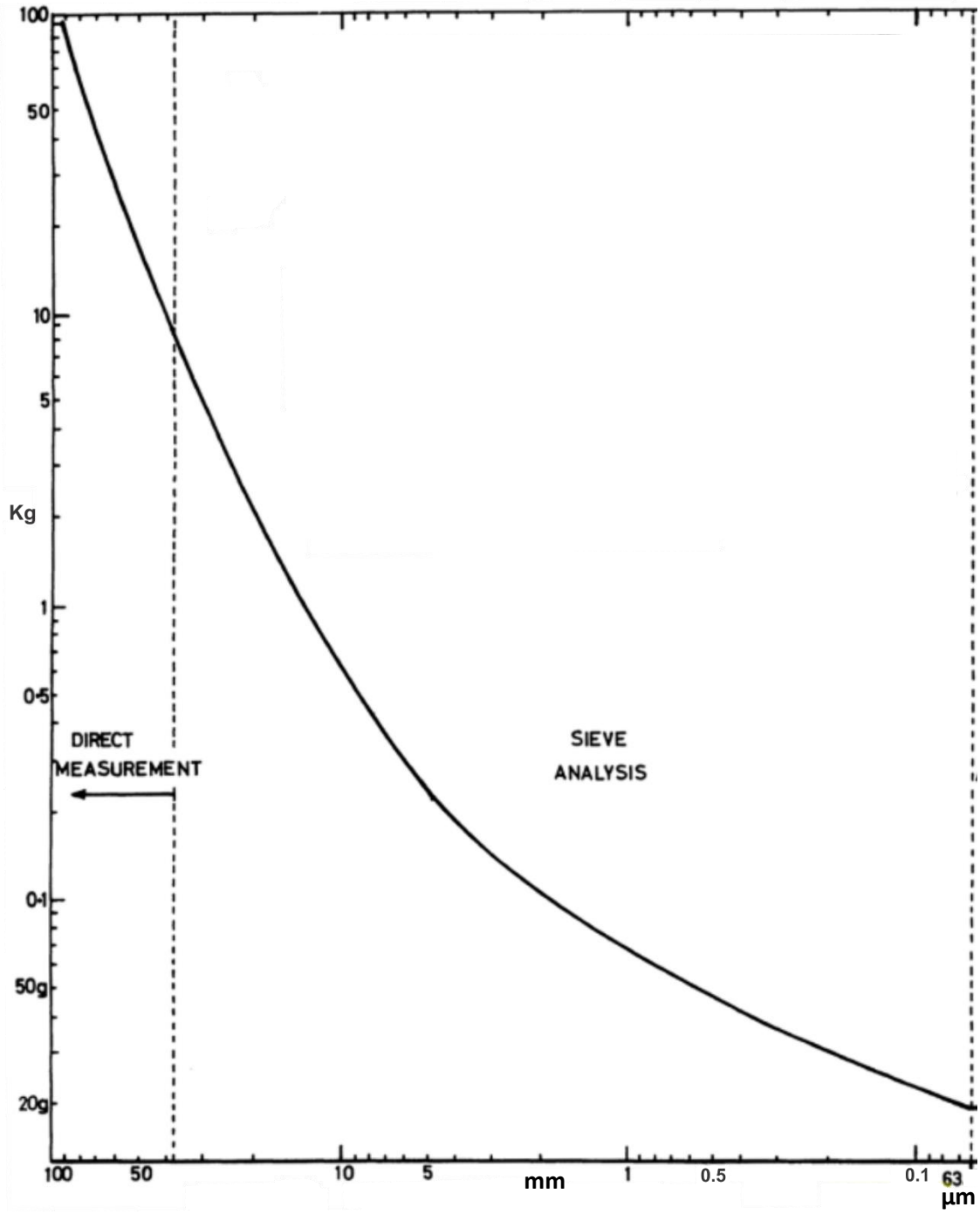

Fig.16. Diagram for minimum sample weight (kg) for standard grain size and size of the largest particle present substantial proportion (abscissa scale in mm and µm). Diagram by G. Coates (Lewis & McConchie, 2012).

3.1.2 Logging

The sedimentary log (Fig. 22) was sketched on a millimeter paper with a pencil where the sedimentary layers and structures were drawn with designated signs, described by a legend. The layer coarseness was based on the most abundant grain size in each layer, measured by a grain size ruler and a hand magnification lens. The size of each layer and occurring carbonate concretions

were measured by ruler. In the logging process, the maximum pebble size (MPS) were measured in each conglomerate layer. The MPS is measurement of the longest axes of the 10 biggest clasts in the conglomerate layer. The strike and dips were measured in dipping layer by a Silva clinometer compass with 360® scale and 90® clinometer.

In the field, the sedimentary log was drawn in 1:10 scale to get a sufficient overview of the details in each section. The presented sedimentary log (Fig. 22) is redrawn in a 1:100 scale to display the bigger picture of the layers, facies and the vertical profile.

3.1.2.1 Carbonate concretions

The excavated sections could often contain several types of shape and size of carbonate concretions. Only the representative carbonate concretions in the sections were sampled. After extraction, lose sediments on the concretion were brushed away and with a permanent marker, the upper surface was marked with an arrow or a line. This was done to get the right orientations for later work on the sample. In addition to the carbonate concretions, small amounts of sediments were sampled, laterally on each side of the concretion if possible.

3.1.2.2 Sand injections

Several places in the study area large injection zones of sand occurred (Fig. 27). These injections of sand also occurred in smaller excavated sections. Samples of these areas was therefore also taken. The same sampling procedure was used here as in normal sediment samples, where the size was decided by the grain size of the injections.

3.1.2.3 Leveling

A handheld Silva Clino Master was used to give a fairly accurate vertical height in the profile area. In the measuring procedure of the vertical profile and in the excavated section the Silva Clino Master and a yardstick were used.

The measurements were taken from the start of the slope at the highest tide erosional boundary (20cm a.s.l.), during middle high tide, to the top of the slope. Plastic bags with written height attached to metallic screws (Fig. 14 and Fig. 15) was used as markers in each section. The markers were placed for each 50cm/100cm, were the height for the markers was based on the height of each individual section and where it was most practical to place it for later logging.

3.1.3 Special concretion cases

In the study area, some special cases of concretion occurred (4.5.4.1.2.1.1 and 4.5.4.2). These concretions were much bigger (Fig. 43 and Fig. 47) and appeared to be in situ. The concretions inspected were carefully excavated with shovel and brush in the more delicate areas. Pictures of the concretions was taken from several different angles to get as much as details documented. The concretions were measured in maximal height and length.

3.1.4 Large-scale bedding-plane traces

The large-scale bedding-plane traces was investigated by observations mainly from the photographs from Hjellneset as they gave the full overview of the bedding planes. In addition, investigations were also done at the beach zone in Skarmunken as supplements to the big picture.

3.1.5 Photographs

The photos were taken with a Sony α 3000 camera. The lens used for photos was an E 18- 55mm and were taken on intelligent auto function with auto focus. The strategy for the photographing was to take the photos during cloudy days, or as the sun stood directly on the exposed sections. Of the photos, most of them were taken during cloudy days, only a few pictures were taken after sunset and in the evenings.

3.2 Procedures

3.2.1 Sample preparation

80 sediment and 45 carbonate concretion samples were collected from the Skarmunken area. The preparation of the samples was conducted at the University of Tromsø.

3.2.2 Grainsize analysis

To determine the grain size distribution of the samples, the sieving method is used. The method was divided into wet sieving and dry sieving, where the samples were first wet sieved, before they were dried sieved. Both procedures were used to get a more accurate result.

3.2.3 Wet sieving

A standard sieving tower consisting of 63µm, 125µm, 250µm, 0,5mm, 1mm and 2mm sieves were chosen after consulting with the laboratory staff. The sieving tower were built in the same order, where 63µm sieve were the lowermost and the 2mm sieve where the uppermost. Beneath the sieving tower a 2L bowl was placed to gather sediments <63µm. A shower head connected to the sink was used to pour water on the tower.

The material in the sieves were placed in separate bowls. The bowls were marked with name and grain size on a tape piece and placed in a drying closet holding 40°C for 24 hours. The 2L bowls with water and material <63 µm were also put in the same drying closet. Due to the water amount in these bowls, some water was emptied in the sink to speed up the drying process. This was done as soon as the particles in the bowls had settled at the bottom. This took usually 1-2 days.

Due to low or none salinity in the water, some of the 2L bowls were introduced to NaCl to either speed up of force particles to settle. By introducing the NaCl, a flocculation process could initiate, causing an increased particle settling speed (Kahn, 1957; Rasmusson et al., 2004) of the particles. In the first round 0,5 g of salt was introduced as a test to see the effect first. The first two subjects were 4,87m A and B (Table A1). The settling time took around a day. The next subjects (Table A1) were introduced to 1 gram NaCl to see if there was any notable difference in time. The complete settling time were not observed to settle within the observation hours (10h), but rate of settling of the bigger particles appeared to be faster.

3.2.4 Dry sieving

When the drying of the samples was finished, all the material from the sample were dried sieve. This was done to get even more accurate grain size distribution.

The dry sieve uses the same type of sieves for the sieve tower except for the 2mm sieve. Several of the samples were split due to their big size to prevent clogging of the sieves. The 2mm sieve where removed due to the common occurrence of poorly cemented carbonate nodules in the samples. The wet sieved ≥2mm grains were removed from the rest of the sample during the dry sieving, but were included in the final result. The sieve tower was put in a sieve shaker machine, Retsch AS 200 basic and set to shake 10min at 60 rpm. All the different grain sizes were placed into separate bowls marked with name and grain size.

3.2.5 Weighing of samples

All the different grain sizes were weighed (Sartorius ED 2202S- CW and LP2200P) and put into a datasheet in an excel table (Table A 8). When each grain size fraction was measured, the material was put in their respective plastic bag, marked with name, Grain size and weight. After each weight measurements, the weight surface was cleaned with paper.

3.3 Total carbon, organic carbon and sulphur analysis

3.3.1 Sample preparation

3.3.1.1 Total carbon and total sulphur

From the finer 63 to <125µm clayey samples, 14 dry samples (Table A 3) were chosen for the total carbon (TC), total organic carbon (TOC) and total sulphur (TS) analysis. 10g from each sample were removed, where 2g were extracted. The extracted sample material was then placed in a mortar Retcsh RM 100 machine, crushing the sample for about 10 seconds. The sample was then brushed into the middle of the mortar bowl and the machine was started and the procedure was repeated. This was done to get a more optimal crushing of the material. After the crushing process, the samples were placed in small metal bows, on a plate of aluminum foil.

3.3.1.2 Total organic carbon, original method

0,45-0,5g sample material were extracted from the crushed material and placed in white crucibles on a plastic tray. The name and weight were noted on a paper map of crucibles and the tray. The tray was placed in a heater, holding 40 °C for 1 night.

The tray was moved to a protected location where each sample were introduced to 10% warm HCL, were only a few drops were added each time. This was done to remove calcite and dolomite (Eq.1). The acid seeped through samples 3 times.

$$CaCO_3 + 2HCl \rightarrow CaCl_2 + CO_2 + H_2O \quad \text{(Eq.1)}$$

Distilled water was added to each sample to wash out the HCl, as the Cl could destroy the combustion instrument and the analysis. The water amount was limited to the height of the containers to prevent spilling of sample material. When the water had seeped through the samples, the procedure was repeated 7 times.

After the washing procedure were completed, the tray with the samples were placed in a drying closet holding 105®C for 12 hours.

3.3.2 Combustion analysis procedure

3.3.2.1 Total carbon and total sulphur

The pressurized air and oxygen vents were opened and the combustion oven was turned on. The combustion oven was heated for at least 1 hour before the CS-200 program was started. After the program was started, a system leak test was conducted. 0,2-0,4g of the sample material from the

metal bowls were added to crucible, where the weight was transferred to the datasheet in the Leco CS-200 machine. One scoop of Lecocel ll and one scoop of iron chip accelerator was added to each sample before they were inserted into the combustion oven. After each 10th analyze the oven is cleaned automatically.

3.3.2.2 Total organic carbon

The analyze of the test is done in the same manner as the analyze of the TC/TS. The procedure for the sample weight was conducted, inserting the weights into the datasheet in the Leco-CS-200. The total result was transferred to an excel sheet and can be viewed in Table A 6.

3.4 Thin sections

11 concretions were chosen for production of the thin sections (Table 4). Coarse –grained concretions had priority as they contained more pore space than more fine-grained rocks. Both coarse-grained and fine-grained concretions was chosen for thin section production. Due to poorly cementation of the carbonate concretions, all the concretions had to be vacuum impregnated with blue epoxy gel to prevent the carbonate concretions to fall apart during the process of making of thin sections. 11 standard thin section were made by the personnel at the laboratory with blue epoxy gel, polished surface without cover glass or lacquer. The thin sections were analyzed by Leica DFC450 with planpolarized, polarized and incident light.

3.5 Methodological background

3.5.1 Assessment of data quality.

3.5.1.1 Logging

The quality of the results obtained from logging method were highly dependent on human individual factor where the personal artistic ability and the eye for important, but not necessary obvious structures and features were important. The log represents the combination of 15 millimeter papers, which lead to the loss of distinct features and immense compaction of already thin layers. Minor errors in the height assessment of the layers were observed and correction by comparison of pictures and the vertical log. The correction result by using photos for correction might deviate to some degree but it is not significant.

3.5.1.2 Grain size distribution

By the choice of a standard sieving tower (63µm-2mm sieves), the grain size distribution results are somewhat limited. In addition to the standard 0,1% error margin, all the grains below 63µm and above 2mm are not accounted for and only fall under the category <63µm and >2mm. Clogging, coating of rocks and the lower surfaces of sieves occurred in some of the sample and have probably affected the grain size distribution to some degree, but most likely it is not significant. The grains sieved by wet sieving below <63µm were extracted after wet sieving and was therefore, not affected by the coating events during dry sieving.

Due to the lack of usage of additional finer and coarser sieves, the result was not satisfactory and showed to little information and was therefore left out of the result. It can however be viewed in the appendix (s. 203) if it is of interest.

3.5.1.3 MPS analyze

The maximum pebble method is to be considered a rough and purely statistical approximation, where the analyze is very dependent on the environment and certain requirements must be met before use (3.5.1.3).

3.5.1.4 TOC/TS

The data quality is highly dependent of the routines and standards for the sample preparations and combustion analysis. If the correct routines and standards are not met, it will alter the result significantly. If all the correct requirements are met, the standard deviations for carbon is 2ppm or 0,5% and 2ppm or 1,5% for sulphur, or the biggest component.

3.5.1.5 Thin section analysis

The chosen carbonate concretions were not all representative and usable in the analyze. This was due to poor choices and bad cutting of the carbonate concretions. A few of the thin sections only display on big clasts with little cement around. This limited the result of the analysis to some degree.

3.5.2 Total organic carbon/total sulphur ratio

The TOC/TS ratio plot can determine the sedimentary depositional environments and diagenetic processes (Leventhal, 1995). The TOC/TS plots were first used for modern marine setting and presented by (Berner, 1970) and (Sweeney, 1972), where Leventhal (1983, 1987) was the first to use the method for ancient depositional environments.

TOC/TS method derives from the process of sedimentary pyrite formation (Goldhaber & Kaplan, 1974; Berner, 1984). The formation of the pyrite takes place in the early diagenesis when the H_2S reacts with detrital iron minerals. The source of H_2S is bacterial reduction of dissolved SO_4^{2-} supplied by the overlying water. Buried organic material in the sediment oxidize in this process represented by Eq.2 (Berner & Raiswell, 1984).

$$2CH_2O + SO_4^{2-} \rightarrow H_2S + 2HCO_3^- \qquad \text{(Eq.2)}$$

From the TOC/TS method, Morse and Berner (1995) determined that fine grained, normal marine siliciclastic sediments have a relatively narrow range of TOC/TS ratios. Berner (1982) calculated from own and other 's previous work, (Goldhaber and Kaplan, 1974; Volkov & Rosanov, (1983) the value of normal marine sediments to be 2.8^{+}_{-} 0,8 for the TOC/TS weight ratio. Deposition under alternating freshwater and marine water or high variable inputs of organic matter, can lead to TOC/TS ratios, which is not in the range of 2.8^{+}_{-} 0,8 (Morse & Berner, 1995).

Sediments deposited under fluctuating conditions, such as alternating freshwater and marine deposits or highly variable inputs of organic matter, may not have TOC/TS ratios in the range of 2.8^{+}_{-} 0,8.

The definition of fine-grained, normal marine siliciclastic sediments is "sediments overlain by oxic seawater of typical oceanic salinity. Excluded from the larger coarse sandy sediments, $CaCO_3$- rich and sediments overlain by freshwater and anoxic marine waters" (Morse & Berner, 1994).

Berner and Raiswell (1984) and Tanaka et al. (1981) states that freshwater sediments contains on average less than 1% SO_4^- of that found in oceans due to the low salinity. For this reason, the formation of pyrite is low, in contrast to the abundance of organic matter and detrital iron minerals. From these facts, marine and freshwater paleosediments are distinguishable (Fig. 17). Berner and Raiswell (1984) propose that, "C/S ratios for sedimentary rocks containing more than 1% organic carbon by weight can be useful tool for distinguishing freshwater from marine sediments". If salinities are lower than half the salinity of seawater, brackish water sediments might be distinguishable (Berner & Raiswell, 1984).

It should be noted that the burial rates influence the organic carbon buried positive and the burial rate correlate directly with the fraction of sulphur that is fixed as pyrite negative (Morse & Berner, 1994).

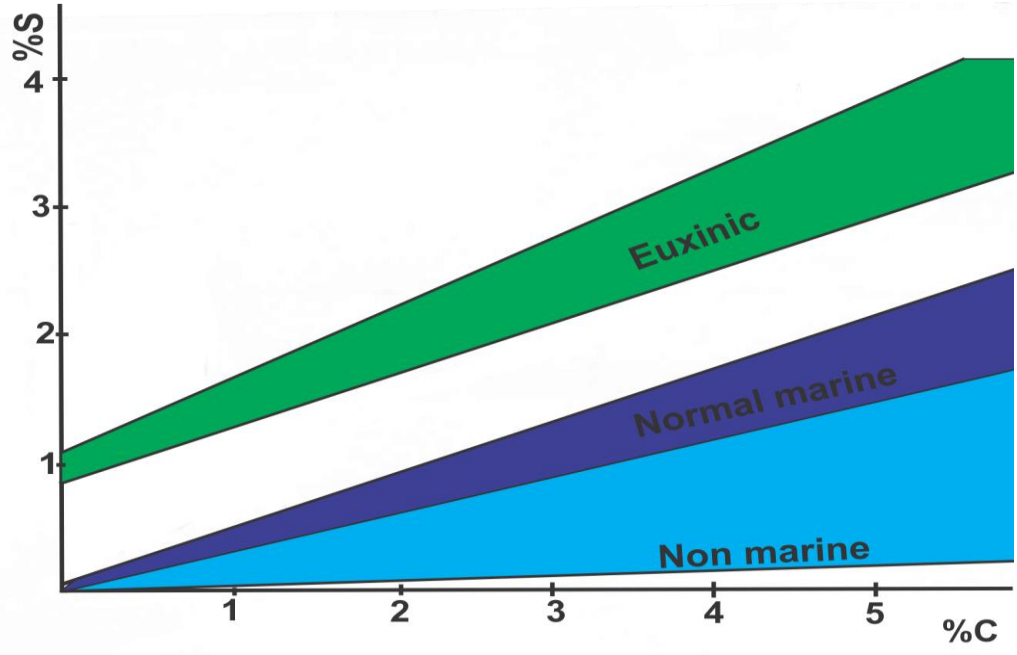

Fig. 17. Carbon- Sulphur plot displaying commonly recognized fields euxinic water column, normal marine oxic depositional settings and nonmarine depositional setting. The figure is modified after Leventhal (1995)

3.5.3 Carbonates concretions

Carbonate concretions are cemented and lithified sedimentary deposits, which display various morphologies. They are often affiliated with hydrocarbon seeps, whether marine, lacustrine or terrestrial, (Jørgensen, 1992a; Peckmann et al., 2001; Hovland et al., 2005; Niemann et al., 2005; Naehr et al., 2007; Pearson et al., 2010) where they form by the migration of hydrocarbons through sediments.

It is confirmed that seep sediments are characterized by high horizontal and vertical heterogeneity (Dando et al., 1994; Treude et al., 2003; Treude & Ziebis, 2010), which represents chemically suitable horizons for carbonate precipitation. The idea of sediment heterogeneity is supported by Jørgensen (1992a), which reports both of vertical chimney carbonate concretions and horizontal cementation parallel to the bedding planes, where Jørgensen (1992a) speculate that the latter may have formed in directly contact with vertical gas chimneys, or as the result of more diffuse gas discharge trough the sediments (Jørgensen, 1992a).

Peckmann et al. (2001) suggests different morphology of the carbonates depending on the oxic, anoxic environment and the interface zone between the oxic-anoix (Fig. 18). The oxic zone is suggested to contain flat, pancake-shaped, 20-30cm in diameter, or con-spicuous, central, 1-2cm wide channel, where gas seep through the holes, carbonates. These carbonates are confined to anoxic sediments without any positive seafloor relief. In the oxic-anoxic interface, the carbonates are porous with cavity walls, increased thickness up to 10cm and are abundantly lined by microbial films. The anoxic zone contains irregular, small chimney concretions, which arises from flat carbonates plates that range up to 20cm in thickness and about 1m in diameter, where the chimney size increases with depth (Peckmann et al., 2001). Jørgensen (1992a) supports increased sizes in carbonate growth in the anoxic diagenetic zone of the sediments and reports of the occurrence of blocky sandstone carbonate boulders and vertical pillars of several meters.

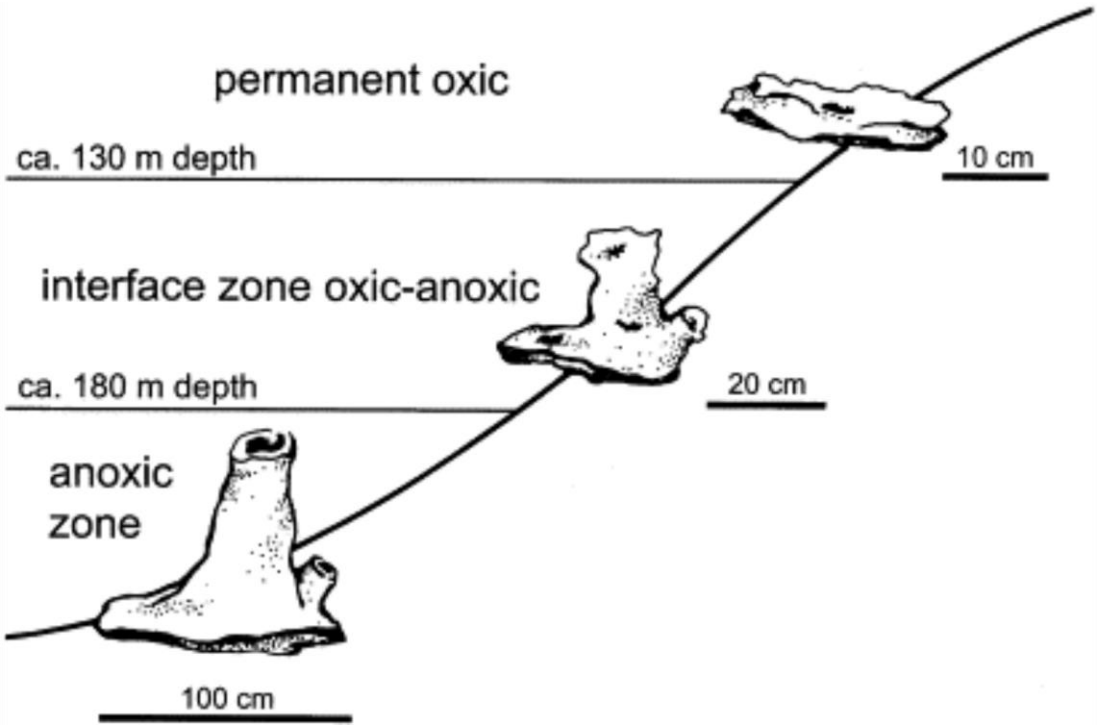

Fig. 18. Schematically carbonate concretions morphologies, divided into three groups: permanent oxic zone, oxic-anoxic interface and anoxic zone. The anoxic zone has the highest relief, where it is reduced moving towards the permanent oxic zone. Figure by Luth et al. (1999).

3.5.3.1 Chimney concretions

Chimney morphologies are a common occurrence in submarine gas seeps, with commonly irregular surface with nodule protuberances and fluid channel ways (Fig. 19) (Diaz del-Rio et al., 2003). The chimneys can occur as straight, tortuous, ramified and helical (Fig. 19), where growth layers can appear on the walls of the chimneys (Diaz del-Rio et al., 2003). The chimney sizes vary from 15-55cm in length and 5-30cm in diameter, where the chimneys represent the long term effect of channelized hydrocarbon gas stream (Jørgensen, 1992a; Diaz-del-Rio et al., 2003; Treude & Ziebis, 2010).

A common feature within the chimneys is the termination of the chimney top. Two types (Fig. 19) of terminations of the pipe-like chimneys is recognized: 1) bullet-like termination, displaying progressive thinning of cylindrical pipe towards the top and 2) mushroom-like termination, characterized by a protuberance enclosing the top of the pipe-like tubes (Diaz del-Rio et al., 2003).

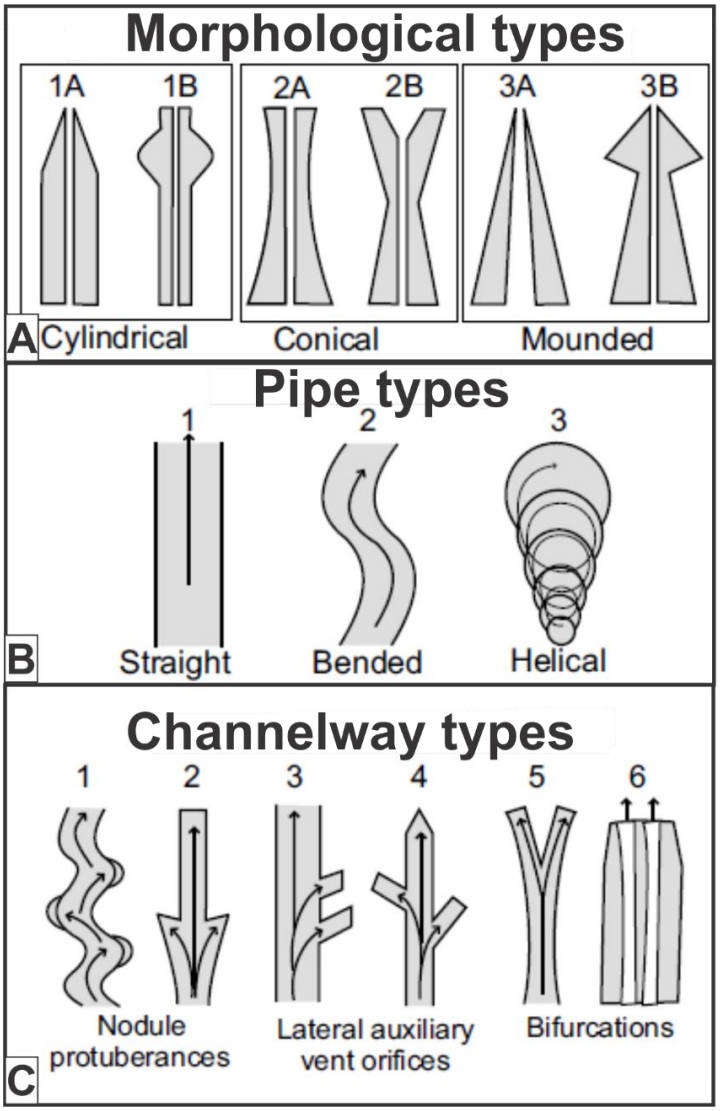

Fig. 19 Schematically figure of the recognized chimney types located in the Gulf of Cádiz. (A) 1A and 1B represents cylindrical pipes, 2A and 2B represent conical pipes and 3A and 3B represent mounded pipes. 1B, 2B and 3B display mushroom termination, and 2A display bifurcation venting. (B) Three different types of pipe morphologies, straight, bended and helical. (C) The effect of different types of channel pathways on the pipes. 1 and 2 display nodule protuberances, where 2 only have nodule protuberance at the base. 3 and 4 represent lateral auxiliary vent orifices on one side (3) and on alternating sides (4). 5 and 6 represent bifurcated pipes, where 5 is bifurcated vent orifices at the top and 6 is a chimney with two vent orifices. Figure by Diaz-del-Rio et al. *(2003).*

3.5.3.2 Carbonate cement

The nucleation and growth of crystals within pore spaces in porous sediments is the processes of cementation. The cementation lithifies the sediment into a rock, reducing the porosity and permeability, where only cementation of a few percentage of the pore spaces is needed for lithification and creation of nodules and concretions/concretions (Nichols, 2009).

3.5.3.2.1 Carbonate precipitation

The precipitation of authigenic carbonates, only occur if the pore fluids are sufficient supersaturated with respect to the carbonate phase and uninterrupted crystallization by kinetic

factors (Burton, 1993), which require thousand times the pore volume of fluid to pass through the sediment in order to cement the pore spaces, due to low solubility of carbonate mineral phase in aqueous solutions (Luff et al., 2004)

The main process for carbonate precipitation in shallow subsurface is the anaerobic oxidation of methane (Naehr et al., 2007). Whereas the anaerobic oxidation of methane (AOM) is responsible for carbonates formation in the shallow subsurface, carbonates precipitation deeper into sedimentary section may be associated with methane production (Orphan et al., 2004), gas hydrate formation (Kastner et al., 1990), or decomposition (Matsumoto, 1989).

3.5.3.2.1.1 Methane oxidation

In general, in marine environments, methane oxidation is the most important process of carbonate precipitation. This occurs when methane migrates upwards into overlying diagenetic zones and is oxidized by oxygen or sulfate bearing water (Fig. 20) (Claypool & Threlkeld, 1983; Gautier & Claypool, 1984). The oxidation is a bacterial reaction and takes place in an anoxic or oxic environment. In anoxic environment (Fig. 20), the methane is consumed as an energy source by sulphate- reducing bacteria (Eq.3) and in oxic environments (Fig. 20) the methane is also used as an energy source, utilized through the activities of aerobic methane oxidizing bacteria (Eq.5) (Reeburgh, 1983; Iversen & Jorgensen, 1985; Whiticar et al., 1986). The biogenic methane is formed in the carbonate-reducing zone (Fig. 20), by either CO_2 reduction (Eq.8) or CH_3COO^- fermentation (Eq.7) (see Biogenic methane formation pathways).

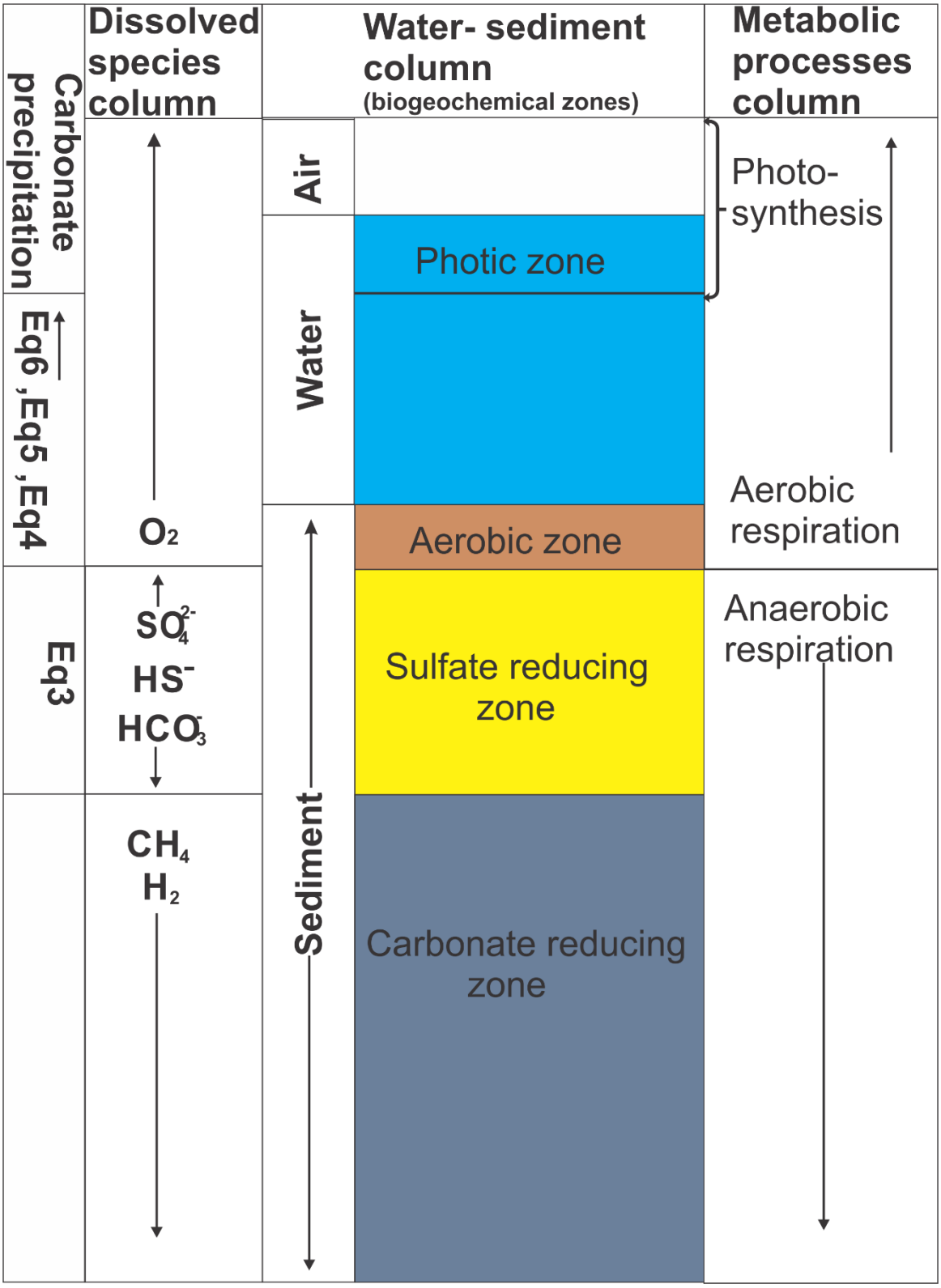

Fig. 20. Schematically figure for an open marine environment showing the different processes, which leads to methane generation. The rightmost column displays where the different metabolic processes occur. The right middle column gives an overview of the biochemical zone, which zone who consists of sediments, water and air. The left middle column represents the dissolved species in the different biogeochemical zones. The leftmost column shows where the different carbonate precipitation reactions occur represented by Eq.3, Eq.4, Eq.5 and Eq.6. The figure is modified from Rice & Claypool, (1981).

As biogenic gas is seeping upwards it in encounters the carbonate reducing zone (Fig. 20), which is the most important zone for the formation of CH_4 in marine sediments. In this zone, bacterial fermentation processes occur and is the biogenic methane accumulation zone, stretching down too approximate 1000m. Here the CO_2, produced by anaerobic oxidation of organic matter, is reduced by H_2 (Rice & Claypool, 1981; Nichols, 2009). Over the carbonate reducing zone is the sulphate reducing zone located (Fig. 20). The migrating gas encounters sulphate-reducing bacteria's, which oxidizes the methane and produces HS^-, HCO_3^- and $H_2\mathrm{O}$ (Eq.3). In the uppermost part of the sediment column in the sediment/water interface is the aerobic zone (Fig. 20). This is the start of the aerobic respiration zone, where aerobic bacteria consume CH_4 and O_2 , which can produce either $CO_2\ and\ H_2O$ (Eq.4) (Ritger, Carson, & Suess, 1987) or $HCO_3^-, H^+ and\ H_2O$ (Eq.5) (C. Paull & Iii, 2008).

The CO_2, is in turn consumed by bacteria, e.g. *Beggiatoa*, producing H_2SO_4 and organic matter (Eq.6). If the methane seepage is strong enough, it will reach the photic zone, eventually the water/air interface and beyond. In the photic zone, the photosynthesis is the dominant metabolic process (Rice & Claypool, 1981).

The methane oxidation is divided into two main processes: methane oxidation by sulfate reduction and methane oxidation by aerobic bacteria.

3.5.3.2.1.1.1 Methane oxidation by sulfate reduction

The methane oxidation by bacterial sulfate reduction is an anoxic reaction, where the sulfate reducing bacteria uses the methane as an energy source. The process commonly occurs beneath the sediment/water interface, stretching down to approximate 10 cm (Nichols, 2009) and is most active near the base of the sulfate reduction zone (Iversen & Jørgensen, 1985; Whiticar & Faber, 1986). The methane oxidation by sulfate reduction is represented by Eq.3 (Ritger et al. , 1987):

$$CH_4 + SO_4^{2-} = \mathrm{HS}^- + HCO_3^- + H_2\mathrm{O} \qquad \text{(Eq.3)}$$

Early diagenetic pyrite formation and preservation of organic material, in anoxic conditions, commonly accompanies the sedimentary sulfate reduction (Berner, 1981). Therefore, carbonate precipitated in sulphur reduction zone in general contain pyrite and the host sediment can be relatively enriched with organic matter (Hudson, 1978; Gautier & Claypool, 1984;). Other distinct features of the methane oxidation by sulfate reduction is nodular form and often relatively fine crystal size, micrite or microspar, of the carbonate (Hovland et al., 1987).

3.5.3.2.1.1.2 Aerobic methane oxidation

The aerobic methane oxidation is a bacterial process, concentrated at the oxic-anoxic boundary (Fig. 20) (Hovland et al., 1987). The oxidation occurs due to excess of methane distribution from deeper sources reaching the surficial sediments and the sediment-water interface (Jørgensen, 1992a). The aerobic methane oxidation is represented by (Eq.4 (Ritger et al., 1987) and Eq.5 (Paull & Iii, 2008):

$$CH_4 + 2O_2 = CO_2 + H_2O \quad \text{(Eq.4)}$$

$$CH_4 + 2O_2 = HCO_3^- + H^+ + H_2O \quad \text{(Eq.5)}$$

The produced CO_2 from Eq.5 and H_2S is further consumed by bacteria's, e.g. *Beggiatoa, reducing the* CO_2 amount and producing organic matter, represented by Eq.6 (Sassen et al., 1993):

$$CO_2 + H_2S \rightarrow H_2SO_4 + CH_2O\ (organic\ matter) \quad \text{(Eq.6)}$$

The aerobic oxidation of methane is assumed to have the opposite effect, leading to pH decrease and resulting in carbonate dissolution rather than precipitation (Hovland et al., 1987). However, in several sites in northern Kattegat, where a continuous gas ebullition is frequently observed, intertidal and beach sediments are carbonate cemented, interpreted to most likely be the product of aerobic methane oxidation (Jørgensen, 1992a).

3.5.3.2.1.2 Environmental precipitation control

Aksu et al. (1995) recognize that stratified, colder and more saline water masses prevent the development of cemented carbonate nodules, clasts and the total carbonate content of sediments. In contrast, Burton & Walker (1987) observed an increase of $MgCO_3$ with increase in temperature.

Fluid expulsions and possibly subsequent feeding sources for precipitation of carbonates is suggested to link with the presence of glaciers, where the expulsions is suggested to be triggered by rapid sediment loading by glacial derived sediments (Hustoft et al., 2009).

Feng et al. (2008) suggests that the main factor controlling the redox condition of seep carbonates is the flux rate of fluids at the seep site. Under relatively slow seepage conditions, carbonate precipitated deep below the water/sediment interface where conditions are anoxic, carbonate concretions appear generally not very porous and have depleted ^{13}C values. Fast seepage however, leads to precipitation in shallower subsurface and even near the water/sediment interface, where conditions are aerobic. These carbonates are considerable porous and less depleted ^{13}C values.

3.5.3.3 Carbon source

The carbon source for precipitation of carbonates in hydrocarbon seeps are mainly methane, derived from organic matter. The origin of the methane oxidized is divided into biogenic methane and thermogenic methane.

3.5.3.3.1 Biogenic carbon

Biogenic gas in nature forms from organic matter by anaerobic microorganisms (Rice & Claypool, 1981) suggested to form at temperatures <50®C (Stolper et al., 2014). Biogenic gas occurs in geologically predictable events, widespread and in large quantities at shallow depths, commonly formed at depths <1km (Rise & Claypool, 1981).

Rice and Claypool (1981) propose certain requirements that must be satisfied for methane production: 1) the environment must be anoxic. 2) The environment must be sulfate-deficient, in marine environments the sulfate level needs to be reduced almost completely before significant amounts of methane can accumulate. In fresh and brackish water, the sulfate level is low, and methane production starts as soon as O_2 is depleted. 3) The temperature when generation methane must be <50®C. 4) A minimum of 0,5% carbon in the sediments is required to support methane production (Claypool & Kaplan, 1974; Rashid & Vilks, 1977) , where the organic matter is commonly concentrated in fine grained sediments (Hunt, 1972). 5) Bacteria have an average size of 1-10µm (Momper, 1978) and therefore require sediment pore spaces bigger than this to function in the sediments (Rice & Claypool, 1981).

3.5.3.3.1.1 Biogenic methane formation pathways

The biogenic methane is generated from two primary metabolic pathways (Balch et al., 1979), 1) fermentation of acetate and 2) reduction of CO_2 (Whiticar et al., 1986). The acetate fermentation refers to collectively to methanogenesis involving the transfer of a methyl group from any substrate, represented by Eq.7 (Whiticar et al., 1986):

$$CH_3COO^- + H^+ \rightarrow CH_4 + CO_2 \qquad \text{(Eq.7)}$$

In Eq.7, the methane is derived from the methyl group of acetate (Pine & Barker, 1956; Smith & Mah, 1980). The second method of methane generation is the oxidizing of acetate forming CO_2 and H_2O, where the CO_2 is metabolically reduced to CH_4 with H as electron, represented by Eq.8 (Whiticar et al., 1986):

$$CO_2 + 8(H) \rightarrow CH_4 + 2H_2O \qquad \text{(Eq.8)}$$

In freshwater environments, fermentation of acetate is considered as the main source of CH_4 (about 70%) (Koyama, 1963; Takai, 1970; Beliaev et al., 1974; Winfrey & Zeikus, 1977). In marine environments the $C0_2$ reduction is recognized as the main CH_4 source and can be the dominant one source in low sulphate freshwater environments (Whiticar et al., 1986) e.g. hot-spring algal mats (Sandbeck & Ward, 1981).

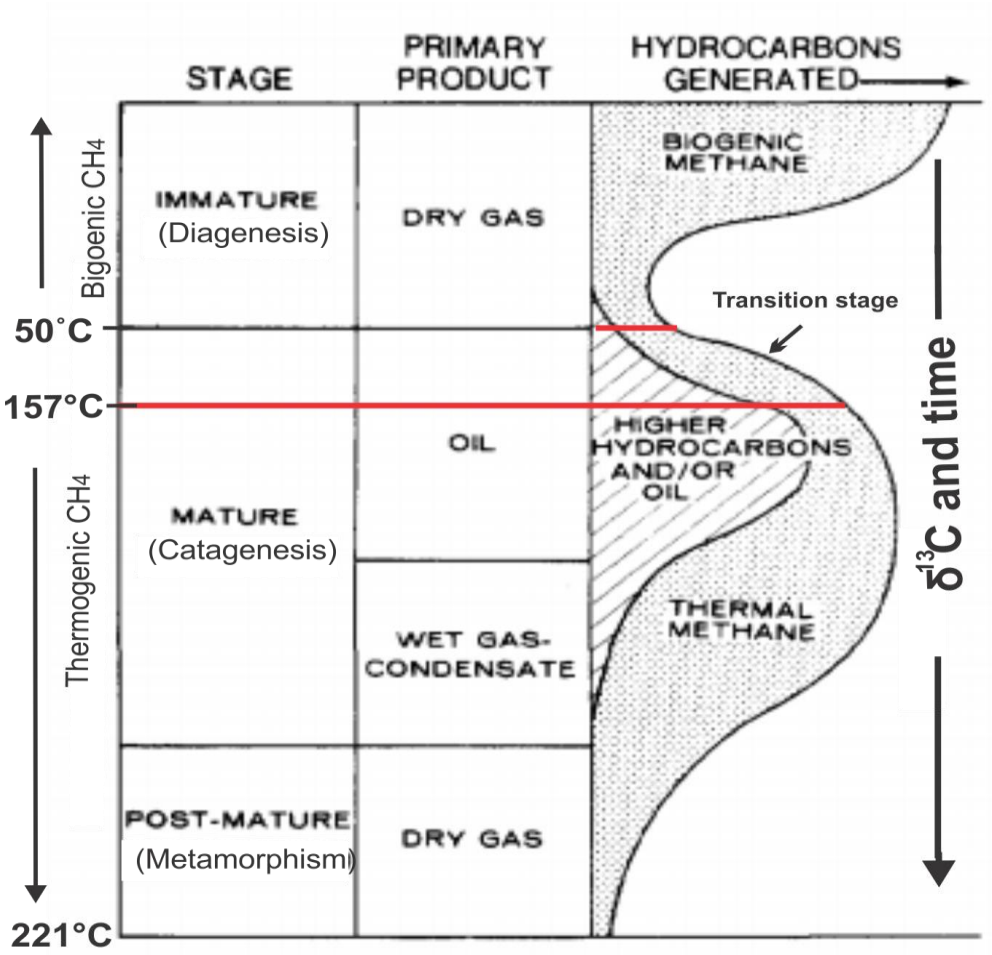

Fig. 21. Schematic figure of the methane generation, divided into tree columns. The left column refers to the thermal maturity stages of organic matter in sedimentary rocks with the increase of time and temperature, represented, by tree main stages. The middle column displays the primary hydrocarbon product produced as time and temperature increase. The right column displays the general distribution of hydrocarbons distributed at the different thermal maturity stages and the $\delta^{13}C$ general concentration. The red line indicates the boundary for biogenic and thermogenic methane. Modified figure from Rice & Claypool (1981) with data from Stolper et al. (2014).

3.5.3.3.2 Thermogenic carbon

Thermogenic gas forms at temperatures from 157®- 221®C (Stolper et al., 2014), in the oil window and into the advance stages of the catagenesis (Fig. 21), where the gas becomes progressively drier and isotopically more positive (Schoell, 1983). The thermogenic gas is characterized by low depletion of $\delta^{13}C$ values, ranging from -25% to -35% (Diaz-del-Rio et al., 2003).

3.5.4 Maximum pebble size

The maximum pebble size (MPS) analysis uses the layer thickness of a conglomerate and the ten largest clasts to calculate the thickness and competence of depositing flow at the point of measurement (Bluck, 1967b; Nemec & Steel, 1984). From the analysis, the mean MPS is plotted towards the layer thickness (Bth), where the diagram must be considered as a rough and purely statistical approximation of the latter relationship, and the entire estimation must be done on an assemblage of beds. The diagram is considered to distinguish cohesive flows from non-cohesive flows (Nemec & Steel, 1984).

Ungraded beds commonly indicate high shear-strength, or high viscosity, whereas divided beds with inverse graded lower part and non-grading in the upper part most likely indicate the occurrence of no-sheared plug and the distinct presence of frictional strength (Nemec & Steel, 1984). It is suggested that reliable MPS/BTh data can help distinguish subaerially deposits from subaqueously deposited debris flow conglomerates (Nemec & Steel, 1984).

4 RESULTS

4.1 Logging

The data acquired from the subvertical sedimentary sections are presented in the sedimentary log (Fig. 22). The log displays the depositional layers, facies, structures, grain size and to some degree sorting.

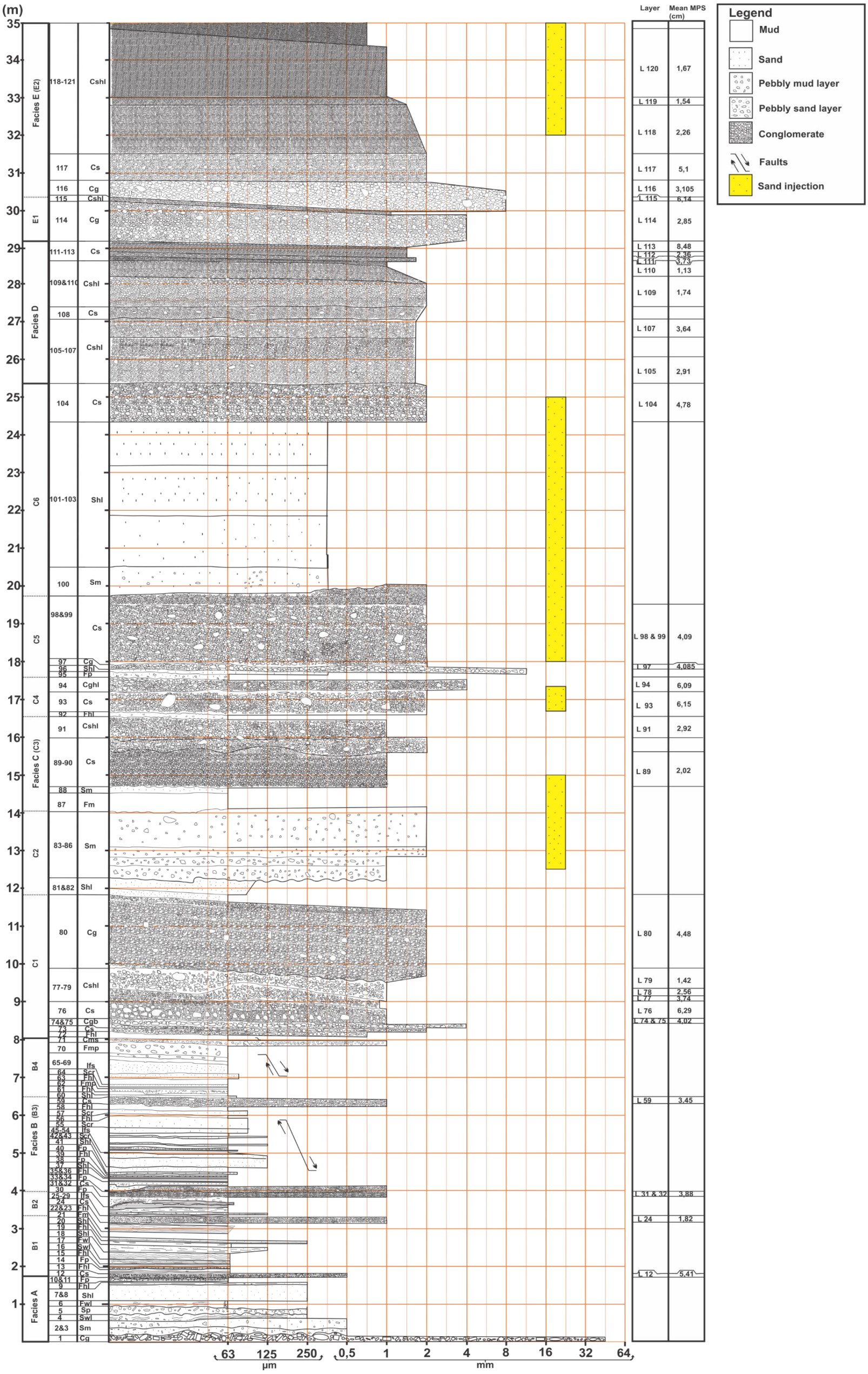

Fig. 22. Sedimentary log and the vertical profile of the study area at Skarmunken, the location of the profile is shown on Fig. 2, where the red rectangle 1 indicate the position of 0-28m of the profile and the red rectangle 2 represent the rest of the vertical profile. The profile is located 20cm a.s.l. during middle high tide. The log is a 1:100 scale, the vertical axis represents the height in meters and the horizontal axis represents the grain size. Of the 3 leftmost columns, the leftmost display the different facies, the one in the middle show the number for each layer and the on to the right show the facies code. The column in the middle of the figure display the layers and their coarseness. The yellow columns represent sands injections. The column on the right side of the vertical profile is the mean MPS values for measured conglomerate layers.

4.1.1 Facies codes

The facies codes marked on the layers in Fig. 22 are listed in Table 1. The first big letter e.g. “C, S or F” represent the definition of the layer, conglomerate, sand or silt/mud layer. The following letters e.g. “hl, wl, cr, m or p” represent the depositional structures occurring in the layers. The conglomerate layer’s facies codes contain one extra letter. After the big letter “C”, the next letter “g or s” represent the most abundant material occurring in the pore spaces. The last letters “b, hl, wl, or m” represent the depositional structures occurring the layers.

Table 1. The facies codes and the lithofacies type explanation.

Facies codes	Lithofacies type
Cg	Gravel grained conglomerate, massive clast supported
Cgb	Very fine-very coarse gravel grained conglomerate, bedded or laminated, may contain mud clasts and carbonates.
Cghl	Gravel grained conglomerate, clast supported, horizontal laminated, may contain carbonates and mud clasts.
Cs	Medium-very coarse sand grained conglomerate may contain carbonates.
Cshl	Medium-very coarse sand grained conglomerate, horizontal laminated, may contain carbonates and mud clasts.
Cms	Medium sand-very coarse gravel grained conglomerate, matrix supported.
Shl	Very fine –very coarse sand, horizontal laminated, may contain carbonates and pebbles.
Swl	Very fine-very coarse sand, wavy laminated, may contain carbonates and pebbles.
Scr	Very fine- very coarse sand, ripple cross lamination, may contain carbonates and pebbles.

Sm	Very fine- very coarse sand, massive, scattered pebbles, may contain carbonates.
Sp	Very fine- very coarse sand, pebbly, massive, may contain carbonates.
Fhl	Silt-mud, horizontal laminated, may contain carbonates and pebbles
Fhl/Scr	Very fine- very coarse sand, horizontal laminated and ripple cross-lamination, may contain carbonates and pebbles.
Fwl	Silt-mud, horizontal laminated, may contain pebbles, may contain carbonates
Fm	Silt-mud, massive, may contain pebbles
Fp	Silt-mud, massive, pebbly
Ifs	Silt/mud and sand, interbedding

4.1.2 Facies

In total 5 different facies are recognized in the excavated profile (Fig. 22), where the facies will be described in the following subchapter. The repeated occurrence of facies will not be described, only the location will be mentioned.

4.1.2.1 Facies A

4.1.2.1.1 General description

Facies A (Fig. 22) is the lowermost facies and is located from 0-1,74m in the vertical profile. It consists of 11 layers, 6 sand layers, 3 mud layer and 2 conglomerate layers at the bottom and the top of the facies. The facies display a normal graded trend from 0-1m. From 1m the facies is inverse graded before it is interrupted by mud layers, which is terminated by a conglomerate layer, marking the end of facies A. From 0m to <1m, the layers are characterized by chaotically and massive bedding, where only one sand layer contains partly wavy laminations. From 1m to 1,74, the main trend of the layers is laminated depositional structures, only interrupted by the conglomerate layer and the underlying pebbly mud layer.

4.1.2.1.2 Carbonate concretions

The first occurrence of carbonate concretion is located in the second layer (Fig. 22) at 0,19m, represented by a coarse poorly cemented concretion. A few carbonate concretions of the same type are located in layer 3 (Fig. 22). The general trend of the carbonate occurrence is scarce in this part of the facies. Carbonate concretions occur more abundant in layer 8 (Fig. 22), as strata bound and following the laminations. These carbonate concretions are fine-grained and display intergrown pipes and plate morphology.

4.1.2.2 Facies B

4.1.2.2.1 General description

Facies B (Fig. 22) is repeated 4 times in the vertical profile, from1,74m-3,10m, 3,10m-3,78m, 3,78m-6,16m and 6,16m- 8,20m. The facies consist of maximum 20 layers and display in all cases an inverse graded trend. The main part of the facies consists of interbedding of very fine- fine-grained sand and mud layers, where the layers are mainly horizontal laminated, but wavy lamination occur in some cases. The laminated sand layers show in some cases a coarsening variation in each repeated facies, where the coarsest layers are documented to be of 250µm in grain size. A conglomerate layer terminates the interbedded sand and mud layers, representing the end of facies B. At 4,5-5,8m, 6,97- 7,52m and 7,81- 7,94m normal faults (Fig. 22) are observed to cut through the interbedded sand and mud layers (4.2.2).

4.1.2.2.2 Carbonate concretions

The carbonate concretions occur abundant in the horizontal and wavy laminated sand layers. The concretions occur as strata bound, fine grained intergrown pipes and plate concretions, following the laminations. In the conglomerates, scarce and scattered coarse intergrown pipes carbonate concretions occur.

4.1.2.3 Facies C

4.1.2.3.1 General description

Facies C (Fig. 22) is repeated 4 times in the vertical profile (Fig. 22) at 8,20m-14,56m, 14,56m-16,6m, 16,6m-17,7m and 17,7m- 24,4m. The general trend for facies C is inverse grading, with laminated or massive mud and sand layers in the lowermost section, succeeded by massive – laminated sand and gravel conglomerates, terminating the facies. At 12,5m-15,5m, 16,7-17m and 18m-25m yellow sand injection is observed cut through and/or intrude pore space of original layers (4.2.3).

4.1.2.3.2 Carbonate concretions

The carbonates concretions are most abundant in the sand layers, occurring as fine-grained intergrown pipes and plate concretions. The carbonates concretions are more scarce and scattered in the conglomerate layers, occurring as coarse-grained and often bigger intergrown pipes concretions compared to the ones in the sand layers. The sand injections observed in the facies contains a high concentration of carbonate concretions, represented by intergrown pipes and plate shaped concretions.

4.1.2.4 Facies D

4.1.2.4.1 General description

Facies D (Fig. 22) is located at 24,4m- 29,2m, consisting of 10 coarse sand conglomerate layers. The facies trend is inverse grading, where all the layers are moderately-well sorted. The conglomerate layers alternate in being horizontally laminated and massive layers. Sand injections occurs in the lowermost layer of the facies, where it only intrudes the pore spaces while not disturbing the original depositional structures.

4.1.2.4.2 Carbonate concretions

The occurrence of carbonate concretions in facies D is extremely scarce, occurring as scattered coarse-grained concretions in the conglomerates and in sand lenses. The carbonate concretions occur also in the sand injection section.

4.1.2.5 Facies E

4.1.2.5.1 General description

Facies E (Fig. 22) occurs twice in the vertical profile and is located at 29,2m- 30,25m and 30,25m-35m. The facies is normal graded with massive gravel conglomerate in the bottom, succeeded by massive sand conglomerate before it transitions into horizontal laminated sand gravel. The conglomerate layers display an increased sorting grade, starting at moderate –poorly sorting in the bottom and ends at very well sorting and the top of the facies. The facies show three distinct upward fining steps before the vertical profile ends. Sand injections are observed from 27,8m and 32-34,75m cutting through depositional structures of original layers.

4.1.2.5.2 Carbonate concretions

No carbonate concretions were observed in facies E.

4.1.3 Interpretation of the facies

4.1.3.1 Facies A

The fine-grained sediments indicate a calm depositional environment, where the mud layers may indicate a meltwater plume deposition as a bottomset or on distal foresets. The sand layers might also be of the same type of deposition, but could also represent turbiditic sand foresets or bottomset deposit. The terminating conglomerate layer most likely represent debris flow deposit on the foresets, or could be basal till deposit. The origin of the conglomerate base is not known and could possibly belong to another facies but could also represent the same deposit as the overlying conglomerates layers.

4.1.3.2 Facies B

The main components of the facies are mud and very fine sand layers. These components may indicate meltwater plume deposition as either bottomsets in the distal parts of the fan slope or foreset- bottomset transition deposition. The observed subhorizontal layers indicates foresets or the foreset-bottomset transition deposits. The conglomerate layers could either represent debris flow deposit or basal till deposit, as foresets or foreset- bottomset transition deposition. Due to the dominance of very fine components in the facies, a longer period of calm depositional environment is indicated. The very fine components could reflect reduced subglacial discharge, which could be due to a smaller retreat of the glacier terminus.

4.1.3.3 Facies C

The mud and silt deposits indicate calmer depositional environment, where a possible deposition mechanism could be meltwater plume deposition as bottomset or in the transition zone to bottomset. The sand layers could also represent meltwater plume deposition as bottomsets or turbiditic sand foresets deposits. The observed wavy lamination indicates dominating marine setting. The large sections of conglomerate deposition could indicate till deposit or debris flow deposition, where the subhorizontal dipping units indicate foresets or foreset-bottomset transition deposition. Turbidity currents could be a possibly explanation for the coarse-grained sand, as meltwater plume deposit do not consist of such coarse components. The coarse sand was probably deposited somewhere between the foresets and the bottomsets. The large amount of coarse deposits may indicate a closer presence of the glacier terminus, or an increase in water discharge.

4.1.3.4 Facies D

The alternating subhorizontal – horizontal, horizontally laminated and massive conglomerate layers could represent till deposits with shifting flow regime, possibly representing the distance from the glacier or season variation, causing alternating lamination and massive layers. The coarseness of the sediments in the facies may indicate deposition on the frontal fan slope near the glacier terminus by traction currents. The subhorizontal layers could indicate foresets deposition, where the horizontal layers most likely indicate foreset-bottomset transition deposition.

4.1.3.5 Facies E

The massive and subhorizontal-horizontal conglomerates probably represent till deposits or debris flows, where the subhorizontal beds may indicate foresets deposition and the horizontal beds could represent foreset-bottomset transition deposition. The upward fining trend and the increased sorting grade upward in the facies could represent reduced flow rate caused by either glacial retreat or seasonal variation.

4.1.4 Large-scale bedding-plane traces

To the south of the vertical profile, several large-scale lineation's are located (Fig 23). These large-scale feature occur as continuous and scattered lineation`s throughout the exposed slope, cutting through the excavated vertical profile. Due to the frailness and continuous erosion of the slope, the visibility of the lineation`s is dependent on areas which have not been disturbed enough to erode or cover the large-scale structures.

The lowermost lineation`s are marked with blue and occur as slightly subhorizontal, were they transitions into horizontal lineation`s northwards. These lineation`s are almost exclusively located in the southernmost sections of the exposed slope (Fig 23). Terminating the lowermost lineation`s sequence is slightly bending subhorizontal lineation`s, marked with red color. The boundary to the red subhorizontal lineation`s marked by a sharp boundary. The red subhorizontal lineation`s is the most visible lineation`s in the exposed slope and they appear to become progressively more horizontal towards north. Succeeding the red subhorizontal lineation`s are horizontal- subvertical lineation's, marked with green. These are horizontal in the southernmost end of the exposed slope and transitions quickly into subvertical lineation`s. The uppermost lineation's are marked with purple color and occur horizontal in the southernmost area of the exposed slope.

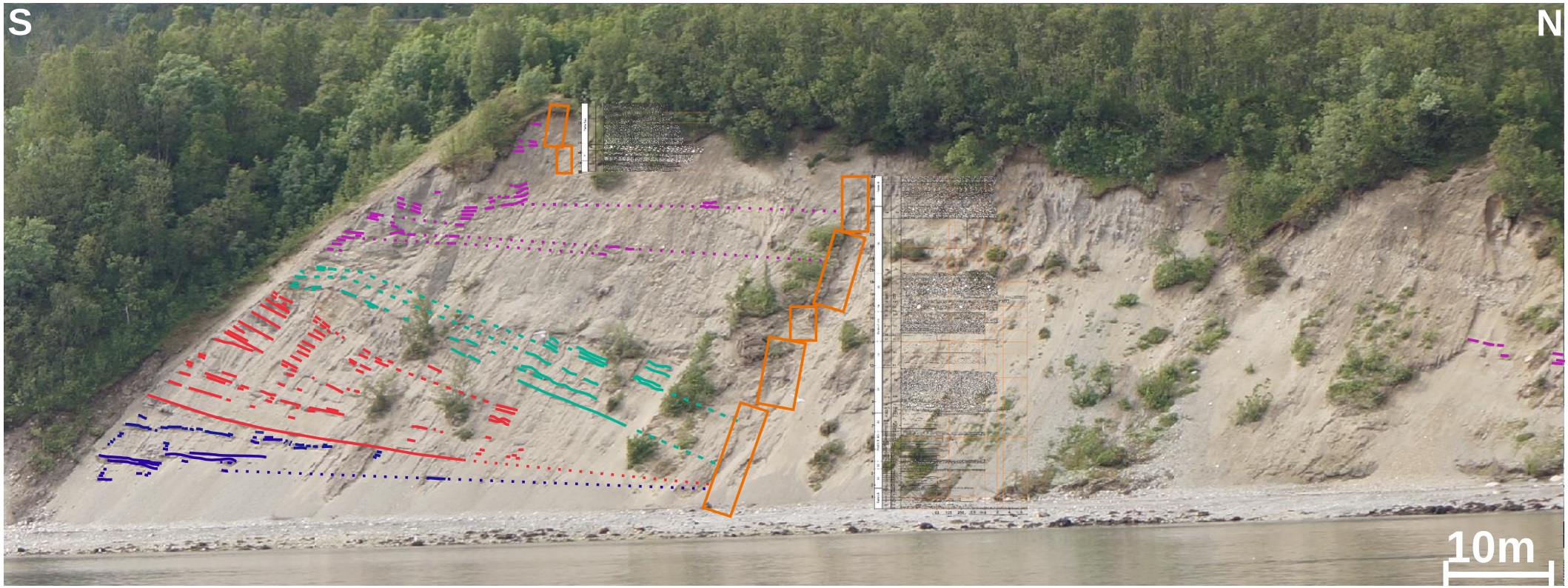

Fig 23. The large-scale lineations in the southern exposed slope with the location of the vertical profile indicated by orange rectangles. The vertical profile layers are also indicated on the layer, by a semitransparent log. The lowermost lineation`s are marked with blue color, the lower middle lineation`s are marked with red color, the upper middle lineation`s are marked with green and the uppermost lineation`s are marked with purple color.

Towards north the lower lineation`s appear to bend upwards, towards the upper ceiling of the exposed slope (Fig 23). However, the lineation`s observed vertically above these are horizontal. In the uppermost lineation`s and between the uppermost and underlying lineation`s, there is a lot of open space with no exposed lineation`s, creating uncertainties of orientations of the lineation`s and where the boundary is located.

4.1.4.1 Interpretation

From the observed orientations and the morphologies, the large-scale lineation`s have the potential to contribute to the interpretation of the deposition. The horizontal blue lineation`s morphologies might indicate that the lowermost deposits in the vertical profile consists of bottomset deposits, based on the flat morphology. The inclined lower middle red lineation`s probably indicate foresets deposits or it could represent deposition in the foreset-bottomset transition. The indicated deposition would further indicate a glacial front advance, going from bottomsets to foreset deposition. The upper middle green lineation`s appear to be the most inclined ones, indicating foreset deposition based on the inclination. The stratigraphically higher foresets deposition could indicate a standstill in the glacier front. The uppermost purple lineation`s horizontal- slight subhorizontal appearance could indicate deposition in the topset or the bottomset area or the foreset-bottomset transition area. Deposition in the topset would indicate that these deposits represent the delta top deposition. However, if the deposits represent bottomset or foreset-bottomset deposits, this would indicate a retreat in the glacier terminus. The observed upward bending lineation`s is located in a sand injection area, which could explain the bending in this particular area and not further above.

4.2 Depositional special features

4.2.1 Mud clasts

Throughout the logged sections, abundant amounts of mud clasts and chunks were encountered, where the clasts varied in sizes from 2-15cm and the chunks ranged from 50cm to >1m (Fig. 24). Some were even large enough to be mistaken of being layers (Fig. 24, B). The content of the clasts varied from being massive mud clasts to containing pebbles, sand pockets and sometime carbonate concretions inside the occurring sand pockets. The mud chunks commonly occurred together with sand injections (3.1.2.2) with areas of abundant carbonate concretions occurrence. In addition, the mud chunks and clasts were also located in conglomerate layers.

Fig. 24. Excavated section at 14,5m, the red dotted area (1) represent a mud clast in the sand layer and the red dotted area (2) represent a huge mud chunk with several sand pockets. Photo taken at Skarmunken (2016).

4.2.1.1 Interpretation

The occurrence of mud in different types of sediment layers, indicate different types of creational processes for the mud clasts and chunks. The mud clasts in the sand injections indicate the same transportation process as the sand, which is probably due to the result of mobilization of sand and mud layers by fluid migration, where overlying and/ or underlying mud is transported with the sand. The fluid migration could also explain the occurrence of carbonate concretions in the sand injections. The mud clasts in the coarse-grained units, could be due to erosion of finer material, probably by debris flows, or it could be due to glacial transport of diamictons. The mud chunks occurring in finer sediments, occur with carbonate concretions and sand injections, which could either indicate transportation by fluid migration or erosion and transportation of fluid migration affected areas. The scattered pebbles occurring in the mud chunks are probably preexisting depositional features, indicating transport of the mud. The mud clasts and chunks occurring in the palaeochannel are probably due to erosional process of fine-grained sediments elsewhere and redepositing during infilling of the channel.

4.2.2 Faults

In the sand and silt laminated part of the vertical profile (Fig. 22), high amounts of normal faults were recognized. From 4,5-5,8m (Fig. 25) 6,97- 7,52m (Fig. 26) and 7,81- 7,94m W, NW- E, SE oriented normal faults were observed to break and/or deform the present laminas in the layers. Carbonate concretions were also observed to grow in the displaced parts. At 4,5-5,7m the faults are on at intermediate size, varying from 6 – 13cm in length. The biggest fault occurs in the 6,97- 7,52m interval, ranging from 9 – 56cm in length. The smallest faults occur at 7,81- 7,94m, ranging from 5-8cm in length.

4.2.2.1 Interpretation

The faults observed in the fine-grained sediment sequences are probably the result of load and stress from local layers as they only occur in a limited area in the vertical profile. The conglomerate layers occurring in the middle and above the fine-grained sediment sequence are probably debris flow deposits, which could result in faulting in the soft sediment due rapid applied external load. The separating conglomerate layer is probably not thick enough to cause the faulting, however, the overlying >3m conglomerate sequence is probably thick enough. If the conglomerate sequence were deposited as till in the subglacial zone, the faults could have formed due to shearing and might explain the upper part of the faulted sequence but no the lower part.

The compaction of the fine-grained faulted sequence could have led to fluid migration, which is extensively observed in the vertical profile (4.2.3). Sand and mud-silt are commonly observed together in the fluid migration areas, which display remarkably similar often deformed depositional characteristics as the faulted fine-grained sequence. If they are of same origin, this would indicate mobilization of the fine-grained sequence due to fluid migration. The occurrence of carbonate concretions in the fault surfaces supports the presence of fluid migration.

From 12,5m-15,5m a big boulder carbonate concretion occurs. The boulder is fractured, where the large fractures is re-cemented by pebbly material. The boulder is enveloped by a yellow sand injection, indicating major fluid flow. The fractures where likely caused by the fluid flow and the rock shows multiple stream direction pattern, which could indicate rotation of the boulder. This fracturing and multiple direction pattern indicate some movement of the boulder. Movement of such a rock, even small, would have caused tremors forming seismic energy, which could explain the faulting in the fine-grained layers beneath the carbonate boulder.

Fig. 25. Excavated section beneath 5m, display W-E and NW-SE oriented normal faults in the laminated layers. The dominating trend of the faults are W-NW oriented with southern hanging wall. The sand layers are the most affected by the faults, where the mud layer, especially in the thicker layers, display plastic deformation. The faults terminate at the lower pebbly mud layer. The W-NW faults displacement range from 0,05-1cm and the SW faults displacement range from 0,02-1,6cm. The faults are marked with light blue. Photo taken at Skarmunken (2016).

Fig. 26. Excavated section at 5,5m, displaying a network of small and bigger W, NW and SW oriented normal faults. The dominating trend of the faults are western oriented faults, closely followed by SW faults. The W faults range from 0,1cm- 0,5cm, the NW faults range from 0,05-0,3cm and the SW fault range from 0,4 - 6cm. The sand layers are clearly broken off and displaced, where the mud layers are plastic formed. Some of the mud layer appears to be more displaced than others within the same fault plane. The faults tend to terminate against the pebbly mud layer, except for two NW-W faults. The faults are marked with light blue color. Photo taken at Skarmunken (2016).

4.2.3 Sand injections

In the excavated profile, sand injections occur in numerous occasions (Fig. 27), mixing with the original layers throughout the vertical profile. The sand injections, occur at 12,6m to 15m, 16,7m-17,40m, 18m-25m and 32-34,75m (Fig. 22). The sand injections can appear as a distinct contrasting boundary, infiltration of sand in pore space in the original layers or as a combination of both. The sand injections can consist of pure sand, sand with scattered pebbles, sand containing deformed or rotated laminations or sand with clay clasts and chunks and silty-clayey structures. Common for most of the sand injection occurrences is the distinct yellow sand, but in some cases, the sand is similar to the original layer.

The first occurrence of the sand injections is observed from 12,5m-15,5m enveloping a big carbonate concretion (Fig. 46 and Fig. 47). The injection boundaries are observed on the southern, northern side of the carbonate concretion (Fig. 27, A, B and C). The sand injection on southern side is characterized by a distinct boundary of pure yellow sand (Fig. 27, A and B), which follows closely the outer rim of the carbonate concretion. The sand injection on the northern side (Fig. 27, C) is also marked by a distinct boundary of pure yellow sand, but is also observed to inject into the pore spaces of the adjacent sediments. Despite the sand filled pore spaces, the sediments retain its original depositional features (Fig. 27, C).

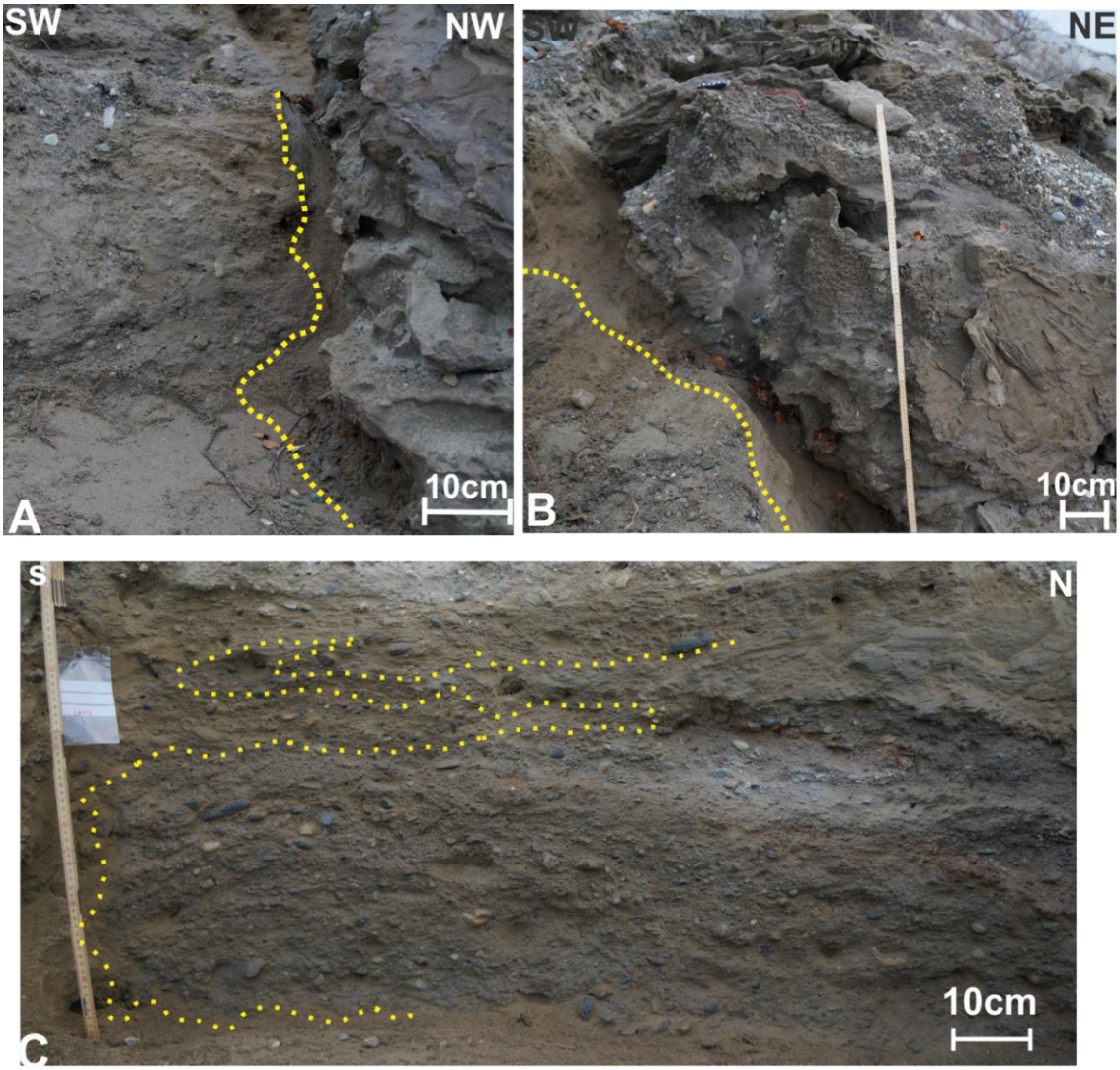

Fig. 27. (A) and (B) are located on the southern side of the boulder carbonate concretion (Fig. 49), showing the occurrence of sand injections, marked by a distinct yellow pure sand. The sand follows the carbonate concretion outer rim, where the outer boundary is marked with yellow dotted lines. (C) Occurrence of sand injection on the left side of the figure, characterized by distinct yellow sand located on the northern side of the big boulder concretion. The figure C also display injection of sand into the pore spaces of the adjacent original layers. The outer boundary of the sand injections in the pore spaces are indicated by yellow dotted line. Photo taken at Skarmunken (2016).

From 16,7-17m, the sand injections appear as sub horizontally injections with mostly infilling of pore space of the original layer and a few sub horizontal distinct small veins, 1-4cm in thickness. At 17m- 17,40m the sand injections appear as distinct boundary, represented by a large sub vertical vein, 20-30cm in thickness, crossing the whole excavated section.

The sections from 18m-25m in the vertical profile (Fig. 22) is heavily distorted by the sand injections. From 18m-20m the sand injections cover more than 50% of the excavated sections and appeared distinct contrasting areas. Inside the injections, large mud chunks, deformed laminations and carbonate concretions appear. The 20-25m section contain more abundant carbonate concretions. The sand injections appeared as distinct contrasting areas, whereas at the section at 25m, a combination of pore space infilling and distinct contrasting boundary occurred. The smaller carbonates appear inside the injections, whereas the biggest ones occur in the sand injection boundaries to the original layers. Inside the sand injections, pipe structures of silt-clay appear. The sand injections occurring from 32-34,75m (Fig. 22) were not observed in the section, but clear sandy veins were observed penetrated the conglomerate layers adjacent to excavated sections.

4.2.3.1 Interpretation

The sand injections located in abundance in the vertical profile is likely the result of fluid migration. The occurrence of horizontal to vertical sand injections probably represent the heterogeneity of permeability and porosity of the host sediments, which would also explain the shape and the length of the observed sand injections. The injections sharp boundaries probably represent the main fluid migration pathway, whereas the injection of sand into the pore spaces most likely represent the transition from undisturbed sediments to the boundary of the fluid migration

The sand injections content of carbonate concretions indicates the presence of hydrocarbons, where the mud clasts and mud chunks and pipe-like structures might indicate mobilized sediments. The preexisting rotated and deformed laminations in the sand injections indicate mobilization and transportation of sediments, which is common in fluid migration influenced areas.

The high and rapid sediment depositional rate by a glacier is a likely candidate for the fluid migration, which could mobilize the injecting sand and clay observed. Probably a pressure buildup by glacier overriding the sediments combined with the sediments deposited could be the cause for the fluid migration. The hydrocarbon seepage most likely caused the carbonate cementation that in addition would increase the pore pressure in the sediments.

Fluid migration by a thermogenic origin could also be the cause for the mobilization of the sand and clay. However, due to the glacier presence, thermogenic fluid migration would probably not be the single cause for the mobilization of the sediments.

4.2.4 Fluid Migration Structures

From 19,6m-20,1m very fine sand- silt is observed to break through laminations of sand injections, bending the laminations upwards towards contact point (Fig. 28) The fine material creates a lobe structure, reaching upwards with distinct boundaries. The clay in this area display same features, oriented upwards, breaking through the laminations. There were not observed any carbonate concretions inside the circular lobes or the pipe-like lobe.

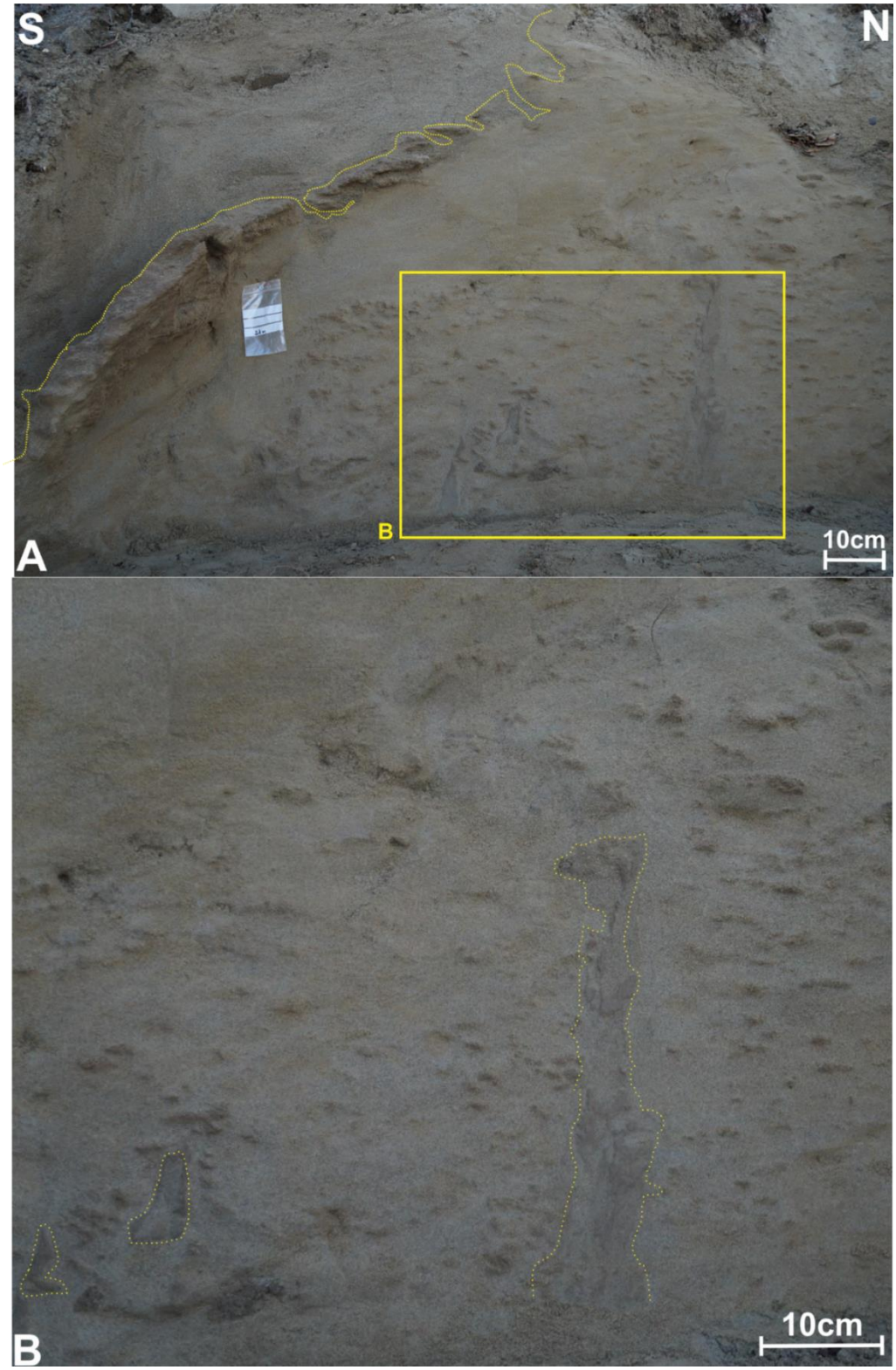

Fig. 28. (A) Excavated section at 21m, where the square is the location of figure B. The section consists of almost exclusively a sand injection, where only a small part of the original layer is visible in the upper left corner of the figure, where the boundary is marked by a yellow dotted line. (B) The figure is located inside the sand injection and contain fluid migration structures. The fluid migration structures are characterized by distinct darker finer silt-clayey particles forming floating structures or pipe-like structure. These fluid migration structures are not affected by the carbonate concretions in the layer, where the concretions grow around the structures. Photo taken at Skarmunken (2016).

From 20,7- 21m two more distinct lobe/pipe structures is observed. They consist of finer material than the surrounding sand injection. The lobe/pipes are thick in the lower part and thins out towards the top. No carbonate concretions are located inside the lobes/pipes, only at the boundaries between the lobes/pipes and the sand injections. At 21,60m to 21,68m a single similar structure is recognized with a silt core coated by a very fine sand membrane.

At 22,20-22,5m the same pipe/lobe structures found at 20,7-21m is recognized. They are in general thinner and are also dismembered into several pieces as they reach upwards. They carbonate concretions are also here not located inside the pipe/lobe structures, but around and in the boundaries.

The same trend of local finer material in a layer occur in the excavated section at 33,5m, represented by a subvertical pipe (Fig. 29) The surrounding layer is a normal graded layer, starting at 1,5mm and ends at 1mm. The subvertical pipe structure consists of material ranging from 0,5mm-1mm. The thickness of the pipe varies vertically, where it is thickest in the middle of the excavated section and thinnest in the uppermost and lowermost part of the excavated section.

Carbonate concretions were not observed to occur in any of the lobe/pipe structures in the coarse-grained sediments.

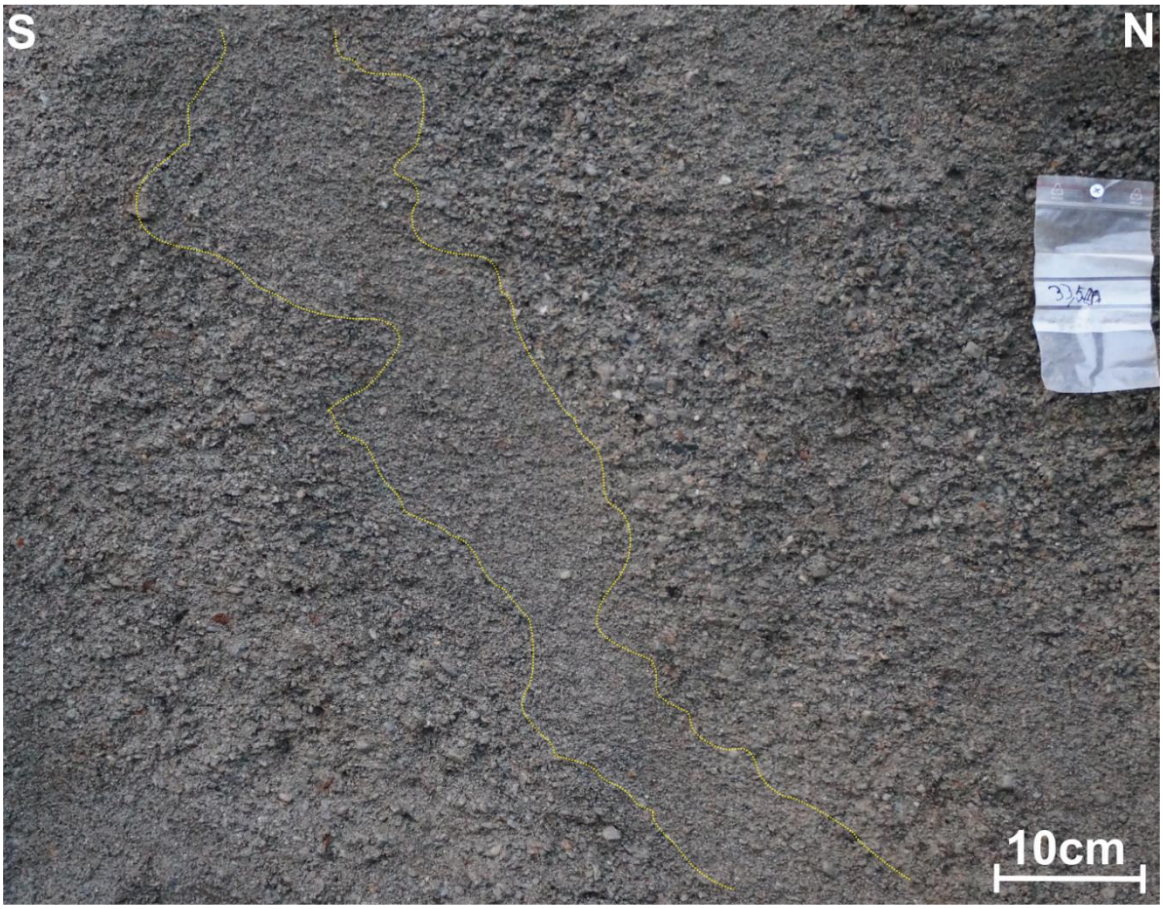

Fig. 29. Excavated section at 33,5m in the vertical profile. The section contains a sub vertical pipe structure of finer material, marked with yellow dotted line. The adjacent material consists of 1mm- <2mm grains, where the sub vertical pipe consists of finer 0,5mm-<1mm grains. Photo taken at Skarmunken (2016).

4.2.4.1 Interpretation

The observed structures clearly indicate fluid migration processes in the sediments, where the finer grains inside of the structures indicate the fluid migration of finer particles. The structures in the fine-grained sediments (Fig. 28 A and B) could either display some kind of intrusion by fluid migration, however, the circular lumps could indicate ball and pillow structures. There were not observed any termination in the pipe-like structures in the coarse-grained sediments (Fig. 29), therefore the structures could either be a channelized fluid flow of finer particles or the same kind of pipe- like intrusion observed in Fig. 28 B. The lack of carbonate concretions in the structures of both the fine- and coarse-grained sediments, could either mean that the hydrocarbons were absent or not sufficient enough to precipitate carbonate concretions. However, in the fine-grained sediments, carbonate concretions are observed to occur in close proximity or around of the lobe structures. This could indicate that the structures were formed by processes which did not contain hydrocarbons.

4.2.5 Paleochannel

At 0,5m to approximate 1,5m in the excavated profile and horizontally north, a distinct erosive boundary is observed (Fig. 30), forming the contour of a preexistent channel, cutting through the adjacent sediments. The height of the paleochannel is observed to be approximate 1m, whereas the width of the paleochannel is undefined. However, the paleochannel width is recognized to be >15m by excavation. From the maximum height of the down towards the bottom, three distinct erosive steeps are recognized in the excavation of the channel. The content of the channel consists of mainly sand where the deposition is chaotic, containing laminations with different orientations, mud clasts and large mud chunks, pebbles.

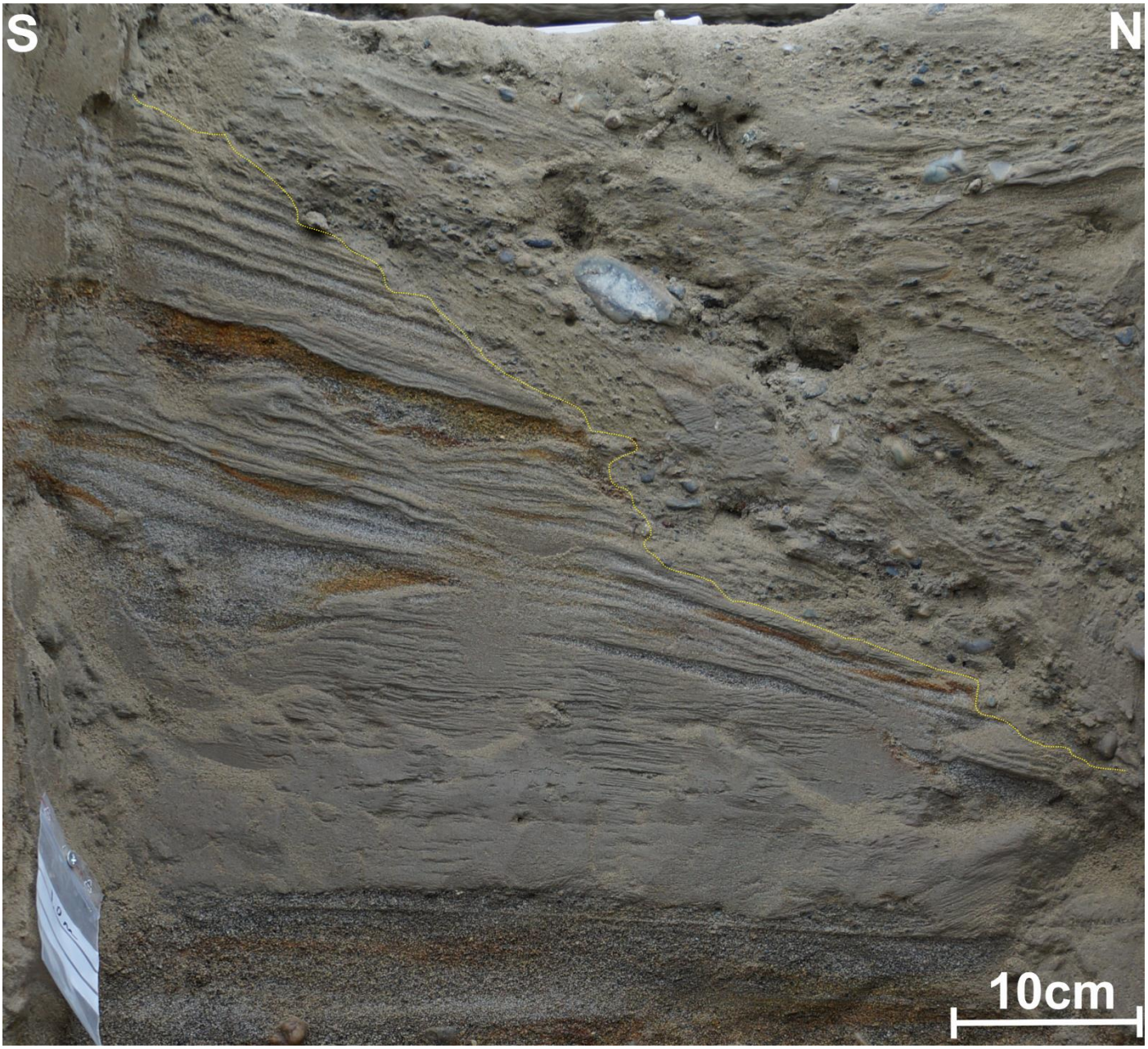

Fig. 30. Excavated section at 1m displaying an paleochannel. The paleochannel consist of generally coarser grains and pebbles that have eroded the fine-grained laminated layers. The erosive boundary is indicated by the yellow boundary. The channel approximate maximum height is 1m, stretching from 0,5m-1,5m. The width of the channel is not defined but reaches a width >15m. Figure 18 is the only usable picture, as the whole horizontal excavated section of the paleochannel collapsed before pictures were taken. Photo taken at Skarmunken (2016).

4.2.5.1 Interpretation

The erosional features interpreted as a paleochannel could have been formed erosion of finer sediments by a passing or deposition of a debris flow, or by erosional processes during slumping with a later refill. However, the observed minimum width of the erosional feature appears to be too large to be any of the proposed mechanisms. The width and the three observed steps rather

indicate the occurrence of a channel, where the steps represented former channel position. However, the chaotically deposited infilling material contradicts a usual channel deposit.

4.3 Maximum pebble size

The maximum pebble size (MPS) values were taken from the clast supported conglomerate layers. In total 32 layers were measured (Fig. 22).

4.3.1 MPS vs conglomerate layer thickness

In Fig. 31 the measured MPS values from 30 conglomerate layers is plotted against the thickness of the layers. Of the 32 layers, the lowermost and uppermost conglomerate layers mean MPS (Fig. 22) were excluded Fig. 31. The lowermost layer thickness was impossible to measure due to the seeping groundwater, causing the layer to collapse when excavated further down in the slope. The uppermost conglomerate layer was eroded, making the total thickness is unknown. The complete data used for the plot is listed in Table A 2

The mean MPS vs layer thickness plot displays a concentration of values from mean MPS values interval from 1-6cm and layer thickness interval from 5-60cm. The layers between 0,12-0,32m to 8,39-8,495m, 8,985-9,095m to 9,265-9,8m, 15,5-15,88m to 17,03-17,26m, 17,71-17,82m, 26,48-27m, 28,26-28,63m to 28,84-29,92m, 30,4-30,75m 31,5-31,85m and 32,75-33m (Fig. 22), which makes up 23 layers fall inside these MPS values and layer thickness intervals.

The sample 8,495-8,985m, 17,26-17,52m, 25,38-26m, 30,3- 30,4m (Fig. 22) lay right outside or in close proximity of these intervals. 9,95-11,67m, 17,82- 19,49m and 33-34,8m (Fig. 22) lay in the mean MPS value interval, but exceeds the layer thickness interval. 28,84-29,2m (Fig. 22) lay in the layer thickness interval but exceeds the mean MPS value interval. Three of the conglomerate layers, 9,95-11,67m, 17,82- 19,49m and 33-34,8m (Fig. 22) occur as extreme outliers. They occur in the mean MPS value interval, but exceeds the layer thickness by far, with thickness varying from 1,67m to 1,80m.

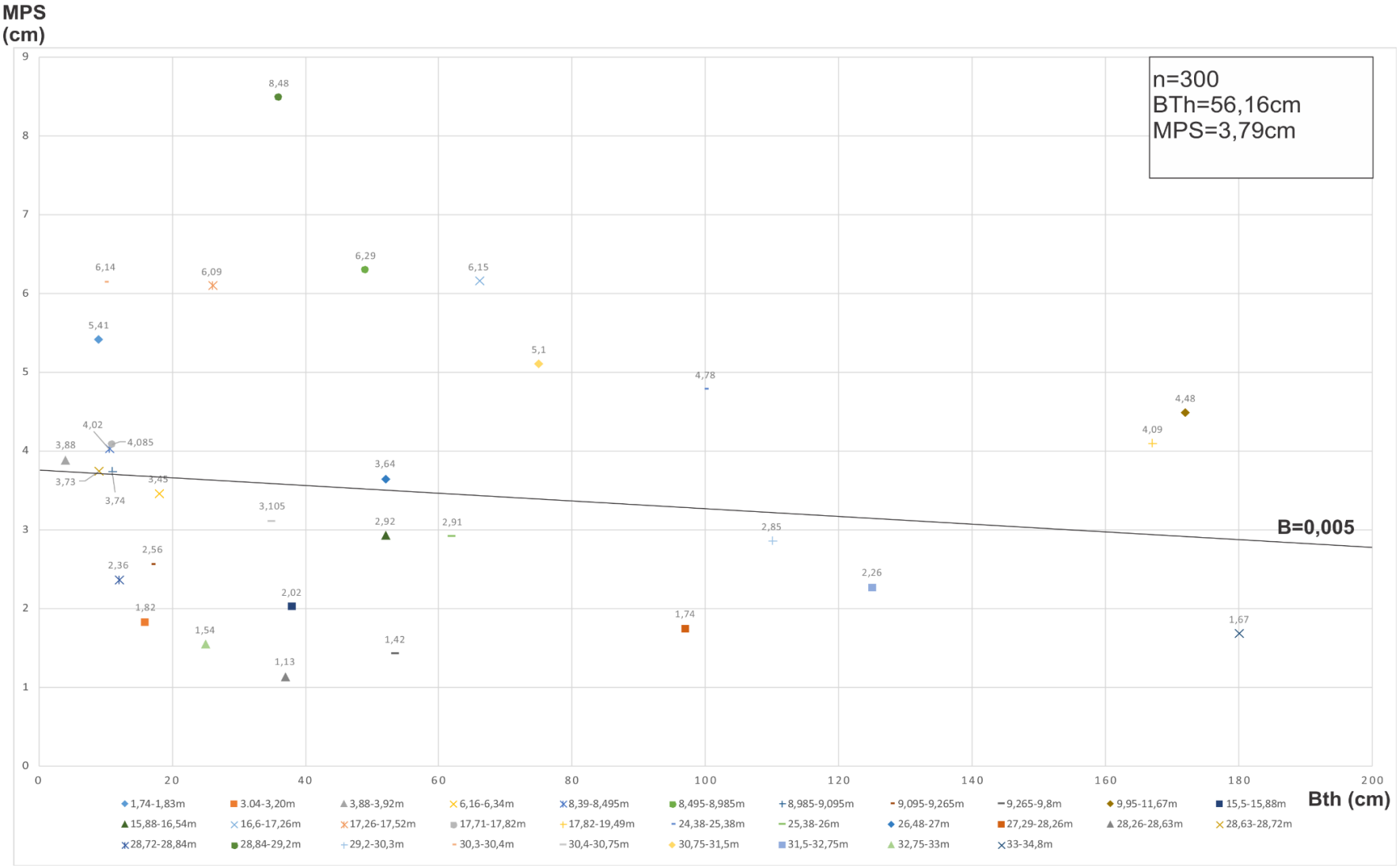

Fig. 31.The mean MPS values of 30 samples plotted against the layer thickness for the respective samples. The symbol "n" in the square represent the amount of pebble measured, the BTh and the MPS in the square represent the mean values for all of the samples. The black line B represents the best fitted line for the data.

4.3.1.1 Interpretation

The thickness of the layers appears not to affect the clasts sizes. However, the largest clasts only occur from 1-80cm. This could indicate that the depositional conditions for such clasts sizes only occur in shorter periods based on the thickness. The correlation between the sizes of the largest clasts sizes in the layers, indicate that this size interval had more or less the same depositional conditions. The same trend is observed in the intermediate clasts sizes, whereas the layers with smaller clasts sizes varies slightly in size, indicating a slight variation in the depositional settings. The outliers with large layer thickness, indicate stable environment over a longer period of time during deposition.

4.4 Leco – analysis

The 14 crushed samples (Table A 3) were used for the leco analysis. This includes the amounts of the samples that were introduced to HCl.

Table A 4 present a selected part of the data from the leco combustion analysis, of the 14 crushed samples. The complete data can be viewed in Table A 6. The table display the total carbon (TC) and sulfur content for the samples. The total amount of carbon is relatively low in these samples and rarely exceeds 1%, only in 2 samples. The amount ranges from 0,6- 1,315 % with a mean of 0,86%. The TC values is relatively stable with no distinct outliers. The maximum value is 1,31% (2,875m) and minimum value is 0,64% (17,59m). Upward stratigraphically, the values indicate upward decrease in cycles, where each cycle is terminated by a higher value. The cycles are observed from 1,02m-1,99m, 2,785m-3,2m, 4,31m- 4,91m, 6,35m- 15,6m and 16,51m-17,59m.

The total sulfur (TS) content have a maximum value of 0,039% (2,93m) and a minimum value of 0,0095% (6,35m) with a mean value of 0,024%. The TS values are relative stable, but at 4,31m, 6,35m two distinct low values appear. Moving upwards stratigraphically, the samples display an upward value decreasing cycles, terminated by a higher value. The cycles are observed from 1,02m-2,785m, 2,93m- 4,31m, 4,51m-6,35m and 14,29m-16,51m. Sample 7,255m deviates from the general pattern of cycles and sample 17,59m marks the termination of the last documented cycle.

Table A 5 displays the total organic carbon (TOC) from the HCl introduced samples by leco analysis. The results (Table A 6) show that total organic carbon is distinct less than the total carbon amount. The deviation of the TC and TOC range from 0,57-1.24%. The mean value of the TOC is 0,071%, whereas the maximum and minimum lay at 0,1% (3,2m) and 0,04% (7,225m). In the lower parts,

1,99m-3,2m and 4,31m-4,91m the TOC display upward increase in value. From 6,35m-7,225m and 14,29m-15,6m two cycles of stratigraphic value decrease occur. 16,51m-17,59m display the same trend as the cycles from the lower parts (1,99m-3,2m and 4,31m-4,91m).

4.4.1 TOC/TS

Fig. 32 show a TOC/TS diagram calculated from the leco combustion analysis of the samples. The diagram is combined with the sedimentary log, where the TOC/TS data is plotted stratigraphically, starting at 1,02m and ending at 17,59m. This give an indication of which layer the data is extracted from. The TOC/TS detailed values are described in Table A 5. The TOC/TS values display 3 cycles of stratigraphically upwards increase, at 1,99m-4,31m, 4,51m- 6,35m and 7,255m-16,51m. At the lowermost sample, 1,02m, the TOC/TS is 2,46 (Fig. 32 and Table A 5). For sample 1,99m, 2,785m, 2,93m, 3,2m and 4,31m the TOC/TS is 2,13, 2,34, 2,53, 2,75 and 4,78 (Table A 5). This section in the vertical profile clearly show an upward increasing trend. The same pattern occurs from 4,51- 6,35m (Fig. 32), with ratios of 2,87 (4,51m), 5,84 (4,91m) and 6,45 (6,35m) (Fig. 32 and Table A 5). Sample 7,255m, 14,29m, 15,6m and 16,51 show the repetitive pattern of increasing ratios, represented by 1,98 (7,255m), 2,5 (14,29m), 3,09 (15,6m) and 3,97 (16,51) (Fig. 32 and Table A 5). The last sample at 17,59m show a decrease in ratio, sinking from 3,97 to 2,89 (Fig. 32 and Table A 5).

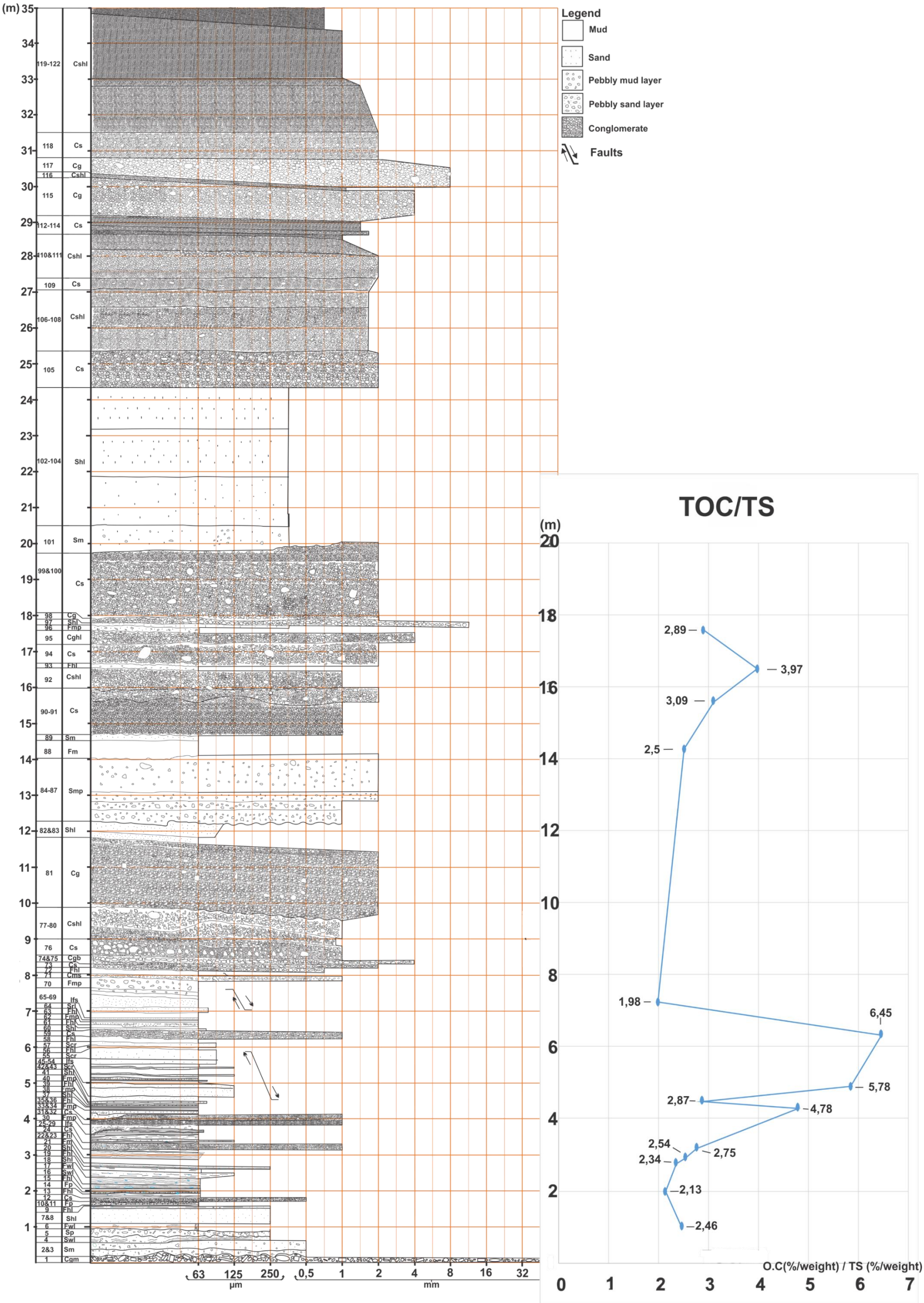

Fig. 32. The sedimentary log of the vertical profile combined with TOC/TS diagram for the leco analyzed clay-silt samples. The TOC/TS show the varying amounts of the total carbon content to the total sulfur content in the clay-silt samples in the vertical profile.

Fig. 33 show the %TOC and %TS plotted into a normal marine and nonmarine plot by Leventhal (1995). A significant amount of the samples is located well in the nonmarine area Fig. 33, however, the main part of the samples (1,99m, 2,785m, 4,31m, 4,51m, 7,255m, 15,6m and 16,51m) is located close to the marine environment boundary. These samples are located in the interval between 0,055-0,08% TOC and 0,01-0,02%. Outside of this interval the rest of the samples, 2,93m, 3,2m, 4,31m and 7,255m, are located. Sample 4,31m consists of 0,047% TOC and 0,0102% TS and 7,255m consists of 0,041% TOC and 0,009% TS, which is slightly located outside the main concentrated interval. 2,93m and 3,2m represent the outliers in the nonmarine area, consisting of 0,098% TOC and 0,019% TS and 0,1% TOC and 0,025 TS. A particular feature of this plot is the large part of the samples (1,99m, 2,785m, 4,31m, 4,51m, 7,255m, 15,6m and 16,51m) that are located close to the marine environment boundary (Fig. 33).

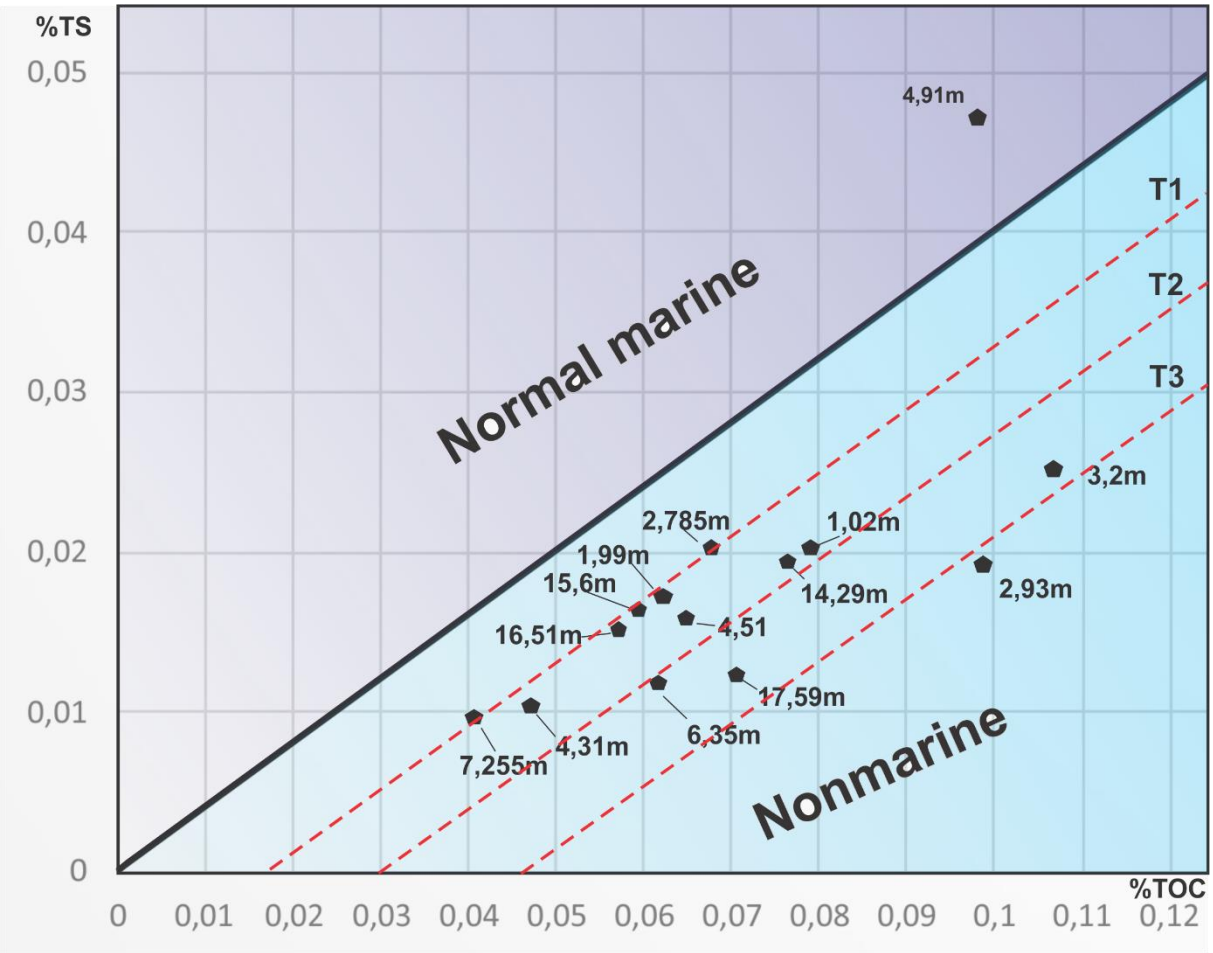

Fig. 33. TOC and TS plot of the results from the combustion analysis of organic carbon and sulfur. The blue dots represent the results, where the black line represent the boundary between the normal marine and the nonmarine environments. The red dotted lines, T1-T3 are constructed trend lines from the data. The X-axis represent the amount of % total organic carbon in the samples, where the Y-axis represent the amount % total sulfur in the samples. The normal marine and nonmarine boundary is taken from Leventhal (1995).

4.4.2 Interpretation

Based on the TOC/TS ratios sample 1,02-3,2m, 4,5m, 7,255m, 14,29m and 17,59m (Fig. 32) are indicated to fall into the range of normal marine sediment ratio of $2{,}8 \pm 0{,}8$ (Morse & Berner, 1995), whereas the rest are indicated to be nonmarine. However, the TOC% and TS% plot (Fig. 33) display that only sample 4,91m is marine, where the other samples are located in the nonmarine zone. Taking the presence of the glacier in the Sørfjord-Ullsfjord into consideration, it is likely that the depositional system is influenced by glaciofluvial conditions and subsequent glaciomarine depositional conditions. This could certainly explain the main trend of nonmarine depositional environment in Fig. 33.

The occurrence of the samples close to the marine environment boundary (Fig. 33) could indicate fluctuations in nonmarine and marine conditions, which could create brackish or close to brackish conditions in these samples. The 4,91m sample might represent a time when the glacier front were absent from the Skarmunken-Hjellneset area and marine conditions dominated, whereas sample 2,93m and 3,2m most likely represent dominant glaciofluvial conditions during deposition.

4.5 Thin sections

In total 11 thin sections (Table A 7) were investigated, where the blue color represents the epoxy gel in vacant pore space. The result revealed growth patterns to be meniscus, poikilotopic, and rim cemented, where only small portions of the concretion is cemented. The thin section was investigated under normal light, planpolarized light and incident light, and are oriented with the uppermost side pointing upwards.

4.5.1 Growth

The carbonate cement displayed usually brownish color with green stripes or brown greenish color. The growth pattern were observed to be meniscus (Fig. 34 A and B), poikilotopic (Fig. 34 C and D), and rim cementation (Fig. 34 E and F).

The meniscus, poikilotopic and rim cementation growth commonly appeared together. Meniscus and poikilotopic growth dominated in areas with moderate – very well cementation, where the meniscus growth dominated in areas that were moderate cemented. As cementation increased, the poikilotopic cementation increased as well, dominating the well- very well cemented areas. In very poor – poor cemented areas the rim cementation was the main cementation type.

A typical appearance of the cementation growth in the fine- grained carbonate concretions were zones of moderate-very well cementation with meniscus, poikilotopic cementation and larger areas of poorly-very poorly cementation with rim cement.

The coarse-grained carbonate concretions displayed similar cementation growth trends. However, the areas of well-very well cementation were much more scare, scattered and the areas of poorly-very poor cementation dominated.

4.5.1.1 Interpretation

From the thin section analyze, the characteristically brownish green color could indicate calcium carbonate cement (Fig. 34). The TOC/TS analysis indicate that the environment is dominatingly nonmarine up to 17,59m in the vertical profile. This could indicate that the Ca^{2+} in the calcium carbonate concretions derives from what it is most likely a glaciofluvial environment. The potential calcium sources are terrestrial derived Ca^{2+} from animals, plants, soil and rock, and eroded rock from the glacier, where the Breivikeidet marbles and the Sjursnes phyllite are potential sources for both Ca^{2+} and $CaCO_3$. The TOC/TS analysis also show one marine and several samples in the nonmarine zone close to the marine conditions boundary. This could indicate possible brackish or close to brackish depositional environment and a possible Ca^{2+} and CO_2 contribution by marine water. The different styles of cementation growth could represent different stages in cementation, where the rim cementation is the first, followed by meniscus cementation, which further evolves into poikiloptopic cementation. This could explain why poikiloptopic dominates in well-very well cemented areas, meniscus dominates in the moderate -very well cemented areas and rim cementation dominates in poorly cemented areas.

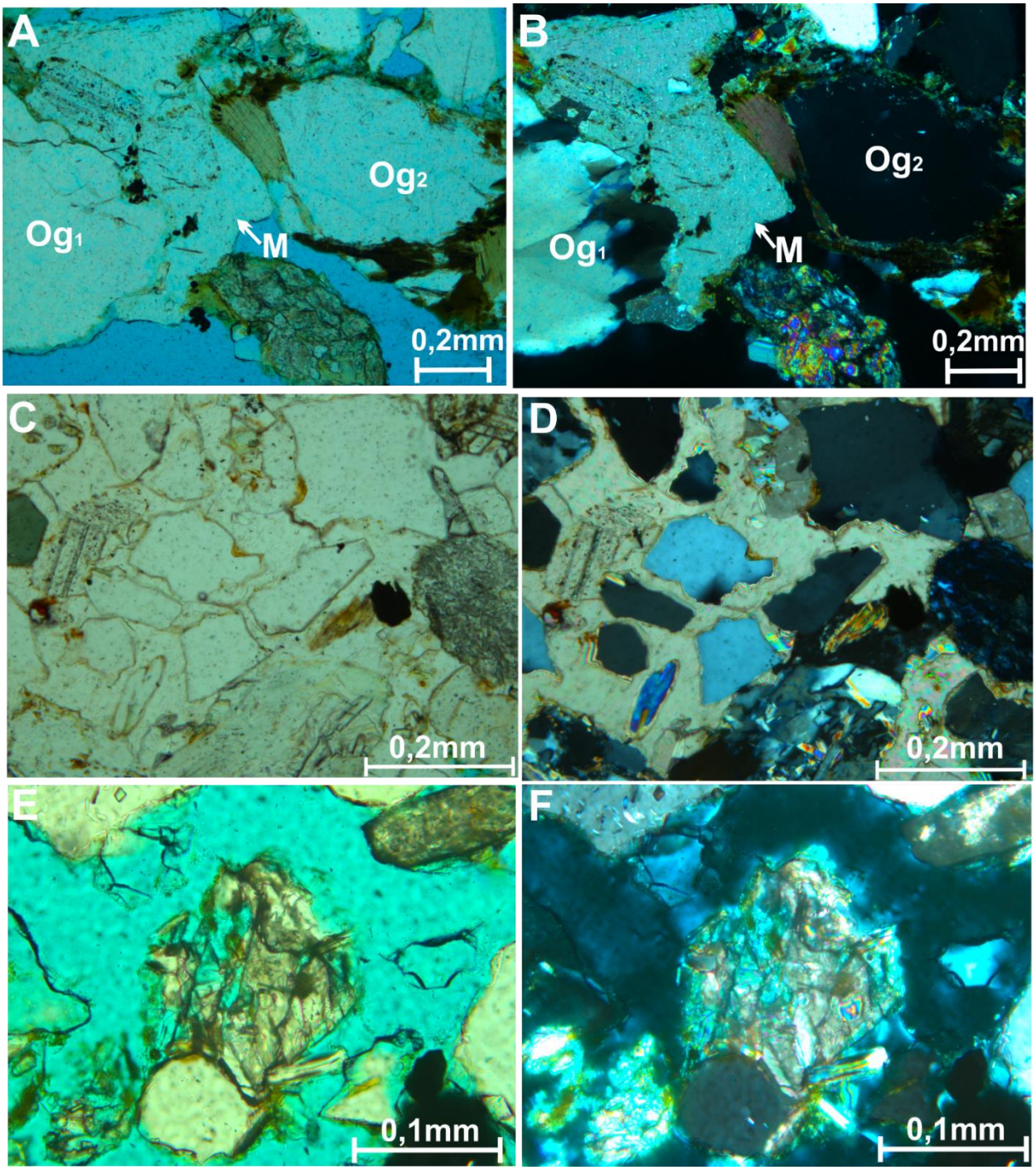

Fig. 34. (A) and (B) is located on thin section 2, where figure A is taken under planpolarized light and figure B is is taken under polarized light. The cemented area is hard to locate with the planpolarized light condtitions, but with polarized in figure B, the cement boundaries is easy to recognize. The polarized light display clearly where the boundary of the cement is, where the Og1 and Og2 represent overgrowth cement and M represent the intergrown meniscus cement growth. (C) and (D) is located on thin section 1. (C) is taken under planpolarized light ions and (D) is taken under polarized light. In figure C the cement envelops almost all of the grains, both coating and filling the pore spaces. Figure D display the grains inside the cement and showing that the cement is poikiloptopic cementation, completely enveloping the grains and acts as one entity. (E) and (F) is located on thin section 1 (Fig. 35), with planpolarized light and polarized light, and display rim cementing. The cementation occurs as an extremely thin cement around the grains, where the cementation is displayed by greenish color on figure F.

4.5.2 Cement behavior

The cement in the thin section displayed three main trends of cementing: (1) sub-horizontal to horizontal laminae`s, (2) sub-vertical to vertical pipe structures and (3) cement growth on top of clasts and larger grains. In the thin sections, the cementation variated from poorly to well cemented both within the same section and as the main trend for the whole section.

4.5.2.1 Sub- horizontal to horizontal laminae's

The sub-horizontal to horizontal laminations are distinguished by poikilotopic cemented areas, which are connecting over a larger area (Fig. 35). This type of cement behavior occurs in thin sections 1, 5 and most likely 11, which are very well-cemented in the center, where the cementation degree declines towards the boarder. At the border, the cementation appears fragmented but well cemented and is poikilotopic-cemented.

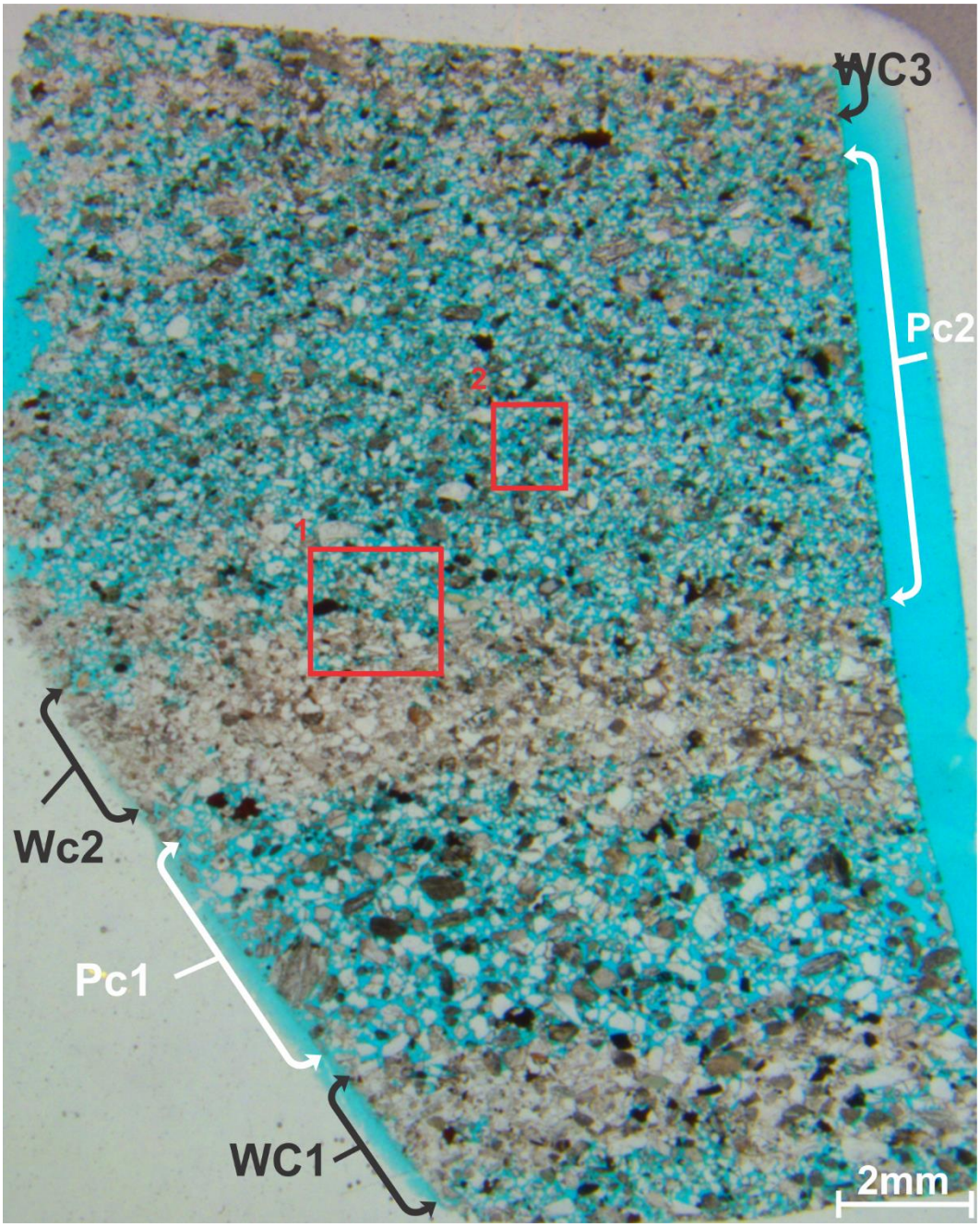

Fig. 35. Thin section 1 from 1,55m in the vertical profile. The light brownish horizontal section represents well- cemented subhorizontal – horizontal laminas, where the areas in between are poorly cemented. The red rectangle 1 represents Fig. 34 C and D and rectangle 2 represents Fig. 34 E and F. The Wc represent well cemented zones and the Pc represent poorly cemented zones. The top of the figure represents the uppermost surface of the concretion

4.5.2.2 Sub-vertical to vertical pipe structures

The sub-vertical to vertical pipe structures (Fig. 36) are characterized by moderate-poor cementated areas connected to very well to well cemented sub-horizontal to horizontal laminae`s. The pipes occur abundant to few, in thin section 1 and 5 (Fig. 37). They commonly occur toghether with other adjacent pipe structures.

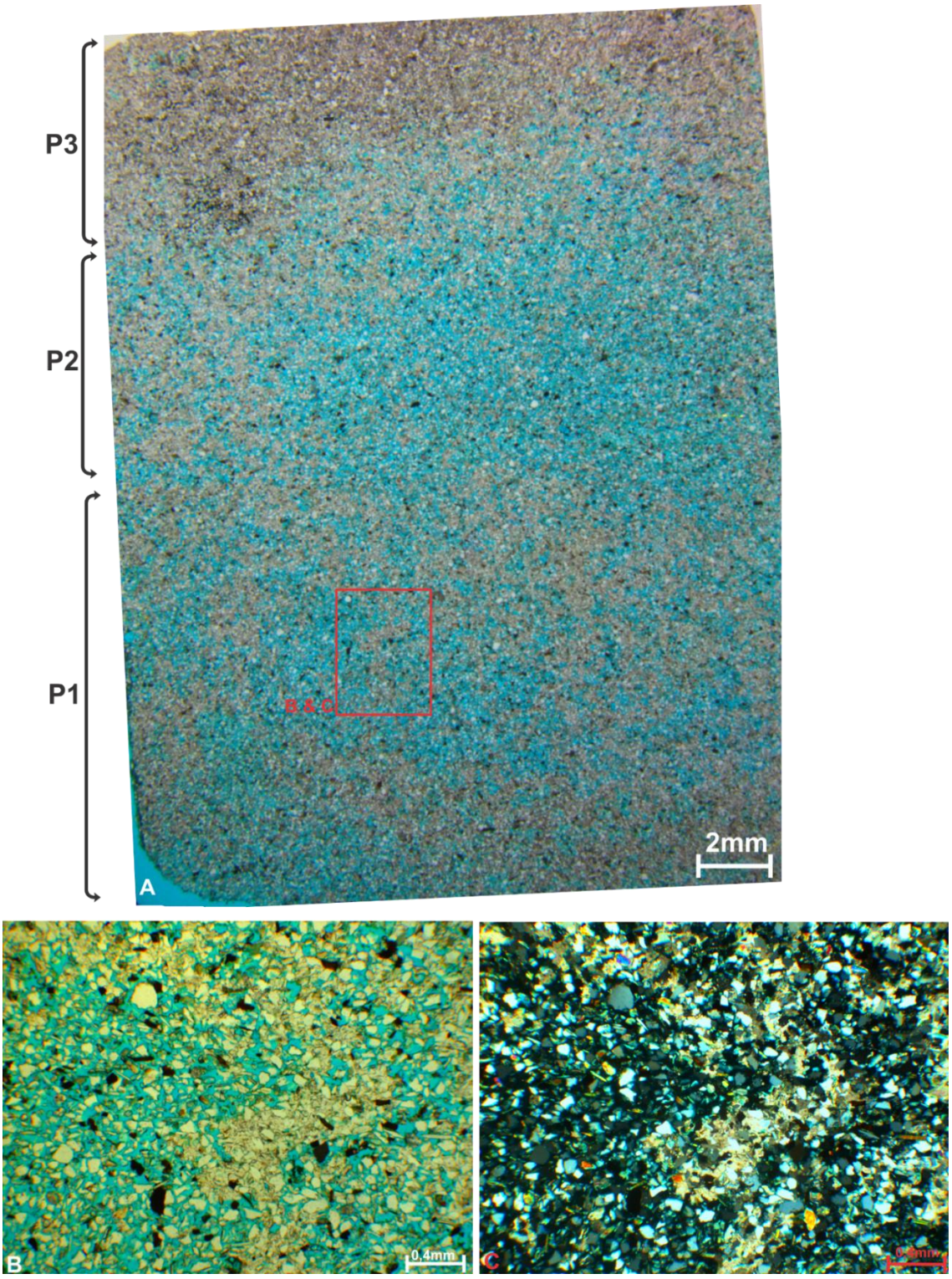

Fig. 38. Thin section 5 from 13,85-13,87m in the vertical profile. (A) Thin section of a fine-grained concretion, which is divided into three parts based on the grade of cementation, marked with P1-P3. P1 and P3 represents the more well cemented areas, where P2 is the less cemented areas. The red square represents the location of B and C. The top of the figure represents the uppermost surface of the concretion. (B) and (C) is located in P1 showing sub-vertical cementation, showing resemblance of veins or pipes. Figure B is acquired with planpolarized light and figure C is acquired with polarized light.

4.5.2.3 Cementation on the upper surface of clast and larger grains

This cementation trend is characterized by meniscus and poikilotopic cementation of fine-grained particles on the upper surface of bigger clast (Fig. 39). In several occasions the pore space between two larger clasts are filled by cemented fine-grains and intermediate grains, where the finer grains occur commonly at the uppermost surface of the clasts. The intermediate grains occur in the vacant space between the clasts, generally poorly cemented and commonly connected to the finer, well cemented grains.

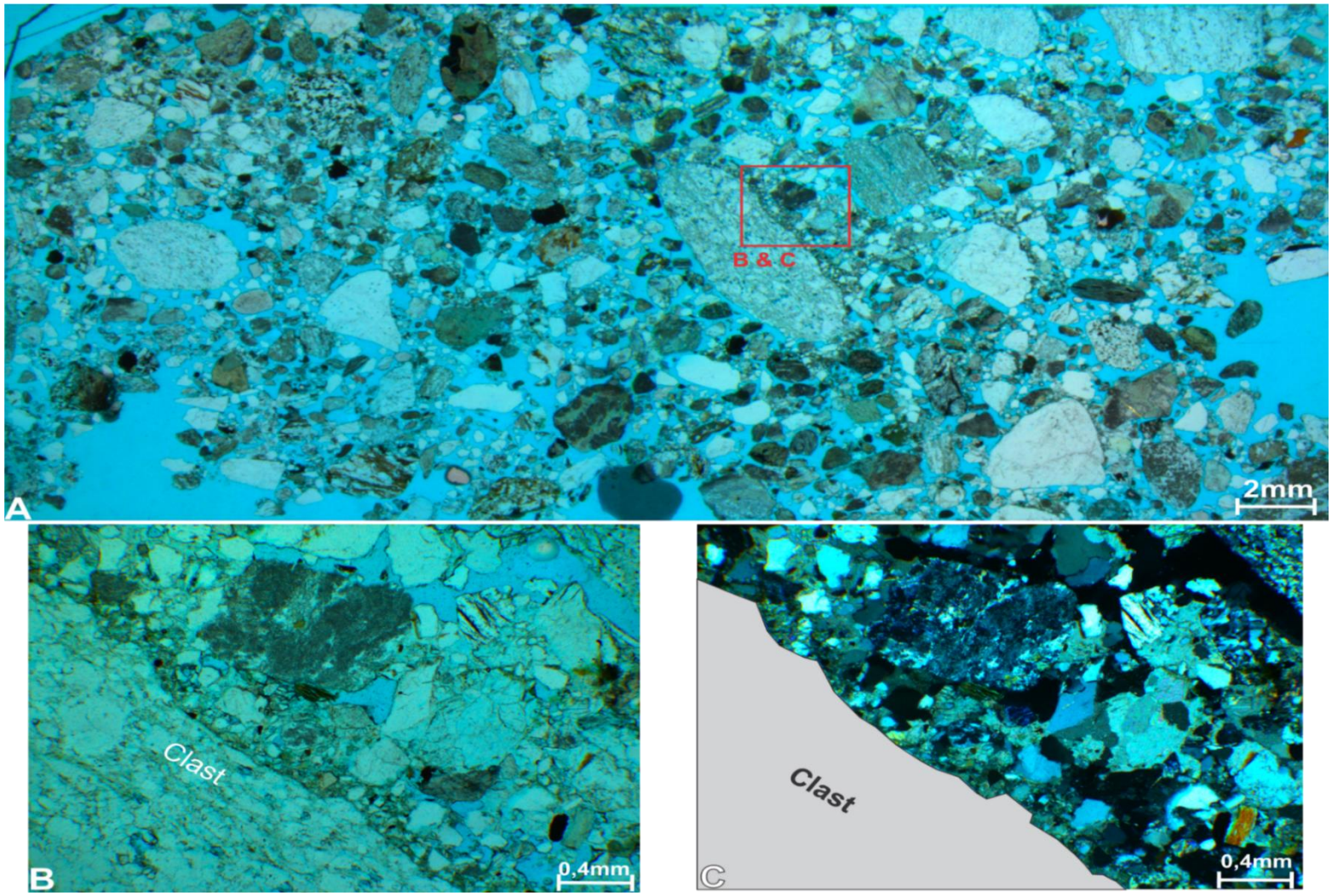

Fig. 39. (A) Coarse-grained thin section 3 from 11,22m in the vertical profile. The cementation is poor-moderate. The red square, represents figure 43 B and C. The top of the figure represents the uppermost surface of the concretion. (B) Planpolarized photo showing the smaller grains are cemented on the surface of the bigger clast. (B) The same figure with polarized light, where the big clasts have been colored grey.

4.5.2.4 Coarse-grained concretions and fine-grained concretions

The characteristics for the coarse-grained concretions are the large areas of non-very poorly cementation. It is generally specific and localized locations that is cemented. The moderate-well cemented areas consist of poikilotopic and meniscus cementation, whereas the very poorly areas are rim cemented. The cemented areas often exhibit cemented smaller grains on the upper surface of larger clasts (Fig. 39, 4.5.2.3).

The fine-grained concretions are characterized by a more intense cementation, where the cementation commonly occur well- very well cemented laminas and pipe structures (Fig. 35 and Fig. 38). However, as in the coarse-grained concretions, large areas are poorly to non-cemented. The laminas and pipe structures are characterized by poikilotopic and meniscus cementation, where the poorly cemented areas are commonly rim cemented but local areas can display scarce meniscus cementation.

4.5.2.5 Interpretation

The subhorizontally -horizontally laminations and subvertical-vertical pipe-like structures display remarkably resemblance with the observed concretions growth. Especially thin section 5 (Fig. 38 A-C) and the big boulder concretion (Fig. 46 and Fig. 47). The horizontal laminations in thin section 1 (Fig. 35) also display the same resemblance as the horizontal laminated concretions in (Fig. 47, rectangle A and Fig. 49A). The miniature structures observed in the thin section 1 and 5 might be explained by the same processes as the concretions, where the cemented areas represent hydrocarbon migration pathways in the most suitable horizons in the layers and the subsequent cementation, explained by the heterogeneity in the sediments. The more local scattered cemented areas, might also be due to the heterogeneity of the sediments, where the cemented areas are the most suitable areas for cementation of the sediment. Exactly why the cementation occurred as specific spots, could be due to a bottle neck points in the migration pathways, leading to accumulation of hydrocarbons at specific points and subsequent cementation.

The particular feature of smaller grains on bigger clasts upper surface (Fig. 39 and Fig. A 3) indicates transportation and deposition of the smaller grains on the clasts surfaces. This could be explained by fluid migration, carrying fine-grained sediments, which were redeposited when the fluid flow was now longer capable of transporting the grains, or the friction between the grains in the flow towards the clasts and preexisting grains in the concretions might also have caused deposition. The

cementation of the smaller grains on the bigger clasts, indicate that fluid flow was present in the area at some point.

Exactly why the coarse-grained concretions are less cemented than the fine-grained concretions could be explained by grainsize difference. The coarse-grained concretions contain large and vacant pore spaces in contrast with the fine-grained concretions which have much smaller pore space between the grains. The fine grainsize gives the fine-grained concretions much more contact points for the passing hydrocarbons and which could favor an increased cementation at these points.

4.5.3 Pyrite occurrence

In most of the thin sections the general occurrence of pyrite crystals in pore spaces are very poor – poor (Fig. 40). However, in thin section 10 and 11 (Fig. A 19 and Fig. A 21) the pyrite content was poor- moderate. The pyrite crystal rarely appeared as complete crystals and occurred mainly as scattered, scarce, in vacant pore spaces with other grains but not in contact with cement or within cement. In thin section 8 (Fig. A 15) the pyrite occurred zoned, and were concentrated towards the boundary of the big clast.

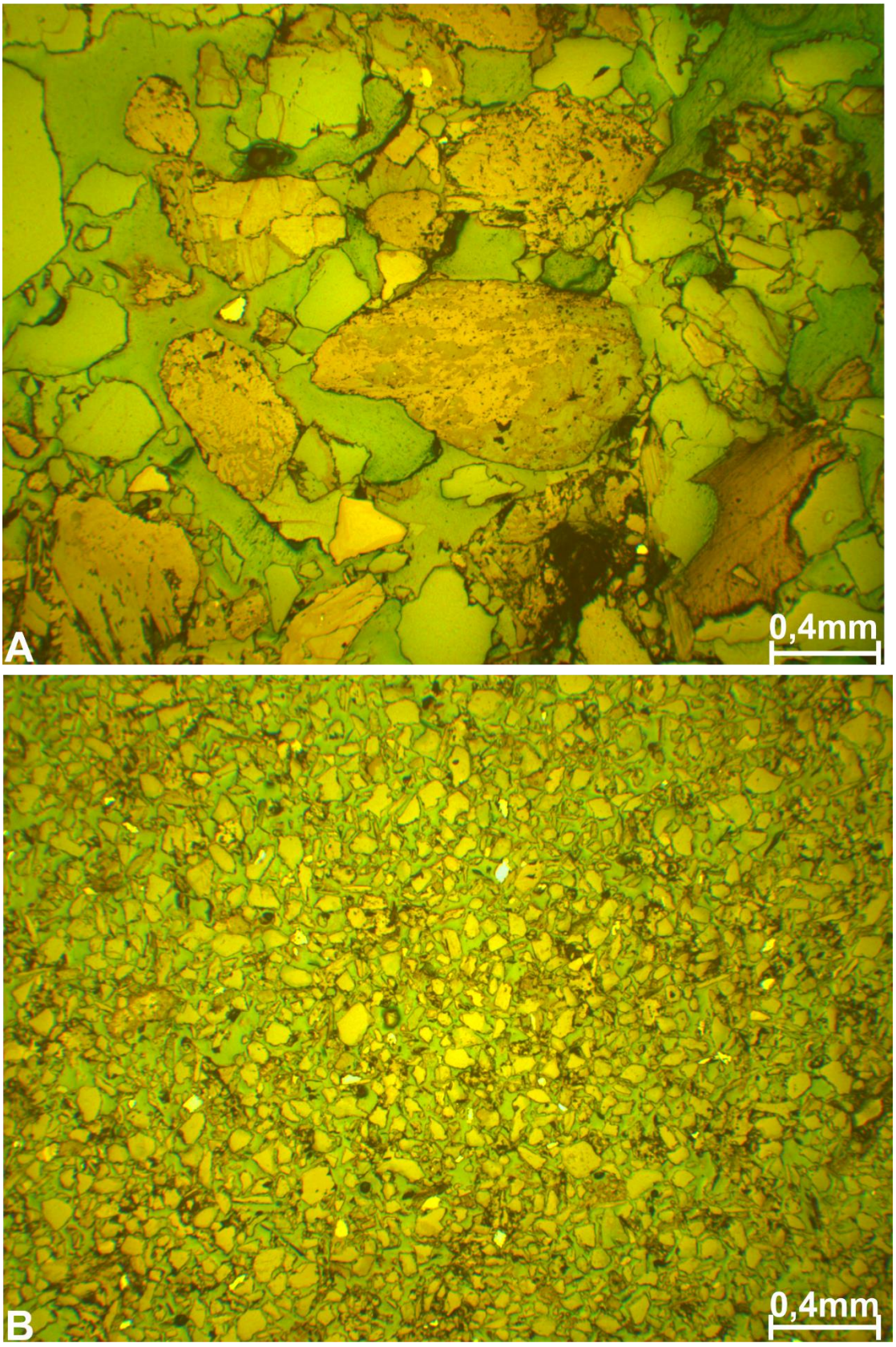

Fig. 40. (A) The thin section 3 of a coarse-grained carbonate concretion displaying the general pyrite occurrence in the section. (B) The thin section 5 of a fine-grained calcium carbonate concretion displaying the general pyrite content in the section. Figure A and B is taken with incident light and the location is marked in Fig. A 5.

4.5.3.1 Pyrite and carbonate cement

In the carbonate concretions, the pyrite crystal and cement commonly occur together with the carbonate cement (Fig. 41). In thin section 5 (Fig. 41, A) a pyrite crystal occurs in party vacant pore space, where it is in contact with the outer boarders of the carbonate cement. In thin section 1, 2, 3, 4, 9 and 11 the pyrite crystals occur either within carbonate cement or, at the base of growth nucleus, (Fig. 41, B, C and D). This marks a slightly dominating trend of pre-pyrite crystal growth of the pyrite occurring in contact with cement, whereas the dominate pyrite growth trend is the occurrence in vacant pore space commonly occurring alone or in contact with other grains.

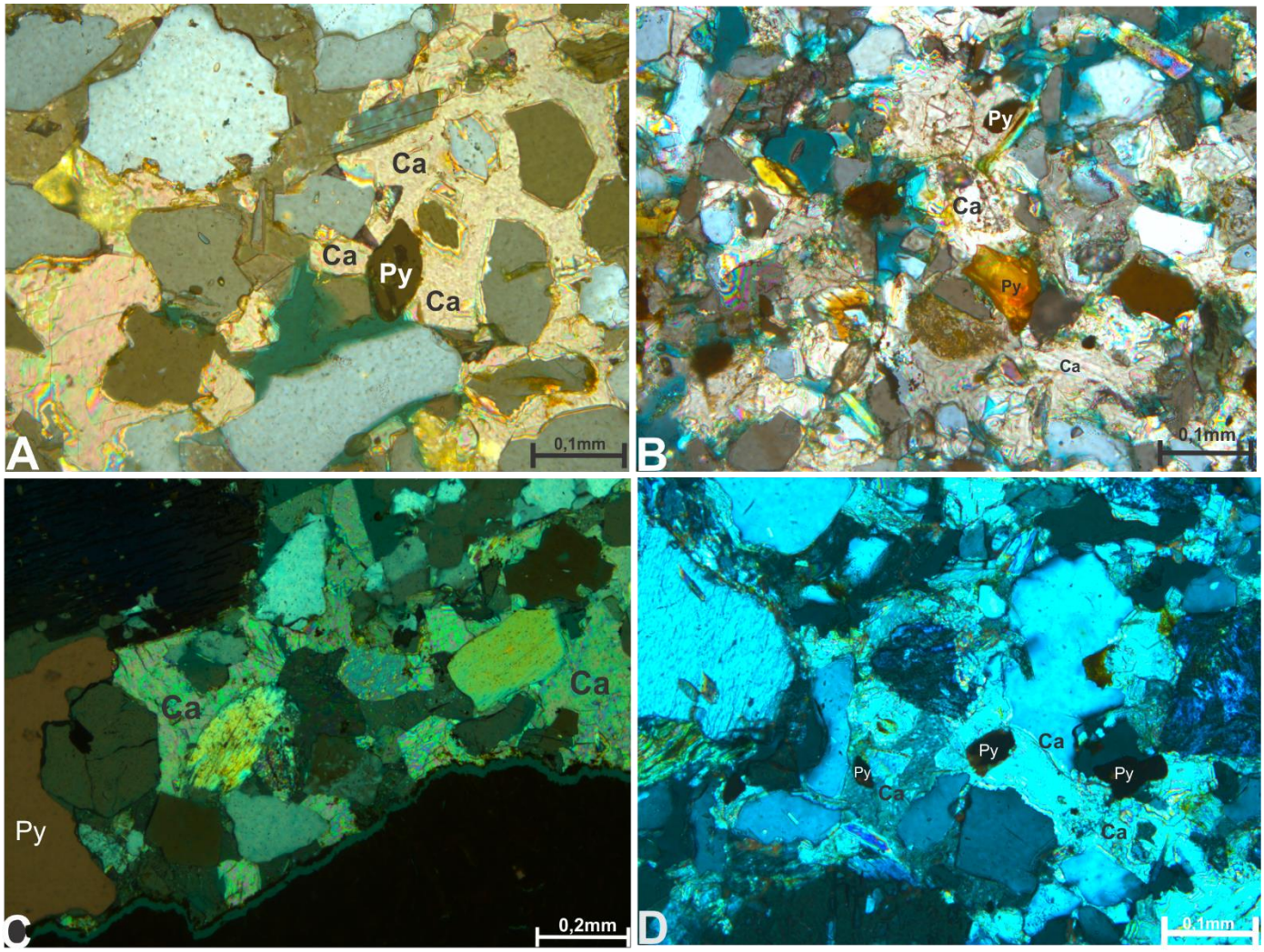

Fig. 41. (A)Thin section 1 displays a pre-carbonate cement (Ca) growth to the pyrite crystal (Py), where the pyrite crystal occurs at the outer boundary of the cement. (B) Thin section 5 displaying pre-pyrite crystal (Py) growth to the carbonate cement (Ca), where the pyrite crystal is enveloped by the cement. (C) Thin section 9 displaying pre-pyrite crystal (Py) growth to the carbonate cement (Ca), where the pyrite crystal occurs most likely at the base of the cement nucleus. (D) Thin section 11 showing pre-pyrite crystal (Py) growth to the carbonate cement, where the pyrite crystals are enveloped by cement. All of the figures is taken with polarized light, where the pyrite occurs as yellow brown, grey and black, marked with Py and the carbonate cement occur as greenish-brown, brow, greenish-blue marked with Ca.

4.5.3.2 Interpretation

The general poor amounts of pyrite content in the thin sections could be explained by the presence of the glacier and subsequent a glaciofluvial environment. A dominating glaciofluvial environment would explain the samples with low pyrite content, whereas samples with a higher pyrite content could represent more marine environment.

The abundance of pre-pyrite formation to the carbonate cementation indicate favorable conditions for pyrite crystal formation and a probably low carbon content in the sediments. This indicate that the cementation occurred at a later stage, and possible by an external carbon source. However, the other samples contain pyrite crystal in contact with the cement in such a way that the cementation appears to have occurred first. This could contradict the other samples, which could indicate a possible significant carbon content in the sediments, or it could represent more marine conditions during deposition

4.5.4 Carbonate concretions

The first carbonate concretion occurs at 0,19m and the uppermost concretion is documented at 27,97m in the vertical profile (Fig. 22). Aside from this, the carbonate concretions occur all over the exposed ice- contact system, from the northern tip of Skarmunken that faces Ullsfjord, to the southern part which lay adjacent to the northern end of Sørfjord (Fig. 7A). The size of the concretions varies from 1mm, found during sieving samples, to boulder size concretions of several meters in diameter.

The carbonate concretions in the excavated vertical sediments are observed to occur only in layers containing silt/clayey, sand and gravel. The sand and gravel concretions are the most common occurring concretions, where only one silt/clayey concretion occurred in the entire vertical profile, located at 2,72m (Fig. 22). The carbonate concretions are often observed to be strata bound in the lower half of the vertical profile, but do also occur fault planes, boundaries between layers and structures, in sand injections and lenses and around/on granule and pebbles.

4.5.4.1 Morphologies

The carbonate concretions are observed to take various different shapes throughout the vertical section, and it is also observed in the rest of the ice-contact glaciomarine system. Of the occurring carbonate concretions, the pipe concretions appeared to be the main type.

4.5.4.1.1 Pipe concretions

The pipe concretions are carbonate concretions with pipe-like morphology (Fig. 42). The pipes vary in size and length, from a few cm to tens of cm. The pipes are at its thickest in the middle part and thins out towards the terminating ends, on both ends. Two types of termination in the upper end is observed on the pipes. 1) The termination with a marked pointy end (Fig. 42, A). 2) Termination with a sudden break in the structure, leaving a blunt upper end (Fig. 42, B and C). Some of the blunt ends display a degree of horizontal cementation in the top (Fig. 42). The pipes are found in sand, gravel and conglomerate layers. The pipe concretion appears to be the main component in almost all of the occurring carbonate concretion and appear in various variants throughout the vertical profile.

4.5.4.1.2 Interpretation

The pipe concretions most likely represent the direction of the fluid flow saturated with hydrocarbons. The orientations probably represent the most suitable horizons in the sediment for the fluid migration to travel. The pointy ends termination of the pipes might indicate gradually cementation of the pipes, where less and less saturated hydrocarbon fluids were let through, before it was completely cemented. The blunt end terminations could indicate an abrupt vertical stop. This could be explained by a sudden change in the orientation of the fluid flow, going from vertical to more horizontal pathways

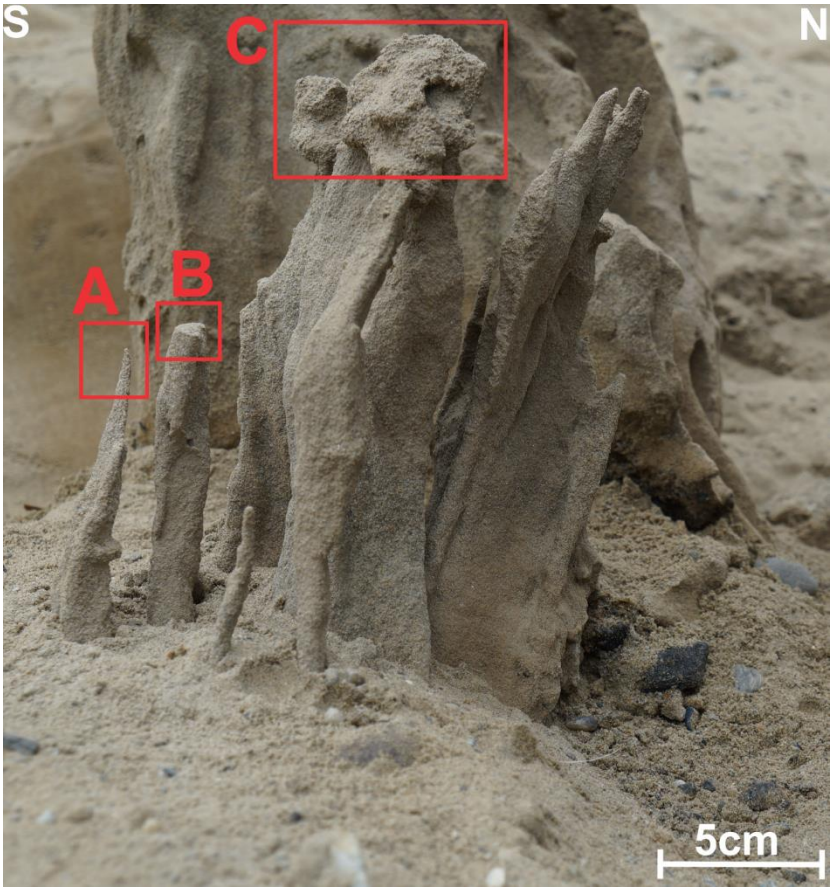

Fig. 42. Pipe carbonate concretions at 18m, excavated 13m from the excavated vertical profile. Rectangle A display a pipe concretion with a point upper end, whereas rectangle B and C show pipe concretion with blunt upper end.

4.5.4.1.2.1 Intergrown pipes

A variant of the pipe concretions is the secondary cementation by intergrowth of the pipes (Fig. 43), which is the most abundant occurring carbonate concretion variant. The pipes connect to the adjacent pipes and creates one big concretion. The number of intergrown pipes vary from 2 up to <20 intergrown pipes. In most cases, the pipes are distinct and visible, but in several cases, the pipes are cemented so well that it alters the appearance of the concretion. In these cases, commonly plate/flat shape surface is observed, in the upper or lower surface (See 4.5.4.1.4.1).

4.5.4.1.2.1.1 Carbonate chimney

As the intergrowth of pipes progress, the common feature is the creation of the carbonate chimney (Fig. 43). Several chimney structures were located both in the investigated area (Fig. 43 and Fig. 47 A) and in several locations in the beach zone in the adjacent outcrop. The in-situ chimney (Fig. 43) clearly display the intergrown pipes on the outer surfaces of the chimney, both horizontally- sub horizontally and vertically. It is 60cm at its highest and 25cm and its widest, where the intergrown pipes on the chimney surfaces varied from 3cm to over 40cm. The top of the chimney reveals a

complete cementation of the inside and a rather sudden termination, which is also observed in the smaller intergrown pipes.

Fig. 43. Several subvertical intergrown pipes carbonate concretion creating one big pipe concretion at 18m, excavated 13 m to the North from the excavated vertical profile. The pipe concretion contains their distinct shape, where the secondary cement in between has no distinct features. On the exposed surface of the sub vertical intergrown pipes, horizontal pipes are observed, indicated by the red rectangle.

4.5.4.1.3 Interpretation -intergrown pipes

The horizontal -vertical growth could most likely be explained by the heterogeneity of porosity and permeability of the seep sediments, where the cemented area represent the most suitable horizons for cemenation in the sediments. As fluid migration, could explain all of the observed intergrown

pipes concretions, the cementation could also be the result of diffuse gas discharge or a combination of both.

The most common type of intergrown pipes concretions consists of horizontal intergrow pipes with often one flat surface or two, the uppermost and the lowermost surface, with the pipes in the middle. Another type of intergrown pipes were the subvertical pipes, which are terminated by a flat horizontal surface that grew parallel to the laminations.

The distinct pipes surfaces in the concretions could indicate that these features were probably the first phase of cementation and probably represent fluid migration pathways, where the second stage is represented by the connection of the adjacent pipes.

The flat surfaces could indicate that these features are probably the end-product of the second stage cementation. The surface could represent the continuous product of cementation fluid migration pathways, resulting in the interconnection between the pipes, where the flat morhpology could represent a layer boundary, acting as a impermeable barrier.

Another type of intergrown pipes were the subvertical pipes, which were terminated by a flat horizontal surface that grew parallel to the laminations. The same processes would probably be the most likely scenario. The horizontal -vertical growth could most likely be explained by the heterogeneity of the seep sediments, where the cemented area represent the most suitable areas for cemenation in the sediments. Fluid migration could explain the observed intergrown pipes concretions but it could also be the result of diffuse gas discharge or a combination of both.

4.5.4.1.4 Interpretation - chimney concretion

The chimney concretions represent most likely a localized intense fluid migration pathway saturated with hydrocarbons content, where the external horizontal textures might represent laminations from the adjacent sediment layers. Some of the chimneys located on the beach displayed hollow structures going through the chimney. In contrast, the in-situ chimney and the adjacent pipes (Fig. 43 and Fig. 42) is completely cemented with no holes. The termination of the pointy ends, might indicate gradually cementation of the feeding hole, where less and less hydrocarbons is let through, before it is completely cemented. The blunt end, indicate some horizontally cementation in the top before it is completely cemented.

The carbonate chimney is located in sand injection, where at the top of the chimney, the injecting sand displays horizontal placement intrusion in the sediments (Fig. 56). This indicate a possibly termination of vertical fluid flow and the beginning of horizontal flow.

4.5.4.1.4.1 Plate concretions

These carbonate concretions consist of intergrown pipes (Fig. 44, B), where the secondary cementation has created a plate surface (Fig. 44, A), either on one side or both. The carbonate concretions occur very often as single intergrown pipes with the upper surface is plate shaped occur. However, the concretions also occur as plates grown on top of each other, creating layers (Fig. 44, B). In all cases, can the previous intergrown pipes be observed on the vertical sides of the concretions. The shape of the plates is observed to appear either as more or less straight plates, but also as wavy pattern is recognized. In some cases, the lower surface displays elongated spikes, pointing at a specific direction (Fig 48, E).

4.5.4.1.5 Interpretation

The plate concretions, or rather the plate surfaces appear to be the result of the cementation between two or more pipes. The plate surface could represent the boundary between two layers or it could be internal boundary in the layers, inhibiting further cementation from this point. The sorting grading of a layer could have the potential of creating such a barrier. The elongated spikes in the plate surfaces probably indicate the fluid flow direction.

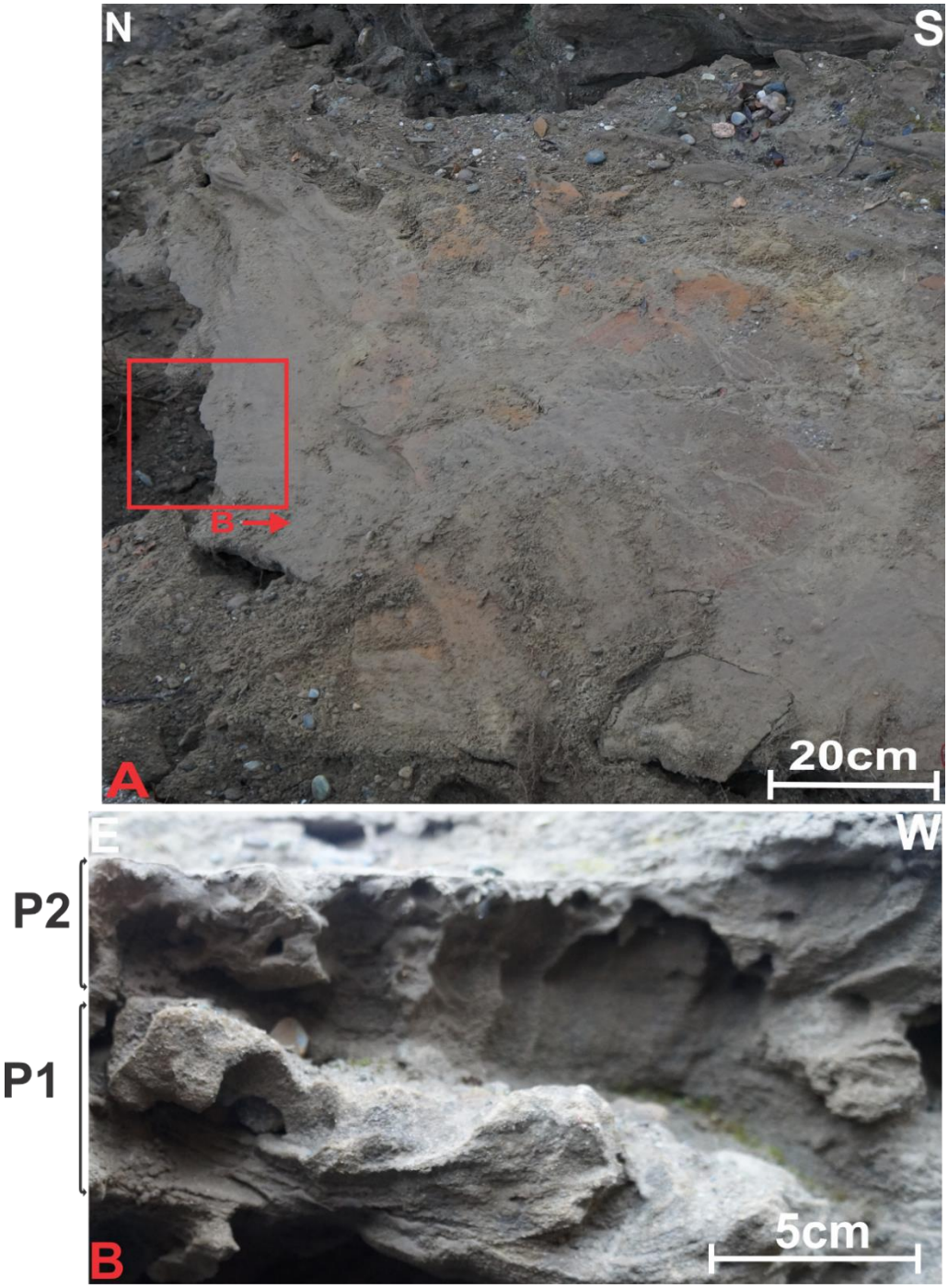

Fig. 44. Plate carbonate concretions at 14,5m, on the big boulder carbonate concretion. Figure A shows the plate upper flat surface. Figure B, located on figure A, shows the intergrown pipes, making up the fundament of the plate carbonate concretions, the flat surface and the building of layering. The layers of plate concretions are named P1 and P2.

4.5.4.1.5.1 Spherulites concretions

Spherulites concretions (Fig. 45 A and B) consists of intergrown pipes as a base, where spherulites shaped structures has been cemented on the exposed surfaces of the intergrown pipes. The spherulites grow outwards from the concretions, adjacent to each other. The surface of the spherulites is rough and the size of them varies locally and from area to area.

The spheres are observed to grow in two different ways; 1) the spherulites grow on top of each other, creating a thicker wall of spherulites concretions (Fig. 45 A and B). 2) The spherulites become large enough to connect into adjacent spherulites and grows into them, forming dumbbell-like shape (Fig. 45, C and D). The spherulites concretions usually occur in sandy material, but it also recognized in a single silt/clayey plate carbonate concretion and in coarse-gained concretions located south of the vertical profile, in the beach zone.

The spherulitic concretions only occur at the big boulder surface in the investigated outcrop. In the adjacent areas, both in the North and the South, the spherulitic concretions occur in big boulder concretions at the beach zone.

4.5.4.1.6 Interpretation

The growth on the outer surface of other concretions indicate that the formation of the spherulitic concretions were most likely a late stage cementation, possibly a third stage cementation. The two-different growth pattern could represent the different stages in cementation, where the singles spheres represent the first stage, followed by the intergrowth of the spheres. The gradual cementation window could potentially be viewed in Fig. 45 C, D and E.

The boulder concretions in the beach zone is clearly not in situ and most likely fell down from the exposed sediment slope. The common occurrence of boulder sized carbonate concretions with spherulitic carbonates at the beach zone, could indicate that theses concretions actually derives from the same layers, but not enough evidence is gathered for this statement.

The rather scarce occurrence of spherulitic concretions in the vertical profile indicate that certain special conditions must be met before formation of such concretions. The formation of the spheres could be due heterogeneity within the sediments with possibly particular porosity areas controlling and forming the morphology into sphere shapes.

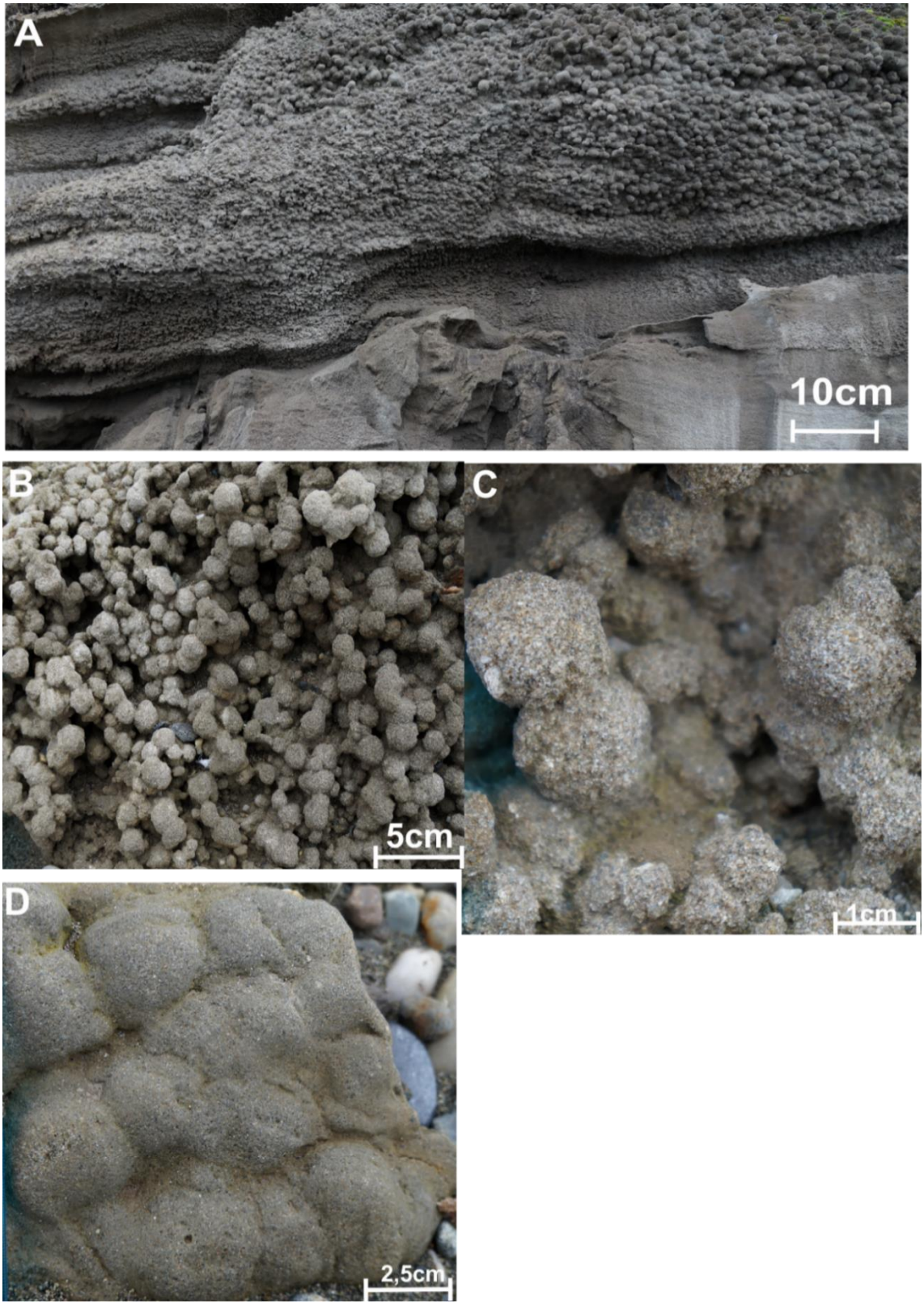

Fig. 45. (A) Spherulites concretions, at 13m, on the exposed surface of intergrown pipes concretions in the big boulder carbonate concretion). (B) The spherulites grows on top of each other and into adjacent spherulites at this location. (C) Spherulites growing into each other. (D) Intergrowht of several spherulites making up one big entity. Figure B, C and D are located on the beach and are not in-situ.

4.5.4.2 Special case- carbonate boulder

Adjacent to the excavated vertical profile from 12,5m- 15,5m, a huge boulder sized sand carbonate concretions occur (Fig. 46). The boulder concretion is the biggest occurrence of the carbonate concretions in study location. It contains horizontal and vertical cementation with, intergrowth of pipes, plate structures with striations on them and spherulite shaped concretions (Fig. 47) on some of the plate structures surfaces. The rock composes of several layers cemented together, making three distinct steps. The rock is approximate 11,46m in diameter, where the shortest and longest axis are 2,74m and 3,57m. On the southern and northern side of the concretion, two areas of gravelly material occur, cemented into the carbonate concretion. On the adjacent side, north and south, yellow sand envelops the carbonate concretion (Fig. 27).

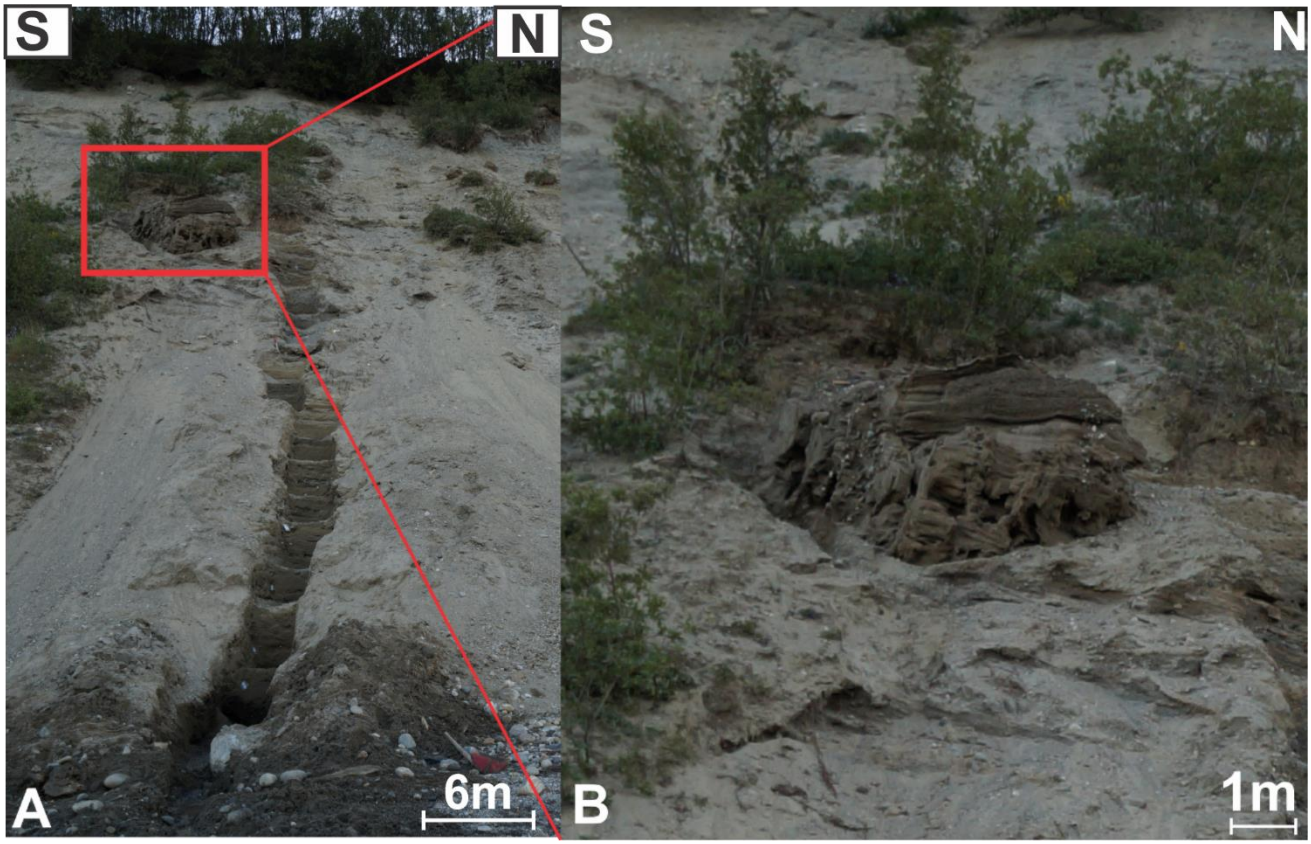

Fig. 46. (A) The excavated trench, which represent the vertical profile, and the biggest occurring carbonate concretion in the study area, marked with a red rectangle. The carbonate concretion is located at 12,5m-15,5m vertically, adjacent on the southern side of the excavated vertical profile. (B) The red rectangle in figure A, showing the biggest occurring carbonate concretion in more detail. Photo taken at Skarmunken (2016).

The boulder consists of two main types of cementation styles, intergrown pipes carbonate concretions (Fig 48, A and B), which make up almost all of the rock, and spherulites carbonate concretions (Fig 48 C) occurring on the outer surface of the intergrown pipes carbonate concretions.

The boulder is considered a special case as it contains every cementation growth variation observed in the excavated section.

4.5.4.3 Intergrown pipes concretions

Most of the giant carbonate concretion consists of intergrown pipes, creating several horizontal layers of cemented concretions, whereas three distinct packages of layers, steps emerge. From observation of the rock, the pipes started as separate pipes, which have later grown together as they expanded vertically. The main part of the intergrown pipes are horizontal, but on several places, vertical pillars occur, indicating vertical fluid migration. Some of the intergrown pipes carbonate concretions have grown together and created huge flake shapes (Fig 48 D) with flat surfaces (Fig 48 E). On this flat exposed surfaces, fluid flow directions are indicated by pointy ends towards the flow direction (Fig 48 E).

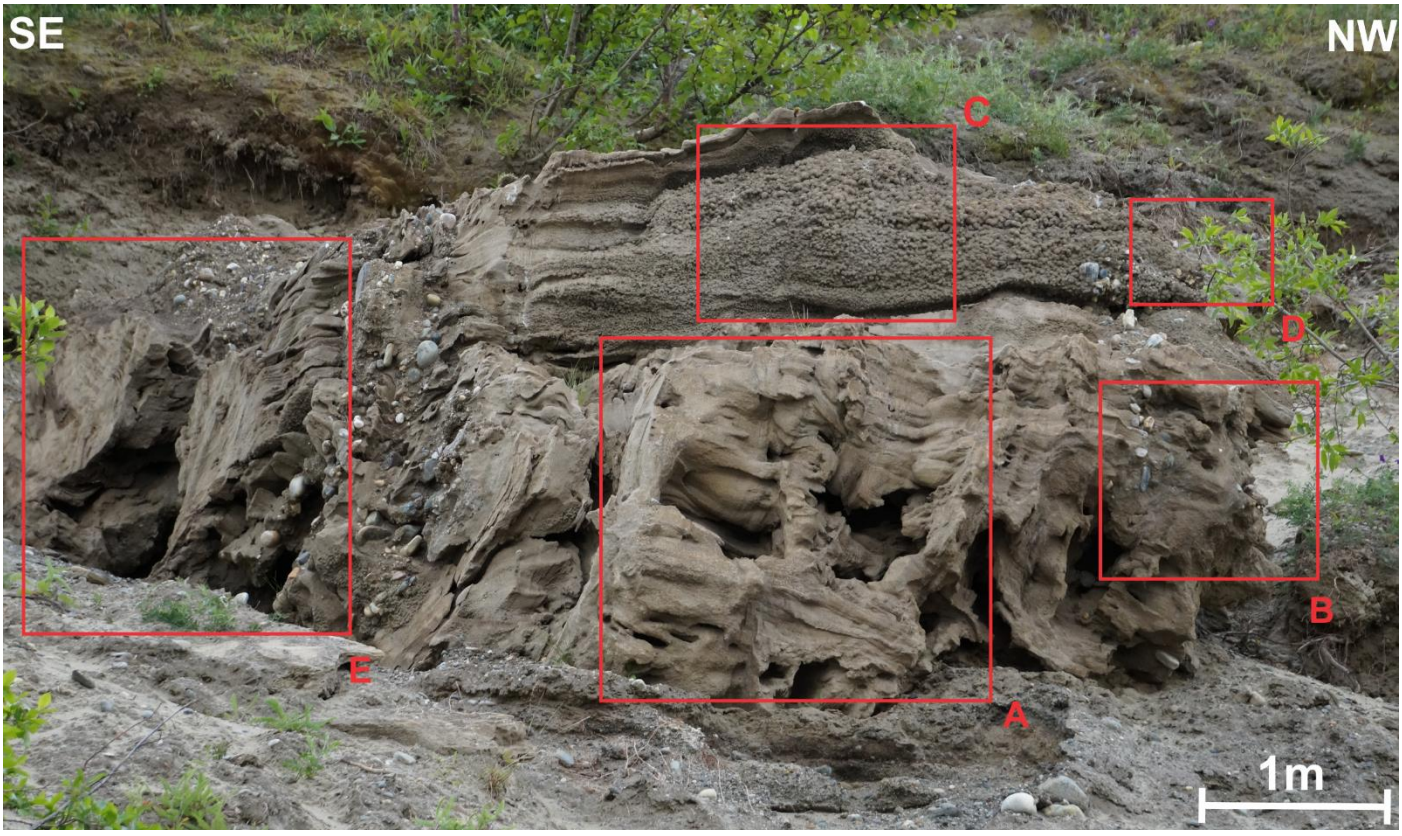

Fig. 47. The big boulder carbonate with markings of where Fig 48 A-E is located with red rectangles. Photo taken at Skarmunken (2016).

4.5.4.4 Spherulitic concretions

On several exposed intergrown pipes carbonate concretions surfaces, spherulite carbonate concretions occur (Fig 48 C). The concretions vary greatly in sizes, locally and in the different areas they occur (See 4.5.4.1.5.1 for further explanation).

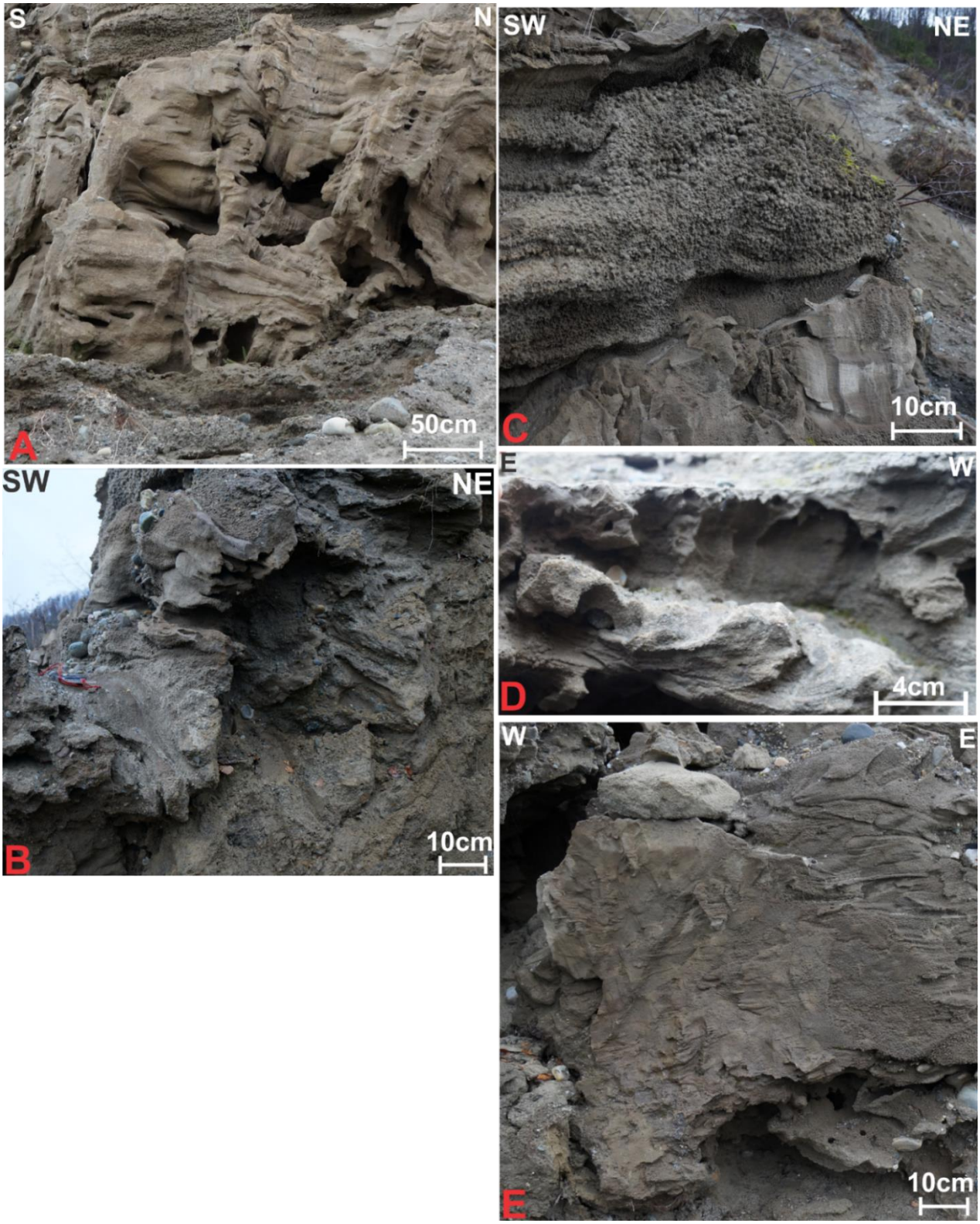

Fig 48. Figures of the big boulder carbonate concretions, where the location of each figure is marked on Fig. 47. (A) intergrown pipes on the giant boulder carbonate concretion, both vertically and horizontally. (B) The same type of growth as in (A), where the pipes have grown together and created horizontal plate structures. (C) The spherulites carbonate concretions growing on the outer surface of the intergrown pipes. (D) intergrown pipes carbonate concretions grown together as flake structures with a flat surface. (E) The flat surfaces of the flake structures with fluid migration striation. Photo taken at Skarmunken (2016).

4.5.4.5 Gravelly sections

On the southern (Fig. 49 B) and the northern side (Fig. 49 c) of boulder carbonate concretion, two areas of gravelly material occur as veins. The boundaries are distinct in most areas, but areas with intergrown pipes concretions with pebbles attached to it appears in the middle of the gravelly section on the southern side. The gravelly sections start at the top of the conglomerate and cut through the whole boulder.

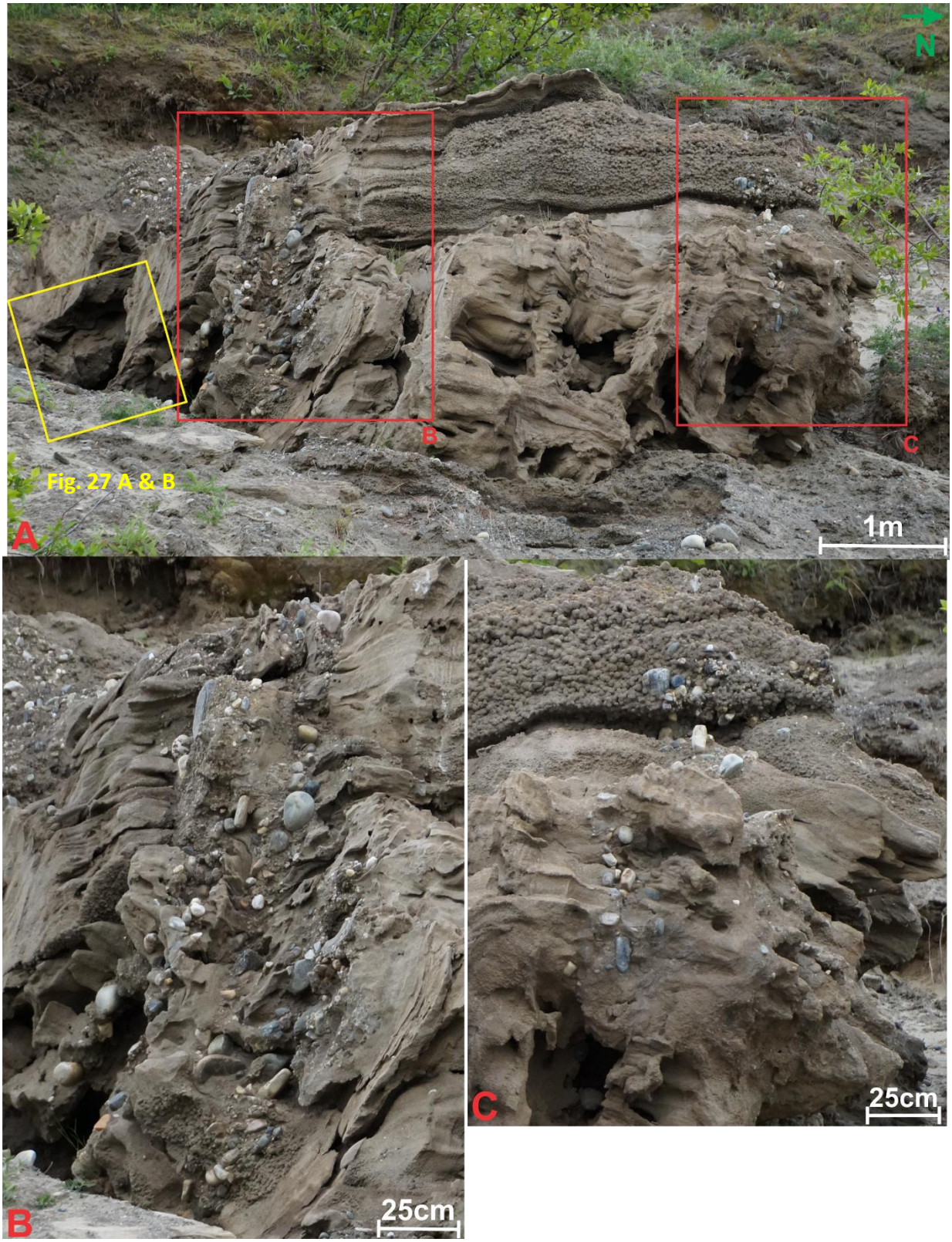

Fig. 49. (A) The boulder carbonate concretion, where the red squares represent the location of figure B, C and D, and the yellow squares represent the location of Fig. 27 A and B. (B) and (C) show conglomerate sections within the big carbonate concretion on the southern side (B and on the northern side (C)). The area is distinguished by the high concentration of clasts, which cuts completely through the big carbonate concretion. Photo taken at Skarmunken (2016).

4.5.4.6 Interpretation

The size of the carbonate concretions boulder reveals that most likely large amounts of hydrocarbons were present or passed through this area. The vertical-horizontal cementation pipes most likely represent the fluid migration main pathways, where the different orientation could be explained by the heterogeneity of the layers. The horizontal lamination/pipe structures on the outer surfaces of the vertical pipes could indicate stages of cementation. However, whether the pipes or the laminations were cemented first or simultaneously is difficult to decide.

The different orientations of the plate surfaces, could indicate that the surfaces do not represent layer boundaries and could perhaps represent special cases of horizons with continuous subvertical-vertical straight pore spaces, etc. internal grain packing, internal boundaries or faults. The different orientation of the striation on the plate surfaces show evidence of multiple stream directions, which could indicate multiple fluid flow incidents with different origins.

The spherulitic shaped concretions (see 5.5.3.4) are probably a late phase of cementing, as it its located on the plate surfaces and on the subvertically intergrow pipes. The growth pattern of the different morphologies indicates that the horizontal to vertical pipes and laminations were probably the early stages of cementation, as they appear to make up the base of the concretion boulder. As the cementation progressed, most likely the plate surfaces were formed, and the spherulitic concretions was probably the last stage of cementation of the boulder.

The pebbly sections are most likely of another origin than the rest of the boulder concretion. The veins of pebbly material appear to have formed after or during the late stages of the cementation event, as the pebbly sections pierce through the preexisting structures of the boulder. The gravelly sections appear to not disturb significantly the spherulitic concretions growth (Fig. 49 C), which probably indicate that it occurred before the formation of the spherulitc concretions. A possible culprit for the pebbly sections could be cracking by fluid migration, due to pore pressure buildup. Conglomerate and pebbly units are located both beneath and above the boulder concretion, which could have been transported into the cracks by fluid migration.

5 DISCUSSION

5.1 The depositional environment

The first authors to describe and investigate the Skarmunken and Hjellneset were Andersen (1968), Neeb (1981), Møller *et al*. (1986), where Lønne (1991) have followed in their work for further investigation of the sedimentary environment. The classification of the depositional environment will mainly be discussed towards the work of Lønne (1991) and Andersen (1968), concentrating on the Skarmunken area.

5.1.1 The vertical profile

5.1.1.1 Facies A

Comparing the result from the vertical profile with Lønne`s (1993) facies work, the vertical profile can be located on the schematically interpretation of Skarmunken (Fig 50) by Lønne (1993).

Facies A (Fig. 22) is indicated to be located in Lønne (1993) facies 2 (Fig 50), which comprise of sandy pebble layers, interbeds of stratified sand and sandy mud. Facies 2 is classified as upper-slope multiple chute-fill and shallow gravitational failure deposits (Lønne, 1993).

The sandy pebbles beds could explain the lower conglomerate and the coarse-grained pebbly sand beds. According to Lønne (1993), the sandy pebbles represent debris flow deposits. The stratified sand and sandy mud represent lower slope deposits (Lønne, 1993). This indicates that the observed intermediate sand and the sandy mud represents lower slope deposits.

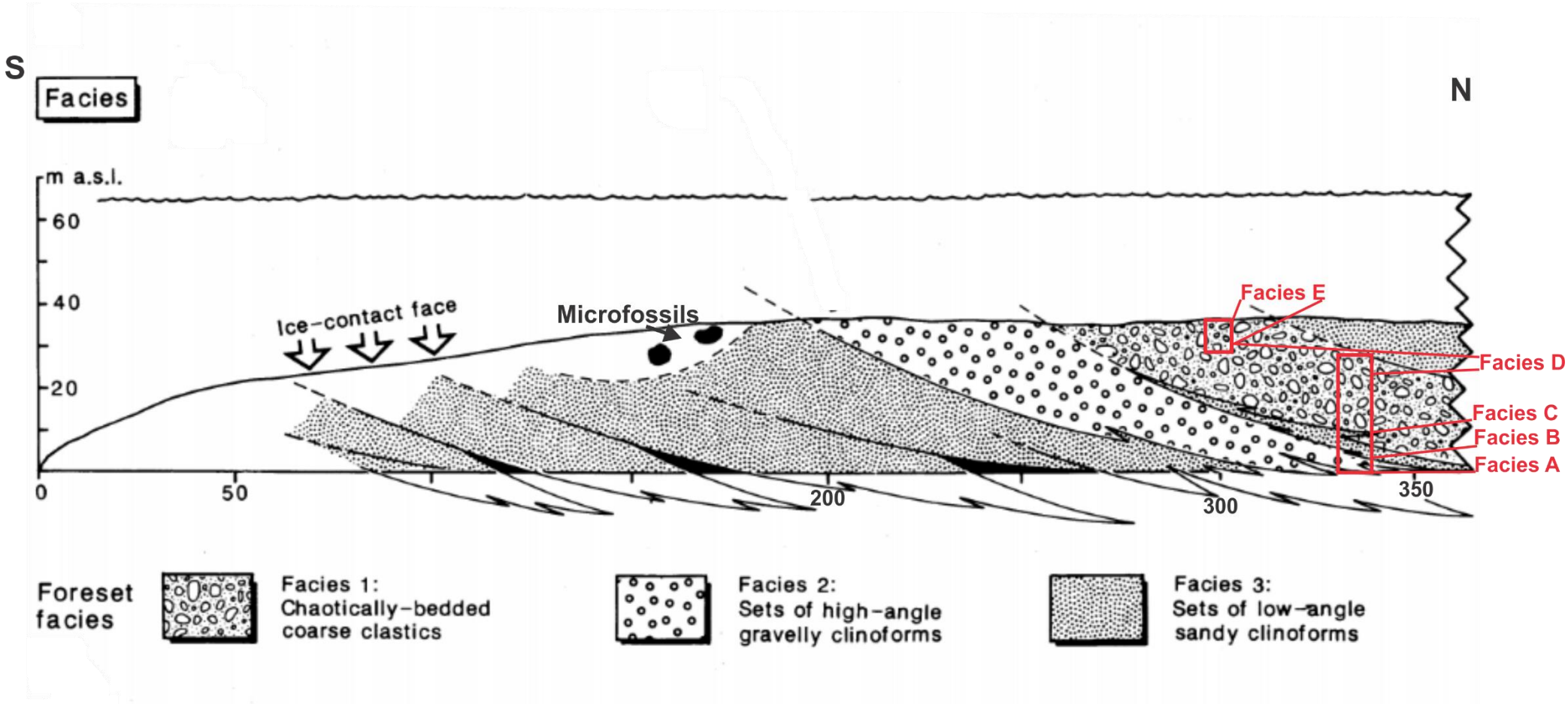

Fig 50. Schematic figure of the exposed slope at Skarmunken with interpreted foreset facies by Lønne (1993). The different facies are indicated with each specific pattern, indicated by the three squares at the bottom of the figure. The red rectangles indicate the location of the excavated vertical profile (Fig. 22, where the red lines indicate the approximate position of the investigated faces A-E (See 4.1.2). The black arrow indicates the microfossils located by Andersen (1968). The figure is modified after Lønne (1993).

5.1.1.1.1 Paleochannel

The shape of a paleochannel and the chaotically deposited material could be explained by the passage or deposit of a turbidity current suggested by e.g. Pirmez and Flood (1995), Twitchell *et al*. (1991) and Schwenck *et al*. (2003). The infilling material could then probably represent eroded, transported and redistributed of sediments. The chaotically deposit could be explained by "freezing" during depositing when the current cannot longer sustain the mass flow. A passing or deposition of a debris flow could also create similar features (Krzyszkowski (2002), but the deposited material in the channel is most likely too fine-grained, and it would be expected to observed a higher content coarse-grained material. Nemec (1990b) recognized often channel- like scours, chutes, in fan forest successions. The chutes can consist of turbidity deposits (Postma and Cruickshank, 1988) or debris-flow deposits (Postma, 1984a, b; Nemec, 1990b), which could correlate with the content in the paleaochannel. The structure is also located in Lønne (1993) facies 2, which were interpreted to represent chute-fill deposits and shallow gravitational failure deposits. In addition, Lønne (1993) also observed an erosional trough 425m from the southernmost exposed part of Skarmunken, which was interpreted as a large chute structure.

Based on the depositional content, the shape of the erosional structure and the fact that it is located in facies 2, which were reported to contain multiple chute-fill deposits, I believe that the paleochannel most likely is a chute structure, consisting of turbidity deposits.

5.1.1.2 Facies B

Based on the location of facies B (Fig 50), it is located in Lønne (1993) facies 3. Facies B composition fits the description for facies 3, with clinoforms and the dominance of stratified sand with interbeds of mud and gravel, where the gravel most likely represents the conglomerate units. This could indicate that the sediments in facies B represent middle slope chute-fill deposits.

5.1.1.3 Facies C

The facies C location (Fig 50) indicates that it is located in Lønne (1993) facies 3 and/or facies 1. However, facies C do not correlate with Lønne`s facies 3 in terms of sedimentary content. Facies C is dominated by large conglomerates sequences interrupted by sand layers, which is interpreted to be sand injections. Facies C rather show resemblance with facies 1 by Lønne (1993), which represents glacial contact foreset deposits, representing glacial advance during delta-front progradation. Facies 1 consists of diamicton, gravel beds and thinner beds of sand and mud. The foreset deposits of diamiction and gravel units could certainly explain the large conglomerate sequences, where the thin beds of sand and mud correlate with the fine-grained beds observed in

facies C. The erosional boundary located in facies C1 in the upper parts of the conglomerate sequence indicates glacial advance, which correlates with the interpretation of facies 1 (Lønne,1993).

5.1.1.4 Facies D

Facies D location (Fig 50) indicates that it is located in facies 1 (Lønne, 1993). The conglomerate units in facies D could be explained by foresets of diamictions and gravel beds located in facies 1. This could indicate that facies D represent foreset deposit, which represent glacial front advance.

5.1.1.5 Facies E

Facies E is located further to the south (Fig 50) that the rest of the vertical profile, and is indicated to be located in facies 1 (Lønne, 1993). The conglomerate units and the gravel beds could be explained by facies 1 (Lønne, 1993) foresets of diamictions and gravel beds. The transition from conglomerate beds to stepwise normal grading of the gravel could indicate glacial front retreat, which deviates from facies 1 glacial advance foreset deposits.

5.1.1.6 The allostratigraphic model

This subchapter compare the investigated sediments and facies in the vertical profile with the allostratigrapic model (2.4.5.2.3) by Lønne (1995).

The bottomsets A4, B4 or C4 (Fig. 11) proposed by Lønne (1995), consists of silty mud intercalated with fine-grained turbiditic sand, which could explain the fine-gained sediments in facies A and B. The area between foreset subunit 3 and bottomset subunit 4 of unit A, B or C (Fig. 11) is recognized to contain deposition of basal till and sorted debris deposits (Lønne, 1995), which could explain the termination of the fine-grained sequence by conglomerate layers observed in facies A and B in the vertical profile (Fig. 22). The occurrence of conglomerates in facies A and B might indicate that the fine-grained sediments were deposited in the foreset-bottomset transition area (Lønne, 1995). The large amounts of fine-grained material in facies B could represent a longer calm periods and possible stagnation periods for the glacier, compared to facies A.

Facies C display similar trend as facies A and B in the finer sections, which may indicate deposition of subunit 4, as unit A, B or C (Fig. 11) (Lønne, 1995). The deposition of the conglomerate layers could indicate foresets (A3, B3 or C3) or deposition between foresets-bottomset (A3-A4, B3-B4 or C3-C4) (Fig. 11). However, erosive boundaries are recognized in the conglomerates units, which potentially indicates glacial advance, which according the allostratigraphic model (2.4.5.2.3) represent the advancing unit A. This might indicate that the lowermost conglomerate sequence in

facies C1 represent either A3 or A3-A4 (Fig. 11) deposition by debris flows. Due to the dominance and repetition of coarse-grained sequences in facies C, it points towards deposition of foresets, as unit A3. The thin fine-grained beds in between the conglomerate sequences indicate bottomset deposits, by buoyant meltwater plume deposits. This switch from coarse-grained deposits to fine-grained deposits might indicate short periods of glacial retreat, which would indicate deposition of unit B. The large sand sequence located in facies C6 further supports the switch in deposition and the idea of glacial retreat. This indicates that the mud-muddy sand units most likely represent B4 bottomsets, by buoyant meltwater plume deposits, and the large sand sequence in facies C6 most likely represent turbiditic sand deposits in either B3-B4 or B4 (Fig. 11).

Facies D coarse-grained deposition sequence might indicate another foreset sequence by debris flow deposits. The foreset sequence combined with the inverse grading indicate deposition by unit A, as unit A3 (Fig. 11). The subhorizontal inclination could fit to this type of deposition. The lowermost part of facies E, in the conglomerate part, correlate with a foreset sequence and subsequent deposition of unit A (Fig. 11). The inclination and the coarseness indicate deposition upslope as unit A3, represented most likely by debris flow deposits. The upper part of facies E is characterized by a switch to sandy gravel and a stepwise normal grading. The switch to finer-grained units and stepwise indicate a gradual glacial retreat event. This indicates deposition of unit B or D as subunit 2 or 3 (Fig. 11). However, the horizontal inclination of the beds favors unit B2 (Fig. 11) deposit, by subglacial processes and tractional currents (Lønne, 1995).

5.1.2 Large- scale bedding-plane traces

The large-scale lineation`s observed are of importance as they cut through the vertical profile (Fig 51A and B). The observed lineation`s variations from abundant to non-existent occurrences in the exposed slope (Fig 51 B) is most likely the result of the continuous erosion and disturbance of this area, resulting in vertically higher sediments covering the vertically underlying sediments. However, the observed lineation`s to the south is enough to create extrapolated lines, which can show the large scale depositional trend of the area.

Lønne (1993) made schematic figures of the exposed bedding-plane traces (Fig 51A) and it is therefore of interest to compare the observed lineation`s with Lønne`s (1993) observations. The same bedding-plane traces are most likely observed in Fig 51B from approximately 250-350m.

5.1.2.1 Lowermost bedding-plane trace sequence

Lønne`s (1993) lowermost bedding-plane traces (Fig 51A) display very similar inclinations as the observed lowermost bedding- plane (Fig 51B). It is therefore likely that these bedding-plane traces are in the same depositional sequence. In Fig 51A more inclined bedding-plane traces, marked with blue, are observed further south in the figure, which are most likely the same as the lowermost bedding planes observed in Fig 51A and B. Based on this assumption, extrapolations with blue dotted lines have been constructed (Fig 51A). The extrapolation of the bedding planes of the lowermost bedding planes show subhorizontal inclination bending into horizontal bedding planes towards the vertical profile. Both Fig 51A and B indicate that most likely only the uppermost parts of the lowermost bedding-planes traces are present in the vertical profile.

Lønne (1993) classified the lowermost bedding-plane traces as delta foreset sequence, facies 2 deposits, consisting of sorted beds of sandy pebbles with subordinate interbeds of stratified sand, sandy mud and clast-supported pebbles and cobbles. The lowermost layers of the vertical profile consist of a conglomerate layer, coarse-grained pebbly sand and stratified mud layers which could correlate with facies 2. This correlates with the previous idea that suggested that facies A (5.1.1.1) consists of Lønne`s (1993) facies 2.

By comparing the morphology of the lowermost bedding-plane traces with the allostratigraphic model (2.4.5.2.3) by Lønne (1995), the deposition is indicated to be deposited in the transition between subunit 3 to 4 or in subunit 4 area. The conglomerate and the coarse pebbly sand units observed in the vertical profile could be explained by debris flow deposition by either A3-A4, B3-B4 or C3-C4 deposition (Fig. 11). The sand could potentially be due to turbidity currents, however, the coarse-grained content of pebbles suggest that a debris flow is more likely. The vertical profile (Fig. 22) display normal grading in facies A, which removes the option of C3-C4 deposit. This indicate that either A3-A4 or B3-B4 (Fig. 11) deposition is the likely explanation. The stratified fine-grained layer could be explained by buoyant meltwater plume deposit in bottomset area (subunit 4) or in the foreset-bottomset transitional area (subunit 3-4) as either unit A or B (Fig. 11). However, it is more common for mud layers to occur in the bottomset area due to the depositional processes and distance from the glacier.

Based on the morphology of the lowermost bedding-plane traces, they most likely represent foreset-bottomset deposition as either A3-A4 or B3-B4 (Fig. 11), where the debris flows could explain the coarse-grained units. Due to the fine-grained nature of the uppermost layer, it its most

likely that the deposit represents bottomset deposit, as buoyant meltwater plume deposit. The facies 2 (Lønne, 1991) could fit the description for the bedding-plane sequence, where the high angle gravelly clinoforms is most likely located in the southernmost part of the bedding-plane sequence (Fig 51 A). The microfossils reported by Andersen (1968) is located in the lower part of the lowermost bedding-plane trace sequence (Fig 51A), which could explain why the microfossils are not observed in the vertical profile. The occurrence of the microfossils in this sequence reveal that the sequence was deposited during approximate 10ka c. yr BP (Andersen, 1968).

5.1.2.2 Lower middle bedding-plane trace sequence

The red lower middle bedding-plane trace sequence (Fig 51B) correlates most likely with Lønne (1993) red bedding-plane traces in Fig 51A, representing most likely the same depositional sequence.

Lønne (1993) classified the lower middle bedding-plane sequence to be part of facies 3, consisting of sets of low-angle sandy clinoforms. The facies were interpreted to be middle-slope chute-fill deposits (Lønne, 1993). Based on the extrapolated red lines (Fig 51B), the bedding-plane trace sequence appears to intersect the vertical profile at approximately 1 to >2m. The layers in this range is represented by massive intermediate sand, stratified sand, where the intermediate sand is observed to contain a chute-like structure (5.1.1.1.1). These deposits could indeed correlate with low-angle sandy clinoforms and chute- fill deposits.

In comparison with the allostratigraphic model (2.4.5.2.3), the morphology of the bedding-plane traces indicate deposition in the foreset or foreset-bottomset area. The bending pattern is similar to the pattern observed in the northernmost lowermost bedding-plane trace sequence. This indicates that the bending bedding-plan traces could represent foreset-bottomset deposition. The intermediate sand in the vertical profile indicate that turbiditic sand in the foreset or foreset-bottomset as possible deposits, whereas the fine-grained sand could represent turbiditic bottomset sand deposits. Succeeding the sands is pebbly sand layer and a conglomerate layer. These deposits could be explained be either foreset or foreset-bottomset deposit as either unit A, B or C (Fig. 11), as the result of turbidity currents and debris flows.

The fact that turbidity currents can create chutes (Plink-Björklund & Steel, 2004) could explain Lønne (1993) facies 3 and the deposition as either foreset or foreset bottomset deposition, where the morphology of the bedding-plane trace sequence indicate foreset-bottomset deposition. The turbidity currents could explain the intermediate to fine-grained sand, most likely as a foreset-

bottomset deposits due to the low occurrence of debris flow deposits of what one would expect to occur in a foreset sequence. The succeeding pebbly sand and conglomerate unit most likely represent debris flow deposits in the foreset-bottomset area. A problem with the current data is that not enough is gathered to decide whether A3-A4, B3-B4 or C3-4 (Fig. 11) represent the deposit in the lower middle bedding plane trace sequence.

5.1.2.3 Upper middle bedding-plane sequence

This green bedding-plane traces sequence (Fig 51B) show the greatest resemblance with the green colored bedding-plane traces by Lønne (1993) (Fig 51A) and probably represent the same depositional sequence. However, in between the red and the green bedding- plane traces in Fig 51A, a different inclined bedding- plane trace, marked with yellow, occur. The northern half of the yellow bedding-plane traces show similar morphology to the green bedding-plane sequences in both Fig 51 A and B. An explanation for this could be an advance by the glacier front during this deposition, and that the southern half of the yellow bedding-plane trace represent up slope morphology of the upper middle bedding-plane sequence.

The upper middle bedding-plane traces are located in Lønne (1993) facies 1 and 3. The lower bedding-plane traces location in facies 3 is interpreted to represent low-angle clinoforms in the forest section, as middle-slope chute-fill deposits (Lønne, 1993). However, the only observed potential chute structure is located beneath facies B. This could indicate that facies 3 is located further down stratigraphically or only parts of the deposits in the area consists of chute-fill deposits. The rest of the bedding-traces are located in facies 1 and is interpreted to consists of glacial contact foreset deposition, representing glacial advance during delta-front progradation (Lønne, 1993). The glacial advance evidence might be located in the upper part of the conglomerate sequence, represented by the erosive boundary (5.1.1.3).

By comparing the observed morphologies of the bedding-plane traces and the bedding-planes of the allsotratigaphic model (2.4.5.2.3), the deposition area show greatest resemblance with area between subunit 3 and subunit 4 areas as unit A, B or C (Fig. 11). The bedding-plane horizontal orientations in the south and the transition to subhorizontal orientations (Fig 51B) indicate that the deposition is located in the elevated area close to subunit 4 (Fig. 11). The yellow bedding-plane trace (Fig 51A) morphology indicate the same type of depositional area. From the allostratigraphic model the yellow bedding-plane trace show greatest similarity with the depositional area close to

subunit 4 in the 3-4 transition area (Fig. 11). This indicates that this bedding-plane actually represent a glacial retreat and not a glacial advance.

The extrapolating of the upper middle plane-bedding trace sequence indicates that at least 3,8-9,5m of the vertical profile (Fig 51B) is intersected by the plane-bedding sequence, stretching from facies B into the lower parts of C, subfacies C1 (Fig. 22). Facies B dominantly consists of interbeds of mud and sand, terminated by conglomerate units. The fine-grained layers could most likely be explained by bottomset (subunit 4, Fig. 11) as buoyant meltwater plume deposits or deposition in the foreset-bottomset area by buoyant meltwater plume deposition, close to the bottomset area due to the occurrence of mud layers. The scattered coarser fine-intermediate sand layers in facies B might indicate turbiditic sand, deposited in the foreset-bottomset or bottomset area. The terminating conglomerate units indicate debris flow deposits, either in the foreset or foreset-bottomset area. The occurrence of conglomerate units together with the fine-grained packages might indicate that these conglomerates represent debris flows in the foreset-bottomset area.

The conglomerate layers in facies C1 most likely represent debris flow deposits, most likely located either in the foreset or foreset-bottomset area. The erosive contact in sub facies C1 in the upper conglomerate sequence (Fig. 22) could indicate a progradation foreset sequence, which removes unit B as an option.

Based on the morphology and the location of the yellow bedding-plane trace, the bedding-plane is most likely the lower part of the upper middle bedding-plane trace sequence and probably represent a minor glacial retreat. The lower part of bedding-plane traces located in facies B most likely consists of foreset-bottomset transition deposits, as the interbeds of sand and mud occur together with conglomerate units. The fine-grained layers most likely represent buoyant meltwater plume fine-grained mud, where the fine-intermediate sand represent turbiditic sand and conglomerate units represent debris flow deposits. Facies C1 conglomerate units most likely represent debris flow deposits, where the conglomerate sequence represents a glacial advance. The erosive boundary located in the upper part of the conglomerate sequence (Fig. 22) represents most likely further advance of the glacier. Facies C1 represents most likely Lønne (1993) delta-front progradation facies 1. Lønne (1993) facies 2 is most likely located further down stratigraphically in the underlying bedding-traces. The glacier advance evidence classifies the upper middle bedding-plane sequence deposits as unit A deposits (Lønne, 1995), where the deposits in facies B most likely represent A3-A4 deposits and the facies C1 represents most likely foreset A3 deposits (Fig. 11).

5.1.2.4 Uppermost bedding-plane trace sequence

By comparing Lønne (1993) uppermost purple bedding-plane traces (Fig 51A) and the observed uppermost purple bedding-plane traces (Fig 51B), only the northern part correlate, as the southern area in Lønne (1993) bedding-planes are lacking. Based on the height and the northern correlation they are presumably the same bedding-plane sequence (Fig 51B). The morphology of the bedding-plane traces indicate that the deposition could be located in the topset area in the south, which transitions into a foreset sequence towards north (Lønne, 1993). It could also be located in the transition between foreset-bottomset area, which also display horizontal deposition that transitions into subhorizontal deposition.

The main part of the uppermost bedding-plane sequence is located in Lønne (1993) facies 1 and the uppermost part is located in facies 3 (Fig 50). This indicate that the main part of the bedding-plane sequence represents glacial advance as foreset deposition (Lønne, 1993). The location of the uppermost part of the bedding-plane in facies 3 indicate that this deposits consists of low-angle sandy clinoforms as middle slope chute-fill deposits (Lønne, 1993). From extrapolation of the bedding-plane traces (Fig 51B), the first extrapolated intersection between the of uppermost bedding-plane trace sequence and vertical profile occur at approximately just above 20m (Fig. 22 and Fig 51B). The occurrence of bedding-plane stretches from facies C6 to E in the vertical profile (Fig 51A). It is likely that the bedding-planes are located even further down in the vertical profile, but the lack of observed bedding-plane traces inhibits further extrapolation. Facies C6 consists of fine-medium-grained sand sequence terminated by a conglomerate unit. The uppermost conglomerate unit correlate with what one could expect of foreset deposition by glacial advance as Lønne`s (1993) facies 1, however, the sand sequence deviate from the foreset deposition. An explanation for this could be that the sand sequence represent deposition in the foreset-bottomset transition area, which could indicate that the conglomerate represents debris flow in the same area. The succeeding facies D and E could correlate with ice advance foresets, where the conglomerate units and the coarse sandy gravels represent debris flow deposits. The transition from conglomerate units to coarse sandy gravel in the uppermost part of facies E might indicate reduction in the meltwater discharge or mark the gradual retreat of the glacial front. The upper parts of facies D and facies E is excavated further south (Fig 51B) than the main vertical profile area, which will influence the type of sediments located during excavation. This might explain why Lønne (1991) facies 3 is not observed in the uppermost part of the bedding-planes in the vertical profile.

The allostratigraphic model (2.4.5.2.3) (Lønne, 1995) suggests that the morphology of the bedding-plane traces could represent ice-proximal deposits, basal till and sorted debris flow deposits, in the fan top, which further north transitions into foresets deposits. The model suggests subunit 2 and 3 deposits as either unit A or B (Fig. 11). The horizontal bedding-plane traces could also represent topset deposition in the delta top, which transitions into foreset deposition northwards. The model suggests unit C2 and unit C3 as potential candidates in this scenario (Fig. 11) (Lønne, 1995). The last possible scenario according to the allostratigraphic model is deposition in the area between subunit 3 and 4, close to the subunit 4, as either unit A, B or C (Fig. 11) (Lønne, 1995). The sand and the termination by a conglomerate unit in facies C6 could fit the description of subunit C3, which consists of turbidites, debris flow deposits and is inverse graded. Unit A is also characterized as inverse graded, where the bottomset A4 contain turbiditic fine-grained sand, and the foreset A3 and A3-A4 deposits could contain basal till and debris flow deposits. This makes unit A3, A3-A4 and A4 potential candidates for the deposition of facies C6. The occurrence of sands above the large conglomerate sequence in the underlying subfacies C3-C5 could indicate glacial retreat, which might indicate deposition of either unit B or D. Facies D and E correlate with foreset deposits, however, their inclination might suggest topset deposition, unit C2 (Fig. 11), in the southern part of the exposed slope. The horizontal- close to horizontal bedding-plane traces could also represent A2 or B2 deposition, as they can be easily mistaken for glaciofluvial topset (Lønne, 1995). Towards north, the bedding-planes transitions into subhorizontal inclination, indicating transition into foreset deposition. This leaves A3, B3 or C3 potential candidates for deposition (Lønne, 1995). The stepwise manner of reduction in grainsize in facies E might indicate glacial front retreat or reduction in meltwater discharge. Unit D is deposited during glacial retreat, where D1, D3 and D4 could correlate with conglomerate and gravelly deposits.

Based in the morphology of the bedding-plane traces, the area furthest to the south in the exposed slope represent glacial advance deposit. Of the three large conglomerate sequences, the upper two show similarity to the lowermost, which most likely represent glacial advance. This most likely indicates that these also represent glacial advance, where the uppermost one is according to Lønne (1993) a glacial advance sequence. This indicates that these sequences represent unit A (Lønne, 1995), where they most likely represent foresets deposits. The foreset deposits is most likely A3 deposits, due to their large conglomerate sequences and subhorizontal inclination, as basal till and

debris flow deposits. The large sand sequence indicates a glacier front retreat, which represents most likely unit B deposit, in the foreset-bottomset area (B3-B4 deposit) as turbiditic sand.

The microfossils (Andersen, 1968) age infers that during the deposition of the ice-contact glaciomarine system, the sea level was indicated to reach 50-51m a.s.l. (Corner & Haugane, 1993). This removes a delta topset as a possible explanation for the horizontal-subhorizontal bedding-plane traces in facies D and E. This indicates that the facies D and E represent subglacial horizontal units, as unit A2 or B2. The retreating tendencies in facies E most likely represent gradual glacier retreat, which indicate either B2 or D2 deposits. However, D2 consists of more fine-grained units (Lønne, 1995) than what is observed in the vertical profile, indicating that B2 is the most likely candidate for deposition. Most likely are the southernmost bedding-plane traces subglacial deposits, where the bedding-plane transitions into a foreset sequence towards north.

5.1.2.5 Bedding- plane traces summary

The sea level height (Corner & Haugane, 1993) indicate that none of the excavated deposits consists of unit C (Lønne, 1995). The three large conglomerate sequences most likely represent glacial front advance and subsequent the advancing unit A (Lønne, 1993). The sands and fine-grained units in between the coarse-grained sequences most likely represent periods of glacial retreats, which indicates deposition of unit B. The sediments below the coarse-grained conglomerate sequences (Fig. 22) consist of most likely either A or B units as they can consist of similar deposits (Lønne, 1995). However, the characteristic trait for unit B is the occurrence of foresets without signs of synsedimentary ice-front advance (Lønne, 1995), where the first occurrence of a foreset sequence and ice-front advance is located at approximately 8m in the vertical profile. This indicates the deposits below 8m are unit B deposits.

This means that most likely, the lowermost bedding-plane traces sequence consists of foreset-bottomset and bottomset deposits of B3-B4 and B4 deposits. The mud most likely represents bottomset deposits, by buoyant meltwater plume deposits. The coarse pebbly sand and the conglomerates most likely represent debris flows in the foreset-bottomset area. The southernmost part of the bedding-plane trace sequence indicated by Lønne (1993) (Fig 51A) most likely represent a foreset sequence. The occurrence of microfossils in the bedding-plane trace sequence (Fig 51 A) indicates that all the sediments succeeding this sequence is older than 10ka c.yr BP.

The lower middle bedding-plane trace sequence most likely consists of foreset-bottomset deposits, as B3-B4 deposits, where turbiditic sand could explain the sands and chute-fill deposits. Debris flow in B3-B4 depositional area most likely represents the pebbly sand and the conglomerate unit.

The upper middle bedding-plane sequence lower section most likely represent foreset-bottomset transition deposit, represented by B3-B4 deposition. The lowermost part of the bedding-plane sequence, the yellow bedding-plane trace, most likely represents a minor retreat. This indicate, that this bedding-plane represent foreset-bottomset deposition in unit B, as B3-B4 deposit. The fine-grained layers most likely represent buoyant meltwater plume deposits, where the sand represent turbiditic sand. The conglomerate sequence most likely represents debris flow deposits.

The upper part of the bedding-plane traces, represented by the large conglomerate sequence, most likely represent glacial advance and deposition of a foreset sequence. The erosive boundary in the conglomerate indicates that the deposition most likely consists of unit A deposits, as unit A3. The conglomerate units represent most likely basal till and or debris flow deposits.

The uppermost bedding- plane trace sequence represents most likely both a glacial advance and glacial retreat. The lower sandy part of the sequence in facies C6 most likely represents glacial retreat and deposition of unit B3-B4, where the sand represents turbiditic sand. The succeeding conglomerate sequence in facies D indicate glacial advance and deposition of a foreset sequence, unit A3, represented by subglacial deposits. The uppermost part of facies D and the lowermost part of facies E most likely represent subglacial unit A2 deposit, represented by basal till and or debris flow deposits. Facies E represent most likely a gradual glacial retreat, where the deposit consists of unit B2 by subglacial deposits.

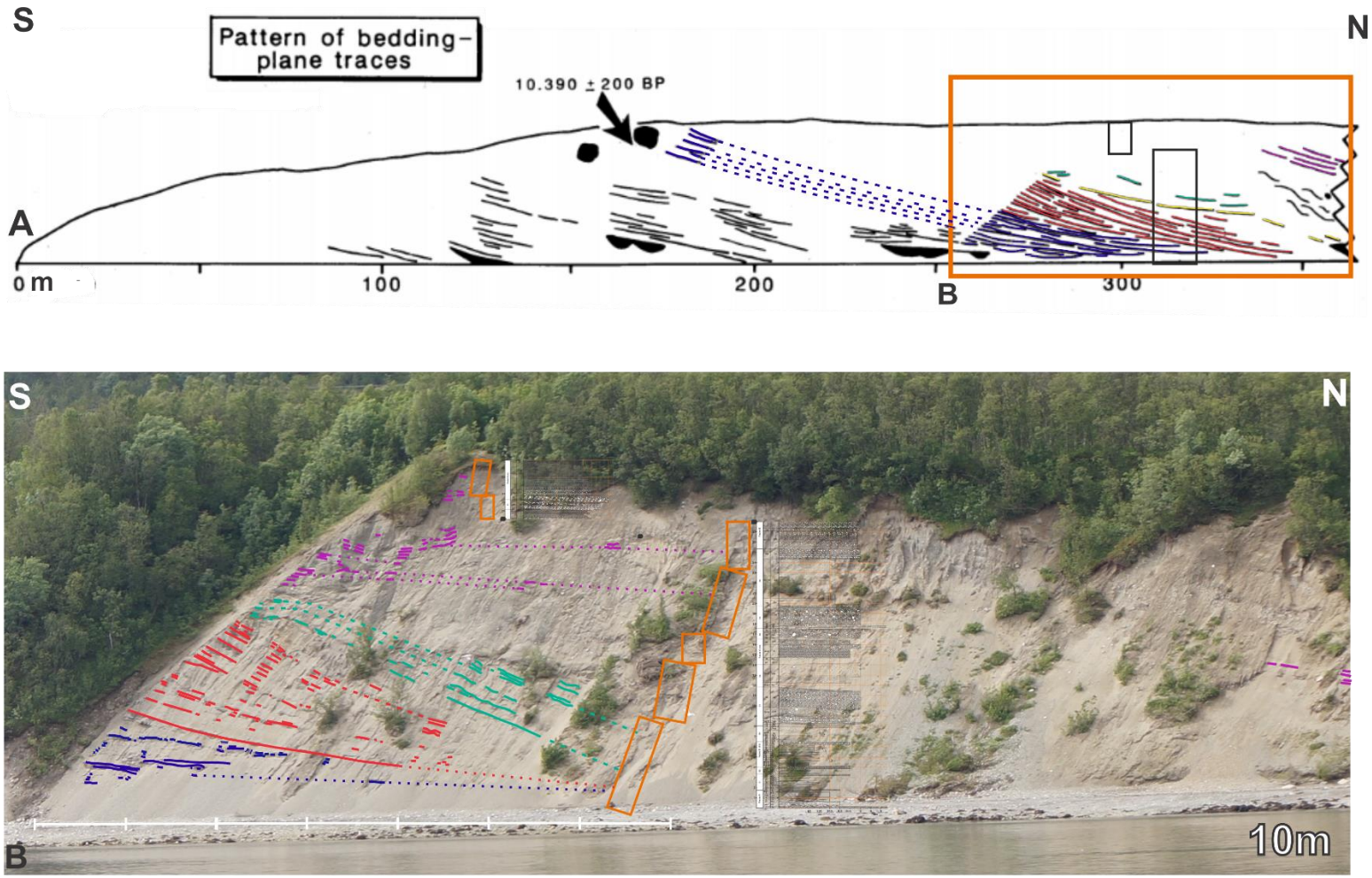

Fig 51 A) Modifies figure of bedding-plane traces in the exposed slope in Skarmunken by Lønne (1993). The lowermost bedding-plane trace is marked with blue, the lower middle bedding plane trace is marked with red, the middle bedding plane trace is marked with yellow, the upper middle bedding plane trace is marked with green and the uppermost bedding plane trace is marked with purple. The orange rectangle show the location of figure 2B and the black rectangles represent the approximate location of the vertical profile. The black arrow indicates the position of the mollusc shell fragments reported by Andersen (1968). B) The observed bedding-plane traces in 2016 in the exposed slope in Skarmunken. The different inclined bedding-plane traces are marked with their own respective color; blue, red, green and purple. The rectangles show was the vertical profile was excavated and the log of the vertical profile is placed adjacent to the excavation areas. The dotted lines in A and B are extrapolated lines.

5.1.3 Maximum pebble analysis

Investigations has been conducted on Quaternary raised ice-contact deposits in Svalbard (Lønne, 1995), which reveal that clast supported gravel units can be the result of cohesionless debris flows, dominated by clasts collision and dispersive pressure. This would further support the suggestion of conglomerate deposition by debris flows indicated by the allostratigrapic model (5.1.1.6 and 5.1.2). However, these MPS/BTh data (Lønne, 1995) deviates with the current investigated MPS/BTh data (4.3) of 27,16cm in mean bed thickness and 6,21cm in mean maximum pebble size. The deviation in mean maximum pebble size could be explained by weaker debris flows, which were unable to transport larger pebbles. The mean bed thicknesses most obvious explanation are longer periods of environmental conditions favoring such deposits, e.g. colder or warmer periods causing glacier front advance against the investigated depositional area.

Nemec and Steel (1984) values for subaqueous depositional environment correlate with the analysis of the conglomerate units located in Skarmunken. The mean BTh deviate by 6,36cm whereas the mean MPS of 3,79cm fall into the interval of into the subaqueous interval for mean MPS. Aside from the line gradient, the small BTh deviation and the mean MPS indicate that the conglomerate units were deposited under subaqueous conditions. Even though the MPS method is considered as a rough estimate, the shoreline displacement curve (Fig. 5) supports the indication of subaqueous conditions during deposition. The shoreline was reported to be around 50-51m during the deposition of the ice-contact subaqueous fan (Corner & Haugane, 1993) and the highest conglomerate unit is located at 34,75m, which indicates that the conglomerate was most likely deposited subaqueous. The subaqueous deposition supports the indication of subaqueous ice-contact fan deposit, represented by unit A and B (5.1.1.6 and 5.1.2)

5.1.3.1 Summary

The comparison of result with Lønne`s (1995) work, the analysis indicate that the conglomerate units were most likely deposited by cohesionless debris flows. The values from Nemec and Steel (1984) reveals that the conglomerates most likely were deposited in subaqueous conditions, which is further supported by the shoreline data by Corner and Haugane (1993) and indicated sedimentary depositional unit's A and B (5.1.2.5).

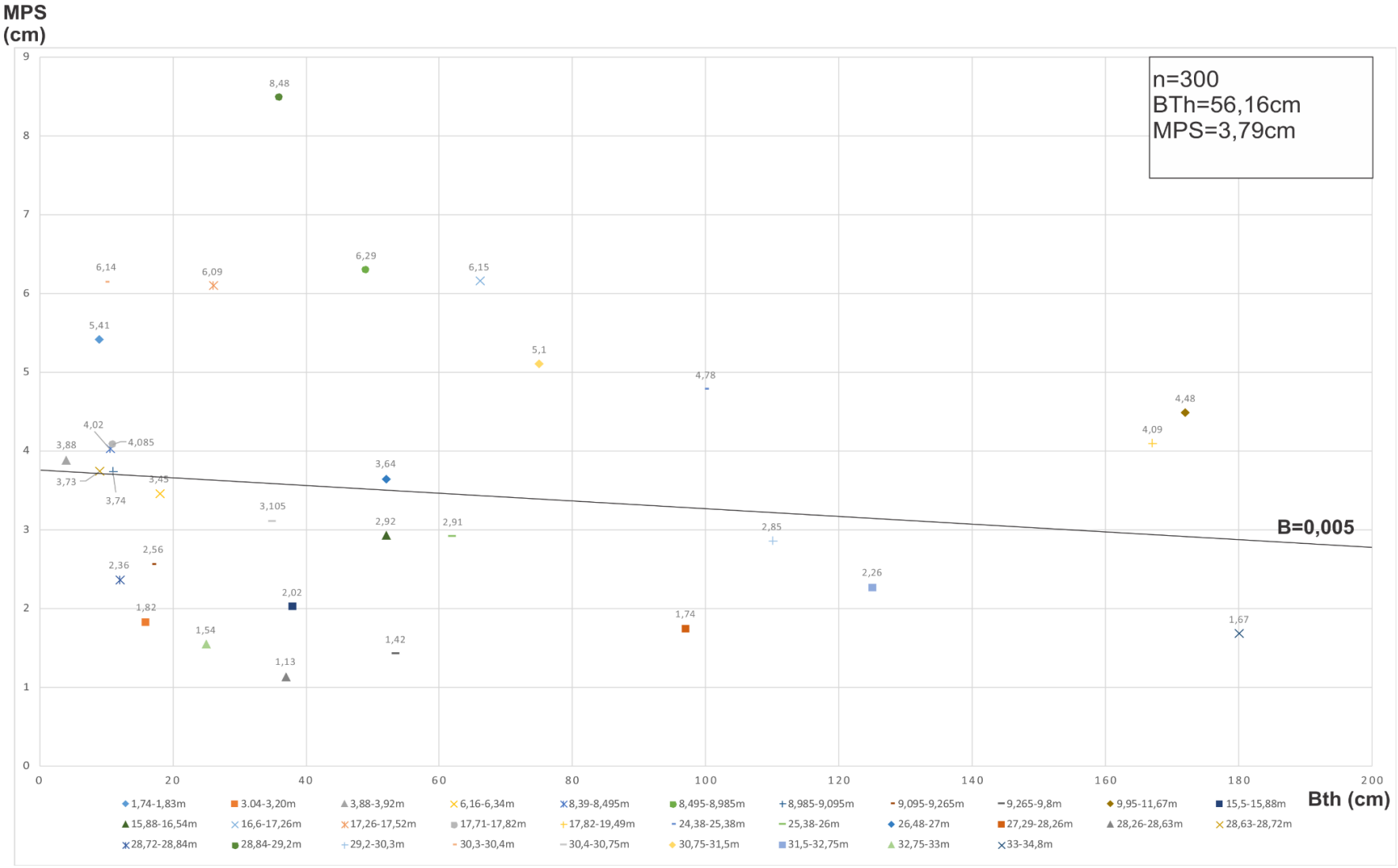

Fig. 52.The mean MPS values of 30 samples plotted against the layer thickness for the respective samples. The symbol "n" in the square represent the amount of pebble measured, the BTh and the MPS in the square represent the mean values for all of the samples. The black line B represents the best fitted line for the data.

5.1.4 TOC and TS analyze

From the TOC/TS plot (Fig. 33), the result indicates clearly dominantly nonmarine conditions, with one occurrence of marine condition. The dominantly nonmarine result could be explained by the glacier located in Skarmunken during the deposition ice-contact glaciomarine system (Andersen, 1968, Neeb ,1981; Møller *et al*., 1986, Lønne, 1993). Glaciomarine conditions could certainly explain the dominating nonmarine results but also the fluctuating results (Fig. 33). Several glacial advances and retreats are indicated in both facies C and D, which could explain the fluctuating nonmarine conditions. Sample 14,29m, 15,6m, 16,51m and 17,59m are all located in these facies. They are all located in fine-grained units between the larger conglomerate sequences, which indicate to belong to unit B and represent most likely periods of glacial retreats. Both 15,6m and 16,51m are located close to the normal marine boundary, which potentially indicate that the retreat was sufficient enough to create close to normal marine conditions. Sample 14,29m and 17,59m are located further away from the normal boundary, which could indicate glacial retreat with distinct nonmarine conditions. This could indicate that the front retreat was more distinct during the deposition of sample 15,6m and 16,51m.

The rest of the samples are located beneath the suggested glacial advance unit A, in unit B sediments, represent glacial retreat (Lønne, 1995). However, all of the samples except for 1,99m, 2,785m, 4,91m and 7,255m are located well into the nonmarine zone, indicating that the glacial retreat was not sufficient enough to create normal marine conditions.

The samples from 2,93m- 4,91m show a gradual retreat trend from nonmarine conditions to marine conditions. At approximate 4,91m a distinct grainsize reduction is observed in the sedimentary layers (Fig. 22), which could potentially explain the shift from nonmarine to marine conditions by a sufficient enough glacial retreat to create marine conditions.

It is recognized 6 major halts of the glacier terminus in the Skarmunken and several advances (Lønne ,1993), where the advancement and retreat is supported by Andersen (1968) and Corner (1980). These halts and advancements could indeed influence the glacifluvial and marine conditions in the depositional conditions. The back and forth fluctuating nonmarine and marine conditions observed in the TOC/TS data would then be the likely result of these advances and retreats reported by Andersen (1968), Corner (1980) and Lønne (1993). Another possibility for the fluctuating pattern could be seasonal increased meltwater discharge during spring. A problem with

this hypothesis is that the time of the deposited layers is not known, and it is therefore, hard to distinguish which layer is deposited in which season.

The explanation for the nonmarine conditions is most likely the result of the influence by the glacier and subsequent glaciomarine conditions. The fluctuating pattern in the nonamarine conditions can most likely be explained by fluctuations in the glacier terminus represented by advances and retreats. The normal marine sample 4,91m represent most likely a glacier retreat, which allowed dominance of marine conditions.

5.1.5 Summary sedimentary environment

Extrapolation of the lowermost bedding-plane trace sequences display that Andersen (1968) documented microfossils is most likely deposited beneath the excavated vertical profile. This means that the vertical profile was deposited after around 10ka c. yr BP. During this period, the sea level was documented to lay around 50-51m (Corner & Haugane, 1993). This indicates that the deposit observed in the vertical profile were deposited submerged. The MPS/BTh analysis display also submerged deposition of the conglomerate units, which further supports this claim. Based on these facts, the facies most likely consist of the allostratigraphic model unit A or B and potentially unit C.

Facies A and B most likely consists of B, deposited in the foreset-bottomset area. The fine-grained mud, silt and sand most likely represent buoyant meltwater plume deposits. The more coarser sand most likely represents turbiditic sand. The erosional channel-like structure in facies A represent most likely chute-fill deposit, where the chute was probably caused by turbidity currents and the later refill were also caused by turbiditic processes. The gravel and conglomerates most likely represent debris flow deposits.

Facies C represent both glacial advance and most likely also retreat. The large conglomerate sequences most likely represent glacial advance, classified as unit A3. The deposit represents prograding foresets, most likely formed by subglacial processes and debris flows. The most fine-grained units in facies C most likely represent buoyant meltwater plume B4 bottomset, B3-B4 turbiditic deposits and subsequent glacial retreat. The lower part off facies D is indicated to represent glacial advance as unit A3 prograding foreset deposits. The conglomerate deposit most likely represents the result of subglacial processes and debris flows. The uppermost part of facies D most likely represent glacial fan top deposits as unit A2

The lower part of facies E most likely also represent a subglacial deposit as unit A2, where the deposit represent deposition by subglacial processes and debris flow. The upper part of facies most likely represents a gradual glacial retreat and the deposition by B2 deposit, where the deposit most likely represents subglacial processes and tractional currents.

The TOC and TS analysis show that the dominantly depositional environment was nonmarine and most likely glaciomarine. The fluctuating pattern observed represent most likely minor glacial retreat terminus movement. The one sample of marine conditions most likely display a sufficient enough glacial retreat to create dominating normal marine conditions.

The marine limit, represented by terraces related to the end-moraine on the delta surface (Lønne, 1993), suggests that the ice-contact glaciomarine system is represented by an ice-contact delta at Skarmunken, where the investigated sedimentary units consist of unit A and B from the allostratigraphic model. The sedimentary thickness down to the crystalline bedrock suggests that the environment was shallow, with fluctuating glaciofluvial and marine conditions.

5.2 Grainsize distribution

The chosen grainsize sieves did not incorporate smaller than 63µm and larger than 2mm in the sieved result. The result revealed that large quantities of the sieved samples contained grainsizes >2mm. Also, the fine-grained samples contained significant amounts of <63µm. This lead to a distinct limiting result, where only the large trends could be recognized. The grainsize revealed an unsatisfactory result and contributed minimal to the interpretation of the sedimentary environment. Therefore, the grainsize distribution result was left of the result chapter and placed in the appendix (s. 203), and will not be discussed in this thesis.

5.3 Soft-sediment deformation structures

5.3.1 Mud clasts

The mobilization of fine-grained particles by fluid migration (e.g. Hovland *et al*., 2005; Truede and Ziebis, 2010) could explain the mud clasts in the sand injections. This could also explain the larger mud chunks, which would indicate mobilization on a larger scale. However, gravitational currents have also the potential to erode and transport mud pieces. The occurring mud clast in the coarser-grained units could be due to erosional processes by passing debris flows (Selby & Evans, 1997) or it could be explained by glacial diamictons transport (Hill & Fleisher, 1996)

Based on the nature of the sand injections (4.2.3) it is likely that the mud clasts and chunks located in these injections are the result of mobilization by fluid migration. The clasts in the coarse-grained units are most likely the result of both erosional processes by passing debris flows, as the layers in which they are deposited in is the result of debris flows, and diamicton transport.

5.3.2 Faults

Fluid migration has been observed in the depositional environment (5.4), indicating that compaction and dewatering has taken place. This is probably caused by rapid sediment loading during the glacier presence in Skarmunken, where the conglomerate at the top of the fine-grained faulted sequence might be the explanation for the compaction. The glacier front advancement in the Skarmunken (Andersen, 1968; Corner, 1980; Lønne 1993) would add additional compaction to the sediments. Glacial advances are indicated in facies C -E (5.1.5), where facies C1 is located right above the faulted area. Deposit of coarse-grained conglomerate sequences would certainly apply stress on the fine-grained faulted sequences.

Trincardi et al. (2004) supports the proposal of soft-sediment deformation by rapid sediment loading, where Cartwright and Dewhurst, (1998) have recognized polygonal faults forming as the result of compaction and dewatering of fine-grained sediments. This is further supported by Løseth et al (2003), Hovland et al (2005) and Berra & Felletti (2011), which recognize faults forming as a result of fluid migration processes. The sand injections (4.2.3) observed throughout the investigated slope consists of fine-grained sand and clay content, showing often residual laminations from the original deposition. The similarity between the injection material and the faulted sequence is rather striking and the proposal of faulting by compaction, dewatering and fluid migration could explain this similarity.

Another possible alternative is faulting by induced strain from the conglomerate sequence (Maltman, 1994; Eyles & Boyce, 1998; Le Heron et al., 2005) where the conglomerate sequence was deposited as till in the subglacial zone. A third option could be by the movement of the carbonate boulder located above, creating faults by seismic energy (Rodríguez-Pascua et al., 2000).

The faulted area is located just beneath of what is most likely glacial advance foresets deposits, which indicates that faulting by sediment compaction, dewatering and fluid migration is the more likely candidate. Based on the depositional environment and the observed sand injections, fluid migration is indicated in the area. Rapid sediment loading and glacier compaction is the most likely

the cause for the compaction and dewatering, leading to the fault process. The similarity between the sand injections and the faulted sediments further strengthens the idea of faulting by fluid migration. A suggestion for this similarity is mobilization of the fine-grained sequence by fluid migration, causing the fine-grained sequence to continuously thin out, causing the faulting (Løseth, 2003) in non-mobilized areas in the sequence (Fig. 53).

5.3.2.1 Soft-sediment deformation structures summary

The mud clasts and chunks in the sand injections are most likely the product fluid migration, whereas the mud clasts and chunks in the coarse sediments are the result of erosion by passing debris flows and diamiction transport. The faults can most likely be explained by rapid sediment loading and glacier compaction. As a result, compaction and dewatering caused the host sediment sequence to fluidize, causing a thinning of the sediment sequence which lead to the formation of faults.

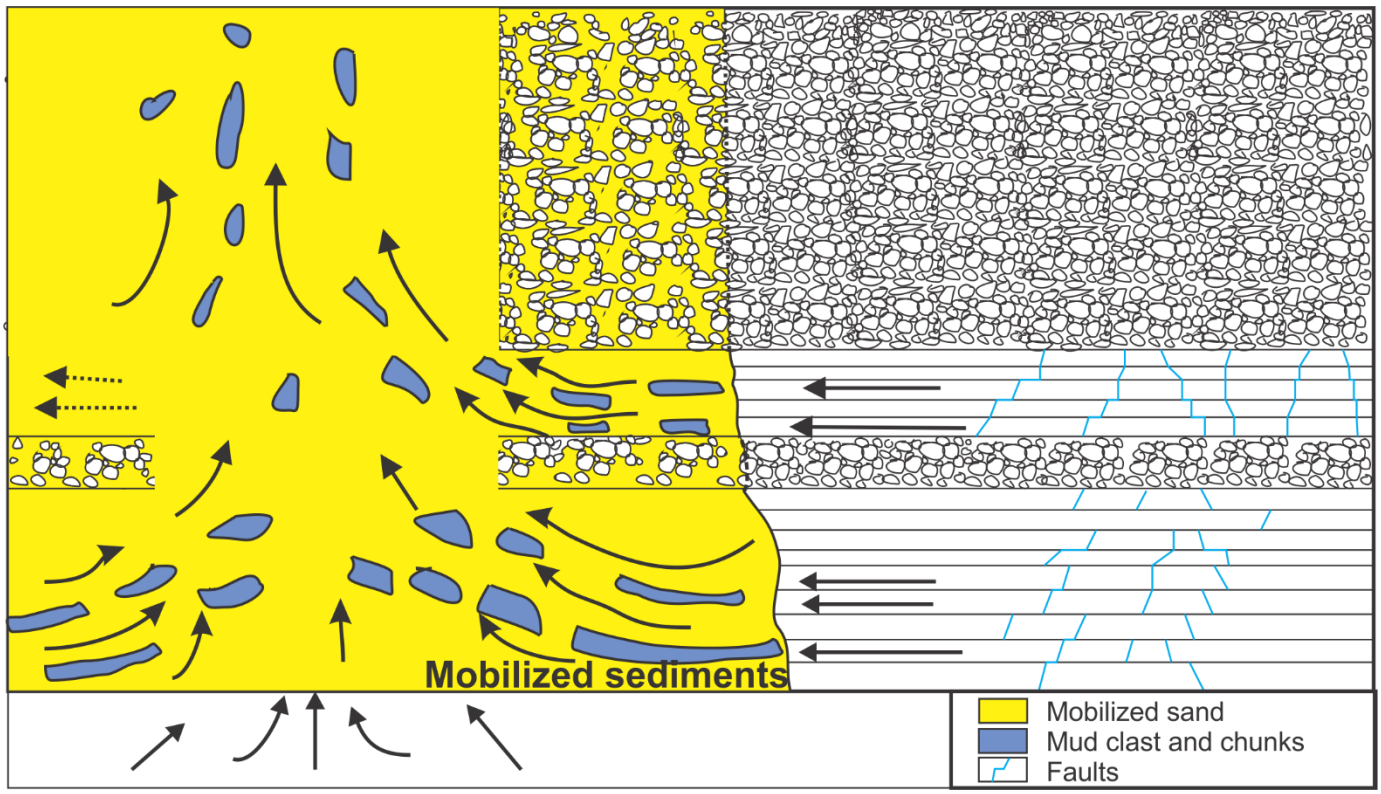

Fig. 53. Schematically figure of fluid migration in the faulted fine-grained sediment sequence, divided by a conglomerate unit. The figure display mainly one vertical fluid migration pathway, indicated by black arrows, but could necessary not be the real case. Horizontal-subhorizontal fluid migration, indicated by black dotted arrows might also a possible alternative for the fluid migration. The normal faults are marked with light blue lines. The black arrows indicate sediments movement, where the non-mobilized sediments move towards the mobilized sediments due to the vacancy of space, creating the normal faults. The mud clasts and chunks

represent former ripper apart mud units. The mobilized sand represent are indicated by yellow color and represent a mix fluid migration, sand and silt grains, were the sand could also be transported in pieces containing preexisting laminations. The yellow colored conglomerate units mark the transition from undisturbed sediments to the fluid migration pathway and represents the observed areas of sand injections into pore spaces of original units. The figure is modified after Løseth et al (2003).

5.4 Fluid migration

5.4.1 Sand injections

The main process responsible for sand injection into hydraulic fractures is recognized to be fluidization (Cartwright & Dewhurst, 1998; Hurst et al., 2011), it is therefore likely to believe that fluidization is the culprit for the sand injections observed in the vertical profile and multiple locations in the exposed outcrop in Skarmunken. The sand injections form as a network of hydrofractures of the host strata is filled by fluidized sand, which subsequent forms a network of intrusion (Hurst et al., 2003). The hydrofracturing occurs during overpressure, which occur when the pressure is greater than the weight of an equivalent column of water (Ravier et al., 2014).

The most relevant causes for overpressure in Skarmunken is most likely glacial compaction by advancing front (Ravier et al., 2014) and rapid loading (Strachan, 2002; Hildebrandt & Egenhoff, 2007). Gravitational instability along submarine slopes that generates large-scale, downward mass-transport as sediment slides and slumps (Strachan, 2002; Jonk, 2007) are potentially candidates for rapid loading. However, the results of such event tend to be localized sand injections. Glacial advances are indicated in facies C-E in the vertical profile, which clearly favors glacial compaction of underlying sediments. The glacier also contributes to high and rapid sediment deposition, which would also indicate compaction by rapid loading. The conglomerate sequences in facies C, D and E most likely represent foreset sequences by debris flows, which could contribute to rapid loading at local scale.

The agent for the fluidization of the sand injections could be explained by formation water as it is the most common fluid in the shallow crust. However, hydrocarbons are observed inside the sand injections. Based on the amount of carbonate nodules and encrustations observed in the sand injections, it is likely that the formation water is main agent for the fluidization with contribution from the hydrocarbons. The fact that sand injections occur, could indicate that the injections acts highly permeable pathways through the surrounding sediments for the hydrocarbons (Hurst et al., 2011).

The mud clasts and mud chunk content in the sand injections could be explained by ripping and reworking of the host strata (Macdonald & Flecker, 2007; Hurst et al., 2011). This could explain the common deformed preexisting laminations observed in the sand injections. The resemblance between the sand injection content and the faulted sediment sequence (5.3.2) might indicate that the fine-grained sequence is the source of the mobilized sand. This would also explain why faults are observed in this sediment sequence.

Another possibility for the fluid migration could be subglacial meltwater channels penetrating the deposited sediments, adding fluid content in the sediments and subsequent increasing to increased pore pressure and eventually leading to fluid migration. If this process occurred, it would most likely occur in combination with the sediment and glacial compaction. From the investigation of the layers, the sand injections composition correlate with the faulted fine-grained package (5.3.2). This indicate that only a very specific and small area is actually mobilized. If subglacial meltwater channels played a role in the fluid migration process, coarser sediments e.g. the conglomerates would be expected to be moved in vicinity to of the channel outlets. However, no evidence of subglacial channel outlets was observed, which could indicate that the subglacial channel did not contribute to the fluid migration and that it was located further south of the investigated sediments.

5.4.2 Fluid migration structures

Ductile deformation structures like pillars, ball and pillow structures and plastic intrusions are all possible explanatory structures for the observed fluid migration structure (Berra & Felletti, 2011). Fig. 54 D and E display the pipe like structures, where Fig. 54 E also contain two floating features of fine-grained nature. Clastic dykes (Neuwerth et al., 2006; van der Meer et al., 2009) are common in glacial setting (van der Meer et al.,2009) and show significant similar composition and morphology with the fluid migration pipe-like structures (Fig. 54 D and E). Documented plasitc intrusion (Berra & Felletti, 2011) (Fig. 54 A and B) show even greater similarity and is probably the same as the clastic dykes (Neuwerth et al., 2006; van der Meer et al., 2009).

The two floating structures located in Fig. 54E, could represent concentric sand balls (Fig. 54C), or possibly small detached plastic intrusions.

The pipe-like structure in Fig. 54 E, show greatest similarity with structures reported by van der Meer et al. (2009) and Berra and Felletti (2011), the coarse grained pipe structure in Fig. 54 D deviated from the composition material. Previously reported clastic dykes are recorded to contain

coarse-grained sand (Neuwerth et al., 2006), which could explain the coarse-grained content pipe structure in Fig. 54 D and the morphology. The ball- like structure display not the same morphology as the concentric ball structures, but rather have more similar morphology as the plastic intrusions. Due to the lack of carbonate concretions inside the structures it is likely that the fluid migrating inside the structure did not contain hydrocarbon or not enough to form concretions.

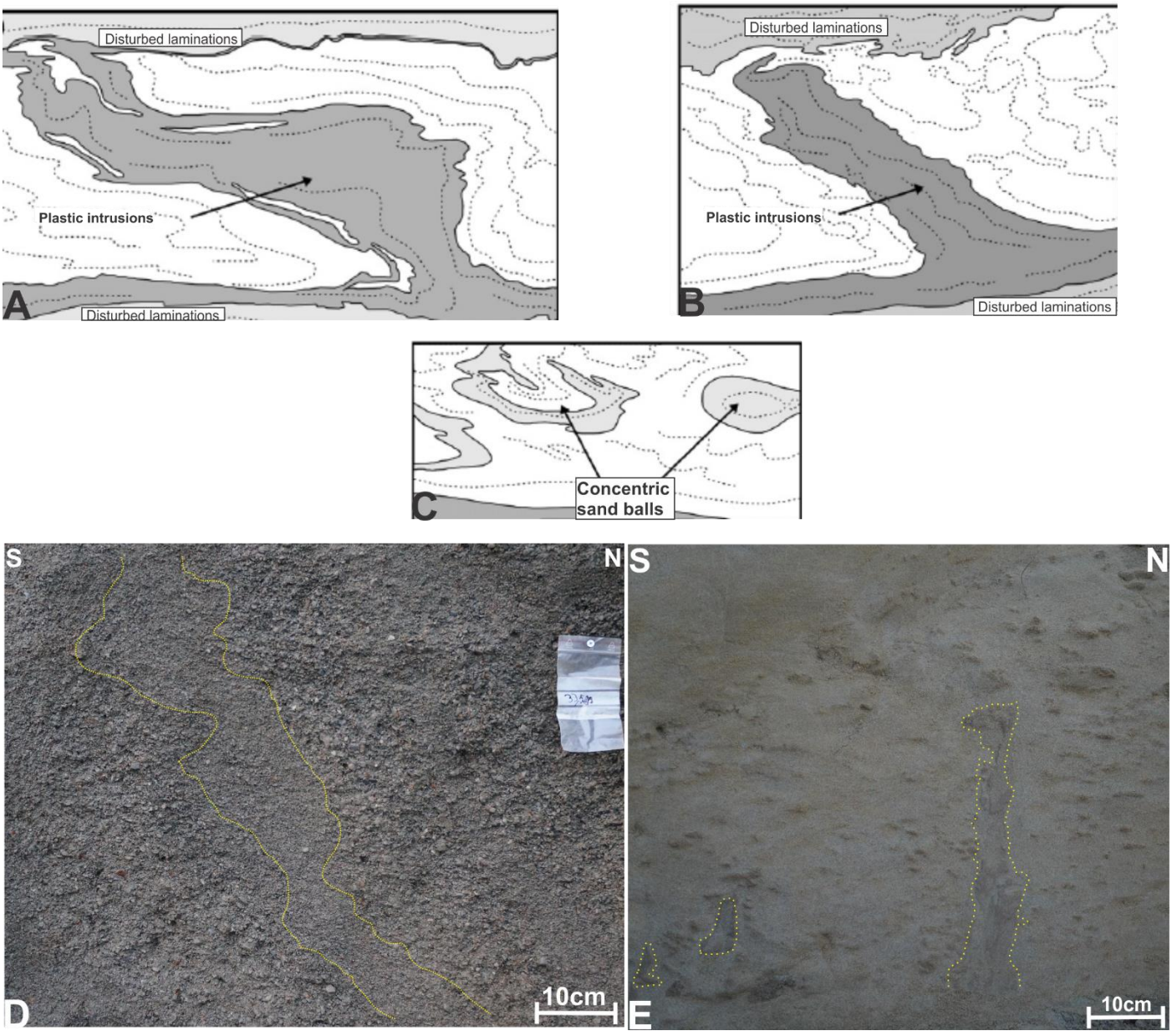

Fig. 54. Comparison of schematically classified soft-sediment structures (A, B and C) with soft-sediment structures observed (D and E) in the excavated sections in the vertical profile. Figure A and B display different cases of plastic intrusion structures that can appear in soft-sediments, where figure C display concentric sand balls. Figure A, B and C are modified after Berra and Felletti (2011).

5.4.2.1 *Fluid migration summary*

The sand injections are most likely due to fluid migration, caused by rapid sediment loading and glacial compaction. The contribution by subglacial meltwater channels is possible but not enough evidence supports the idea in this case. The sand injections most likely comprise of the faulted fine-grained package located at 4,5- 7,94m (4.2.2).

The fine-grained pipe-like structure of the fluid migration structures most likely represent plastic intrusions, whereas the coarse-grained pipe-like structure most likely represent clastic dykes. The ball-like structure most likely also represents plastic intrusions.

5.5 Carbonate concretions

5.5.1 Precipitation processes

The depositional data (5.1) and the sedimentary thickness down to the crystalline bedrock (2.4.4) indicate that the carbonate concretions were precipitated under shallow marine conditions, most likely an ice-contact delta (Andersen, 1968; Lønne, 1993). The presence of the glacier during the deposition of the sediments and the TOC/TS analysis (5.1.4) indicates dominating glaciofluvial conditions. The carbonate concretion content in the sand injections (Fig 55) and the occurrence of chimneys and pipe-structures concretions (4.5.4.1.1 and 4.5.4.1.2.1.1), indicate hydrocarbon migration. Due to the large areas affected by sand injections, it is possible that the fluidized sand transported the hydrocarbons synsedimentary or acted as a later migration pathways for the hydrocarbons (Hurst et al., 2011).

Based on the morphology of the carbonate concretions, the chimney concretion and the boulder concretion indicate that the environment was anoxic up to 18m (Jørgensen, 1992a; Luth et al., 1999; Peckmann et al., 2001). The chimney morphology commonly occurs in submarine gas seeps, which could indicate hydrocarbon seep source. The chimney morphology represent the long term effect of channelized hydrocarbon gas stream (Jørgensen, 1992a; Diaz-del-Rio et al., 2003; Treude & Ziebis, 2010). The chimney morphology and the common carbon concretion affiliation with hydrocarbon seeps (Jørgensen, 1992a; Peckmann et al., 2001; Hovland et al., 2005; Niemann et al., 2005; Naehr et al., 2007; Pearson et al., 2010) , could indicate hydrocarbon seepage.

Another explanation for the chimney concretions could be the fluidization of the fine-grained sand (Fig. 53). However, this would have required a continues fluidization of the sand and sufficient

carbon content over a longer period to supersaturate the pore spaces with HCO_3^- (Burton, 1993; Luff et al., 2004).

The morphology of the carbonate concretions up to 18m indicate that these concretions were precipitated under anoxic conditions. The anoxic conditions, the nonmarine environment and the sediment thickness down to the basement indicate that the 4 of Rice and Claypool (1981) proposed requirements (3.5.3.3.1) for methane production are met. This could indicate methane oxidation by sulfate reduction (Eq.3) up to 18m (Rice & Claypool, 1981; Iversen & Jørgensen, 1985; Whiticar & Faber, 1986) and carbonate precipitation.

The morphology of the concretions occurring above 18m lack the chimney structures and occur as flat carbonate concretions. This could indicate that these carbonates were probably precipitated in the interface zone of the oxic-anoxic boundary and or possibly in the permanent oxic zone (Burton, 1993; Luff et al., 2004). This could indicate precipitation by aerobic methane oxidation ((Eq.4 and Eq.5) (Hovland et al., 1987; Jørgensen, 1992a).

To achieve the carbonate precipitation, supersaturation of pore spaces in the sediments is necessary (Burton, 1993; Luff et al., 2004), where carbonate concretion are commonly related to microbial processes (Jin et al., 2008; Gaines & Vorhies, 2016). Calcite carbonates are the most common in marine conditions (Gaines & Vorhies, 2016), however, in this case the conditions is indicated to be glaciofluvial with the influence of marine conditions. In addition to the chimney structures located in the vertical profile, several chimney structures are located in the beach area in both south and north direction (4.5.4.1.2.1.1). This points towards channelized hydrocarbon migration over significant time. Microbial respiration of carbon could explain the formation of hydrocarbons, which subsequent lead to precipitation of the carbonate concretions (Gaines & Vorhies, 2016).

The indicated shallow glaciomarine environment, with indications of mainly anoxic conditions and hydrocarbon seepage formed by microbial processes would indicate anaerobic oxidation of methane as the main source for precipitation of the carbonate concretions (Naehr et al., 2007). The formation of natural gas by microbial respiration of carbon commonly consists of mainly methane, it would seem that this suggestion is not too farfetched. However, carbon concretions can consist of other hydrocarbons e.g. the calcium carbonate concretions located in the Carolinefjellet Formation in Svalbard (Krajewski & Luks, 2003). In either scenario, the carbonate concretions will

most likely contain significant amounts of methane if not dominant. This indicates that the oxidation of methane is an important process in the precipitation.

If the oxidation of methane is the cause of the precipitation of carbonate concretions, the indicate dominating glaciofluvial environment would favor the fermentation of acetate in the methane production (Koyama, 1963; Takai, 1970; Beliaev et al., 1974; Winfrey & Zeikus, 1977)). However, as sample at 4,91m displayed dominating marine conditions, it is likely that marine conditions would have exerted influence during deposition of the sediments. This would most likely contribute with CO_2, and the reduction of $C0_2$ to produce methane (Whiticar et al., 1986).

Another possible precipitation process which must be taken into consideration, is the oxidizing of the organic material buried in the sediment by Eq.2 (Berner & Raiswell, 1984).

$$2CH_2O + SO_4^{2-} \rightarrow H_2S + 2HCO_3^- \quad \text{(Eq.9)}$$

The marine influence would most likely suggest additional carbon source from shells, plants and other organisms. The microfossils located by Andersen (1968) could support this suggestion. This indicates that the conditions for this kind of precipitation where present in the sediments.

5.5.1.1 Summary

The precipitation process where most likely the result of oxidation of CH_2O and hydrocarbons. In the oxidation of hydrocarbons, the methane oxidation was most likely present, most likely anoxic methane oxidation but also possibly oxic methane oxidation. The glacifluvial environment with marine influence indicate both fermentation of acetate and reduction of CO_2, contributed to the formation of methane, where the morphologies indicate dominating anaerobic oxidation of methane, sulfate reduction, as a significant if not all, contributor to the precipitation of carbonate concretions up to 18m in the vertical profile. The precipitation over this threshold at 18m is indicated to have been significantly if not all, contributed by aerobic oxidation of methane.

5.5.2 Carbon source

In terms of carbonate precipitation, the microbial oxidation of the carbon is the most likely source. Theoretically this could indicate two main types of carbon derivation, biogenic carbon and thermogenic carbon.

The sediments package sequence from the basement and up is between 100-150m in the incised transition zone between Sørfjorden and Ullsfjorden at Skarmunken-Hjellneset area (Plassen & Vorren, 2003), where approximate 34,75m of additional sediments (the vertical profile, Fig. 22) is

located above a.s.l. in Skarmunken. The thickness of sediments is most likely not enough to reach temperatures above 50®C, which favors biogenic carbon formation (Stolper et al., 2014).

The high sedimentation rates and the potentially significant amounts of fine-grained sediments (Hunt, 1972) also suggests favorable conditions for preservation of organic carbon (Morse & Berner, 1994), where only 0,5% carbon (Claypool & Kaplan, 1974; Rashid & Vilks, 1977) is needed for methane production.

The local geology presents potential carbon sources in the Breivikeidet marbles and the lowermost unit of the Balsfjord Group, the Sjursnes phyllite (2.1.1.2.1). The bedrocks could potentially be derived by chemical and mechanical weathering of rainwater and/ or glacial erosion and transportation. It is also possible, that during erosion and transport of bedrocks and sediments, the glacier could have eroded other bedrock or sediments containing carbon.

The indicated ice-contact shallow glaciomarine system could indicate rich nutrition sea containing animal and plant life. The only reports of microfossils are by Andersen (1968), which would suggest probably otherwise. However, the amounts of carbon concretions could potentially support carbon contribution from a nutrient, animal and plant rich depositional environment. But one would expect more microfossil traces if this were the case. These traces might be represented by the stratabound small carbonate concretions observed throughout the vertical profile (Fig 55), where the carbonate concretions could potentially represent microfossils. It is worth noting that these concretions do not occur together with the sand injections and that they are significantly smaller than the carbonate concretions located in conjunction with the sand injections. This might indicate that these concretions represent a different precipitation process than the carbonates occurring within and/or together with the sand injections. Due to their small sizes, only one concretion was sampled for thin section analysis (Fig. A 3). No indication of microfossils was observed in this sample, however, it is a possibility that the microfossils were too small for the lenses used for the thin section analysis. Another explanation for the smaller stratabound carbonate concretions could be diffuse hydrocarbon migration through the sediments.

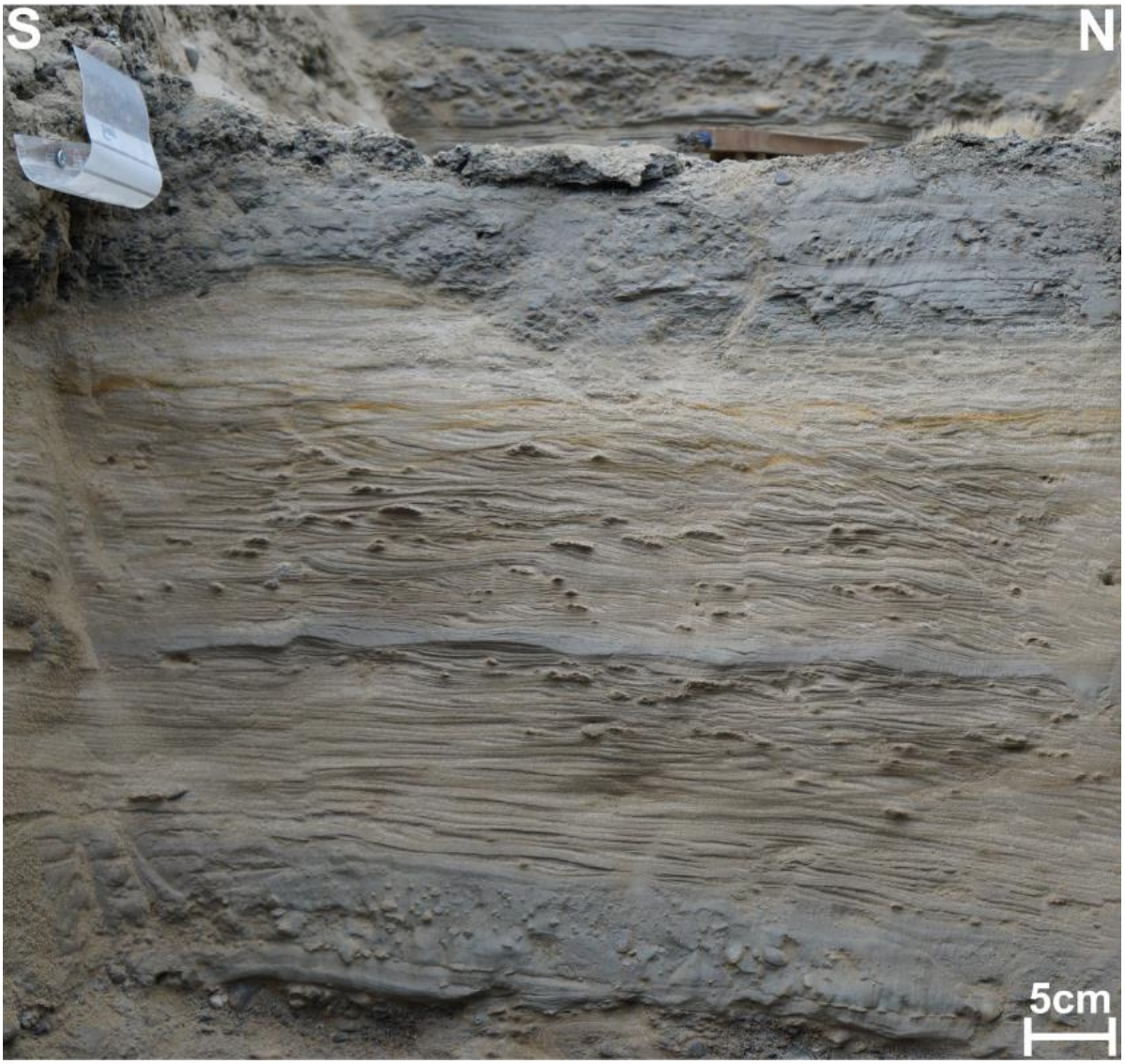

Fig 55. Fine-grained faulted sequence just below the 5m mark. Carbonate concretions are observed to occur scattered, concentrated and stratabound within the laminations and in the fault planes.

Aside from a biogenic carbon source, the thermogenic carbon source is also a potential candidate or contributor. In the adjacent seafloor in Ullsfjord, several doming structures and pockmarks are observed, interpreted to be fluid migration structures. These structures are suggested to be of thermogenic origin (Plassen and Vorren 2003) and they occur in abundance only 2,5-3km (Fig. 7 B) away from the investigated area in Skarmunken. Therefore, aside from a biogenic carbon source, a thermogenic carbon source must also be considered as a potential candidate or contributor.

Fig. 7 A display a regional fault, cutting through Sørfjord to Ullfjord (Plassen and Vorren, 2003), passing through the study location at Skarmunken. A thermogenic carbon source and hydrocarbon migration could be explained by storing of hydrocarbon gas in coal units, either by local hydrocarbon formation or hydrocarbon migration from other source rocks. Here the gas content

varies laterally and vertically within the individual coal units. During exhumation, the gas content decreases with decreasing pressure and temperature, leading to hydrocarbon migration. As the gas content in the coal units varies both laterally and vertically, it could explain the distance between the migration structures occurring Skarmunken and Ullsfjord, and the scattered doming structure outliers in the Ullsfjord (Fig. 7 B, Plassen & Vorren, 2003).

The second process for gas formation in coalbeds is through the process of secondary biogenic gas generation, by metabolic activity of bacteria, introduced by meteoric water moving through permeable coalbeds or other organic rich rocks. The bacteria metabolize wet gas components, n-alkanes and other organic compounds at <56®C to form methane and CO_2. A third option is gas migration from other source rocks upon exhumation of the basement or through the regional fault, where it is widely known that hydrocarbon can migrate from source rocks and up through faults in strata.

5.5.2.1.1 Summary

The amounts of sediments and the most likely rapid sediment deposition by the glaciomarine system favors biogenic carbon source. In terms of where it derives from, glacial erosion of the local geology most likely contributed with carbon, whether it was the Breivikeidet marbles, the lowermost part of the Balsfjord Group or other sediments or bedrock containing carbon. Chemical weathering by rainwater could have occurred, but the extent is not known and could also be close to non-contributory. The indicated organic carbon from microfossils is more likely to represent a distinct carbon source. However, they do not explain the major carbonate concretions located in the sand injections. Most likely they represent another carbonate precipitation process. The carbonate concretions located in the sand injections are so big, that it requires substantial more hydrocarbons than the small stratabound carbonate concretions. One could argue that these also could have been explained by microfossils, by much more carbon rich layers that have been mobilized along with the fluidized sand. The reason for that this layer/layers are not observed in the vertical profile is that over half of the profile represent a foreset sequence of coarse grained conglomerates. Therefore, preservation of such layers is more likely to be in the lower sections, in bottomsets and further out, probably in the <100m of sediments is located beneath the investigated area. Carbon deposition in the bottomset region could explain why doming structures and pockmark are located in the south of Ullsfjord, as they most likely represent bottomset deposition.

Thermogenic carbon contribution could explain the major amounts of carbon needed for the formation of the large carbonate concretions. However, the basement in Ullsfjord is reported to consists of biotite schist to the west and mica schist and phyllite to the south and east (Plassen & Vorren, 2003b). This indicates that the schist and phyllite most likely did not act as a container or a seal for hydrocarbons.

The information indicates that allochthones carbon most likely contributed to the total carbon source for the carbonate concretions. Most likely did a shallow marine nutrient and life rich environment represent the main carbon source for the carbonate precipitation. The carbonate concretions most likely had two different sources and precipitation processes. The carbonate concretions located in connection with the sand injections most likely derives from a major biogenic carbon source, whereas the stratabound carbonate concretions derives from local carbon within the sediments layers they were observed in.

5.5.3 Concretion morphology

5.5.3.1 Pipe concretions and intergrown pipes

Parallel growth of carbonate concretions to layers are reported to occur in methane seep areas (Jørgensen, 1992a; Mazzini et al., 2006), where the both horizontal – vertical growth is suggested to be due to herterogenouse conditions in the seep sediments (Dando et al., 1994; Treude et al., 2003). The horizontal heterogeneity could exhibit chemically suitable horizons for the first stage of precipitation and the formation of the pipe features. It is also likely that the pipes represent the main fluid migration pathways in the sediments. The second phase of gradual intergrowth of the pipes and plate surface formation could represent the result of continuous cementation. The intergrown pipe structures occurred both in the large carbonate concretions and in the smaller stratabound carbonate concretions. As discussed in 5.5.2, the smaller stratabound carbonate concretions most likely represent local organic material deposited with the sediment layers. However, the intergrown pipes in the large structures represent most likely another precipitation event, during the formation of the sand injections, and they most likely represent the main fluid pathway.

5.5.3.2 Chimney concretion

The chimney morphology could indicate hydrocarbon migration in connection with gas seeps, representing a significant localized vertical-subvertical flow, as chimney structures occur commonly in such environment (e.g. Luth et al., 1999; Peckmann et al., 2001; Lein et al., 2002; Michaelis et al., 2002; Diaz-del-Rio et al., 2003; Reitner et al., 2005). The fact that the chimney occur in a sand injection, confirms that the chimney represents significant flow event. Aside from hydrocarbon migration as potential explanation for the concretion, the oxidation of buried organic material (Eq.9) and mobilization of the material could also explain the formation of chimney concretion.

The depositional environment for the chimney is indicated by its morphology, which according to Jørgensen, (1992a), Luth et al. (1999) and Peckmann et al. (2001) represents anoxic conditions.

The morphology of the chimney is probably controlled by the heterogeneity of porosity and permeability in the sediments (Dando et al., 1994; Treude et al., 2003), but it could also be the result of strong fluid flow, which forcefully remove sediments in its path. The chimney structure is located in a sand injection, it is therefore likely that the migration of the sand played a big role in shape of the carbonate concretion (Fig. 56), which is also dependent on the heterogeneity of the overlying sediments.

The possibly horizontally termination could represent the mushroom morphologies (Jørgensen, 1992a), and the possibly link to the horizontally cemented carbonate concretions (Jørgensen, 1992a; Mazzini, 2006). At the top of the chimney, the sand injection displays horizontal intrusion in the sediments (Fig. 56). This indicate a possibly termination of vertical fluid flow and the beginning of horizontal flow, which would explain the blunt termination of the chimney and can possibly explain the mushroom morphologies (Jørgensen,1992a). The chimneys located on the beach are most likely bifurcated chimneys (Fig. 19 C), whereas the in situ chimney probably represents cylindrical chimney(Fig. 19 A).

Fig. 56.The location of the in-situ carbonate chimney and adjacent smaller pipes. From the base to the top of the chimney, distinct sand injection is located, where the sand displays a subhorizontal placement and towards the top it transitions into horizontal placement. Photo taken at Skarmunken (2016)

5.5.3.3 Boulder concretion

The carbonate boulder morphology displays many similarities with horizontal intergrown pipes with plate surface and the chimney structures (Fig. 47 and Fig 48). The boulder pipes distinguish itself from the intergrown pipes and chimney as the boulder pipes appear to only consist of one single pipe. It is also likely that the boulder pipes are the result of the sediment heterogeneity of the host layers (Dando *et al*., 1994a; Treude *et al*., 2003b) as the intergrown pipes and chimney structures are indicated to be.

The vertical pipe morphologies transition into horizontal cemented terminations could be explained by the similar mushroom structures reported by Jørgensen (1992a), where such terminations is also observed in the smaller intergrown pipes (Fig. 47 and Fig 48 A) and chimneys (5.5.3.2). However, the base of the pipes seems to arise from horizontal cemented platform, which is reported to occur in the anoxic zone (Peckmann et al., 2001). Visually, the horizontal laminations are clearly the dominant cement phase in the carbonate boulder, however, they could also represent the continuous cementation of the vertical pipes. Without any samples from the horizontal laminated areas, it is difficult or almost impossible to distinguish which morphologies occurred first.

Based on the other morphologies, the pipe morphologies appear to represent the main fluid migration pathways. In this case, both vertical and horizontal pipes morphologies occur in the same carbonate concretion. By looking at the sand injection it is located in, on the northern and the southern side of the concretion, the injection display sharp boundaries close to the boundaries of the carbonate concretion. This do not favor horizontally fluid migration pathways, which are oriented N-S. This might indicate that the main fluid pathways are represented by the vertical pipes, where they represent the first cementation stage.

The plate morphologies consist of a intergrown pipes base, indicating that the plate morphologies are the result of continues cementation of the intergrown pipes morphology. The explanation for the plate shape could be due to the heterogeneity of the sediment, where the plate morphologies represent internal sedimentary boundaries. This could certainly explain the horizontal plate morphology at the top of the carbonate boulder, where the plate morphology represents the sedimentary boundary to the next layer. For vertical plate morphologies, the internal boundaries could represent heterogeneity by grain to grain packing or different mineral composition in this particular area. The multiple stream direction pattern (Fig. 49), indicate shifting fluid migration patterns, which could explain why both horizontally and vertically cementation occur. The plate morphologies are disturbed by the pebbly material (Fig. 49), indicating that it occurred before or synsedimentary of the pebbly material event.

The spherulitic carbonate concretions located on the horizontal cemented area, display no disturbance by the pebbly material, which indicates that this cementation event occurred after the plate morphology cementation and is probably the last cementation event.

An explanation for the pebbly material cutting through the cementation could be fluid induced breccia event by cracking of the carbonates boulder (Matsumoto, 1990). Looking at the stratigraphy in the vertical profile (Fig. 22), coarse grained material is located both beneath, over and at the sides of the carbonate concretions. Due to the vertical orientations of the pebbles, vertical fluid flow is indicated, where the pebbles show similarity to dropstones. An explanation could be a sudden release of the fluids and cracking, blowing away the finer grained sediments leading to dropstone settlement of the pebbles. The source for the pebbles is most likely to be located either beneath or above the carbonate boulder. The pebbly sections in the carbonate boulder do not display sharp boundaries of what one would expect if the carbonate boulder was completely cemented, which indicates that this event occurred when the carbonate boulder still

was incomplete in terms of solidification. This would explain why the pebbles are incorporated and cemented so well in the carbonate boulder.

The large size of the carbonate boulder may indicate major fluid flow with precipitation or a large concentrated buried carbon source the sediments as potentially explanations for the formation processes. The boulder concretion occurrence in a major sand injections, strongly suggests cementation by fluid migration. This is also indicated by the large vertical chimney structures in the middle of the carbonate boulder and the occurrence of multiple stream directions located on the outer surface of the plate concretions.

5.5.3.4 Spherulite concretions

From the investigation of the carbonate concretions, at least 3 stages of spherulitc growth is observed. These most likely represent the continues formation of the spheres, where the Fig. 45 D display the initial growth and Fig. 45 B represent the final stage. The multiple occurrence of spherutical intergrowth and dumbbell morphology could either indicate that this is a post stage after spherulitic growth, or that this is an earlier stage, a transitional stage before the final stage. In terms of spherulitc sizes, all of the spheres located in the excavated profile have more or less the same small size. However, the allocthonous spherulitic carbonates located in the beach zone both beneath the excavated trench and in the adjacent area display significant bigger spheres, where they display the same dumbbell intergrowth morphology. This indicates that these particular carbonates have a main shape, which is unaffected by the size of the spheres. An experiment by Beck and Andreassen (2010) hypotheses that spherulitic carbonate crystals consists of smaller spherulitic crystals on a nanoscale. In the experiment, the calcite spherulites form by:

$$Na_2CO_3 + CaCl_2 = CaCO_3 + 2H_2O + 2\text{NaCl} \qquad \text{(Eq.10)}$$

The most obvious source for the Na_2CO_3 is NaCl, most likely contributed by the influencing marine conditions, represented by:

$$NaCl + HCO_3^- = Na_2CO_3 + HCl \qquad \text{(Eq.11)}$$

However, the sediments are indicated to have been submerged during deposition and in addition, the spherulitic concretions are located in a fluid migration structure, which indicates that NaCl reaction is most likely negligible, as it NaCl dissolves in water:

$$NaCl + H_2O = Na^+ + Cl^- + H_2O \qquad \text{(Eq.12)}$$

The dissolution of NaCl precipitates the building blocks, Na^+ and Cl^-, for Beck and Andreassen (2010) Eq.10. The theoretical scenario could then be the calcium reaction with chlorine from dissolved NaCl, in most likely marine derived:

$$Ca^{2+} + 2Cl^- = CaCl_2 \quad \text{(Eq.13)}$$

The indicated anoxic conditions give the potential of sulfate reducing processes, which could promote a reaction between $2Na^+$ and SO_4^{2-} given by the following equation:

$$2Na^+ + SO_4^{2-} = Na_2SO_4 \quad \text{(Eq.14)}$$

Fermentation of acetat, oxidation of hydrocarbons and the most likely substantial CO2 contribution frommarine water, would most likely promote a further reaction with CO_2 , which could provide the final piece for Eq.10:

$$Na_2SO_4 + H_2O + CO_2 = H_2SO_4 + Na_2CO_3 \quad \text{(Eq.15)}$$

This chain of reactions could theoretically create the components needed for Eq.10, which is used in the Beck and Andreassen (2010) experiment. This could mean that the spherulitic shape is not a result of sediment control, but rather by chemical control as suggested by Beck and Andreassen (2010). However, a problem with this explanation of the spherulitic carbonate formation is that Beck and Andreassen (2010) is based on experiments and the lack of analyze of the spherulitc carbonates, this explanation can only be speculated on.

Previous studies have document the occurrence of spherulitic shaped calcite carbonate concretions (McBride et al. 1995; Abdel-Wahab & McBride, 2001), where McBride et al. (1995) reports of spherulites located in a subaqueous fan and shallow marine facies, which is similar to an extent of that in Skarmunken. A proposal for the morphology is diffuse cementation over time (Wilkinson & Dampier, 1990). The problem with the proposal is that the model (Wilkinson & Dampier, 1990) is based on precipitation over millions of years, which do not correlate with the Skamunken area. Another suggestion is the formation of spherulitic morphology during rapid nucleation (Folk and Land 1975; Hudson and Andrews 1987; Bjørkum and Walderhaug 1990; Abdel-Wahab & McBride, 2001). This suggestion was originally used on spherulites calcium concretions in Egypt, which differs greatly from the glaciofluvial environment in Skarmunken.

Globular gas hydrate cementation has been observed in deep marine sea, suggested to form in cavities under an impermeable layer by gas bubbles (Bohrmann et al., 1998). Suess et al. (1999) recognize the similarity between the bubble wrap fabric to that experimentally produced by releasing methane bubbles at depth in the ocean to form gas hydrate. However, these observations were done in connection with gas hydrates, but similar processes of gas bubbles in cavities could be a potential alternative. Spherical texture in concretions is reported by Jun et al. (2008), which is thought to represent gas bubbles in sediments. This could indicate that the layer which the spherulitic concretions are located in, acted as a seal for the gas bubbles. The spherulitic shaped concretion occurring in the beach zone, located both north and south of the vertical profile, could indicate that these are from the same impermeable layer. In terms of impermeable layers, both mud and silt are less permeable than sand layers, which the spherulitic carbonates consists of. This fact that the carbonate concretions almost solely occur sand layers and conglomerate, supports the claim that mud and silt are less permeable. This observation does not favor the idea of entrapment of gas bubbles by an impermeable sediment. In addition, the carbonate boulder is located in a sand injection, which according to Hurst et al. (2011) acts as highly permeable pathways through the surrounding sediments for the hydrocarbons.

Due to the lack of analyze of the spherical carbonates, we can only speculate the reason for the formation of such morphologies. As gas bubbles entrapment seems unlikely, the best explanation for the spherulitc carbonates without an analyze, is specific chemical conditions with the interaction of NaCl and HCO_3^-.

5.5.3.5 Summary

The singular pipes and intergrown pipes are most likely the result of fluid flow, where the location of the pipes is due to the heterogeneity of the sediments. The pipe most likely represents the fluid pathways and the cement in between are the result of continuous cementation of the pipes. The intergrown stratabound pipes most likely represent another cementation event than the ones location in the sand injections. The chimneys are most likely the result of significant localized fluid flow, where both migration hydrocarbons or oxidized carbon material could explain its bicarbonate source. Its morphology is most likely controlled by the heterogeneity of the sediments, where the in-situ chimney represents cylindrical shape and the other chimneys are most likely bifurcated chimneys. The boulder concretion consists of all the occurring main morphologies observed carbonate concretions, where the pipe morphologies appear to represent the main fluid migration

pathway. The plate morphologies located in the boulder can most likely be explained by internal boundaries in the sediments. The multiple stream direction pattern observed on the plate carbonates indicate shifting fluid migration pathways which can explain both horizontally and vertically cementation. The location of the spherulitic concertions and the non-disturbance by the pebbly areas indicate that this cementation event was the last one in the carbonate boulder. The pebbly material can most likely be explained by fluid pressure buildup which caused a vertical flow outburst causing pebbly material to relocated in the carbonate boulder. This outburst event most likely occurred before the carbonate boulder was solidified. The boulder concretion is most likely the result of major fluid migration. The spherulitic concretions formation process is rather uncertain but it is suggested to be the result of specific chemical interaction with the bicarbonate in the sediments.

5.5.4 Thin sections analysis

By comparing the calcite cementation from the Jauf sandstone (Al-Ramadan et al., 2004) and the observed cementation (Fig 57) from investigated thin sections, they exhibit strikingly similarity. This could indicate that the investigated cementation consists of calcite cementation, which further indicate that the concretions are calcium carbonate concretions. The formation of calcium carbonate is given by the Eq.16 (Yoshimura et al., 2001):

$$2HCO_3 + Ca = CaCO_3 + CO_2 + H_2O \qquad \text{(Eq.16)}$$

Precipitation of calcium cement is favored in low sulphate environments (Walter, 1986; Raiswell & Fisher, 2000b), which is verified by the TOC/TS samples (Table A 6). This would further indicate favorable calcite cement precipitation conditions. The color of the cementation in the other thin section vary from brown to a more greenish brown color, but display more or less the same growth trend, morphology and transparent properties.

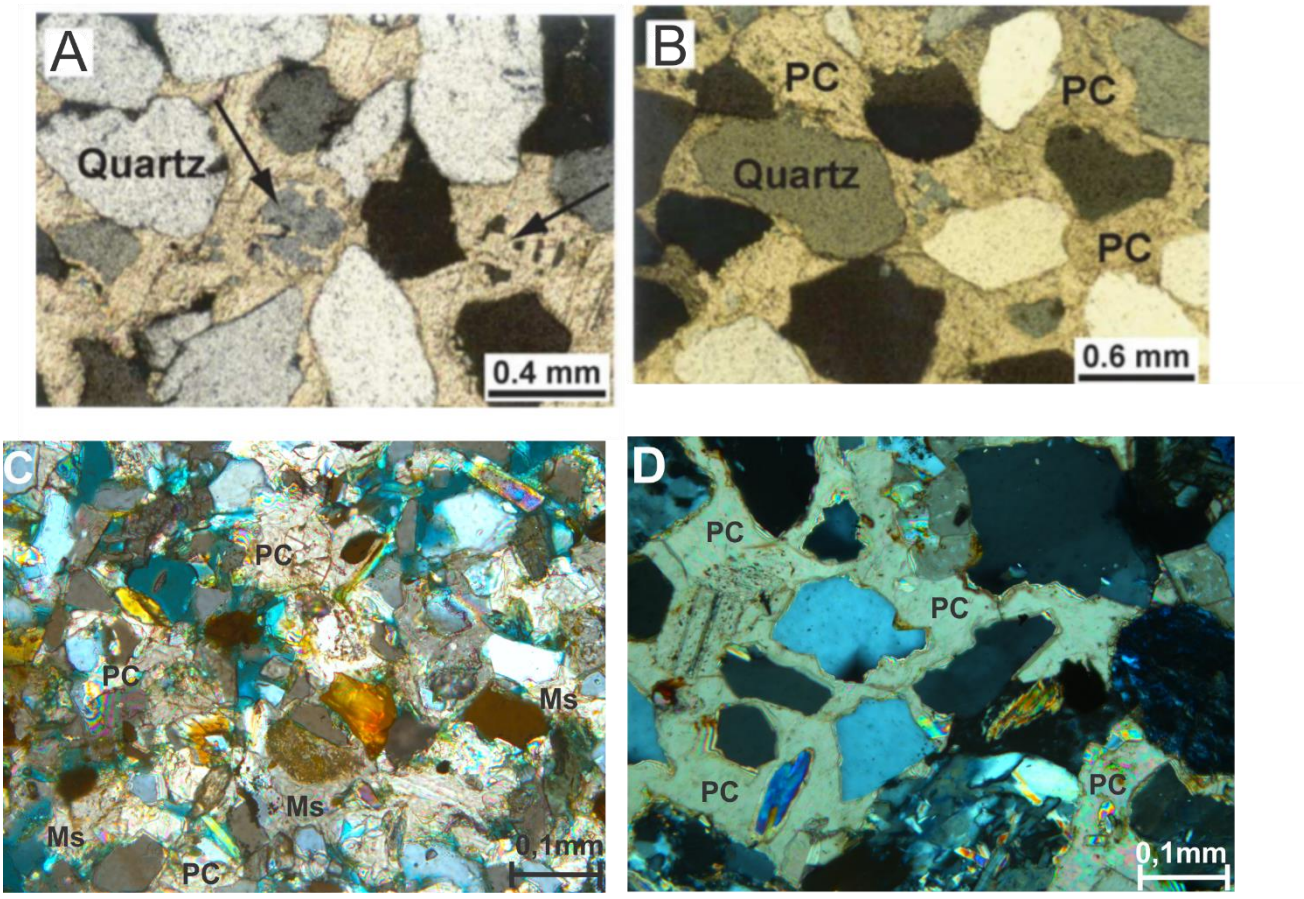

Fig 57 A and B represent calcite cement from the Jauf reservoir sandstone (Ramadan et al., 2004), where the brown area represents poikilotopic (PC) calcite. Figure C is taken with a polarized light from thin section 5, where the cement is indicated by the brownish color. The cementation display both poikilotopic (PC) and meniscus (Ms) cementation. Figure D is taken with polarized light from thin section 1, where the brown color represents poikilotopic (PC) cementation.

The meniscus cement occurring in the pore spaces of the concretions indicate intertidal cementation and sediment heterogeneity Molenaar & Venmans (1993). The poikiloptopic cementation indicate subtidal conditions, where pores completely filled with fluid leads to homogeneously distributed cement (Molenaar & Venmans, 1993). The different fluid migration paths through the sediments could explain why poikiloptopic cementation is only located in specific areas which is well cemented. This could also explain why meniscus cement is located in less well cemented areas, as they represent areas containing meniscus water and were capillary forces are great (Molenaar & Venmans, 1993).

Phreatic cementation could explain the occurrence of rim cementation in the less cemented regions in the thin sections (Rattas et al., 2014).

As for the type of calcite cement, no investigation was made for distinguishing it. The low-Mg calcite is typically found in fresh water conditions, which makes it is a highly relevant candidate

(Molenaar & Venmans, 1993). However, the TOC/TS analysis indicate marine influence on the depositional system, which could have led to high Mg-calcite cementation. More investigation is needed for distinguishing the type of cement.

Fine-grained sediments have more contact points per unit volume, which affects the thickness and texture of the cement connections between grains, than coarse- grained sediments. Due to less contact points, much more cement material is required to achieve the same amount of lithification in coarse-grained concretions than for more fine-grained sediments (Molenaar & Venmans, 1993). This could certainly explain why the fine-grained concretions are much more cemented compared to the poorly cemented coarse grained concretions.

The primary factor controlling the homogeneity of cementation in sediments is grain-size distribution. This leads to faster and more intense cementation of fine-grained laminae and cross-beds in sediments, which most likely occur due to higher capillary forces (Molenaar & Venmans, 1993). This could explain why laminations are commonly cemented throughout the vertical profile and that laminations structures are commonly observed in the concretions and in the thin sections (Fig. 35, Fig. 47 and Fig 55), where they represent fine-grained laminations and therefore require less cement material due to more contact points per volume.

Horizontal and vertical cementation is recognized in carbonate concretions (Jørgensen, 1992a), which correlates with the observed cementation in the thin sections. The horizontal to vertical heterogeneity that can occur in sediments (Dando et al., 1994; Treude et al., 2003) could certainly explain these types of cementation patterns. The occurrence of smaller grains on the upper surface of bigger clasts indicate evidence of fluid flow (Løseth et al., 2003; Hovland et al., 2005; Truede & Ziebis, 2010). This indication is further supported by the morphologies of the carbonate concretions (5.5.3.1 and 5.5.3.2) and the fact that they commonly occur inside sand injections.

The observed sub-horizontal to horizontal lamination cementation is clearly the dominant cementation type and is the most well cemented in all of the thin sections. The sub-vertical to vertical pipe cementation occurrence in the moderate-poor cemented areas indicate that this is probably not the main cementation process.

The fact that several of the thin sections display remarkably similarity with the carbonate concretions, e.g. thin section 5 (Fig. 38) and the carbonate boulder concretion (Fig. 47), show that the cementation trends in the thin sections are also displayed in the morphology of the carbonate

concretions. Based on the observations from the thin sections, the dominant cementation style is indicated to be the sub-horizontal to horizontal cementation. The only problem with this suggestion is that none of the vertical pipe or chimney concretions were sampled for the thins sections analysis as they were either too big or not suited for this type of analysis. However, in term of abundance, the sub-horizontal to horizontal concretions were clearly the dominant ones.

5.5.4.1 Pyrite

Tanaka et al. (1981) and Berner and Raiswell (1984) recognize a significant reduced amounts of pyrite formation in freshwater, where the formation is generally controlled by the amounts of organic matter and the rate of the sulphate reduction (Berner, 1984). The freshwater contribution from the glacier in Skarmunken could explain why the thin sections generally contain little pyrite content. The TOC/TS analysis supports freshwater conditions during deposition of the sediments (5.1.4). Several of the samples indicate conditions close to the marine boundary, which could indicate freshwater conditions with marine water influence. This is further indicated by sample 4,91m, which represent dominating marine conditions.

Thin sections 5 (13,85-13,87m, Fig. A 10), 10 (17,43m, Fig. A 20) and 11 (15,66m, Fig. A 22) contains the highest amount of pyrite crystals. Comparing the pyrite content with the TOC/TS combustion analysis (5.1.4), thin section 11 is located within the range of TOC/TS sample 15,6m (Fig. 33). This sample is located close to the marine boundary, which could explain the higher pyrite content. Thin section 5 and 10 most likely correlate stratigraphically with TOC/TS samples 14,29m and 17,59m (Fig. 33), where both are located well into the nonmarine section. Thin section 1 (Fig. A 2) and 9 (Fig. A 18) contain slightly lesser amounts of pyrite and most likely correlate stratigraphically with TOC/TS samples 1,99m and 1,02m (Fig. 33). Sample 1,99m is located close to the marine boundary, which could be the reason for the higher pyrite content. Sample 1,02m however, is located slightly further away from the marine boundary. The relatively close distance to the marine boundary explain the pyrite content. The rest of the thin sections 2 (2,71m, Fig. A 4), 3 (11,22m, Fig. A 6), 4 (13,98m, Fig. A 8), 6 (15,05m, Fig. A 12), 7 (0,565m, Fig. A 14) and 8 (0,43m, Fig. A 16) display the lowest pyrite content and correlate stratigraphically with TOC/TS samples 2,785m, 7,255-14,29m, 15,6m and 1,02m (Fig. 33). Aside from thin section 3 and 6, the thin sections are located well inside the nonmarine section and not to close the marine boundary. This indicate freshwater environment, which could explain why the samples contained the lowest pyrite content of all of the thin sections. Thin section 3 is located between 7,255m and 14,29m, where moving towards sample

14,29, the environment becomes more dominant nonmarine. As the sample is stratigraphically located in the middle of the two, the nonmarine conditions were most likely located in between those samples. This would indicate not very dominant nonmarine conditions, but not close marine conditions. Thin section 6 is indicated to be close to the TOC/TS sample 15,6m, which would indicate a higher pyrite content. This is not the case in thin section.

The pyrite crystals located within the carbonate cement could be explain by diagenesis, where the pyrite formed during the sulfate reduction phase (e.g. Raiswell & Fisher, 2000; Al-Ramadan et al., 2004). The indicated presence of freshwater is most likely the reason for the low pyrite content. However, the thin sections indicate that other factors play in on the formation of pyrite, where several samples that are close to normal marine conditions do not show a significant higher pyrite content. An explanation for this could be the availability of reactive iron materials (Berner, 1984). The presence of a glacier would also contribute with high and rapid sedimentation depositional rates, which according to Morse & Berner (1995) would affect the pyrite formation negative.

5.5.5 Summary thin sections

The cementation located in the pore spaces of the carbonate concretions are most likely calcite cement. The meniscus and poikilotopic cementation indicate fluid migration, where the poikilotopic cementation most likely represent areas for the main fluid migration pathways. The rim cementation indicate that the sediments was below the water table, which supports the MPS/BTh analysis of subaqueous sediments. The reason for better cementation of the fine-grained carbonate concretions are due to more contact points per unit volume. The grain-size distribution and most likely high capillary forces lead to favoring of cementation of the observed lamination structures in the carbonate concretions and thin sections. Higher amounts of contact points and high capillary forces could explain why the carbonate concretions only occur in specific parts of the sediments, which seemingly display the same sedimentary properties. This could also explain why horizontal and vertical cementation (4.5.2) is observed in the carbonate concretions. However, the fluid flow pathways play also a big part in the cementation morphologies. The smaller grains on the upper surface of bigger grains are most likely the result of fluid migration. The sub-horizontal to horizontal cementation morphology dominates in the investigated area, which could be explained by the fact that fine-grained laminae and cross bed in sediments are cemented faster and more intense (Molenaar & Venmans, 1993). The cementation trends observed in the thin sections indicate that they can most likely be found in the carbonate concretions morphologies. This

indicates that the morphologies of the concretions are controlled by the amounts of grain contact points and the fluid migration pathways through the sediments.

The generally low pyrite content can most likely be explained by the presence of the glacier and subsequent glaciomarine depositional conditions. The pyrite content show generally nonmarine depositional conditions but could also indicate events with more distinct marine influence. The pyrite content does not always correlate with the indicated environment, which could indicate that other factors play a part in the pyrite formation. Suggested by Berner (1984), reactive iron materials play a dominant control on the pyrite formation, which could indicate a low reactive iron content in the sediments.

5.5.6 Calcium source

The comparison with the Jauf sandstone (Al-Ramadan et al., 2004) most likely indicate that the cement consists of calcium carbonate. The precipitation of calcium carbonate favors low sulphate environments (Walter, 1986; Raiswell & Fisher, 2000b), which correlates indicated freshwater environment conditions.

Looking at the local geology around the depositional area, the Breivikeidet marbles and the Sjursnes phyllite are a potential source for the calcium. The calcite and dolomite are known to be have great reactivity with water containing CO_2 (Eq.16) (Yoshimura et al., 2001). Rainwater transporting CO_2 may then have dissolved some of marbles and acted as a Ca^{2+} and $CaCO_3$ source. The glacier located in Skarmunken could also have contributed with erosion of bedrock and transportation of allochthonous bedrock and sediments, where the Breivikeidet marbles and the Sjursnes phyllite also could have been eroded. The TOC/TS analysis most likely indicate dominating glaciofluvial conditions with one occurrence of dominating marine conditions. This indicates that the even though glaciofluvial conditions were dominating during the deposition, the marine influence was most likely present at all times. As the Ca^{2+} concentrations are 100 to 1000 times higher compared to freshwater (Duesing, 1985), the marine contribution could have been significant. The calcium could then potentially derives from biological sources e.g. shells from molluscs to calcite particles from algae (Nichols, 2009). The fact that shells from molluscs (Andersen, 1968) are most likely located beneath facies A (5.1.2.1) strengthens the indication of marine calcium contribution.

This indicates that the calcium source most likely consists of multiple sources, where the marine contribution has the potential to be the main source. The rainwater dissolving of the Breivikeidet marbles, the Sjursnes phyllite and dissolving of calcium silicate from the soil could also have contributed, however, the amount of contribution is unknown and could be very little. The erosion and transportation of bedrock and sediments are more likely to have contributed significantly compared to rainwater transport. As the bedrock units in the Sjursnes phyllites, the Breivikeidet marbles contain significant calcium content, the glacial erosion of these units would certainly have contributed calcium to the Skarmunken deposits. This indicates that the main calcium source most likely consists of marine contributed calcium and glacial transported calcium.

6 CONCLUSION

- The depositional environment in Skarmunken was dominated by a shallow glaciofluvial marine setting. The glaciomarine system is suggested to represent an ice-contact delta, with fluctuating conditions between dominating glacifluvial and marine conditions. The vertical profile in Skarmunken is suggested to consists of alternating unit A and B deposits, mainly consisting of meltwater plume, turbidic and debris flow deposits, as foreset, foreset-bottomset and bottomset deposits. The investigated sediments were deposited submerged and after approximate 10 ka c. yr BP.
- The sand injections, the faulted sequence and the fluid migration structures are the result of sedimentary and glacial compaction, leading to fluidization and mobilization of a fine-grained sediment sequence.
- The carbonate concretions are suggested to consist of calcium cement. Oxidation of hydrocarbons and buried carbon are suggested to be the main precipitation pathways for the carbonate concretions. Two different cementation events are suggested for the carbonate concretions, where the stratabound concretions are suggested to be the result of precipitation of in-situ carbon sources and the concretions located inside the sand injections are suggested to be the result of fluid migration.
- The morphologies of the concretions are the product of the grain contact points in the sediments and the fluid migration pathways, where both are controlled by the sediment heterogeneity. The formation processes of the spherulitic concretions is uncertain and needs further investigation. The morphology of the carbonate concretions suggests that the environment was anoxic up to 18m. The carbon source for the precipitation of the carbonate concretions is most likely biogenic carbon, where the main sources are suggested to derive from shallow marine nutrient and life rich environment and allochthonous glacial derived carbon. The calcium source for the carbonate concretions is suggested to be from marine contribution and allochthonous glacial derived strata.

7 REFERENCES

Al-Ramadan, K. A., Hussain, M., Imam, B., & Saner, S. (2004). Lithologic characteristics and diagenesis of the Devonian Jauf sandstone at Ghawar Field, Eastern Saudi Arabia. *Marine and Petroleum Geology*, *21*(10), 1221–1234. https://doi.org/10.1016/j.marpetgeo.2004.09.002

Andersen, B. G. (1965). Glacial Chronology of Western Troms, North Norway. In *Geological Society of America Special Papers* (Vol. 84, pp. 35–54). Geological Society of America. https://doi.org/10.1130/SPE84-p35

Andersen, B. G. (1968). Glacial geology of Western Troms, North Norway. *Norges Geologiske Undersøkelse*, *256*(256), 160.

Andresen, A., & Bergh, S. (1985). Stratigraphy and tectonometamorphic evolution of the Ordovician-Silurian Balsfjord Group, Lyngen Nappe, north Norwegian Caledonides. *The Caledanide Orogen-Scandinavian and Related Arcas, John Wiley and Sons, London*, 579–591. Retrieved from https://scholar.google.no/scholar?q=Stratigraphy+and+tectonometamorphic+evolution+of+the+Ordovician-Silurian+Balsfjord+Group&btnG=&hl=no&as_sdt=0%2C5

Andresen, A., & Steltenpohl, M. G. (1994). Evidence for ophiolite obduction, terrane accretion and polyorogenic evolution of the north Scandinavian Caledonides. *Tectonophysics*, *231*(1–3), 59–70. https://doi.org/10.1016/0040-1951(94)90121-X

Bakke, J., Dahl, S. O., Paasche, Ø., Løvlie, R., & Nesje, A. (2005). Glacier fluctuations, equilibrium-line altitudes and palaeoclimate in Lyngen, northern Norway, during the Lateglacial and Holocene. *The Holocene*, *15*(4), 518–540. https://doi.org/10.1191/0959683605hl815rp

Ballantyne, C. K. (1990). The Holocene glacial history of Lyngshalvöya, northern Norway: chronology and climatic implications. *Boreas*, *19*(2), 93–117. https://doi.org/10.1111/j.1502-3885.1990.tb00570.x

Beck, R., & Andreassen, J. P. (2010). Spherulitic growth of calcium carbonate. *Crystal Growth and Design*, *10*(7), 2934–2947. https://doi.org/10.1021/cg901460g

Beliaev, S. S., Finkel'shteĭn, Z. I., & Ivanov, M. V. (1974). [Intensity of bacterial methane formation in ooze deposits in lakes]. *Mikrobiologiia*, *44*(2), 309–12. Retrieved from http://www.ncbi.nlm.nih.gov/pubmed/131899

Bergh, S. G., Kullerud, K., Myhre, P. I., Corfu, F., Armitage, P. E. B., Zwaan, K. B., & Ravna, E. J. K. (2014). Archaean Elements of the Basement Outliers West of the Scandinavian Caledonides in Northern Norway: Architecture, Evolution and Possible Correlation with Fennoscandia (pp. 103–126). Springer

Netherlands. https://doi.org/10.1007/978-94-007-7615-9_4

Bergh, S. G., Kullerud, K., Armitage, P. E. B., Zwaan, K. B., Corfu, F., Ravna, E. J. K., & Myhre, P. I. (2010). Neoarchaean to Svecofennian tectono-magmatic evolution of the West Troms Basement Complex, North Norway. *Journal of Geology/ …*. Retrieved from http://search.ebscohost.com/login.aspx?direct=true&profile=ehost&scope=site&authtype=crawler&jrnl=0029196X&AN=97499477&h=ONZv%2FWrQyfRKnYEk%2Fh5nr7NkUeBf35qyfk1J1KQj2UuZfKf%2Bu4B%2BE6wyttPg79E4mgCbKLt1RLTe5jKp43SjSg%3D%3D&crl=c

Bergh, S. G., & Andresen, A. (1985). Tectonometamorphic evolution of the allochthonous rocks between Malangen and Balsfjord, Troms, North, Norway. *Norges Geologiske Undersøkelse*, *405*, 41–56. Retrieved from https://scholar.google.no/scholar?q=Tectonometamorphic+evolution+of+the+allochthonous+rocks+between+Malangen+and+Balsfjord&btnG=&hl=no&as_sdt=0%2C5

Berner, R. A. (1970). Sedimentary pyrite formation. *American Journal of Science*, *268*(1), 1–23. https://doi.org/10.2475/ajs.268.1.1

Berner, R. A. (1982). Burial of organic carbon and pyrite sulfur in the modern ocean; its geochemical and environmental significance. *American Journal of Science*, *282*(4), 451–473. https://doi.org/10.2475/ajs.282.4.451

Berner, R. A. (1984). Sedimentary pyrite formation: An update. *Geochimica et Cosmochimica Acta*, *48*(4), 605–615. https://doi.org/10.1016/0016-7037(84)90089-9

Berner, R. A., & Raiswell, R. (1984). C/S method for distinguishing freshwater from marine sedimentary rocks. *Geology*, *12*(6), 365. https://doi.org/10.1130/0091-7613(1984)12<365:CMFDFF>2.0.CO;2

Berra, F., & Felletti, F. (2011). Syndepositional tectonics recorded by soft-sediment deformation and liquefaction structures (continental Lower Permian sediments, Southern Alps, Northern Italy): Stratigraphic significance. *Sedimentary Geology*, *235*(3–4), 249–263. https://doi.org/10.1016/j.sedgeo.2010.08.006

BINNS, R. E. (1978). Caledonian nappe correlation and orogenic history in Scandinavia north of lat 67°N. *Geological Society of America Bulletin*, *89*(10), 1475. https://doi.org/10.1130/0016-7606(1978)89<1475:CNCAOH>2.0.CO;2

Bjørglykke, A., & Olaussen, S. (1981). Silurian Sediments, Volcanics and Mineral deposits in the Sagelvvatn Area, Troms, North Norway. *Norges Geologiske Undersøkelse* , *365*, 1–38. Retrieved from https://scholar.google.no/scholar?q=Silurian+sediments%2C+volcanics+and+mineral+deposits+in+the+

Sagelvvatu+area&btnG=&hl=no&as_sdt=0%2C5

Bluck, B. J. (1967). Deposition of some Upper Old Red Sandstone conglomerates in the Clyde area: A study in the significance of bedding. *Scottish Journal of Geology*, *3*(2), 139–167. https://doi.org/10.1144/sjg03020139

Burton, E. A. (1993). Controls on marine carbonate cement mineralogy: review and reassessment. *Chemical Geology*, *105*(1–3), 163–179. https://doi.org/10.1016/0009-2541(93)90124-2

Cartwright, J. A., & Dewhurst, D. N. (1998). Layer-bound compaction faults in fine-grained sediments. *Geological Society of America Bulletin*, *110*(10), 1242–1257. https://doi.org/10.1130/0016-7606(1998)110<1242:LBCFIF>2.3.CO;2

Claypool, G. E., & Kaplan, I. R. (1974). The Origin and Distribution of Methane in Marine Sediments. In *Natural Gases in Marine Sediments* (pp. 99–139). Boston, MA: Springer US. https://doi.org/10.1007/978-1-4684-2757-8_8

Claypool, G. E., & Threlkeld, C. N. (1983). Anoxic Diagenesis and Methane Generation in Sediments of the Blake Outer Ridge, Deep Sea Drilling Project Site 533, Leg 76 1 ,. *Proceedings of the Ocean Drilling Program, Initial Reports, Vol. 76*, *76*, 391–402.

Coker-dewey, J., Steltenpohl, M. G., & Andresen, A. (2000). Geology of western Ullsfjord, North Norway, with emphasis on the development of an inverted metamorphic gradient at the top of the Lyngen Nappe Complex. *Norsk Geologisk Tidsskrift*, *80*, 111–128. Retrieved from foreninger.uio.no/ngf/ngt/pdfs/NGT_80_2_111-127.pdf

Corfu, F. (2004). U-Pb age, setting and tectonic significance of the anorthosite-mangerite-charnockite-granite suite, Lofoten-Vester??len, Norway. *Journal of Petrology*, *45*(9), 1799–1819. https://doi.org/10.1093/petrology/egh034

Corner, G. D. (1980). Preboreal deglaciation chronology and marine limits of the Lyngen-Storfjord area, Troms, North Norway. *Boreas*, *9*(4), 239–249. https://doi.org/10.1111/j.1502-3885.1980.tb00700.x

Corner, G. D., & Haugane, E. (1993). Marine-lacustrine stratigreaphy of raised coastal basins and postglacial sea-level change at Lyngen and Vanna, Troms, northern Norway. *Norsk Geologisk Tidsskrift*, *73*, 175–197. Retrieved from www.geologi.no/~geolosnt/images/NJG_articles/NGT_73_3_175-197.pdf

Dando, P. R., O'Hara, S. C. M., Schuster, U., Taylor, L. J., Clayton, C. J., Baylis, S., & Laier, T. (1994). Gas seepage from a carbonate-cemented sandstone reef on the Kattegat coast of Denmark. *Marine and Petroleum Geology*, *11*(2), 182–189. https://doi.org/10.1016/0264-8172(94)90094-9

Dehls, J. F., Olesen, O., Olsen, L., & Harald Blikra, L. (2000). Neotectonic faulting in northern Norway; the Stuoragurra and Nordmannvikdalen postglacial faults. *Quaternary Science Reviews*, *19*(14), 1447–1460. https://doi.org/10.1016/S0277-3791(00)00073-1

Diaz-del-Rio, V., Somoza, L., Martínez-Frias, J., Mata, M. P., Delgado, A., Hernandez-Molina, F. J., … Vázquez, J. T. (2003). Vast fields of hydrocarbon-derived carbonate chimneys related to the accretionary wedge/olistostrome of the Gulf of C??diz. *Marine Geology*, *195*(1–4), 177–200. https://doi.org/10.1016/S0025-3227(02)00687-4

Duesing, B. (1985). Skeletal Materials- Biomineralization: The Calcium Cycle. Retrieved August 14, 2016, from http://teachersinstitute.yale.edu/curriculum/units/1985/7/85.07.08.x.html

Eilertsen, R., Corner, G. D., & Aasheim, O. (2005). Deglaciation chronology and glaciomarine successions in the Malangen-Målselv area, northern Norway. *Boreas*, *34*(3), 233–251. https://doi.org/10.1111/j.1502-3885.2005.tb01098.x

Elverhøi, A., Liestol, O., & Nagy, J. (1980). Glacial erosion, sedimentation and microfauna in the inner part of Kongsfjorden, Spitsbergen. *Norsk Polarinstitutt Skrifter*. Retrieved from http://brage.bibsys.no/xmlui/bitstream/handle/11250/173860/Skrifter172.pdf?sequence=1&isAllowed=y#page=35

Elverhøi, A., & Solheim, A. (1983). The Barents Sea ice sheet - a sedimentological discussion. *Polar Research*, (1), 23–42. Retrieved from onlinelibrary.wiley.com/doi/10.1111/j.1751-8369.1983.tb00729.x/full

Eyles, C. H. (1988). Glacially- and tidally-influenced shallow marine sedimentation of the late Precambrian Port Askaig Formation, Scotland. *Palaeogeography, Palaeoclimatology, Palaeoecology*, *68*(1), 1–25. https://doi.org/10.1016/0031-0182(88)90013-2

Eyles, N., & Boyce, J. I. (1998). Kinematic indicators in fault gouge: tectonic analog for soft-bedded ice sheets. *Sedimentary Geology*, *116*(1–2), 1–12. https://doi.org/10.1016/S0037-0738(97)00122-X

Gaines, R. R., & Vorhies, J. S. (2016). Growth mechanisms and geochemistry of carbonate concretions from the Cambrian Wheeler Formation (Utah, USA). *Sedimentology*, *63*(3), 662–698. https://doi.org/10.1111/sed.12234

Gautier, D. L., & Claypool, G. E. (1984). Interpretation of methanic diagenesis in ancient sediments by analogy with processes in modern diagenetic environments. *Clastic Diagenesis* , *37*(Mem. Am. Assoc. Petrol. Geol.), 111–123. Retrieved from https://scholar.google.no/scholar?q=Gautier+and+claypool+1984&btnG=&hl=no&as_sdt=0%2C5

Goldhaber, M. B., & Kaplan, I. R. (1974). The sulfur cycle. In E. D. Goldberg (Ed.), *The Sea* (Vol. 5, pp. 569–

654). Wiley, New York.

Griffin, W. L., Taylor, P. N., Hakkinen, J. W., Heier, K. S., Iden, I. K., Krogh, E. J., … Tveten, E. (1978). Archaean and Proterozoic crustal evolution in Lofoten–Vesterålen, N Norway. *Journal of the*. Retrieved from http://jgs.geoscienceworld.org/content/135/6/629.abstract

Hildebrandt, C., & Egenhoff, S. (2007). Shallow-marine massive sandstone sheets as indicators of palaeoseismic liquefaction — An example from the Ordovician shelf of Central Bolivia. *Sedimentary Geology*, *202*(4), 581–595. https://doi.org/10.1016/j.sedgeo.2007.04.009

Hill, H. K., & Fleisher, P. J. (1996). Nomenclature Applied to Deposits Formed in Glacial and Ice-Contact Environments. *Geoscience Education*, *44*(3), 277–289. Retrieved from http://www.nagt-jge.org/doi/pdf/10.5408/1089-9995-44.3.277?code=gete-site

Holmes, G. W., & Andersen, B. . (1964). Glacial chronology of Ullsfjord. *United States Geological Survey Professional Paper D* , *475*, 159–163.

Hovland, M., & Judd, a. G. (1988). Seabed pockmarks and seepages — impact on geology, biology and the marine environment. https://doi.org/10.1016/0264-8172(89)90010-X

Hovland, M., Svensen, H., Forsberg, C. F., Johansen, H., Fichler, C., Fosså, J. H., … Rueslåtten, H. (2005). Complex pockmarks with carbonate-ridges off mid-Norway: Products of sediment degassing. *Marine Geology*, *218*(1), 191–206. https://doi.org/10.1016/j.margeo.2005.04.005

Hovland, M., Talbot, M., & Qvale, H. (1987). Methane-related carbonate cements in pockmarks of the North Sea. *Journal of*. Retrieved from http://archives.datapages.com/data/sepm/journals/v55-58/data/057/057005/0881.htm

Hudson, J. D. (1978). Concretions, isotopes, and the diagenetic history of the Oxford Clay (Jurassic) of central England. *Sedimentology*, *25*(3), 339–370. https://doi.org/10.1111/j.1365-3091.1978.tb00317.x

Hughen, K. A., Baillie, M. G. L., Bard, E., Bayliss, A., Beck, J. W., Bertrand, C. J. H., … van der Plicht, J. Weyhenmeyer, C. E. (2004). Marine04 Marine radiocarbon age calibration, 26-0 ka BP. *Radiocarbon*, *46*, 1059–1086.

Hughes, A. L. C., Gyllencreutz, R., Lohne, Ø. S., Mangerud, J., & Svendsen, J. I. (2016). The last Eurasian ice sheets - a chronological database and time-slice reconstruction, DATED-1. *Boreas*, *45*(1), 1–45. https://doi.org/10.1111/bor.12142

Hunt, J. M. (1972a). Distribution of Carbon in Crust of Earth: GEOLOGICAL NOTES. *AAPG Bulletin*, *56*(11), 2273–2277.

Hunt, J. M. (1972b). Distribution of Carbon In Crust of Earth ', (2837), 2273–2277. Retrieved from https://vpn.uit.no/+CSCO+00756767633A2F2F6E657075766972662E716E676E636E7472662E70627A++/data/bulletns/1971-73/images/pg/00560011/2250/22730.pdf

Hurst, A., Cartwright, J., & Duranti, D. (2003). Fluidization structures produced by upward injection of sand through a sealing lithology. *Geological Society, London, Special Publications*, *216*(1), 123–138. https://doi.org/10.1144/GSL.SP.2003.216.01.09

Hurst, A., Scott, A., & Vigorito, M. (2011). Physical characteristics of sand injectites. *Earth-Science Reviews*, *106*(3–4), 215–246. https://doi.org/10.1016/j.earscirev.2011.02.004

Hustoft, S., Dugan, B., & Mienert, J. (2009). Effects of rapid sedimentation on developing the Nyegga pockmark field: Constraints from hydrological modeling and 3-D seismic data, offshore mid-Norway. *Geochemistry, Geophysics, Geosystems*, *10*(6). https://doi.org/10.1029/2009GC002409

Iversen, N., & Jorgensen, B. B. (1985). Anaerobic methane oxidation rates at the sulfate-methane transition in marine sediments from Kattegat and Skagerrak (Denmark)1. *Limnology and Oceanography*, *30*(5), 944–955. https://doi.org/10.4319/lo.1985.30.5.0944

Janák, M., Ravna, E. J. K., & Kullerud, K. (2012). Constraining peak P-T conditions in UHP eclogites: Calculated phase equilibria in kyanite- and phengite-bearing eclogite of the Tromsø Nappe, Norway. *Journal of Metamorphic Geology*, *30*(4), 377–396. https://doi.org/10.1111/j.1525-1314.2011.00971.x

Jin, D., ShiHong, Z., GanQing, J., QingLe, Z., HaiYan, L., XiaoYing, S., & JunLai, L. (2008). Early diagenetic growth of carbonate concretions in the upper Doushantuo Formation in South China and their significance for the assessment of hydrocarbon source rock, *51*(9), 1330–1339. https://doi.org/10.1007/s11430-008-0107-3

Jørgensen, N. O. (1992a). Methane-derived carbonate cementation of Holocene marine sediments from Kattegat, Denmark. *Continental Shelf Research*, *12*(10), 1209–1218. https://doi.org/10.1016/0278-4343(92)90080-4

Jørgensen, N. O. (1992b). Methane-derived carbonate cementation of marine sediments from the Kattegat, Denmark: Geochemical and geological evidence. *Marine Geology*, *103*(1–3), 1–13. https://doi.org/10.1016/0025-3227(92)90006-4

Kastner, M., Elderfield, H., Martin, J. B., Suess, E., Kvenvolden, K. A., & Garrison, R. E. (1990). 25. DIAGENESIS AND INTERSTITIAL-WATER CHEMISTRY AT THE PERUVIAN CONTINENTAL MARGIN—MAJOR CONSTITUENTS AND STRONTIUM ISOTOPES 1. *Scientific Results*, *112*. Retrieved from www.researchgate.net/profile/Jonathan_Martin5/publication/268280327_25._DIAGENESIS_AND_INTE

RSTITIALWATER_CIlEMISTRY_AT_THE_PERUVIAN_CONTINENTAL_MARGIN-MAJOR_CONSTITUENTS_AND_STRONTIUM_ISOTOPES/links/00b49518a5b70f325b000000.pdf

Koyama, T. (1963). Gaseous metabolism in lake sediments and paddy soils and the production of atmospheric methane and hydrogen. *Journal of Geophysical Research*, *68*(13), 3971–3973. https://doi.org/10.1029/JZ068i013p03971

Krajewski, K. P., & Luks, B. (2003). Origin of " cannon − ball " concretions in the Carolinefjellet Formation (Lower Cretaceous), Spitsbergen. *Polish Polar Research*, *24*(3–4), 217–242. Retrieved from citeseerx.ist.psu.edu/viewdoc/download?doi=10.1.1.500.8536&rep=rep1&type=pdf

Krogh, E. J., Andersen, A., Bryhni, I., Broks, T. M., & Kristensen, S. E. (1990). Eclogites and polyphase P-T cycling in the Caledonian Uppermost Allochthon in Troms, northern Norway. *Journal of Metamorphic Geology*, *8*(3), 289–309. https://doi.org/10.1111/j.1525-1314.1990.tb00474.x

Landvik, J., Bolstad, M., & Lykcke, A. K. (1992). Weichselian stratigraphy and palaeoenvironments at Bellsund, western Svalbard. *Boreas*. Retrieved from http://onlinelibrary.wiley.com/doi/10.1111/j.1502-3885.1992.tb00039.x/abstract

Le Heron, D. P., Sutcliffe, O. E., Whittington, R. J., & Craig, J. (2005). The origins of glacially related soft-sediment deformation structures in Upper Ordovician glaciogenic rocks: Implication for ice-sheet dynamics. *Palaeogeography, Palaeoclimatology, Palaeoecology*. https://doi.org/10.1016/j.palaeo.2004.12.007

Lein, A. Y., Ivanov, M. V., Pimenov, N. V., & Gulin, M. B. (2002). Geochemical Peculiarities of the Carbonate Constructions Formed during Microbial Oxidation of Methane under Anaerobic Conditions. *Microbiology*, *71*(1), 78–90. https://doi.org/10.1023/A:1017906501726

Leventhal, J. S. (1979). the relationship between organic carbon and sulfide sulfur in recent and ancient marine and euxinic sediments. *Eos, Trans.Amer.Geophys. Union*, *60*, 286.

Leventhal, J. S. (1983). An interpretation of carbon and sulfur relationships in Black Sea sediments as indicators of environments of deposition. *Geochimica et Cosmochimica Acta*, *47*(1), 133–137. https://doi.org/10.1016/0016-7037(83)90097-2

Leventhal, J. S. (1987). Carbon and sulfur relationships in Devonian shales from the Appalachian Basin as an indicator of environment of deposition. *American Journal of Science*, *287*(1), 33–49. https://doi.org/10.2475/ajs.287.1.33

Leventhal, J. S. (1995). Carbon-sulfur plots to show diagenetic and epigenetic sulfidation in sediments. *Geochimica et Cosmochimica Acta*, *59*(6), 1207–1211. https://doi.org/10.1016/0016-7037(95)00036-Y

Lewis, D. W., & McConchie, D. (2012). *Analytical Sedimentology*. Springer Science & Business Media.

Luff, R., Wallmann, K., & Aloisi, G. (2004). Numerical modeling of carbonate crust formation at cold vent sites: significance for fluid and methane budgets and chemosynthetic biological communities. *Earth and Planetary Science Letters*. Retrieved from http://www.sciencedirect.com/science/article/pii/S0012821X04001074

Luth, C., Luth, U., Gebruk, A. V., & Thiel, H. (1999). Methane gas Seeps Along the Oxic/Anoxic Gradient in the Black Sea: Manifestations, Biogenic Sediment Compounds and Preliminary Results on Benthic Ecology. *Marine Ecology*, *20*(3–4), 221–249. https://doi.org/10.1046/j.1439-0485.1999.t01-1-00073.x

Lønne, I. (1993). Physical signatures of ice advance in the Younger Dryas ice-contact delta, Troms, northern Norway: implications for glacier-terminus history. *Boreas*, *22*(1), 59–70. https://doi.org/10.1111/j.1502-3885.1993.tb00164.x

Lønne, I. (1995). Sedimentary facies and depositional architecture of ice-contact glaciomarine systems. *Sedimentary Geology*, *98*(1–4), 13–43. https://doi.org/10.1016/0037-0738(95)00025-4

Lønne, I. (2001). Dynamics of marine glacier termini read from moraine architecture. *Geology*, *29*(3), 199–202. https://doi.org/10.1130/0091-7613(2001)029<0199:DOMGTR>2.0.CO;2

Løseth, H., Wensaas, L., Arntsen, B., & Hovland, M. (2003). Gas and fluid injection triggering shallow mud mobilization in the Hordaland Group, North Sea. *Geological Society, London, Special Publications*, *216*(1), 139–157. https://doi.org/10.1144/GSL.SP.2003.216.01.10

Macdonald, D., & Flecker, R. (2007). Injected Sand Sills in a Strike-slip Fault Zone: A Case Study from the Pil'sk Suite (Miocene), Southeast Schmidt Peninsula, Sakhalin, 253–263. https://doi.org/10.1306/1209869M871399

Mackiewicz, N. E., Powell, R. D., Carlson, P. R., & Molnia, B. F. (1984). Interlaminated ice-proximal glacimarine sediments in Muir Inlet, Alaska. *Marine Geology*, *57*(1), 113–147. https://doi.org/10.1016/0025-3227(84)90197-X

Maltman, A. (1994). *The Geological Deformation of Sediments*. (A. Maltman, Ed.). Dordrecht: Springer Netherlands. https://doi.org/10.1007/978-94-011-0731-0

Martini, I. P. (n.d.). Pleistocene Glacial Fan Deltas in Southern Ontario, Canada. In *Coarse-Grained Deltas* (pp. 281–295). Oxford, UK: Blackwell Publishing Ltd. https://doi.org/10.1002/9781444303858.ch16

Matsumoto, R. (1989). Isotopically heavy oxygen-containing siderite derived from the decomposition of methane hydrate. *Geology*, *17*(8), 707. https://doi.org/10.1130/0091-

7613(1989)017<0707:IHOCSD>2.3.CO;2

Mazzini, A., Svensen, H., Hovland, M., & Planke, S. (2006). Comparison and implications from strikingly different authigenic carbonates in a Nyegga complex pockmark, G11, Norwegian Sea. *Marine Geology*, *231*(1–4), 89–102. https://doi.org/10.1016/j.margeo.2006.05.012

McCabe, A. M., & Eyles, N. (1988). Sedimentology of an ice-contact glaciomarine delta, Carey Valley, Northern Ireland. *Sedimentary Geology*, *59*(1–2), 1–14. https://doi.org/10.1016/0037-0738(88)90097-8

Michaelis, W., Seifert, R., Nauhaus, K., Treude, T., Thiel, V., Blumenberg, M., … Michaelis, W. (2002). Microbial reefs in the Black Sea fueled by anaerobic oxidation of methane. *Science (New York, N.Y.)*, *297*(5583), 1013–5. https://doi.org/10.1126/science.1072502

Molenaar, N., & Venmans, A. A. M. (1993). Calcium carbonate cementation of sand: A method for producing artificially cemented samples for geotechnical testing and a comparison with natural cementation processes. *Engineering Geology*, *35*(1–2), 103–122. https://doi.org/10.1016/0013-7952(93)90073-L

Momper, J. A. (1978). Oil Migration Limitations Suggested by Geological and Geochemical Considerations, *34*, T.1-60. Retrieved from https://vpn.uit.no/+CSCO+00756767633A2F2F6E657075766972662E716E676E636E7472662E70627A++/data/specpubs/geochem1/images/a034b/a0340001/0000/t1.pdf

Morse, J. W., & Berner, R. A. (1995). What determines sedimentary C/S ratios? *Geochimica et Cosmochimica Acta*, *59*(6), 1073–1077. https://doi.org/10.1016/0016-7037(95)00024-T

MØLLER, J. J., DANIELSEN, T. K., & FJALSTAD, A. (2008). Late Weichselian glacial maximum on Andøya, North Norway. *Boreas*, *21*(1), 1–13. https://doi.org/10.1111/j.1502-3885.1992.tb00007.x

Naehr, T. H., Eichhubl, P., Orphan, V. J., Hovland, M., Paull, C. K., Ussler, W., … Greene, H. G. (2007). Authigenic carbonate formation at hydrocarbon seeps in continental margin sediments: A comparative study. *Deep Sea Research Part II: Topical Studies in Oceanography*, *54*(11), 1268–1291. https://doi.org/10.1016/j.dsr2.2007.04.010

Nemec, W. (1990). Aspects of sediment movement on steep delta slopes. *Coarse-Grained Deltas*. Retrieved from http://www.academia.edu/download/33078404/Nemec_1990b.pdf

Nemec, W., & Steel, R. J. (1984). Alluvial and coastal conglomerates: their significant features and some comments on gravelly mass-flow deposits. *Sedimentology of Gravels and Conglomerates*, *10*(1984), 1–31. https://doi.org/-

Nemec, W., Steel, R., Poreebski, S., & Spinnangr, Å. (1984). Domba Conglomerate, Devonian, Norway:

process and lateral variability in a mass flow-dominated, lacustrine fan-delta. Retrieved from http://archives.datapages.com/data/cspg_sp/data/010/010001/295_cspgsp0100295.htm

Neuwerth, R., Suter, F., Guzman, C. A., & Gorin, G. E. (2006). Soft-sediment deformation in a tectonically active area: The Plio-Pleistocene Zarzal Formation in the Cauca Valley (Western Colombia). *Sedimentary Geology*, *186*(1–2), 67–88. https://doi.org/10.1016/j.sedgeo.2005.10.009

Nichols, G. (2009). *Sedimentology and stratigraphy* (2nd ed.). Blackwell-Wiley.

Niemann, H., Elvert, M., Hovland, M., Orcutt, B., Judd, a., Suck, I., … Boetius, a. (2005). Methane emission and consumption at a North Sea gas seep (Tommeliten area). *Biogeosciences Discussions*, *2*(4), 1197–1241. https://doi.org/10.5194/bgd-2-1197-2005

Orphan, V. ., Ussler, W., Naehr, T. ., House, C. ., Hinrichs, K.-U., & Paull, C. . (2004). Geological, geochemical, and microbiological heterogeneity of the seafloor around methane vents in the Eel River Basin, offshore California. *Chemical Geology*, *205*(3), 265–289. https://doi.org/10.1016/j.chemgeo.2003.12.035

Paull, C., & Iii, W. U. (2008). Re-Evaluating the Significance of Seafloor Accumulations of Methane-Derived Carbonates: Seepage or Erosion Indicators? *Icgh2008*, (Icgh), 1–12. Retrieved from https://circle.ubc.ca/handle/2429/1084

Pearson, M. J., Grosjean, E., Nelson, C. S., Nyman, S. L., & Logan, G. A. (2010). TUBULAR CONCRETIONS IN NEW ZEALAND PETROLIFEROUS BASINS: LIPID BIOMARKER EVIDENCE FOR MINERALISATION AROUND PROPOSED MIOCENE HYDROCARBON SEEP CONDUITS. *Journal of Petroleum Geology*, *33*(3), 205–219. https://doi.org/10.1111/j.1747-5457.2010.00474.x

Peckmann, J., Reimer, A., Luth, U., Luth, C., Hansen, B. T., Heinicke, C., … Reitner, J. (2001). Methane-derived carbonates and authigenic pyrite from the northwestern Black Sea. *Marine Geology*, *177*(1–2), 129–150. https://doi.org/10.1016/S0025-3227(01)00128-1

Pine, M. J., & Barker, H. A. (1956). Studies on the methane fermentation. XII. The pathway of hydrogen in the acetate fermentation. *Journal of Bacteriology*, *71*(6), 644–8. Retrieved from http://www.ncbi.nlm.nih.gov/pubmed/13345749

Plassen, L., & Vorren, T. O. (2003a). Fluid flow features in fjord-fill deposits, Ullsfjorden, North Norway. *Norsk Geologisk Tidsskrift*, *83*(1), 37–42. Retrieved from www.geologi.no/~geolosnt/images/NJG_articles/NJG_83_37-42.pdf

Plassen, L., & Vorren, T. O. (2003b). Sedimentary processes and the environment during deglaciation of a fjord basin in Ullsfjorden, North Norway. *Norsk Geologisk Tidsskrift*, *83*(1), 23–36. Retrieved from

https://www.researchgate.net/publication/289400134_Sedimentary_processes_and_the_environment_during_deglaciation_of_a_fjord_basin_in_Ullsfjorden_North_Norway

Plink-Björklund, P., & Steel, R. J. (2004). Initiation of turbidity currents: Outcrop evidence for Eocene hyperpycnal flow turbidites. *Sedimentary Geology*, *165*(1–2), 29–52. https://doi.org/10.1016/j.sedgeo.2003.10.013

Powell, R. D. (1990). Glacimarine processes at grounding-line fans and their growth to ice-contact deltas. *Geological Society, London, Special Publications*, *53*(1), 53–73. https://doi.org/10.1144/GSL.SP.1990.053.01.03

Powell, R. D., & Molnia, B. F. (1989). Glacimarine sedimentary processes, facies and morphology of the south-southeast Alaska shelf and fjords. *Marine Geology*, *85*(2), 359–390. https://doi.org/10.1016/0025-3227(89)90160-6

R. Jonk, B. T. C. A. H. (2007). Variations in Sediment Extrusion in Basin-floor, Slope, and Delta-front Settings: Sand Volcanoes and Extruded Sand Sheets from the Namurian of County Clare, Ireland, 221–226. https://doi.org/10.1306/1209865M873267

Raiswell, R., & Fisher, Q. J. (2000a). Mudrock-hosted carbonate concretions: a review of growth mechanisms and their influence on chemical and isotopic composition. *Journal of the Geological Society*, *157*, 239–251.

Raiswell, R., & Fisher, Q. J. (2000b). Mudrock-hosted carbonate concretions: a review of growth mechanisms and their influence on chemical and isotopic composition. *Journal of the Geological Society*, *157*(1), 239–251. https://doi.org/10.1144/jgs.157.1.239

Ramberg, I. B., Bryhni, I., & Nøttvedt, A. (2006). *The making of a land*. Norsk Geologisk Forening.

Rashid, M. A., & Vilks, G. (1977). Environmental controls of methane production in Holocene basins in eastern Canada. *Organic Geochemistry*, *1*(1), 53–59. https://doi.org/10.1016/0146-6380(77)90008-0

Rattas, M., Lomp, P., & Jõeleht, A. (2014). Carbonate cementation in the late glacial outwash and beach deposits in northern Estonia. *Estonian Journal of Earth Sciences*, *63*(1), 30. https://doi.org/10.3176/earth.2014.03

Ravier, E., Buoncristiani, J. F., Clerc, S., Guiraud, M., Menzies, J., & Portier, E. (2014). Sedimentological and deformational criteria for discriminating subglaciofluvial deposits from subaqueous ice-contact fan deposits: A Pleistocene example (Ireland). *Sedimentology*, *61*(5), 1382–1410. https://doi.org/10.1111/sed.12111

Reeburgh, W. S. (1983). Rates of Biogeochemical Processes in Anoxic Sediments. *Annual Review of Earth and Planetary Sciences*, *11*(1), 269–298. https://doi.org/10.1146/annurev.ea.11.050183.001413

Rice, D. ., & Claypool, G. E. (1981). Generation, Accumulation, and Resource Potential of Biogenic Gas. *AAPG Bulletin*, *65*(1), 5–25. Retrieved from archives.datapages.com/data/bulletns/1980-81/data/pg/0065/0001/0000/0005.htm

Ritger, S., Carson, B., & Suess, E. (1987). Methane-derived authigenic carbonates formed by subduction-induced pore-water expulsion along the Oregon/Washington margin. *Geological Society of America Bulletin*, *98*(2), 147. https://doi.org/10.1130/0016-7606(1987)98<147:MACFBS>2.0.CO;2

Rodríguez-Pascua, M. A., Calvo, J. P., De Vicente, G., & Gómez-Gras, D. (2000). Soft-sediment deformation structures interpreted as seismites in lacustrine sediments of the Prebetic Zone, SE Spain, and their potential use as indicators of earthquake magnitudes during the Late Miocene. *Sedimentary Geology*, *135*(1–4), 117–135. https://doi.org/10.1016/S0037-0738(00)00067-1

Sandbeck, K. A., & Ward, D. M. (1981). Fate of immediate methane precursors in low-sulfate, hot-spring algal-bacterial mats. *Applied and Environmental Microbiology*, *41*(3), 775–82. Retrieved from http://www.ncbi.nlm.nih.gov/pubmed/16345736

Sassen, R., Roberts, H. H., Aharon, P., Larkin, J., Chinn, E. W., & Carney, R. (1993). Chemosynthetic bacterial mats at cold hydrocarbon seeps, Gulf of Mexico continental slope. *Organic Geochemistry*, *20*(1), 77–89. https://doi.org/10.1016/0146-6380(93)90083-N

Schoell, M. (1983). Genetic Characterization of Natural Gases. *AAPG Bulletin*, *67*(12), 2225–2238. Retrieved from https://vpn.uit.no/+CSCO+00756767633A2F2F6E657075766972662E716E676E636E7472662E70627A++/data/bulletns/1982-83/images/pg/00670012/2200/22250.pdf

Selby, I., & Evans, N. C. (1997). Origins of mud clasts and suspensions on the seabed in Hong Kong. *Continental Shelf Research*, *17*(1), 57–78. https://doi.org/10.1016/0278-4343(96)00018-0

Smith, M. R., & Mah, R. A. (1980). Acetate as sole carbon and energy source for growth of methanosarcina strain 227. *Applied and Environmental Microbiology*, *39*(5), 993–9. Retrieved from http://www.ncbi.nlm.nih.gov/pubmed/16345576

Steltenpohl, M. G., Andresen, A., & Tull, J. F. (1990). Lithostratigraphic correlation of the Salangen (Ofoten) and Balsfjord (Troms) Groups; evidence for the post-Finnmarkian unconformity, North Norwegian Caledonides. *Norges Geologiske Undersøkelse Bulletin*, *418*, 61–77. Retrieved from https://scholar.google.no/scholar?q=Lithostratigraphic+correlation+of+the+Salangen+%28Ofoten%29+

and+Balsfjord+%28Troms%29+Groups&btnG=&hl=no&as_sdt=0%2C5

Stolper, D. A., Lawson, M., Davis, C. L., Ferreira, A. A., Santos Neto, E. V, Ellis, G. S., … Eiler, J. M. (2014). Formation temperatures of thermogenic and biogenic methane. *Science (New York, N.Y.)*, *344*(6191), 1500–3. https://doi.org/10.1126/science.1254509

Strachan, L. J. (2002). Slump-initiated and controlled syndepositional sandstone remobilization: an example from the Namurian of County Clare, Ireland. *Sedimentology*, *49*(1), 25–41. https://doi.org/10.1046/j.1365-3091.2002.00430.x

Stuiver, M., & Reimer, P. J. (1993). A computer program for radiocarbon age calibration. Radiocarbon.

Sweeney, R. E. (1972). *Pyritization during diagenesis of marine sediments*. California, Los Angeles .

Syvitski, J., Farrow, G., Atkinson, R., & Moore, P. (1989). Baffin Island fjord macrobenthos: bottom communities and environmental significance. *Arctic*. Retrieved from http://www.jstor.org/stable/40510825

Syvitski, J. P. M. (1989). On the deposition of sediment within glacier-influenced fjords: Oceanographic controls. *Marine Geology*, *85*(2), 301–329. https://doi.org/10.1016/0025-3227(89)90158-8

Takai, Y. (1970). The mechanism of methane fermentation in flooded paddy soil. *Soil Science and Plant Nutrition*, *16*(6), 238–244. https://doi.org/10.1080/00380768.1970.10433371

Tanaka, K., Terashima, S., & Teraoka, Y. (1981). Sulfur and carbon contents of mudrocks from the Upper Cretaceous Himenoura Group, Koshikijima, Kyushy. *Geological Survey of Japan Bulletin*, *32*, 407–417.

Thomas, G. (1984). A late Devensian glaciolacustrine fan-delta at Rhosesmor, Clwyd, North Wales. *Geological Journal*, *19*(2), 125–141. Retrieved from http://onlinelibrary.wiley.com/doi/10.1002/gj.3350190204/abstract

Treude, T., Boetius, a, Knittel, K., Wallmann, K., & Barker Jørgensen, B. (2003). Anaerobic oxidation of methane above gas hydrates at Hydrate Ridge, NE Pacific Ocean. *Marine Ecology Progress Series*, *264*, 1–14. https://doi.org/10.3354/meps264001

Treude, T., & Ziebis, W. (2010). Methane oxidation in permeable sediments at hydrocarbon seeps in the Santa Barbara Channel, California. *Biogeosciences*, *7*(10), 3095–3108. https://doi.org/10.5194/bg-7-3095-2010

Trincardi, F., Cattaneo, A., Correggiari, A., & Ridente, D. (2004). Evidence of soft sediment deformation, fluid escape, sediment failure and regional weak layers within the late Quaternary mud deposits of the Adriatic Sea. *Marine Geology*, *213*(1–4), 91–119. https://doi.org/10.1016/j.margeo.2004.10.003

van der Meer, J. J. M., Kjær, K. H., Krüger, J., Rabassa, J., & Kilfeather, A. A. (2009). Under pressure : clastic dykes in glacial settings. *Quaternary Science Reviews*, *28*(7–8), 708–720. https://doi.org/10.1016/j.quascirev.2008.07.017

Volkov, I. I., & Rosanov, A. G. (1983). The sulfur cycle in the oceans. In I. I. Volkov & A. G. Rozanov (Eds.), *Scope 19* (pp. 357–447). John Wiley & Sons.

VORREN, K.-D. (1978). Late and Middle Weichselian stratigraphy of Andøya, north Norway. *Boreas*, *7*(1), 19–38. https://doi.org/10.1111/j.1502-3885.1978.tb00047.x

Vorren, T. O., Lebesbye, E., Andreassen, K., & Larsen, K.-B. (1989). Glacigenic sediments on a passive continental margin as exemplified by the Barents Sea. *Marine Geology*, *85*(2), 251–272. https://doi.org/10.1016/0025-3227(89)90156-4

Vorren, T. O., & Plassen, L. (2002). Deglaciation and palaeoclimate of the Andfjord- Vågsfjord area, North Norway. *Boreas*, *31*, 97–125. https://doi.org/10.1080/030094802320129926

Vorren, T. O., Vorren, K.-D., Alm, T., Gulliksen, S., & Løvlie, R. (2008). The last deglaciation (20,000 to 11,000 B. P.) on Andoya, northern Norway. *Boreas*, *17*(1), 41–77. https://doi.org/10.1111/j.1502-3885.1988.tb00123.x

Walker, R. (1990). Facies modeling and sequence stratigraphy: perspective. *Journal of Sedimentary Research*. Retrieved from http://archives.datapages.com/data/sepm/journals/v59-62/data/060/060005/0777.htm

Walker, R. . (1992). Facies, facies models and modern stratigraphic concepts. *Geol.Assoc.Can.St.Johns*, (1–14). Retrieved from https://scholar.google.no/scholar?q=Facies+Models%3A+Response+to+Sea+Level+Changes+Walker+and+James+1992&btnG=&hl=no&as_sdt=0%2C5

Walker, R. ., & James, N. . (1992). Facies Models: Response to Sea Level Changes. *Geol.Assoc.* , 409pp. Retrieved from https://scholar.google.no/scholar?q=Facies+Models%3A+Response+to+Sea+Level+Changes+Walker+and+James+1992&btnG=&hl=no&as_sdt=0%2C5

Walter, L. M. (1986). Relative Efficiency of Carbonate Dissolution and Precipitation During Diagenesis: A Progress Report on the Role of Solution Chemistry. *The Society of Economic Paleontologists and Mineralogists*, *83*(Roles of Organic Matter in Sediment Diagenesis). Retrieved from https://vpn.uit.no/+CSCO+0h756767633A2F2F6E657075766972662E716E676E636E7472662E70627A++/data/sepm_sp/SP38/Relative_Efficiency_of_Carbonate_Dissolution.htm

Whiticar, M. ., Faber, E., & Schoell, M. (1986). Biogenic methane formation in marine and freshwater environments: CO2 reduction vs. acetate fermentation—Isotope evidence. *Geochimica et Cosmochimica Acta*, *50*(5), 693–709. https://doi.org/10.1016/0016-7037(86)90346-7

Winfrey, M. R., & Zeikus, J. G. (1977). Effect of sulfate on carbon and electron flow during microbial methanogenesis in freshwater sediments. *Applied and Environmental Microbiology*, *33*(2), 275–81. Retrieved from http://www.ncbi.nlm.nih.gov/pubmed/848951

Wohlfarth, B., Björck, S., Funder, S., Houmark-nielsen, M., Ingolfsson, O., Lunkka, J.-P., … Vorren, T. (2007). Quaternary of Norden. *Episodes*, *31*(1), 73–81.

Yoshimura, K., Nakao, S., Noto, M., Inokura, Y., Urata, K., Chen, M., & Lin, P. W. (2001). Geochemical and stable isotope studies on natural water in the Taroko Gorge karst area, Taiwan- Chemical weathering of carbonate rocks by deep source CO2 and sulfuric acid. *Chemical Geology*, *177*(3–4), 415–430. https://doi.org/10.1016/S0009-2541(00)00423-X

Appendix A: Flocculation

Table A 1. The table displays the different samples introduced to either 0,5 or 1 gram NaCl. The X marks how much NaCl that were added to each sample. The sample name without any letter behind it means, all of the samples from that particular height (A,B,C,D etc.).

Samples introduced	to NaCl	
Sample name	0,5g NaCl	1,0g NaCl
4,87m A	X	
4,87m B	X	
5,025m A		X
12,92m A		X
2,54m		X
12,93m		X
4,87m		X
12,93m		X
5,024m		X
14,29m		X
6,35m		X

Appendix B: Maximum pebble size

Table A 2. The Maximum pebble size (MPS) values, the mean MPS, with layer thickness and the height at which they occur in the vertical profile.

Layer	Height	Thickness		Maximum	pebble	size									Mean MPS
L 12	1,74-1,83m	9	cm	7	8	6	7	5,5		5	4,5	4	4	3,1	5,41
L 24	3.04-3,20m	16	cm	3,5	1,5	2	1	1,2		2	1	3	1	2	1,82
L 31 & 32	3,88-3,92m	4	cm	5,5	5	3,5	3,6	3,3		4	4	3,4	3	3,5	3,88
L 59	6,16-6,34m	18	cm	2,1	3	3	2,6	3,4		4,1	2,3	1,7	9	3,3	3,45
L 74 & 75	8,39-8,495m	10,5	cm	8,1	4,5	3,6	2,9	4,9		4	3,1	3,6	2,8	2,7	4,02
L 76	8,495-8,985m	49	cm	11	5,6	4,8	6	4,8		7	5,1	7,5	5,9	5,2	6,29
L 77	8,985-9,095m	11	cm	5	3,5	4,4	4,8	3,7		4	4,5	2,5	2,7	2,3	3,74
L 78	9,095-9,265m	17	cm	3,5	1,7	2,8	5,1	1,8		3,7	2,4	2,3	1,1	1,2	2,56

L 79	9,265-9,8m	53,5	cm	1,5	1,7	1,4	2	0,9		1,3	1,6	2,1	1	0,7	1,42
L 80	9,95-11,67m	172	cm	6,7	4	2,5	9	2,9		6	3	3,7	5	2	4,48
L 89	15,5-15,88m	38	cm	3,5	2,5	2,2	1,7	1,6		1,5	2,4	1,5	1,3	2	2,02
L 91	15,88-16,54m	52	cm	2,7	2,6	3	3	2,35		4,1	2,75	2,5	2,7	3,5	2,92
L 93	16,6-17,26m	66	cm	8,2	7,2	6,5	6,7	6		6	5,5	5,4	5	5	6,15
l 94	17,26-17,52m	26	cm	11	4	6	4,1	4,9		10	6,5	5,9	4	4,5	6,09
L 97	17,71-17,82m	11	cm	3,6	4,5	4	5	3,9		4,1	4,3	4,1	4,35	3	4,085
L 98 & 99	17,82-19,49m	167	cm	4,6	4	4,3	3,7	3,7		5	4,2	4	3,8	3,6	4,09
L 104	24,38-25,38m	100	cm	4,5	3	4	5	6		4,9	3,4	8	5	4	4,78
L 105	25,38-26m	62	cm	4,2	3,3	2,5	2,5	2		3,5	2,4	3	2,6	3,1	2,91
L 107	26,48-27m	52	cm	10	2,3	1,9	4,2	2,4		2,5	2,6	4,3	3,3	2,9	3,64
L 109	27,29-28,26m	97	cm	2,1	1,9	1,6	1,2	1,7		2	2,1	1,75	1,4	1,65	1,74

L 110	28,26-28,63m	37	cm	1	0,8	1,2	1,3	1,1		0,9	1,3	1,8	1	0,9	1,13
L 111	28,63-28,72m	9	cm	3,1	2,4	4,5	2,8	3,3		2,5	6	5,5	4	3,2	3,73
L 112	28,72-28,84m	12	cm	1,6	1,8	2,7	2,5	1,6		2	6	1,7	2,2	1,5	2,36
L 113	28,84-29,2m	36	cm	11	11,5	7,6	6,7	7,2		12,5	7	7	6,3	8	8,48
L 114	29,2-30,3m	110	cm	5,3	2,6	2,5	2,9	2		2,9	4,5	2	1,5	2,3	2,85
L 115	30,3-30,4m	10	cm	10	6	4,3	5,7	5		9	6,1	4	4,8	6,5	6,14
L 116	30,4-30,75m	35	cm	4	3,3	2	2,7	2,75		3,5	3,2	3,1	3,5	3	3,105
L 117	30,75-31,5m	75	cm	6	5,4	4,5	5,8	3,5		10	4	5,5	3,3	3	5,1
L 118	31,5-32,75m	125	cm	2,8	2,6	2,5	2,4	2,4		2,2	1,9	2	2	1,8	2,26
L 119	32,75-33m	25	cm	2,5	0,7	2	1,4	1,7		2,4	0,5	1,3	0,7	2,2	1,54
L 120	33-34,8m	180	cm	1,8	2,1	1,65	1,8	1,6		1,7	1,6	1,3	1,4	1,75	1,67

Appendix C: Combustion analysis

Table A 3. The name of the sample that was placed into the Retsch AS 200 basic for crushing. The "Number" column indicates the name of the metal bowls. The" Weigth" column indicate how much of the selected samples that were extracted for total organic and sulfur analyze.

Leco analysis		
Name	**Number**	**Weight**
1,02m	A3	0,4818g
1,99m	H6	0,4564g
1,99m	H1	0,4625g
2,785m	H1	0,4337g
2,93m	H3	0,4816g
3,2m	H2	0,4858g
4,31m	A6	0,4861g
4,51m	H7	0,4996g
4,91m	A5	0,4658g
6,35m	A7	0,4771g
7,265m	B7	0,4871g
14,29m	H5	0,4765g
15,6m	A2	0,4164g
16,51m	B1	0,4800g
17,59m	B0	0,4751g

Table A 4. Simplified results from the Leco analysis of crushed sample material from Table A3. The carbon (TC) and sulfur (TS) is displayed in both mass and percentage.

Name	Carbon mass (g)	Sulfur mass (g)	Carbon % (TC)	Sulfur % (TS)	$C[CO_2]$ (%)	$C[CaCO_3]$ (%)
1,02m	0,002256	0,0000794	0,917	0,032275	3,36	7,64
1,99m	0,001912	0,000066	0,8495	0,029305	3,11	7,08
2,785m	0,003066	0,0000676	1,315	0,02899	4,82	11
2,93m	0,0021	0,0000907	0,9031	0,039015	3,31	7,53
3,2m	0,001671	0,0000868	0,7457	0,038754	2,73	6,21
4,31m	0,001955	0,0000231	0,8385	0,0099091	3,07	6,99
4,51m	0,00182	0,0000529	0,7816	0,022717	2,86	6,51
4,91m	0,001617	0,0000372	0,7305	0,016797	2,68	6,09
6,35m	0,002319	0,0000213	1,042	0,0095835	3,82	8,68
7,255m	0,001861	0,0000464	0,8305	0,020688	3,04	6,92
14,29m	0,001686	0,0000693	0,7469	0,030682	2,74	6,22
15,6m	0,001674	0,0000458	0,7041	0,019289	2,58	5,87
16,51m	0,002345	0,0000338	1,003	0,014464	3,67	8,36
17,59m	0,001564	0,0000595	0,6432	0,024492	2,36	5,36

Table A 5. Simplified result of analyze of the sample material from Table A3 prepared with warm 0,1M HCl.

Name	Carbon mass (g)	Sulfur mass (g)	Carbon % (TOC)	Sulfur %	$C[CO_2]$ (%)	$C[CaCO_3]$ (%) (TS)
1,02m	0,0003826	0,0000968	0,0794	0,020082	0,291	0,662
1,99m	0,0002849	0,0000784	0,06243	0,017176	0,229	0,52
2,785m	0,0002951	0,0000869	0,06804	0,020027	0,249	0,567
2,93m	0,0004756	0,0000919	0,09876	0,019082	0,362	0,823
3,2m	0,0005189	0,000122	0,1068	0,025081	0,391	0,89
4,31m	0,0002306	0,0000501	0,04745	0,010297	0,174	0,395
4,51m	0,0003259	0,0000788	0,06523	0,01577	0,239	0,544
4,91m	0,0004572	0,000219	0,09815	0,047017	0,36	0,818
6,35m	0,0002952	0,0000557	0,06188	0,011671	0,227	0,516
7,255m	0,0001998	0,000046	0,04103	0,0094435	0,15	0,342
14,29m	0,0003661	0,0000915	0,07683	0,019199	0,282	0,64
15,6m	0,0002478	0,0000674	0,05978	0,01626	0,219	0,498

16,51m	0,0002759	0,0000724	0,05748	0,015074	0,211	0,479
17,59m	0,0003365	0,0000575	0,07083	0,012108	0,26	0,59

Table A 6. The results from the LECO analysis of the prepared samples. The name of the samples analyzed is listed in meters

Name	Sample	Method		Carbon Avg. (%)	Sulfur Avg. (%)										
MATS	name	Tromso	#####	0.86075	0.02407										
Sample Mass (g)	in (m)	Operator		Carbon (%)	Sulfur (%)	Carbon Mass (g)	Carbon Adjusted Area	Carbon Peak Height	Carbon Raw Area	Sulfur Mass (g)	Sulfur Adjusted Area	Sulfur Peak Height	Sulfur Raw Area	$C[CO_2]$ (%) (TOC)	$C[CaCO_3]$ (%)
0,2214	4,51		#####	0,7305	0,016797	0,001617	0,00166	34,8	771	0,0000372	0,0000328	0,598	64,9	2,68	6,09
0,2377	15,6		#####	0,7041	0,019289	0,001674	0,00171	22,4	797	0,0000458	0,0000404	0,727	73,7	2,58	5,87
0,2331	2,785		#####	1,315	0,02899	0,003066	0,00314	50	1440	0,0000676	0,0000596	1,59	95,9	4,82	11
0,2257	14,29		#####	0,7469	0,030682	0,001686	0,00173	21,6	803	0,0000693	0,0000611	1,22	97,6	2,74	6,22
0,2328	4,51		#####	0,7816	0,022717	0,00182	0,00186	20,8	864	0,0000529	0,0000467	1,04	80,9	2,86	6,51
0,2251	1,99		#####	0,8495	0,029305	0,001912	0,00196	20,8	907	0,000066	0,0000582	1,11	94,2	3,11	7,08
0,246	1,02		#####	0,917	0,032275	0,002256	0,00231	24,7	1070	0,0000794	0,00007	1,24	108	3,36	7,64
0,2241	3,2		#####	0,7457	0,038754	0,001671	0,00171	21,9	796	0,0000868	0,0000766	1,44	115	2,73	6,21
0,2325	2,93		#####	0,9031	0,039015	0,0021	0,00215	29,1	994	0,0000907	0,00008	1,76	119	3,31	7,53
0,2431	17,59		#####	0,6432	0,024492	0,001564	0,0016	18,3	746	0,0000595	0,0000525	0,91	87,7	2,36	5,36
0,2225	6,35		#####	1,042	0,009584	0,002319	0,00237	25,5	1100	0,0000213	0,0000188	0,542	48,8	3,82	8,68
0,2241	7,265		#####	0,8305	0,020688	0,001861	0,00191	26,8	884	0,0000464	0,0000409	1,19	74,3	3,04	6,92
0,2332	4,31		#####	0,8385	0,009909	0,001955	0,002	18,9	927	0,0000231	0,0000204	0,553	50,6	3,07	6,99
0,2339	16,51		#####	1,003	0,014464	0,002345	0,0024	31,7	1110	0,0000338	0,0000298	0,752	61,5	3,67	8,36
				43,48990891	43,46774										
Name	Sample	Method		Carbon Avg. (%)	Sulfur Avg. (%)										
MATS	name	Tromso	#####	0.071008	0.01845										
Sample Mass (g)	in (m)	Operator		Carbon (%)	Sulfur (%)	Carbon Mass (g)	Carbon Adjusted Area	Carbon Peak Height	Carbon Raw Area	Sulfur Mass (g)	Sulfur Adjusted Area	Sulfur Peak Height	Sulfur Raw Area	$C[CO_2]$ (%)	$C[CaCO_3]$ (%)
0,4658	4,51		#####	0,09815	0,047017	0,0004572	0,000468	4,7	234	0,000219	0,000193	5,02	250	0,36	0,818
0,4146	15,6		#####	0,05978	0,01626	0,0002478	0,000254	2,96	138	0,0000674	0,0000595	0,898	95,7	0,219	0,498
0,4337	2,785		#####	0,06804	0,020027	0,0002951	0,000302	4,29	160	0,0000869	0,0000766	1,22	116	0,249	0,567
0,4765	14,29		#####	0,07683	0,019199	0,0003661	0,000375	4,44	192	0,0000915	0,0000807	1,07	120	0,282	0,64
0,4996	4,51		#####	0,06523	0,01577	0,0003259	0,000334	3,04	174	0,0000788	0,0000695	1,15	107	0,239	0,544
0,4564	1,99		#####	0,06243	0,017176	0,0002849	0,000292	4,18	155	0,0000784	0,0000691	1,27	107	0,229	0,52
0,4818	1,02		#####	0,0794	0,020082	0,0003826	0,000392	5,99	200	0,0000968	0,0000853	1,83	126	0,291	0,662
0,48	16,51		#####	0,05748	0,015074	0,0002759	0,000282	4,11	151	0,0000724	0,0000638	1,2	101	0,211	0,479
0,4858	3,2		#####	0,1068	0,025081	0,0005189	0,000531	6,8	263	0,000122	0,000107	2,21	151	0,391	0,89
0,4816	2,93		#####	0,09876	0,019082	0,0004756	0,000487	7,17	243	0,0000919	0,0000811	2,09	121	0,362	0,823
0,4751	17,59		#####	0,07083	0,012108	0,0003365	0,000344	4,51	179	0,0000575	0,0000507	0,811	85,6	0,26	0,59
0,4771	6,35		#####	0,06188	0,011671	0,0002952	0,000302	3,81	160	0,0000557	0,0000491	0,869	83,8	0,227	0,516
0,4871	7,255		#####	0,04103	0,009444	0,0001998	0,000205	2,74	115	0,000046	0,0000406	0,747	73,9	0,15	0,342
0,4861	4,31		#####	0,04745	0,010297	0,0002306	0,000236	2,51	130	0,0000501	0,0000442	0,786	78	0,174	0,395

Appendix D: Thin sections

Table A 7. Table over the chosen carbonates for production of thin sections. The name of each carbonate is given in meters (m). The numbers are the name of the constructed thin sections.

Thin sections	
Number	Name (m)
1	1,55
2	7,21
3	11,22
4	13,98
5	13,85-87
6	15,05
7	0,565
8	0,43
9	0,19
10	17,43
11	15,66

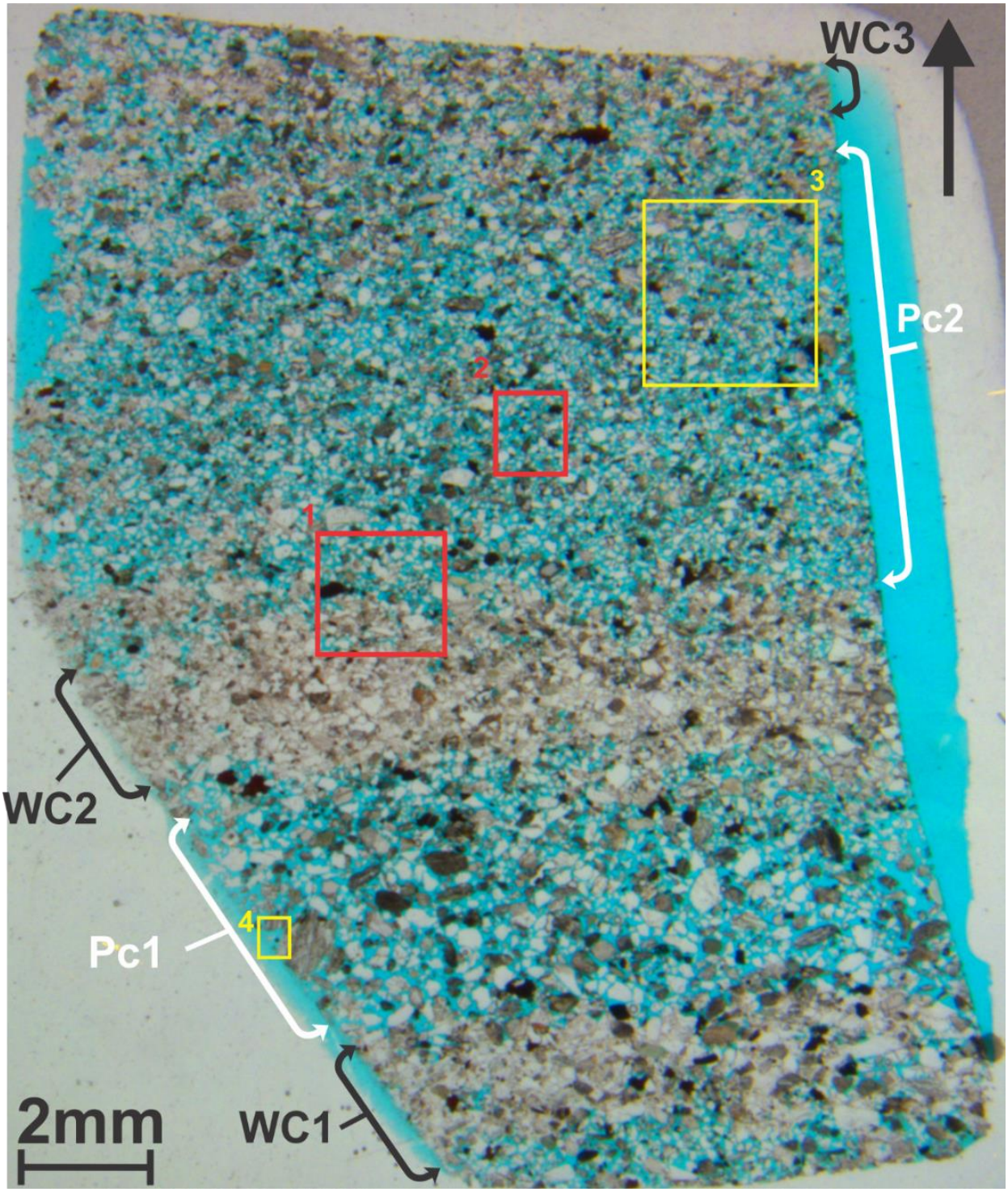

Fig. A 1. Thin section 1 from 1,55m in the vertical profile. The light brownish horizontal section represents well- cemented laminas (WC), where the areas in between are poorly cemented (Pc). The red rectangle 1 represents Fig. 34 C and D and rectangle 2 represents Fig. 34 E and F. The yellow rectangle 3 and 4 show the location of Fig. A 2 A and B. The arrow marks the uppermost surface of the thin section and the orientations of all the rectangles.

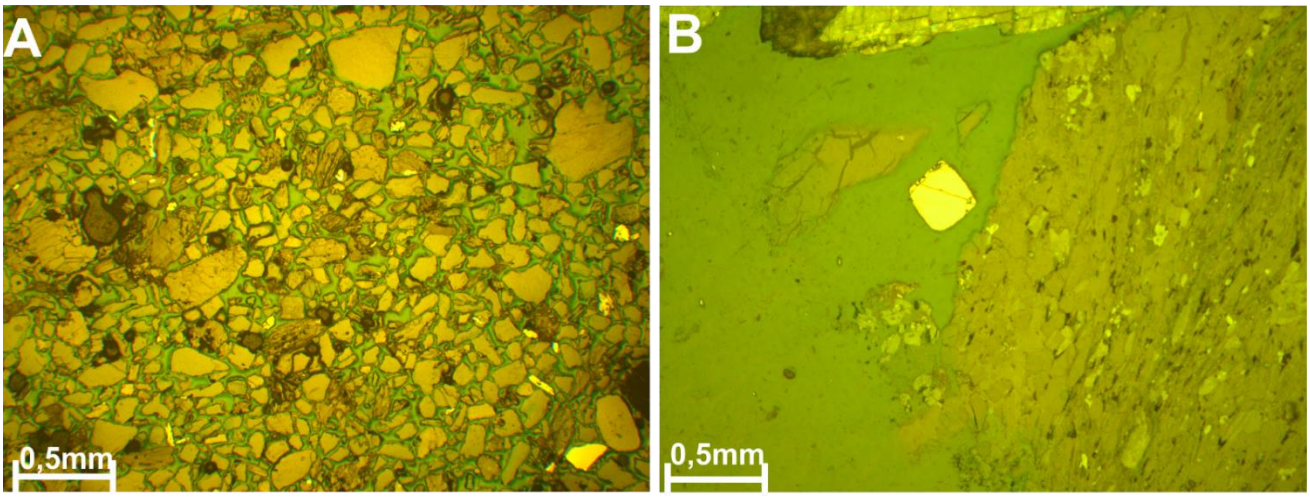

Fig. A 2. (A) The general poor-very poor content of pyrite crystals in the thin section 1 (Fig. A 1), indicated by distinct yellow color. (B) The most complete crystal structure of the appearing pyrite in thin section 1. Both pictures are taken with incident light.

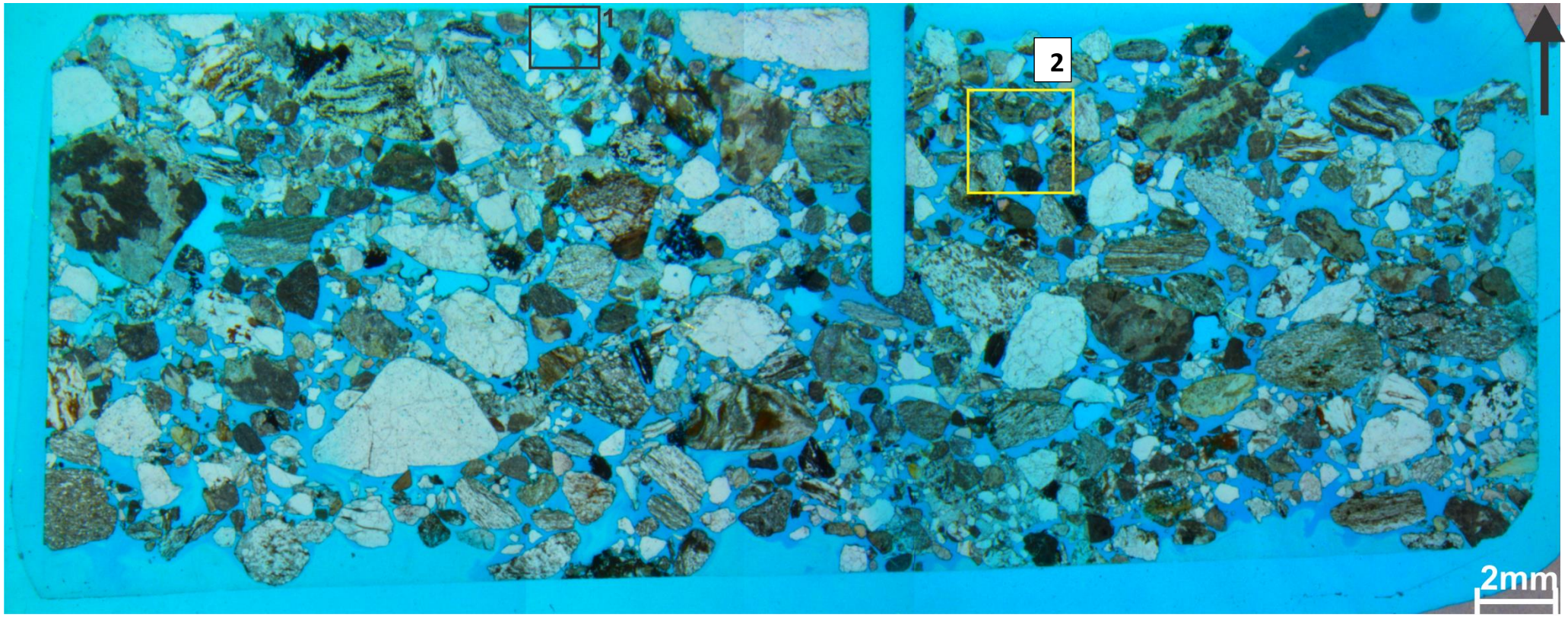

Fig. A 3. Thin section 2 from 7,21m in the vertical profile. The section is poorly-moderate cemented, where the finer grains tend to be cemented on top of the bigger clasts. The yellow square, 2, represents the location of Fig. A 4, the general occurrence of pyrite in the thin section. The black square 1 represents Fig. 34 A and B, and the black arrow indicate the uppermost surface of the thin section and the orientation of Fig. 34 and Fig. A 4.

Fig. A 4. The general picture of the pyrite occurrence in thin section 2, where the pyrite in the grains are the dominant ones, whereas the pyrite in pore spaces are very poor. The pyrite is indicated by distinct yellow color. The figure located on Fig. A 3, marked by a yellow rectangle. The picture is taken in incident light.

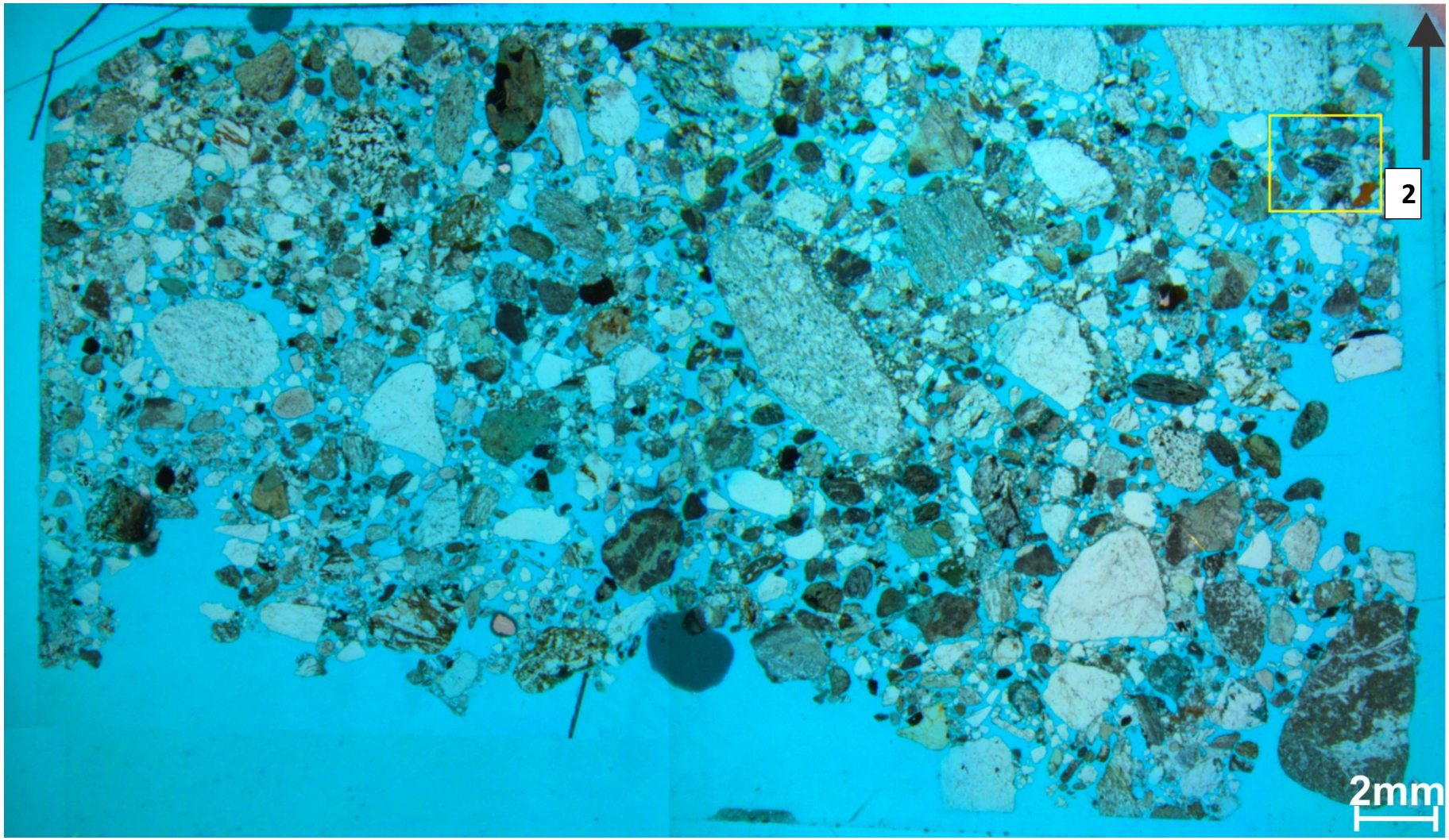

Fig. A 5. Thin section 3 from 11,22m in the vertical profile. The cementation is poor-moderate, where the most cementation is located on upper surface of the bigger clasts. The yellow square, 2, represent Fig. A 6. The black arrow marks the uppermost side of the thin section and the orientation of Fig. A 6 .

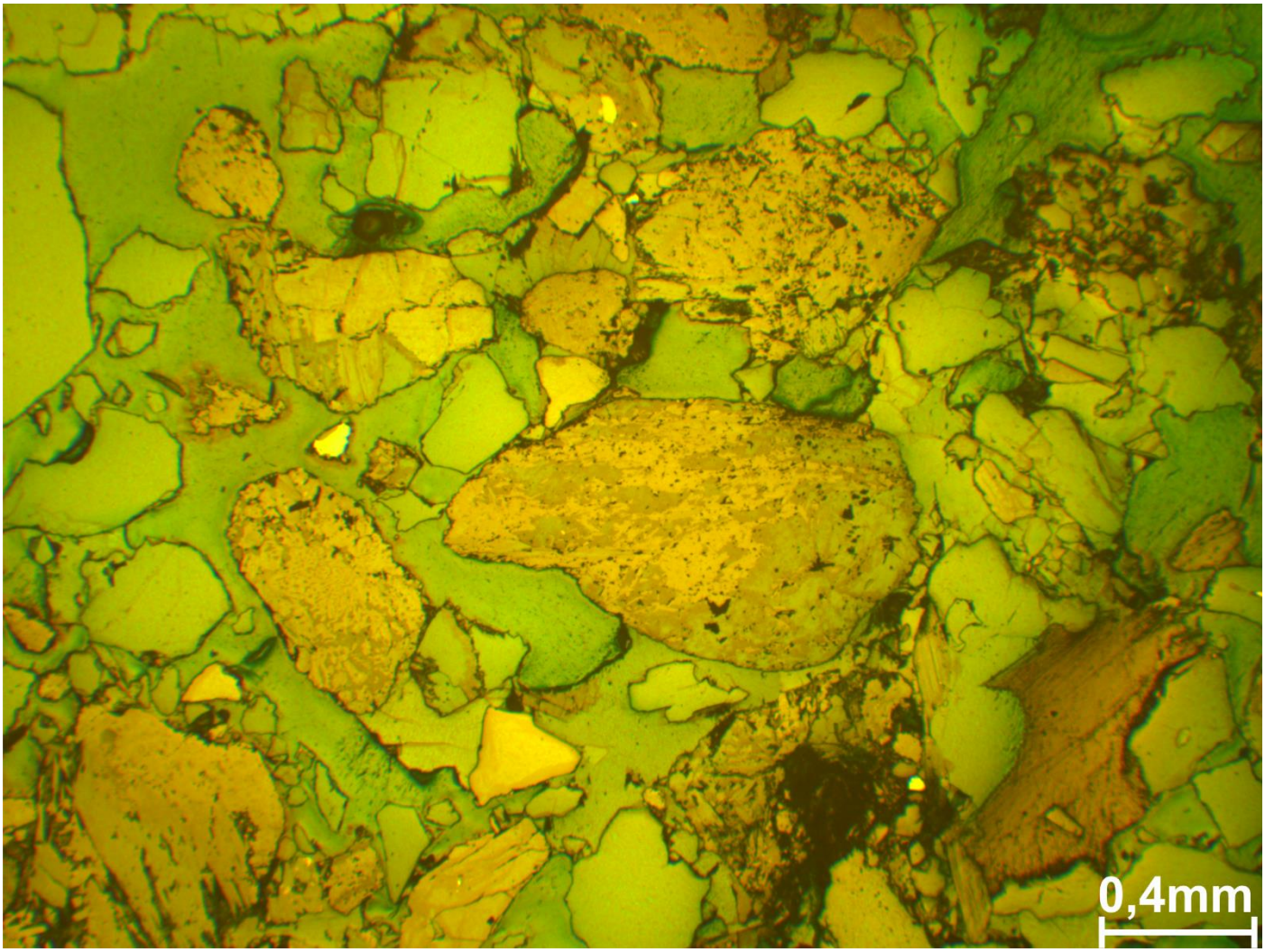

Fig. A 6. The general occurrence of pyrite in thin section 3 (Fig. A 5). The pyrite concentration is generally low and is occurring separately from the carbonate cement. The pyrite is indicated by a distinct yellow color and the picture is taken with incident light.

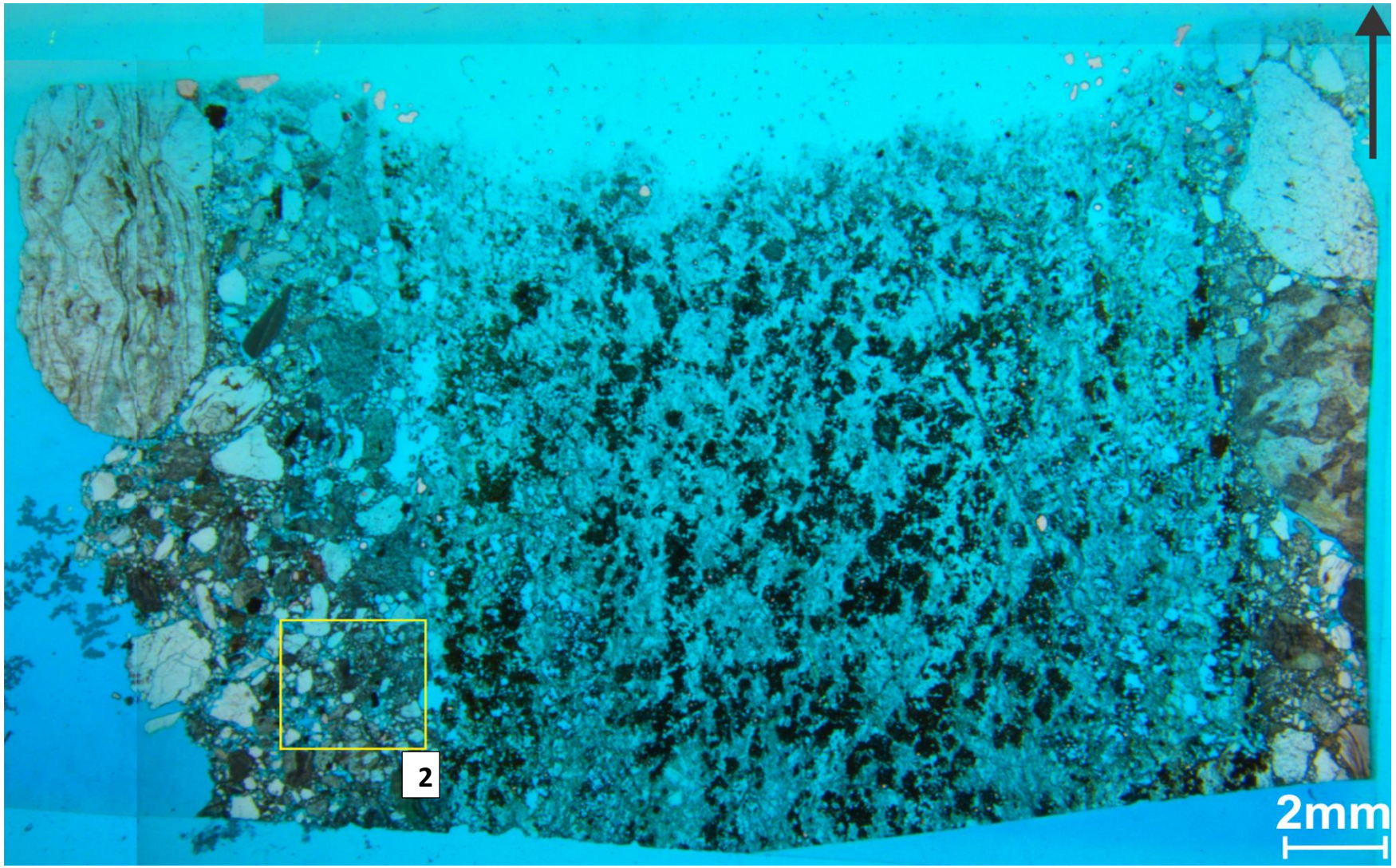

Fig. A 7. Thin section 4 from 13,98m in vertical profile. The section consists of one big clasts in the middle, with cemented areas on the left and right side of the thin section. The cementation occurs as well-cemented. The yellow square, 2, represent Fig. A 8 and the black arrow indicates the upper surface of the thin section and the orientation of Fig. A 8.

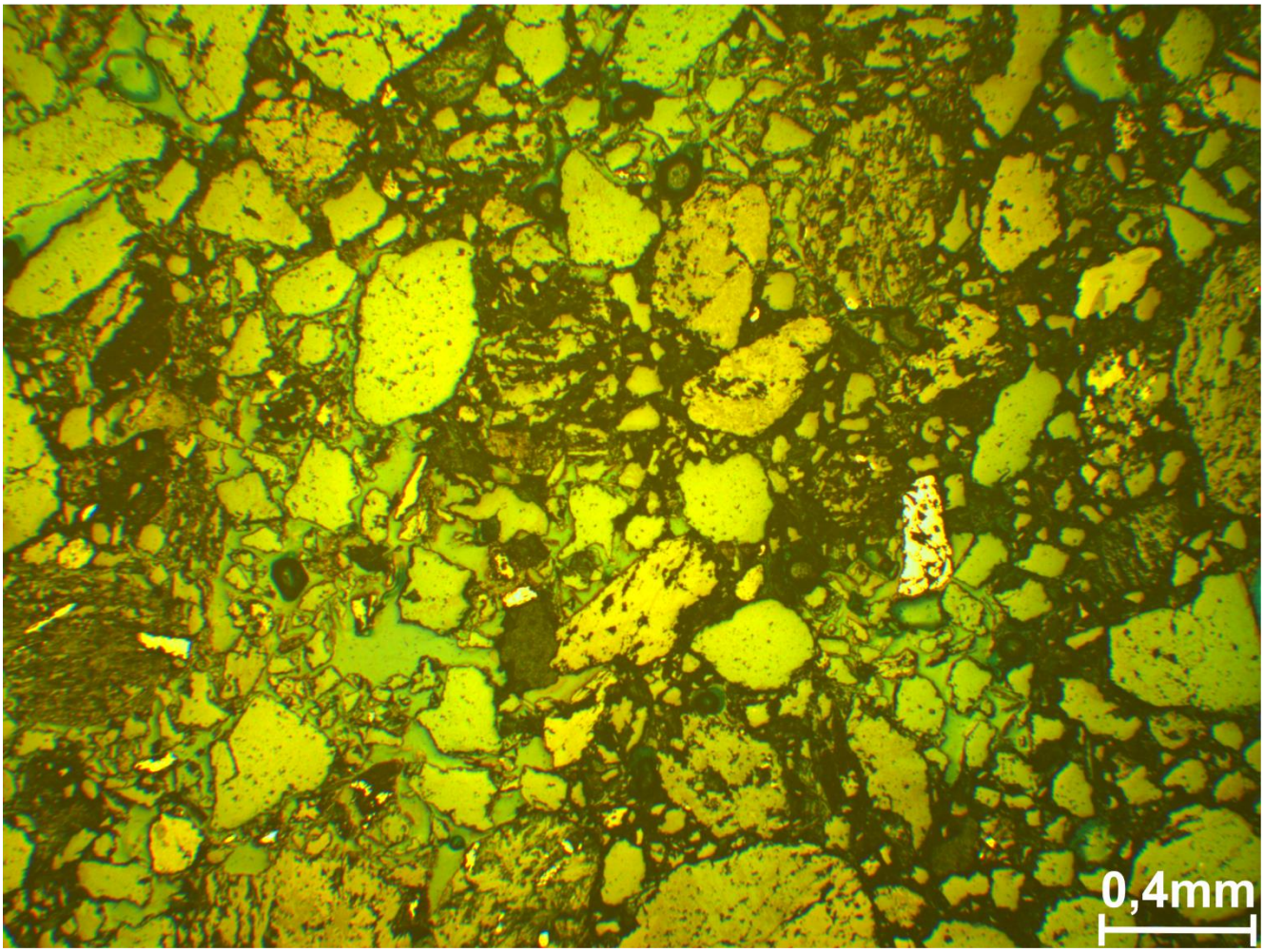

Fig. A 8. The general overview of the pyrite content of thin section 4, represented by the yellow square in Fig. A 9. The pyrite content is poor and occur both inside and adjacent to the carbonate cement. The pyrite is indicated by distinct yellow color and the picture is taken in incident light.

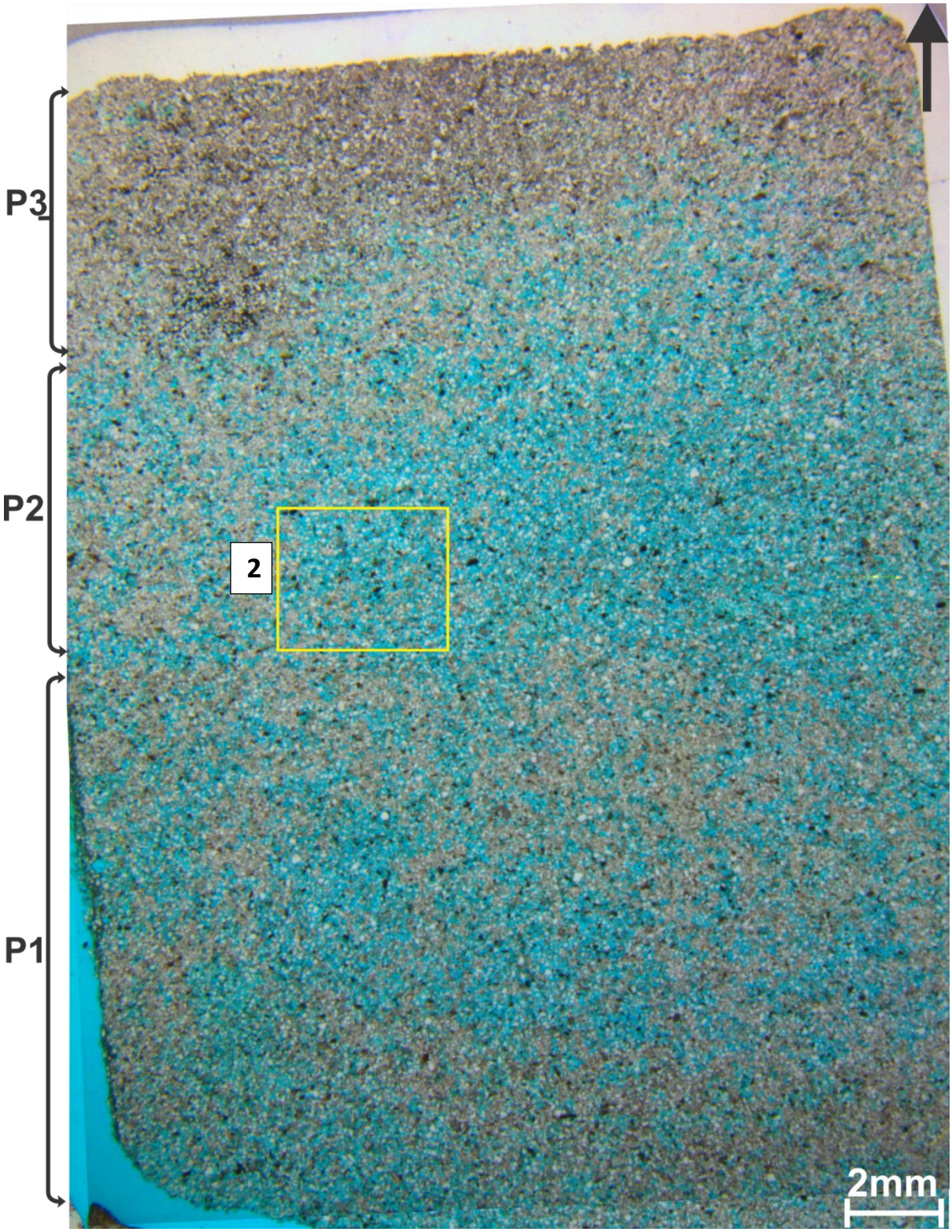

Fig. A 9.Thin section 5 from 13,85-13,87m in the vertical profile. The thin section is divided into three parts marked with P1-P3 based on amount of cementation. The P1 represent very well cemented area, P2 is the least cemented area, where most of the area is poorly cemented. P2 display occurrence of vertical cementation (Fig. 38). The P3 represent a medium-poor cemented area, where the cementation trend is both vertical and horizontal. The vertical cemented areas represent the least cemented areas. The yellow square, 2, marks the location of Fig. A 10 and the black arrow marks the uppermost surface of the section and the orientation of Fig. A 10 .

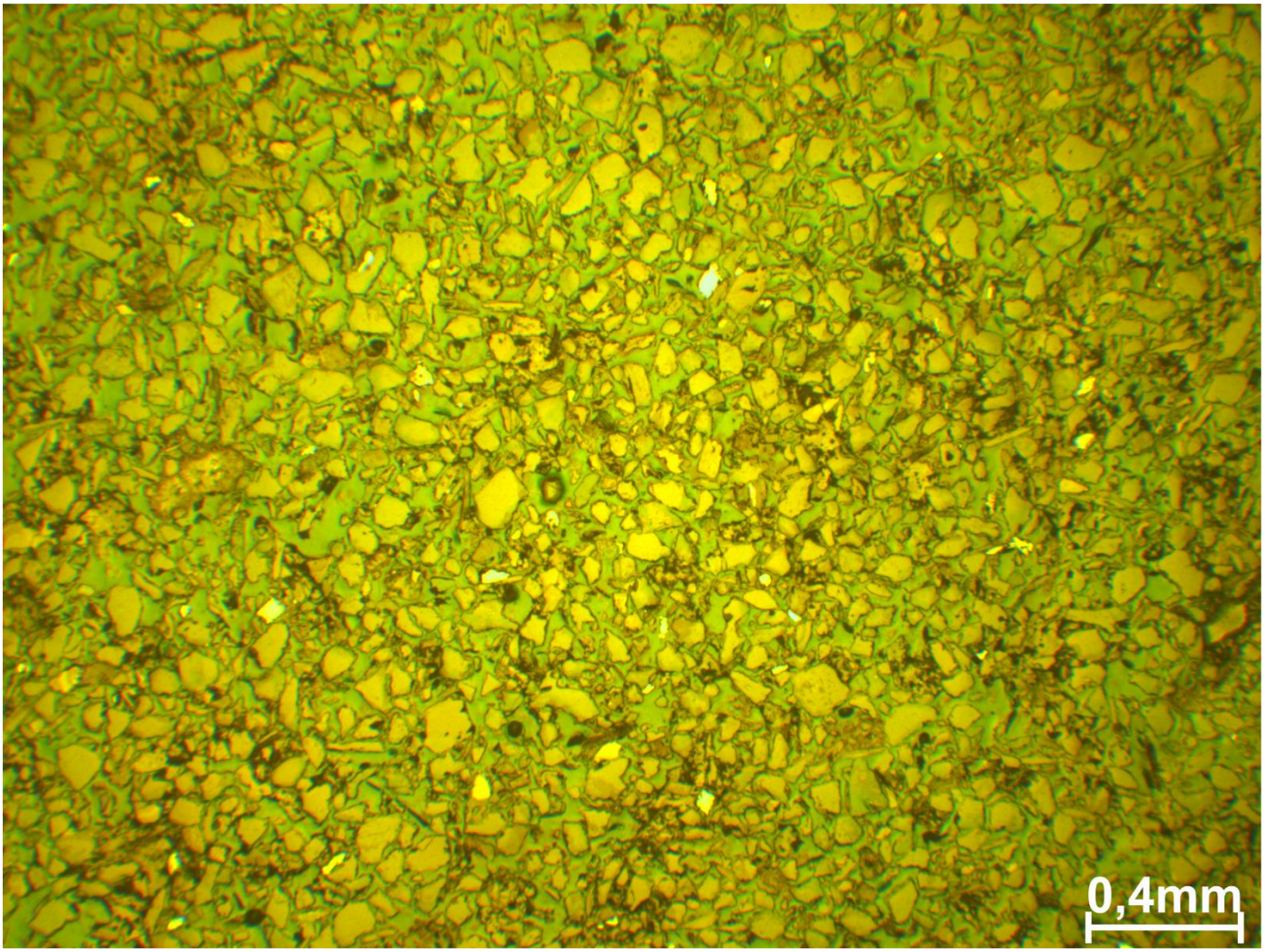

Fig. A 10. The general overview of the pyrite content of thin section 5 (Fig. A 9), located by the yellow square. The pyrite content is intermediated and occur scattered inside carbonate cement, adjacent to carbonate cement and undisturbed by the carbonate cement. The distinct yellow color marks the pyrite crystals, where the picture is taken in incident light.

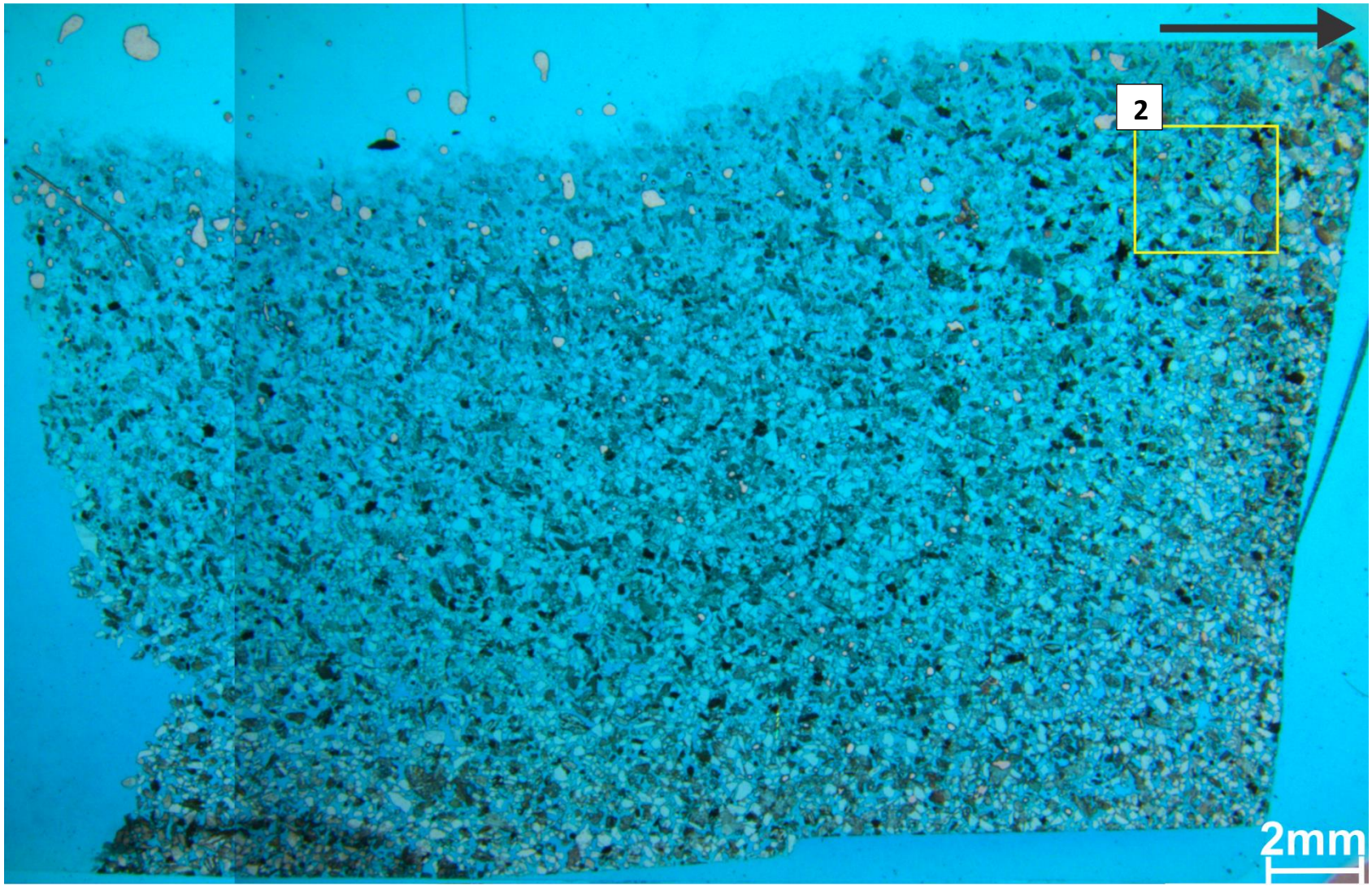

Fig. A 11. Thin section 6, from 15,05m in the vertical profile. The thin section is generally poorly cemented. The yellow square, 2, represents Fig. A 12 and the black arrow indicate the upper surface of the section and the orientation of Fig. A 12.

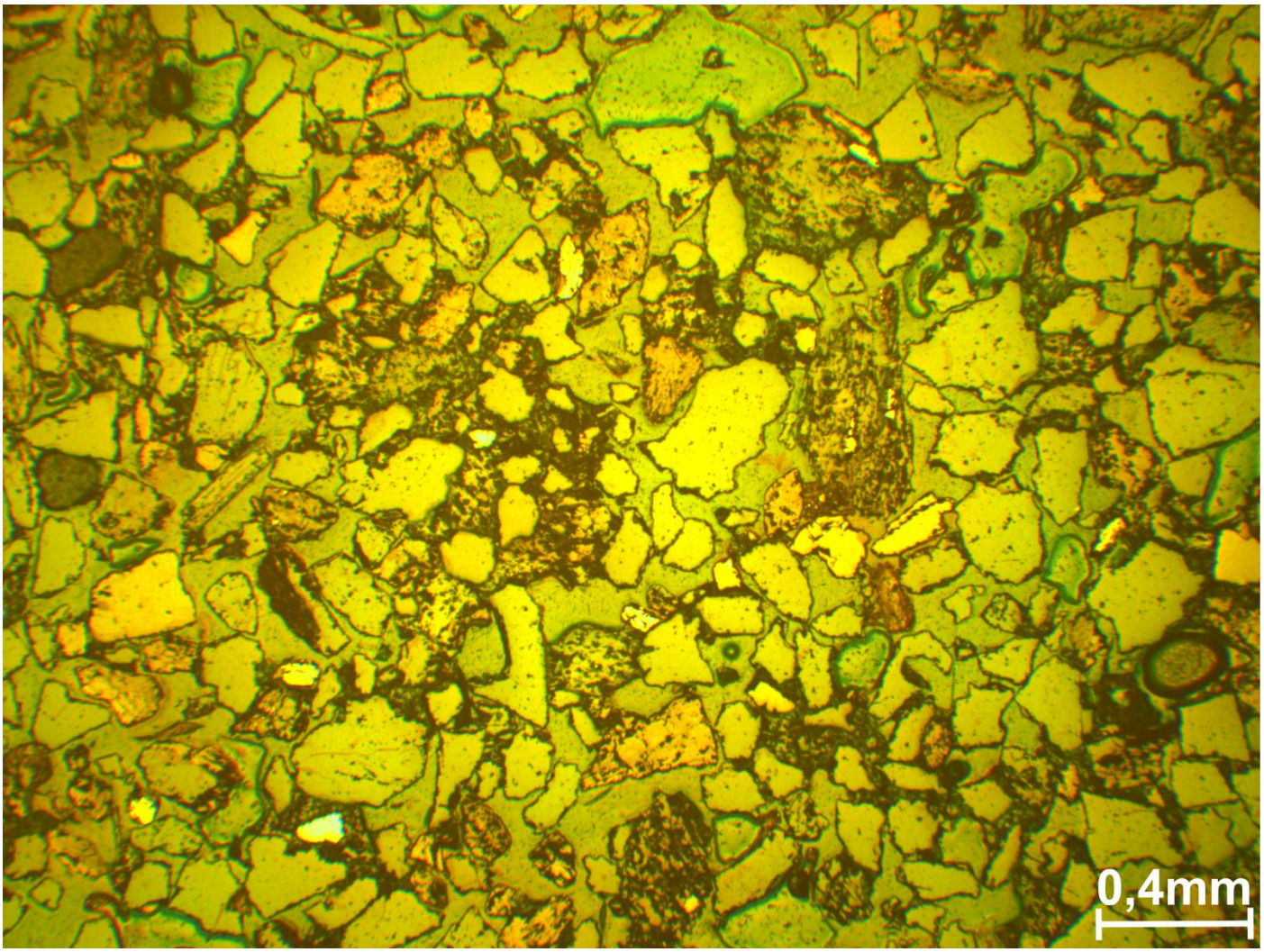

Fig. A 12. Pyrite content general overview in thin section 6, located in Fig. A 11 by a yellow square. The pyrite content is poor-intermediate, where the pyrite generally occurs inside the carbonate cement. The pyrite is indicated by distinct yellow color, where the picture is taken in incident light.

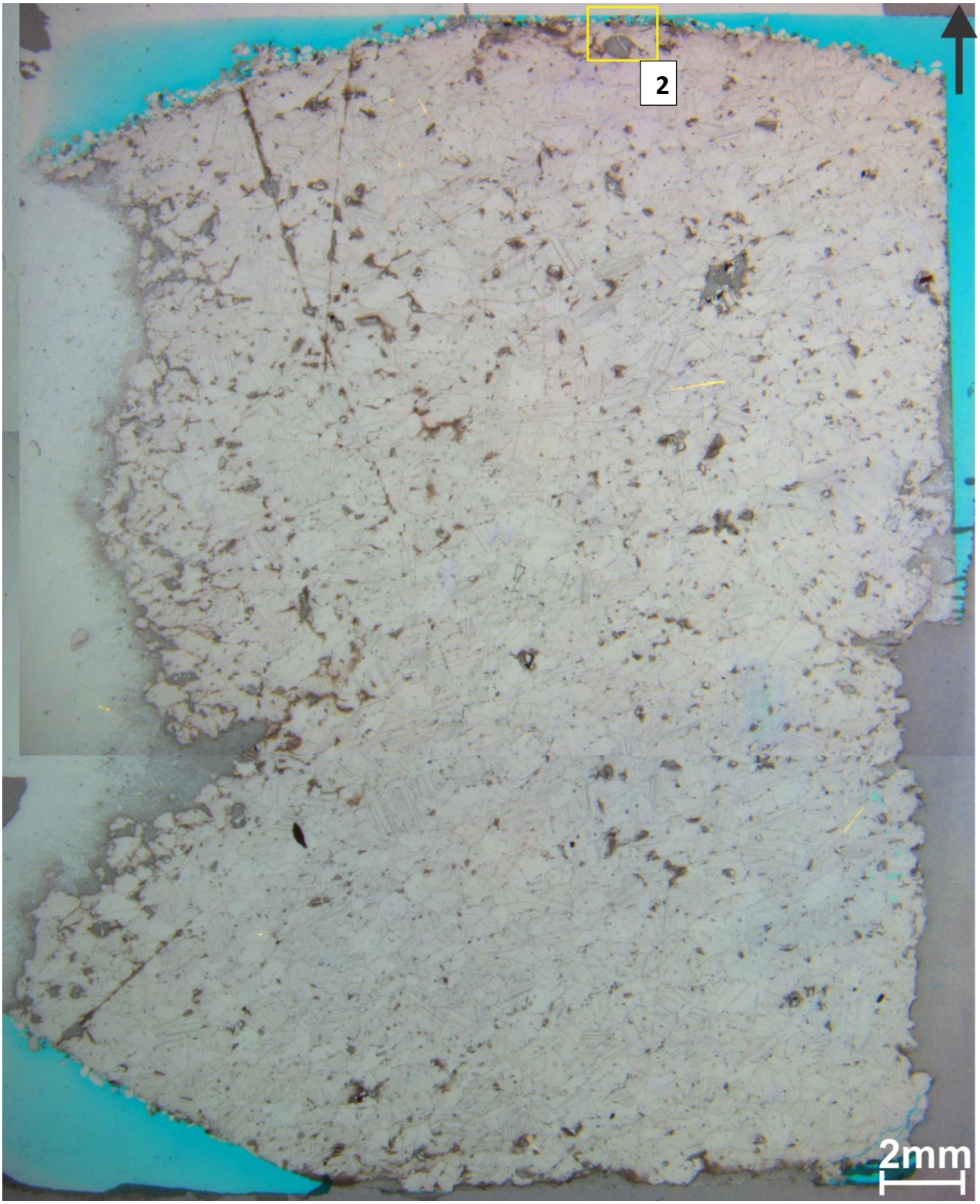

Fig. A 13. Thin section 7, from 0,565m in the vertical profile. The thin section mainly consists of one big clasts, with fine grains cemented on the upper and lower surface. The yellow rectangle, 2, represent Fig. A 14 and the black arrow indicate the upper surface of thin section 7 and the orientation of Fig. A 14.

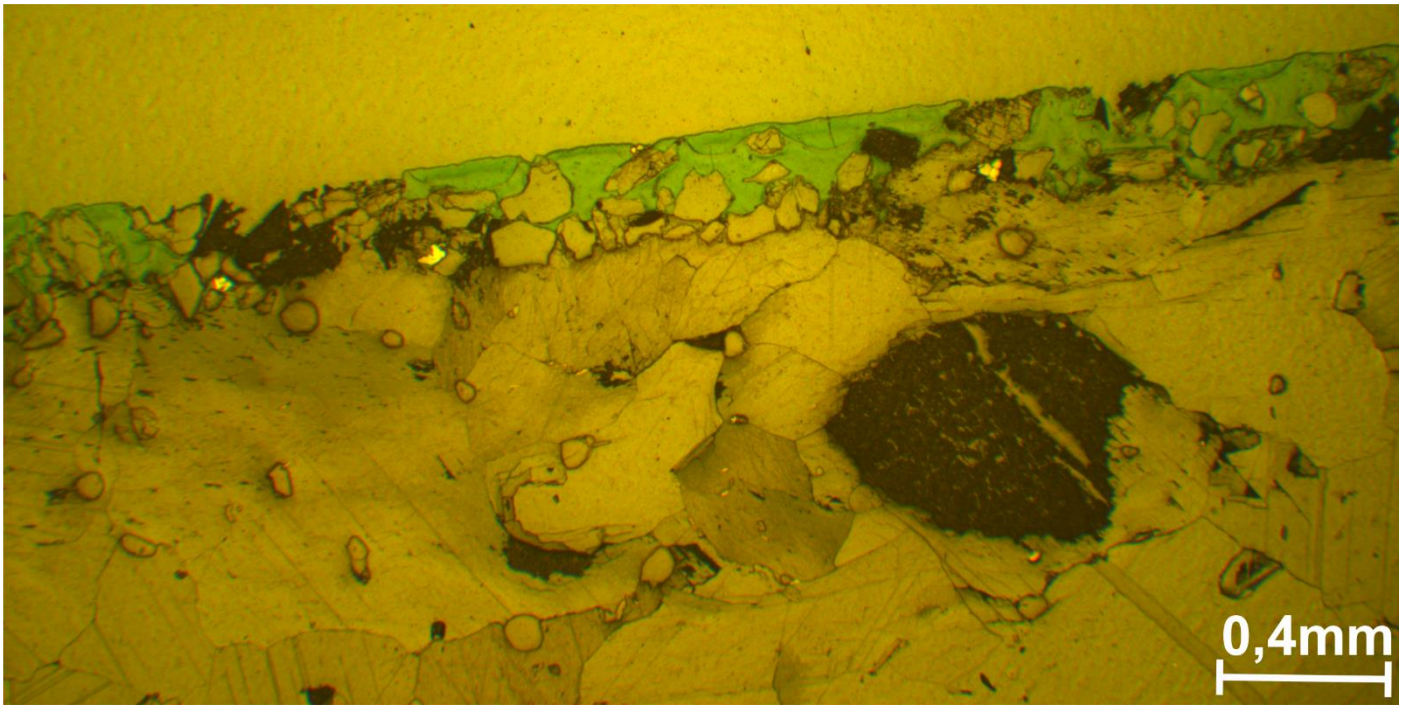

Fig. A 14. The general overview of the pyrite content in thin section 7, located on Fig. A 13 by yellow rectangle. The pyrite occurs scarce, scattered and both inside the carbonate cement and adjacent to it. The pyrite is indicated by distinct yellow color and the picture is taken in incident light.

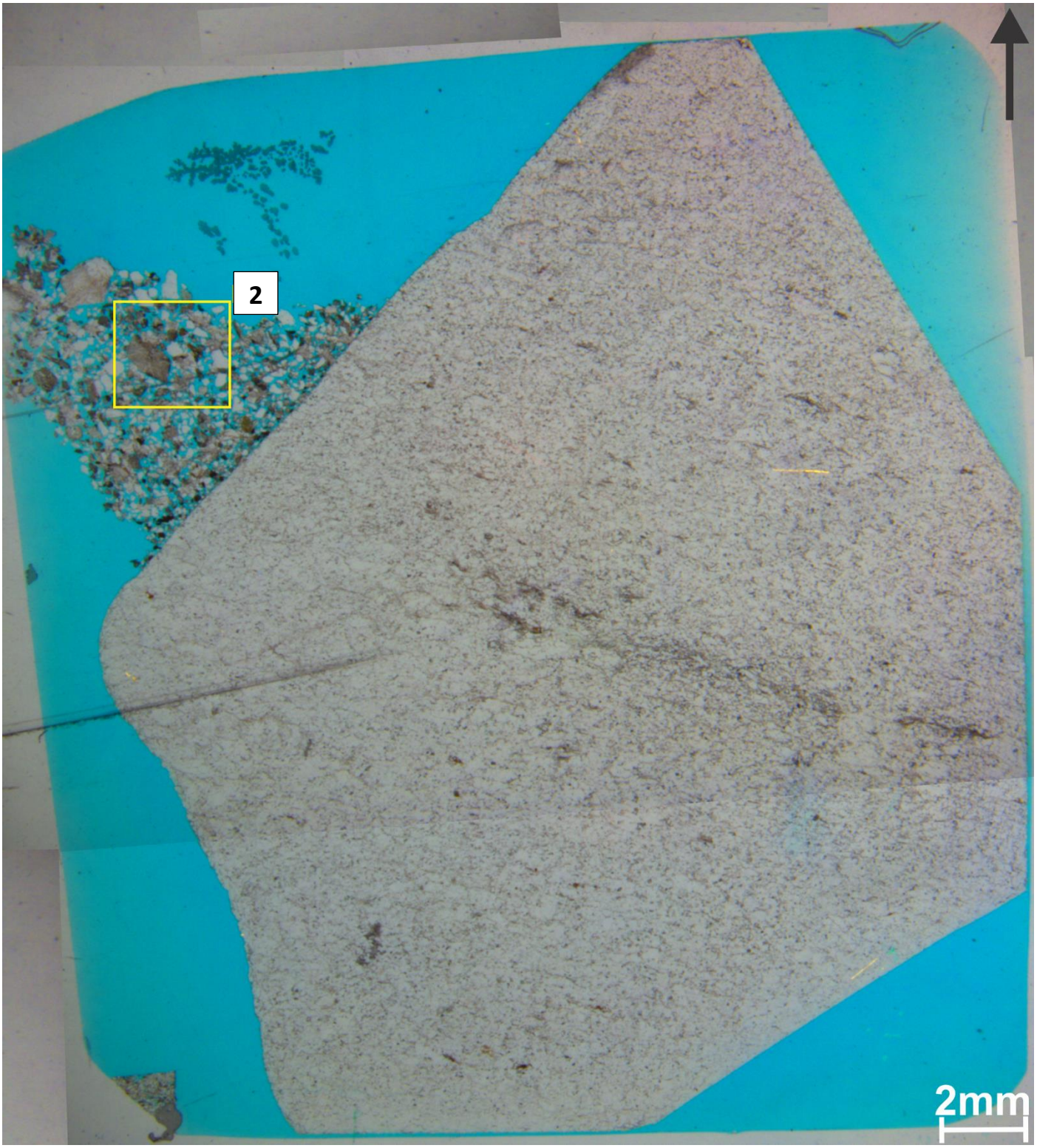

Fig. A 15. Thin section 8 from 0,43m in the vertical profile. The thin section consists of one big clasts and a cemented cone of fine-grained material. The yellow square, 2, represents Fig. A 16 and the black arrow indicate the uppermost surface of the thin section and the orientation of Fig. A 16.

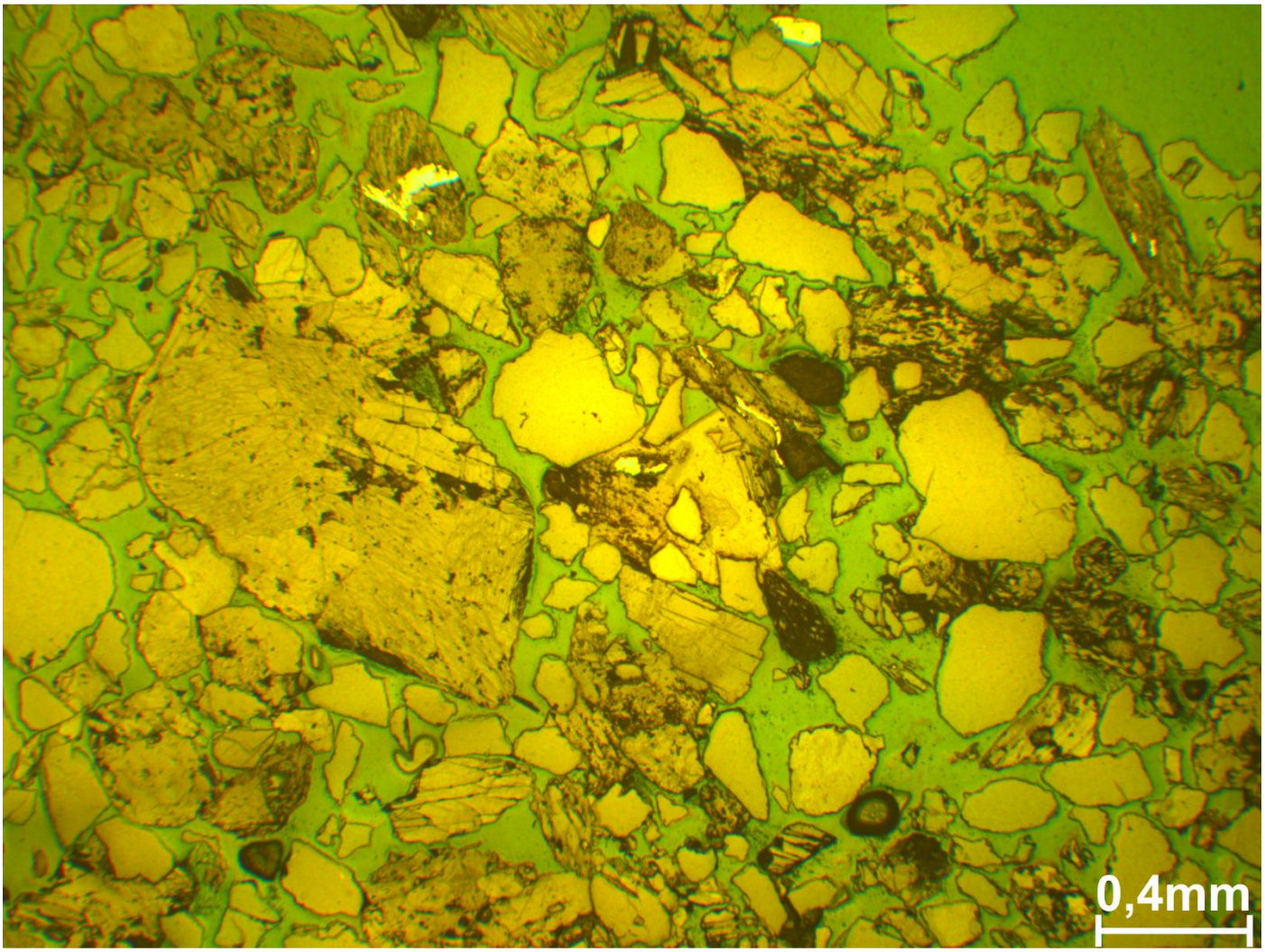

Fig. A 16. The general overview of the pyrite content in thin section 8, marked by the yellow square nr.2 (Fig. A 15). The pyrite content is poor and scattered but also concentrated in some areas. The pyrite occurs both inside the carbonate cement and in other clasts. The pyrite is indicated by distinct yellow color and the picture is taken in incident light.

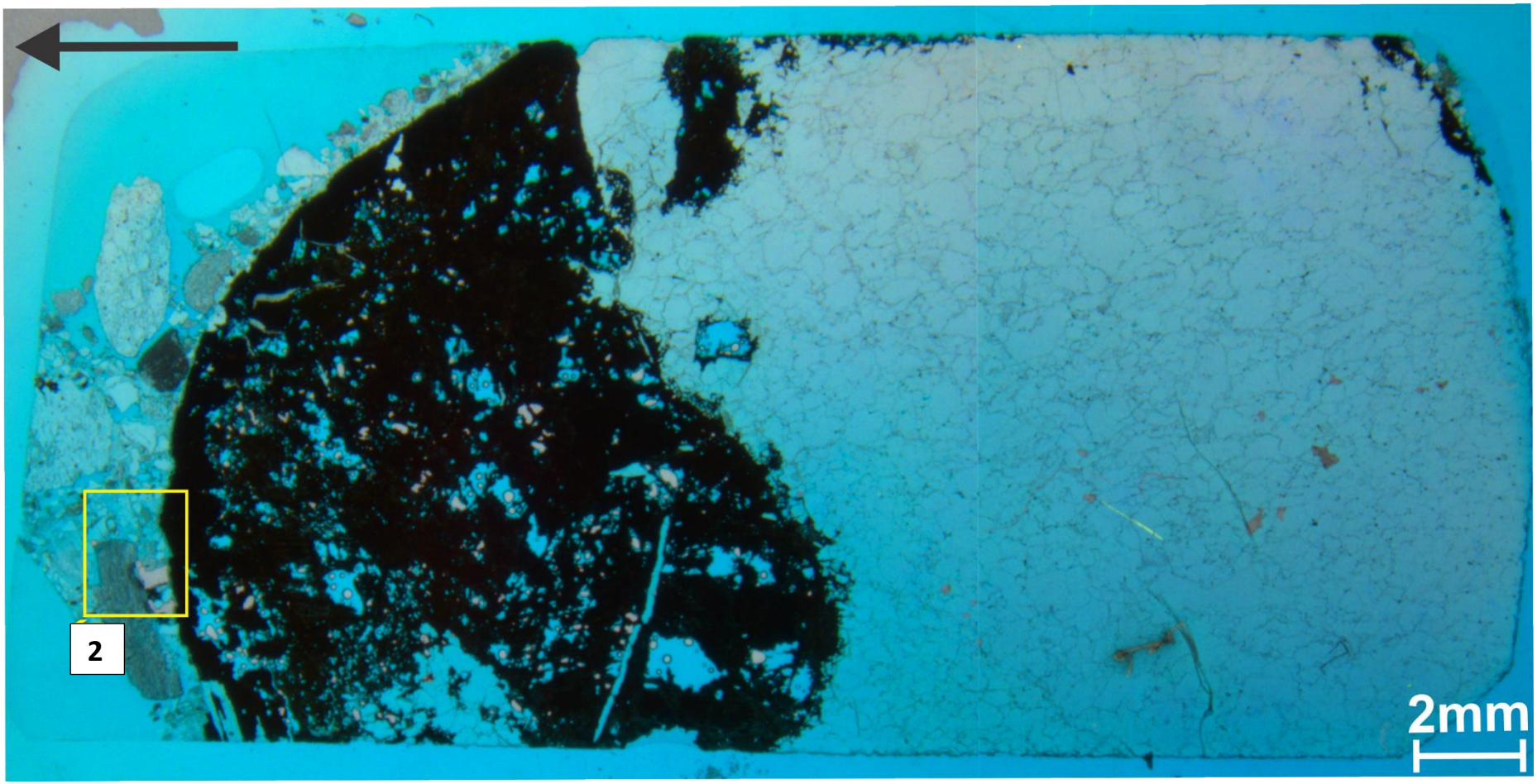

Fig. A 17. Thin section 9, from 0,19m in the vertical profile. The thin section consists of one big clasts with clasts of different sizes cemented on top of, close to the uppermost surface of the thin section. The yellow rectangle, 2, represents Fig. A 18 and the black arrow indicate the upper surface of the thin section and the orientation of the Fig. A 18.

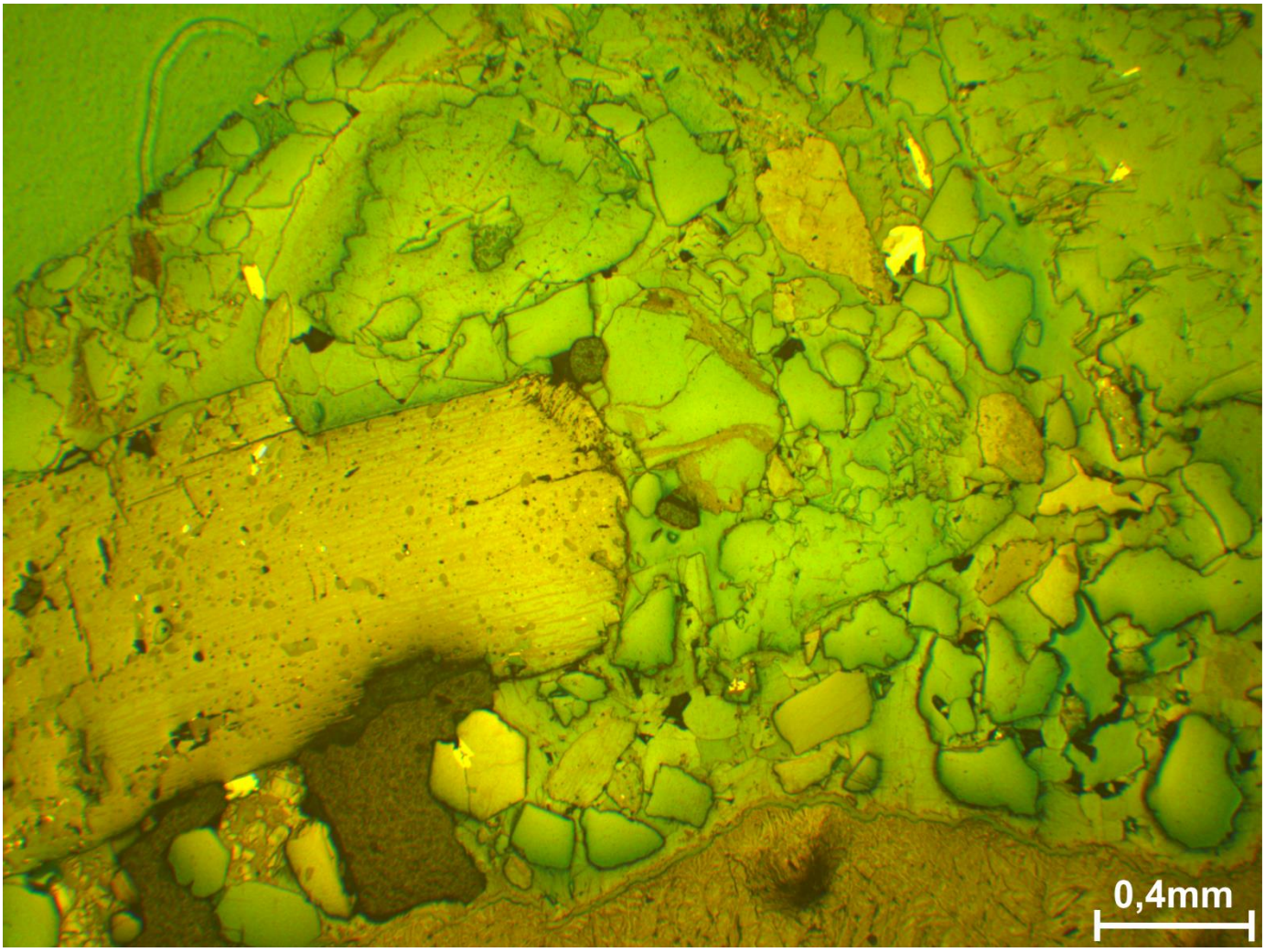

Fig. A 18. The general overview over the pyrite crystals in thin section 9, marked by the yellow rectangle in Fig. A 17. The concentration of pyrite is generally low and occurring in vacant pore spaces, in clasts and both inside and adjacent to the carbonate cement. The distinct yellow color marks the pyrite crystals and the picture is taken in incident light.

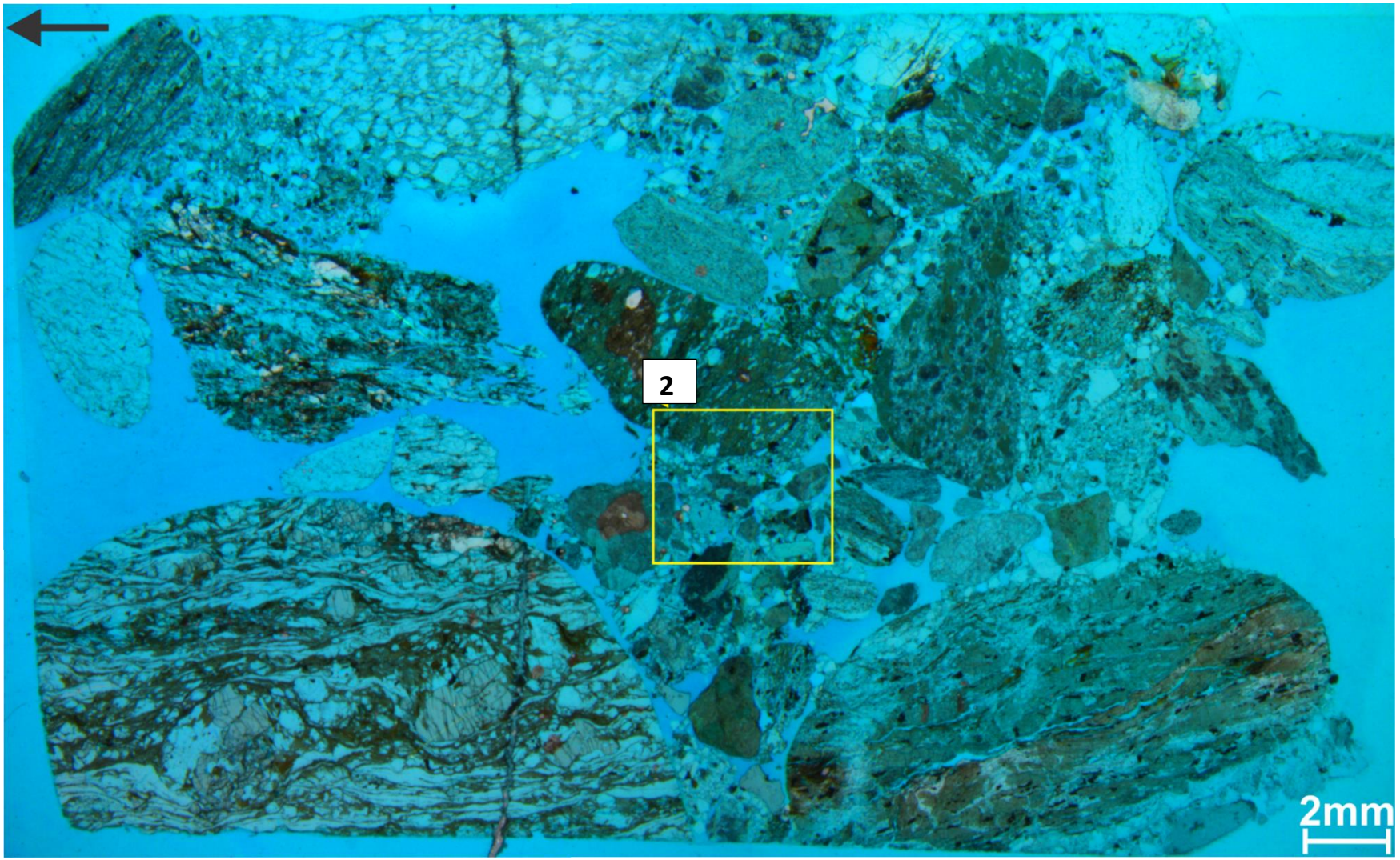

Fig. A 19. Thin section 10, from 17,43m in the vertical profile. It consists of several big clasts with intermediate-fine grains cemented in the space between. The yellow square, 2, represents Fig. A 20 and the general pyrite content in the thin section. The black arrow indicates the upper surface of the thin section and the orientation of Fig. A 20.

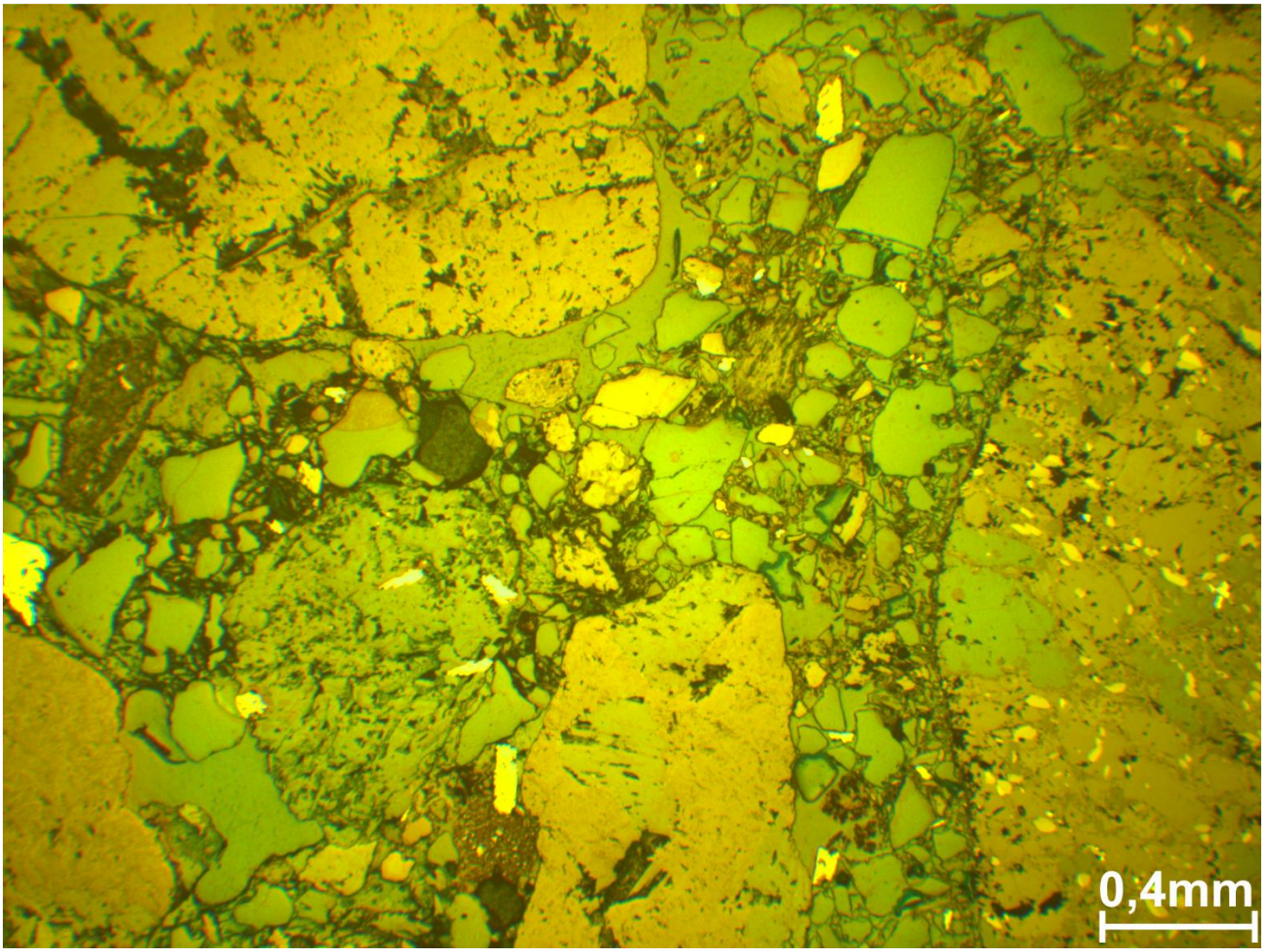

Fig. A 20. The general overview of pyrite content in thin section 10, located on Fig. A 19 by the yellow square. The content is intermediate – abundant. The pyrite occurs in vacant pore spaces, in connection with carbonate cement, inside carbonate cement and as preexisting pyrite inside other clasts. The preexistent pyrite dominates in this thin section. The pyrite crystals are indicated by their distinct yellow color and the picture is taken in incident light.

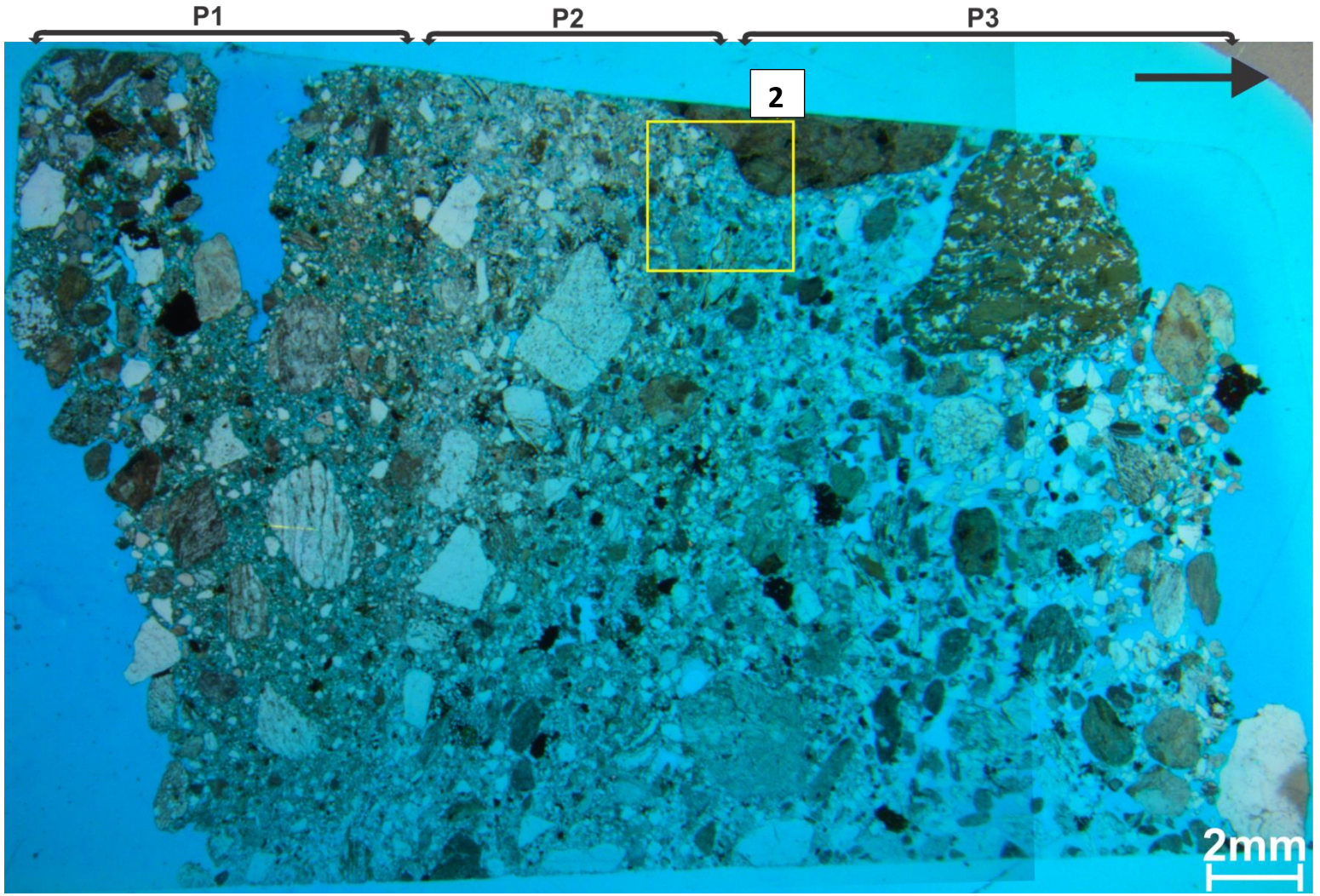

Fig. A 21. Thin section 11, from 15,66m in the vertical profile. The thin section is divided into 3 section based amount of fine grains, termed P1-P3. P1 contains the highest amount of fine grains, where it is gradually decreases towards P3. The cementation is highest in P2 and moderate – poor in P1 and P3. The yellow square, 2, represents Fig. A 22, where the black arrow indicates the upper surface of the thin section and the orientation of the Fig. A 22.

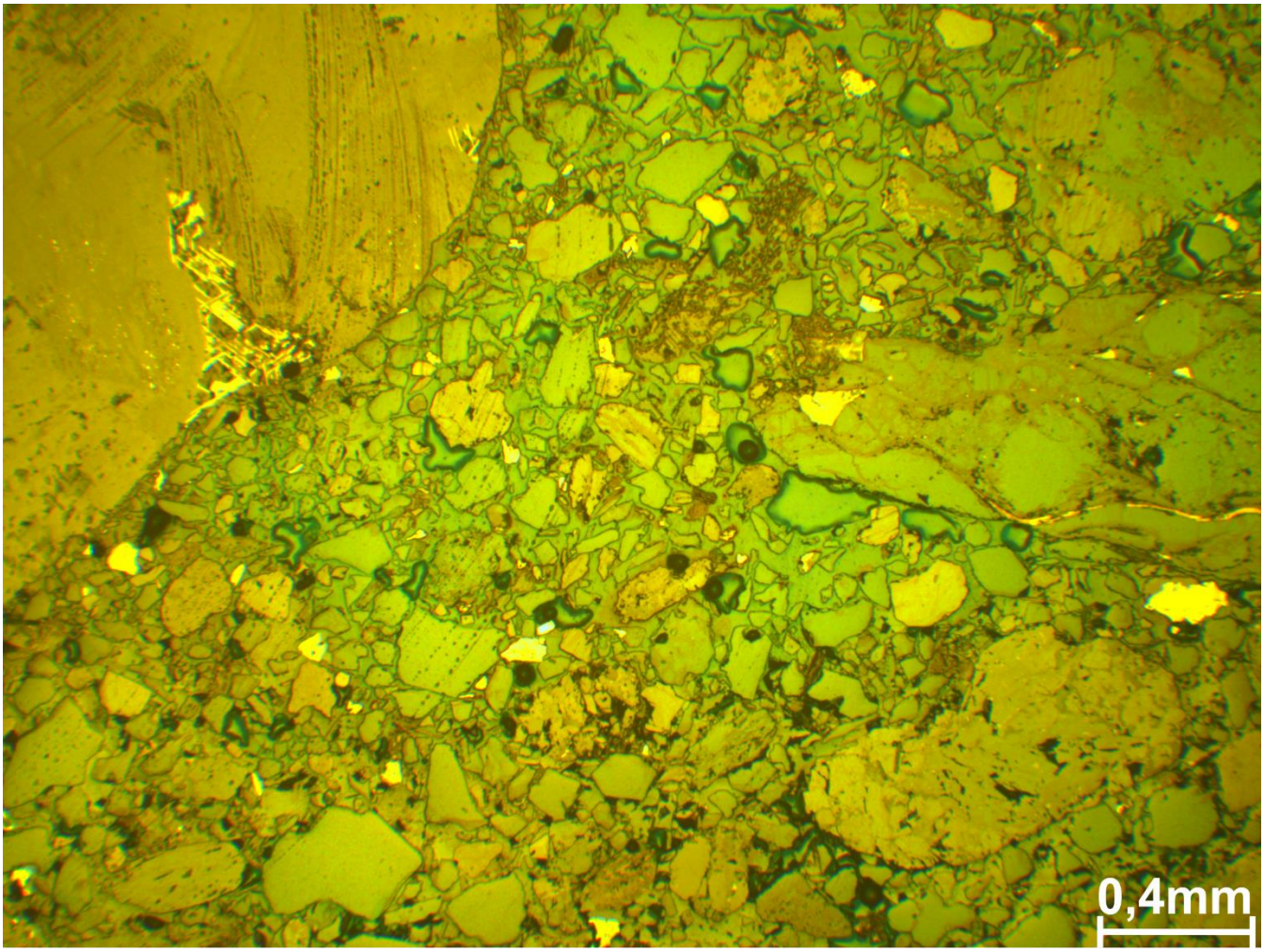

Fig. A 22. The general trend of the pyrite occurrence in thin section 11, located on Fig. A 21 by the yellow square. The pyrite content is moderate to abundant with almost equal amount of preexisting pyrite and pyrite in the pore spaces without carbonate cement. In addition, some of the pyrite crystals occur in connection or inside the carbonate cement. The pyrite crystals are indicated by distinct yellow color and the picture is taken in incident light.

Appendix E: Grainsize distribution

The grainsize distribution is analyzed from 0,19m to 34,75m, where the samples in the analysis is based on being the finest layer in their respective sections. The results are presented in Fig 58 with the sedimentary log. The grainsize distribution is measured from >63µm-≥2mm, where the result is presented in percentage with different colors. In total 76 samples (Fig 58) are presented in the result. The detailed data of the 76 samples are in (Table A 8)

From sample 0,19m- 0,97m (Fig 58) the grainsizes ranging from 125 to <1m mainly dominates. However, from 0,19m-0,55m the ≥2mm grains are distinctively present, before the amount decreases drastically from 0,55m-0,97m.

From 0,97-2,43m (Fig 58) the depositional environment changes, where the <63µm, 63 to <125µm and 125 to <250µm dominates the grainsize distribution. Of the other grainsizes 250µm to <0,5mm is the highest, followed by ≥2mm, where 1 to <2mm is almost non-existent.

At 2,43m-7,92m (Fig 58) the <63µm and 63 to <125µm are the two biggest fraction, where <63µm almost solely dominate the whole grainsize distribution. From 4,1-4,51 minor fluctuation of increased grainsize from 1 to <2mm, 0,5 to <1mm and 250µm to <0,5mm grains occur (Fig 58).

From 8,46-9,5m (Fig 58) the depositional environment shift to a more coarse-grained depositional environment. The dominating grainsize in this interval is ≥2mm, where the 250µm-1mm grains are distinctively present. The <63µm- <250µm grains are extremely low in this interval.

At 9,5m- 12,35m (Fig 58) are mainly dominated by 125- <250µm and 63- <125µm grains, closely followed by <63µm grains. The rest of the grainsizes are very low at this interval.

At 12,56m (Fig 58) a coarse depositional event occurs, dominated by ≥2mm grains, all the other grains are extremely low at this point, except for <63 µm, which is considerably present fraction in the grainsize distribution at this point.

From 12,92m-14,29m (Fig 58), the main dominant grainsize is <63µm. From 13,3m-13,68m the <63µm grains is considerably reduced, where the 63- <125µm grains increase drastically. At this location, the other grainsizes also increase to some degree, but not as distinctively as 63- <125µm. The 63- <125µm is a distinctively present fraction in the rest of the interval, but is reduced. The <63µm grain fraction increase from 13,68m occurring as the largest fraction.

The interval from 14,67m- 18,92m (Fig 58) is characterized by fluctuations. However, the ≥2mm grains are the dominant grainsize throughout the interval. Distinct local fraction peaks of 125- <250µm and 250- <500 µm grains occur at 15,05m-15,6m. One distinct local fraction peak of <63µm occur at 18,09m, where it is the dominant grainsize.

In the interval from 21,12m-24,33m (Fig 58) the distribution between 63µm- <1mm grains is to some degree equal, where the grains from 125µm- <0,5mm are the dominant ones. However, at 23,76m the general grain size distribution trend is disrupted, where the dominant grainsize is ≥2mm grains. The rest of the interval follows more or less the general grainsize distribution trend, where the 125- <250µm is clearly the largest fraction, closely followed by 63- <125µm grains. The 250µm- <1mm grains fraction is more reduced in this part of the interval.

In the interval from 25m-34,75m (Fig 58), the main grainsize fraction is ≥2mm, followed by the minor but considerably fractions 0,5mm- <2mm. In the start of the interval, the ≥2mm grains start at very high fraction, where it is decreases towards 28,17m (Fig 58). The opposite effect is observed with the 125µm- <2mm grains, where the fractions are increasing. At 28,17m (Fig 58) a distinct peak occurs for the 63µm- <0,5mm grains, where the 125µm- <0,5mm grains are the dominating grainsize fractions. The rest of the interval, from 28,36m-34,75m (Fig 58), the ≥2mm grains are again the dominating grain size. Here the 0,5mm- <2mm grains are minor, but considerably fractions are, where the rest of the grainsizes are extremely low.

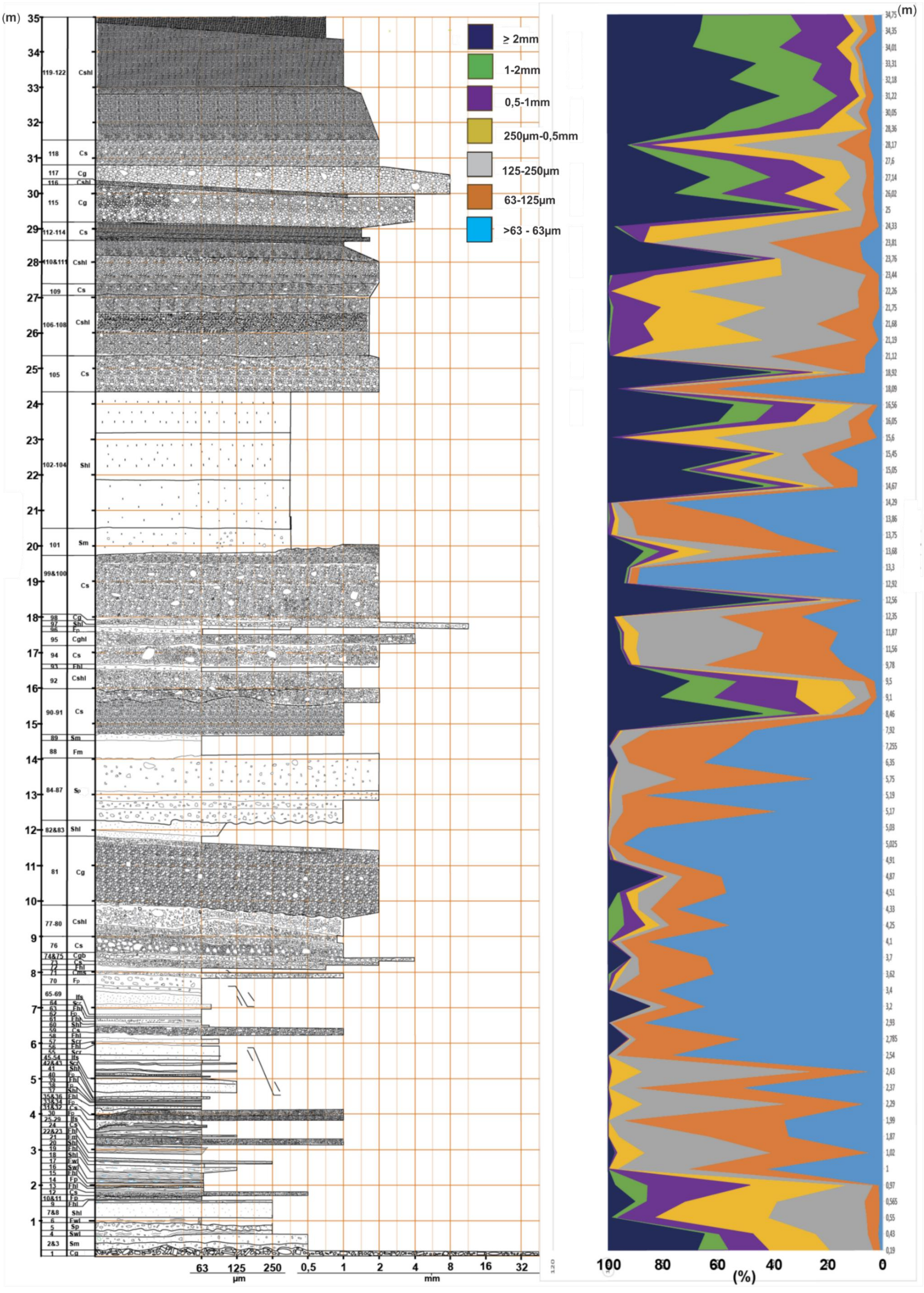

Fig 58. Sedimentary log with the grainsize distribution of the logged layers. The grain size distribution is displayed in a percentage chart, starting at 0,19m up to 34,75m. Each grain size is marked with a specific color.

Table A 8. Overview over the 76 weighed and sieved samples. The total weight of samples, grain size and the grain size percentage for the respective size is summarized in this table. The name of the samples is in meters, in the leftmost row. The C marks the occurrence of carbonate encrustations and at what grainsize it was found.

Grain size distribution						
Name and size	Total weight (g)	Weight bowl (g)	Grain weight (g)	Total sample weight (g)		Grain weight (%)
0,19m/<63µm	5,08	1,3	3,78	389,14	<63µm	0,971372771
0,19m/63µm	11,4	1,26	10,14		63µm	2,605746004
0,19m/125µm	62,73	1,27	61,46		125µm	15,79380172
0,19m/250µm	87,8	1,26	86,54		250µm	22,23878296
0,19m/0,5mm	56,91	1,28	55,63		0,5mm	14,29562625
0,19m/1mm	46,4	1,28	45,12		1mm	11,59479879
0,19m/2mm	128,29	1,82	126,47		2mm	32,49987151
0,43m/<63µm	27,12	1,85	25,27	1430,87	<63µm	1,766058412
0,43m/63µm	56,14	1,85	54,29		63µm	3,79419514
0,43m/125µm	275,7	4,08	271,62		125µm	18,98285658
0,43m/250µm	329,77	4,08	325,69		250µm	22,76167646
0,43m/0,5mm	177,68	1,85	175,83		0,5mm	12,28832808
0,43m/1mm	78,28	1,85	76,43		1mm	5,341505518
0,43m/2mm	505,88	4,14	501,74		2mm	35,0653798
0,565m/<63µm	7,05	1,3	5,75	425,39	<63µm	1,351700792
0,565m/63µm	24,35	1,76	22,59		63µm	5,310421025
0,565m/125µm	137,52	1,75	135,77		125µm	31,91659418
0,565m/250µm	144,23	1,7	142,53		250µm	33,50572416
0,565m/0,5mm	60,15	1,71	58,44		0,5mm	13,73798162
0,565m/1mm	20,43	1,75	18,68		1mm	4,391264487
0,565m/2mm	43,35	1,72	41,63		2mm	9,786313736
0,55m/<63µm	64,78	60,55	4,23	320,02	<63µm	1,321792388
0,55m/63µm	98,94	84,01	14,93		63µm	4,665333417
0,55m/125µm	176,55	62,17	114,38		125µm	35,74151616
0,55m/250µm	217,82	84,59	133,23		250µm	41,63177301
0,55m/0,5mm	101,26	59,28	41,98		0,5mm	13,11793013
0,55m/1mm	69,31	60,87	8,44		1mm	2,637335167
0,55m/2mm	114,73	111,9	2,83	C	2mm	0,88431973
0,97m/<63µm	7,88	1,26	6,62	436,26	<63µm	1,517443726
0,97m/63µm	11,01	1,3	9,71		63µm	2,225736946
0,97m/125µm	45,13	1,84	43,29		125µm	9,922981708
0,97m/250µm	153,08	1,85	151,23		250µm	34,66510796
0,97m/0,5mm	164,03	1,86	162,17		0,5mm	37,17278687
0,97m/1mm	54,2	1,75	52,45		1mm	12,02264705
0,97m/2mm	11,45	0,66	10,79		2mm	2,473295741
Grain size distribution						

Name and size	Total weight (g)	Weight bowl (g)	Grain weight (g)	Total sample weight (g)		Grain weight (%)
1m/<63µm	91,63	61,3	30,33	71,38	<63µm	42,49089381
1m/63µm	104,47	84,15	20,32		63µm	28,4673578
1m/125µm	78,79	60,52	18,27		125µm	25,59540488
1m/250µm	57,41	55,11	2,3		250µm	3,22219109
1m/0,5mm	59,32	59,24	0,08		0,5mm	0,112076212
1m/1mm	57,43	57,38	0,05		1mm	0,070047632
1m/2mm	60,57	60,54	0,03		2mm	0,042028579
1,02m/<63µm	98,61	93,23	5,38	104,71	<63µm	5,138000191
1,02m/63µm	148,59	111,15	37,44		63µm	35,75589724
1,02m/125µm	157,1	109,12	47,98		125µm	45,82179352
1,02m/250µm	60,27	49,75	10,52		250µm	10,04679591
1,02m/0,5mm	61	60,53	0,47	C	0,5mm	0,448858753
1,02m/1mm	57,16	56,69	0,47	C	1mm	0,448858753
1,02m/2mm	61,17	58,72	2,45	C	2mm	2,339795626
1,87m/<63µm	151,5	106,85	44,65	129,99	<63µm	34,34879606
1,87m/63µm	88	50,5	37,5		63µm	28,84837295
1,87m/125µm	97,11	54,64	42,47		125µm	32,67174398
1,87m/250µm	66,61	61,39	5,22		250µm	4,015693515
1,87/0,5mm	82,58	82,45	0,13		0,5mm	0,100007693
1,87m/1mm	62,49	62,47	0,02		1mm	0,015385799
1,87m/2mm	0	0	0		2mm	0
1,99m/<63µm	80,15	61,52	18,63	52,03	<63µm	35,80626562
1,99m/63µm	138,01	107,43	30,58		63µm	58,77378436
1,99m/125µm	98,88	96,11	2,77		125µm	5,323851624
1,99m/250µm	55,15	55,11	0,04		250µm	0,076878724
1,99m/0,5mm	59,34	59,33	0,01		0,5mm	0,019219681
1,99m/1mm	0	0	0		1mm	0
1,99m/2mm	0	0	0		2mm	0
2,29m/<63µm	64,6	51,57	13,03	179,33	<63µm	7,265934311
2,29m/63µm	104,04	53,76	50,28		63µm	28,03769587
2,29m/125µm	151,17	57,55	93,62		125µm	52,20543133
2,29m/250µm	124	103,87	20,13		250µm	11,22511571
2,29m/0,5mm	79,79	78,74	1,05		0,5mm	0,585512742
2,29m/1mm	54,78	54,47	0,31		1mm	0,172865667
2,29m/2mm	49,91	49	0,91		2mm	0,507444376
Grain size distribution						

Name and size	Total weight (g)	Weight bowl (g)	Grain weight (g)	Total sample weight (g)		Grain weight (%)
2,37m/<63µm	96,91	40,96	55,95	109,03	<63µm	51,31615152
2,37m/63µm	103,73	61,47	42,26		63µm	38,75997432
2,37m/125µm	67,14	56,67	10,47		125µm	9,602861598
2,37m/250µm	86,72	86,42	0,3		250µm	0,275153627
2,37m/0,5mm	82,43	82,42	0,01		0,5mm	0,009171788
2,37m/1mm	55,45	55,43	0,02		1mm	0,018343575
2,37m/2mm	58,89	58,87	0,02		2mm	0,018343575
2,43m/<63µm	4,6	0,77	3,83	70,55	<63µm	5,428773919
2,43m/63µm	15,51	0,75	14,76		63µm	20,92133239
2,43m/125µm	44,47	1,22	43,25		125µm	61,30403969
2,43m/250µm	8,63	0,77	7,86		250µm	11,14103473
2,43m/0,5mm	1,25	0,75	0,5		0,5mm	0,708717222
2,43m/1mm	0,91	0,77	0,14		1mm	0,198440822
2,43m/2mm	1,96	1,75	0,21		2mm	0,297661233
2,54m/<63µm	230,05	112,09	117,96	153,73	<63µm	76,73193261
2,54m/63µm	114,43	83,26	31,17		63µm	20,27580824
2,54m/125µm	61,11	56,7	4,41		125µm	2,868665843
2,54m/250µm	61,49	61,33	0,16		250µm	0,104078579
2,54m/0,5mm	55,47	55,45	0,02		0,5mm	0,013009822
2,54m/1mm	56,66	56,65	0,01		1mm	0,006504911
2,54m/2mm	0	0	0		2mm	0
2,785m/<63µm	147,84	59,24	88,6	170,55	<63µm	51,9495749
2,785m/63µm	148,3	83,79	64,51		63µm	37,82468484
2,785m/125µm	62,45	59,23	3,22		125µm	1,888009381
2,785m/250µm	87,72	86,42	1,3		250µm	0,762239812
2,785m/0,5mm	59,38	58,87	0,51		0,5mm	0,299032542
2,785m/1mm	60,51	59,9	0,61		1mm	0,357666373
2,785m/2mm	122,59	110,79	11,8		2mm	6,918792143
2,93m/<63µm	210,85	111,07	99,78	114,54	<63µm	87,11367208
2,93m/63µm	73,72	60,55	13,17		63µm	11,49816658
2,93m/125µm	61,79	60,54	1,25		125µm	1,091321809
2,93m/250µm	49,99	49,76	0,23		250µm	0,200803213
2,93m/0,5mm	61,36	61,34	0,02		0,5mm	0,017461149
2,93m/1mm	83,36	83,27	0,09		1mm	0,07857517
2,93m/2mm	0	0	0		2mm	0
Grain size distribution						

Name and size	Total weight (g)	Weight bowl (g)	Grain weight (g)	Total sample weight (g)		Grain weight (%)
3,20/<63µm	197,12	111,13	85,99	133,04	<63µm	64,63469633
3,20m/63µm	80,82	62,21	18,61		63µm	13,9882742
3,20m/125µm	66,47	59,25	7,22		125µm	5,426939266
3,20m/250µm	55,44	54,63	0,81		250µm	0,608839447
3,20m/0,5mm	58,62	58,55	0,07		0,5mm	0,052615755
3,20m/1mm	61,4	61,37	0,03		1mm	0,022549609
3,20m/2mm	82,78	62,47	20,31	C	2mm	15,26608539
3,4m/<63µm	47,45	0	47,45	47,56	<63µm	99,76871
3,4m/63µm	0	0	0		63µm	0
3,4m/125µm	0	0	0		125µm	0
3,4m/250µm	0	0	0		250µm	0
3,4m/0,5mm	0	0	0		0,5mm	0
3,4m/1mm	0	0	0		1mm	0
3,4m/2mm	58,95	58,84	0,11		2mm	0,231287
3,40m/<63µm	102,56	54,63	47,93	58,75	<63µm	81,58297872
3,40m/ 63µm	81,81	72,55	9,26		63µm	15,76170213
3,40m/125µm	72,63	71,52	1,11		125µm	1,889361702
3,40m/250µm	107,58	107,36	0,22		250µm	0,374468085
3,40m/0,5mm	113,21	113,11	0,1		0,5mm	0,170212766
3,40m/1mm	112,07	112,05	0,02		1mm	0,034042553
3,40m¨/2mm	58,95	58,84	0,11		2mm	0,187234043
3,62m/<63µm	144,29	107,39	36,9	60,08	<63µm	61,41810919
3,62m/63µm	87,84	71,52	16,32		63µm	27,16378162
3,62m/125µm	58,61	54,63	3,98		125µm	6,624500666
3,62m/250µm	73,87	72,56	1,31		250µm	2,180426099
3,62m/0,5mm	75,71	75	0,71		0,5mm	1,181757656
3,62m/1mm	63,05	62,19	0,86		1mm	1,431424767
3,62m/2mm	0	0	0		2mm	0
3,7m/<63µm	179,81	111,03	68,78	107,36	<63µm	64,06482861
3,7m/63µm	76,59	49,78	26,81		63µm	24,97205663
3,7m/125µm	61,29	58,71	2,58		125µm	2,403129657
3,7m/250µm	52,62	52,46	0,16		250µm	0,149031297
3,7m/0,5mm	58,66	58,56	0,1		0,5mm	0,09314456
3,7m/1mm	61,59	61,37	0,22		1mm	0,204918033
3,7m/2mm	71,23	62,52	8,71		2mm	8,112891207
Grain size distribution						

Name and size	Total weight (g)	Weight bowl (g)	Grain weight (g)	Total sample weight (g)		Grain weight (%)
4,10m/<63µm	186,34	96,65	89,69	104,71	<63µm	85,65562028
4,10m/63µm	66,97	56,7	10,27		63µm	9,808041257
4,10m/125µm	59,28	56,68	2,6		125µm	2,483048419
4,10m/250µm	60,11	59,24	0,87		250µm	0,830866202
4,10m/0,5mm	77,02	76,36	0,66		0,5mm	0,630312291
4,10m/1mm	56,06	55,44	0,62		1mm	0,592111546
4,10m/2mm	0	0	0		2mm	0
4,25m/<63µm	137,75	107,42	30,33	54,24	<63µm	55,91814159
4,25m/63µm	68,98	57,28	11,7		63µm	21,57079646
4,25m/125µm	61,09	59,18	1,91		125µm	3,521386431
4,25m/250µm	61,91	58,91	3		250µm	5,530973451
4,25m/0,5mm	65,1	61,14	3,96		0,5mm	7,300884956
4,25m/1mm	58,27	54,93	3,34		1mm	6,157817109
4,25m/2mm	0	0	0		2mm	0
4,33m/<63µm	173,03	111,06	61,97	82,64	<63µm	74,98789932
4,33m/63µm	60,26	52,42	7,84		63µm	9,486931268
4,33m/125µm	62,5	58,71	3,79		125µm	4,586156825
4,33m/250µm	112	110,1	1,9		250µm	2,299128751
4,33m/0,5mm	114,58	112,06	2,52		0,5mm	3,049370765
4,33m/1mm	116,49	111,87	4,62		1mm	5,590513069
4,33m/2mm	0	0	0		2mm	0
4,51m/<63µm	122,41	84,06	38,35	67,34	<63µm	56,94980695
4,51m/63µm	75,35	60,77	14,58		63µm	21,65132165
4,51m/125µm	57,52	50,49	7,03		125µm	10,43956044
4,51m/250µm	61,89	58,85	3,04		250µm	4,514404514
4,51m/0,5mm	83,75	82,44	1,31		0,5mm	1,945351945
4,51m/1mm	50,52	49,77	0,75		1mm	1,113751114
4,51m/2mm	88,56	86,28	2,28	C	2mm	3,385803386
4,87m/<63µm	178,14	111,12	67,02	114,2	<63µm	58,68651489
4,87m/63µm	124,69	108,55	16,14		63µm	14,13309982
4,87m/125µm	116,43	110,13	6,3		125µm	5,516637478
4,87m/250µm	112,4	110,74	1,66		250µm	1,453590193
4,87m/0,5mm	60,83	59,5	1,33		0,5mm	1,164623468
4,87m/1mm	66,28	65,25	1,03		1mm	0,901926445
4,87m/2mm	104,36	83,64	20,72		2mm	18,14360771
Grain size distribution						

Name and size	Total weight (g)	Weight bowl (g)	Grain weight (g)	Total sample weight (g)		Grain weight (%)
4,91m/<63µm	137,77	83,83	53,94	67,91	<63µm	79,42865557
4,91m/63µm	117,46	108,58	8,88		63µm	13,07613017
4,91m/125µm	113,16	110,28	2,88		125µm	4,240907083
4,91m/250µm	109,84	109,04	0,8		250µm	1,178029745
4,91/0,5mm	112,16	111,57	0,59		0,5mm	0,868796937
4,91m/1mm	112,45	112,06	0,39		1mm	0,574289501
4,91m/2mm	111,5	111,07	0,43		2mm	0,633190988
5,025m/<63µm	165,2	76,37	88,83	94,07	<63µm	94,42968003
5,025m/63µm	89,58	84,73	4,85		63µm	5,155735091
5,025m/125µm	110,62	110,31	0,31		125µm	0,329541831
5,025m/250µm	111,9	111,86	0,04		250µm	0,042521527
5,025m/0,5mm	109,11	109,1	0,01		0,5mm	0,010630382
5,025m/1mm	111,57	111,54	0,03		1mm	0,031891145
5,025m/2mm	0	0	0		2mm	0
5,03m/<63µm	155,1	96,58	58,52	68,36	<63µm	85,60561732
5,03m/63µm	68,61	59,86	8,75		63µm	12,79988297
5,03m/125µm	56,46	55,54	0,92		125µm	1,345816267
5,03m/250µm	60,82	60,72	0,1		250µm	0,146284377
5,03m/0,5mm	84,68	84,64	0,04		0,5mm	0,058513751
5,03m/1mm	61,27	61,26	0,01		1mm	0,014628438
5,03m/2mm	63,75	63,73	0,02		2mm	0,029256875
5,17m/<63µm	96,08	81,98	14,1	36,18	<63µm	38,97180763
5,17m/63µm	80,82	60,78	20,04		63µm	55,38971808
5,17m/125µm	63,8	62,18	1,62		125µm	4,47761194
5,17m/250µm	61,49	61,33	0,16		250µm	0,442233278
5,17m/0,5mm	59,32	59,24	0,08		0,5mm	0,221116639
5,17m/1mm	83,46	83,28	0,18		1mm	0,497512438
5,17m/2mm	0	0	0		2mm	0
5,19/<63µm	140,9	76,34	64,56	74,24	<63µm	86,9612069
5,19m/63µm	61,32	55,47	5,85		63µm	7,879849138
5,19m/0,125mm	85,2	82,38	2,82		125µm	3,798491379
5,19m/0,25m	61,64	60,96	0,68		250µm	0,915948276
5,19m/0,5mm	82	81,96	0,04		0,5mm	0,05387931
5,19m/1mm	61,35	61,32	0,03		1mm	0,040409483
5,19m/2mm	86,67	86,41	0,26		2mm	0,350215517
Grain size distribution						

Name and size	Total weight (g)	Weight bowl (g)	Grain weight (g)	Total sample weight (g)		Grain weight (%)
5,19m/<63µm	63,61	0	63,61	88,16	<63µm	72,15290381
5,19m/63µm	75,04	56,72	18,32		63µm	20,78039927
5,19m/125µm	46,45	43,83	2,62		125µm	2,971869328
5,19m/250µm	50,44	50,43	0,01		250µm	0,011343013
5,19m/0,5mm	0	0	0		0,5mm	0
5,19m/1mm	83,87	83,77	0,1		1mm	0,113430127
5,19m/2mm	90,71	87,21	3,5		2mm	3,970054446
5,75m/<63µm	72,9	60,86	12,04	47,49	<63µm	25,35270583
5,75m/63µm	82,56	58,9	23,66		63µm	49,82101495
5,75m/125µm	69,92	59,25	10,67		125µm	22,46788798
5,75m/250µm	86,93	86,28	0,65		250µm	1,368709202
5,75m/0,5mm	62,65	62,25	0,4		0,5mm	0,842282586
5,75m/1mm	57,15	57,08	0,07		1mm	0,147399453
5,75m/2mm			0		2mm	0
6,35m/<63µm	125,24	53,25	71,99	110,48	<63µm	65,16111513
6,35m/63µm	90,71	60,88	29,83		63µm	27,00036206
6,35m/125µm	90,73	86,21	4,52		125µm	4,091238233
6,35m/250µm	58,18	58	0,18		250µm	0,162925416
6,35/0,5mm	84,69	84,59	0,1		0,5mm	0,09051412
6,35m/1mm	64,66	64,55	0,11	C	1mm	0,099565532
6,35m/2mm	65,92	62,17	3,75	C	2mm	3,394279508
7,255m/<63µm	149,48	121,42	28,06	51,25	<63µm	54,75121951
7,255m/63µm	132,56	111,9	20,66		63µm	40,31219512
7,255m/125µm	112,99	110,75	2,24		125µm	4,370731707
7,255m/250µm	71,59	71,53	0,06		250µm	0,117073171
7,255/0,5mm	110,15	110,1	0,05		0,5mm	0,097560976
7,255m/1mm	61,28	61,22	0,06		1mm	0,117073171
7,255m/2mm	52,75	52,63	0,12		2mm	0,234146341
7,92m/<63µm	107,3	60,54	46,76	99,82	<63µm	46,84431978
7,92m/63µm	123,88	86,2	37,68		63µm	37,7479463
7,92m/125µm	93,85	84,03	9,82		125µm	9,837707874
7,92m/250µm	57,87	56,67	1,2		250µm	1,202163895
7,92m/0,5mm	84,95	84,58	0,37		0,5mm	0,370667201
7,92m/1mm	61,16	60,77	0,39		1mm	0,390703266
7,92m/2mm	65,76	62,16	3,6		2mm	3,606491685
Grain size distribution						

Name and size	Total weight (g)	Weight bowl (g)	Grain weight (g)	Total sample weight (g)		Grain weight (%)
8,46m/ <63µm	105,96	86,29	19,67	278,33	<63µm	7,067150505
8,46m / 63µm	106,15	86,18	19,97		63µm	7,174936227
8,46m/125µm	74,58	62,13	12,45		125µm	4,473107462
8,46m/250µm	69,06	56,66	12,4		250µm	4,455143175
8,46m/0,5mm	78,57	60,77	17,8		0,5mm	6,395286171
8,46m/1mm	98,41	58,88	39,53		1mm	14,2025653
8,46m/2mm	267,65	111,14	156,51		2mm	56,23181116
9,10m/<63µm	74,61	55,55	19,06	865,87	<63µm	2,20125423
9,10m/63µm	102,77	84,68	18,09		63µm	2,089228175
9,10m/125µm	101,94	55,44	46,5		125µm	5,37032118
9,10m/250µm	251,33	59,9	191,43		250µm	22,10839964
9,10m/0,5mm	349,7	96,56	253,14		0,5mm	29,23533556
9,10m/1mm	288	111,83	176,17		1mm	20,34601037
9,10m/2mm	271,77	110,29	161,48		2mm	18,64945084
9,50m/<63µm	136,94	110,33	26,61	913,55	<63µm	2,912812654
9,50m/63µm	144,54	110,14	34,4		63µm	3,765530075
9,50m/125µm	185,12	112,09	73,03		125µm	7,994088993
9,50m/250µm	263,5	114,55	148,95		250µm	16,3045263
9,50m/0,5mm	307,78	110,74	197,04		0,5mm	21,56860599
9,50m/1mm	272,02	109,04	162,98		1mm	17,84029336
9,50m/2mm	435,19	164,65	270,54		2mm	29,61414263
9,78m/<63µm	110,18	104,02	6,16	44,45	<63µm	13,85826772
9,78m/63µm	106,77	84,05	22,72		63µm	51,1136108
9,78m/125µm	69,17	58,86	10,31		125µm	23,19460067
9,78m/250µm	62,17	60,77	1,4		250µm	3,149606299
9,78/0,5mm	58,91	58,56	0,35		0,5mm	0,787401575
9,78m/1mm	82,17	81,97	0,2		1mm	0,449943757
9,78m/2mm	64,62	61,31	3,31		2mm	7,446569179
11,56m/ <63µm	128,06	110,79	17,27	88,81	<63µm	19,44600833
11,56m / 63µm	135,6	112,07	23,53		63µm	26,4947641
11,56m/125µm	147,83	109,01	38,82		125µm	43,71129377
11,56m/250µm	114,24	110,1	4,14		250µm	4,661637203
11,56m/0,5mm	111,44	111,05	0,39	C	0,5mm	0,439139737
11,56m/1mm	112,43	111,86	0,57	C	1mm	0,641819615
11,56m/2mm	65,48	61,39	4,09	C	2mm	4,605337237
Grain size distribution						
Name and size	Total weight (g)	Weight bowl (g)	Grain weight (g)	Total sample weight (g)	Grain weight (%)	
11,87m/<63µm	19,92	1,74	18,18	112,64	<63µm	16,13991477
11,87m/63µm	32,43	1,73	30,7		63µm	27,25497159
11,87m/125µm	52,84	1,79	51,05		125µm	45,32137784

11,87m/250µm	8,03	1,78	6,25		250µm	5,548650568
11,87m/0,5mm	2,35	1,75	0,6	C	0,5mm	0,532670455
11,87m/1mm	2,7	1,75	0,95	C	1mm	0,843394886
11,87m/2mm	6,68	1,77	4,91	C	2mm	4,359019886
12,35m/<63µm	132,09	110,28	21,81	73,6	<63µm	29,63315217
12,35m/63µm	86,99	65,2	21,79		63µm	29,60597826
12,35m/125µm	88,47	62,15	26,32		125µm	35,76086957
12,35m/250µm	63,42	61,4	2,02		250µm	2,744565217
12,35m/0,5mm	56,7	56,65	0,05		0,5mm	0,067934783
12,35m/1mm	59,27	59,2	0,07		1mm	0,095108696
12,35m/2mm	84,87	83,33	1,54		2mm	2,092391304
12,56m/ <63µm	157,98	62,38	95,6	1227,08	<63µm	7,790853082
12,56m / 63µm	167,23	108,58	58,65		63µm	4,779639469
12,56m/125µm	174,87	111,56	63,31		125µm	5,15940281
12,56m/250µm	167,81	107,42	60,39		250µm	4,921439515
12,56m/0,5mm	184,05	97,13	86,92		0,5mm	7,08348274
12,56m/1mm	253,14	111,06	142,08		1mm	11,57870717
12,56m/2mm	1239	518,87	720,13		2mm	58,68647521
12,92m/<63µm	179,38	94,26	85,12	95,28	<63µm	89,33669186
12,92m/63µm	53,39	50,48	2,91		63µm	3,054156171
12,92m/125µm	82,74	82,45	0,29		125µm	0,304366079
12,92m/250µm	82,12	81,96	0,16		250µm	0,167926113
12,92m/0,5mm	61,73	61,43	0,3	C	0,5mm	0,314861461
12,92m/1mm	44,8	43,82	0,98	C	1mm	1,028547439
12,92m/2mm	66,32	60,8	5,52		2mm	5,793450882
13,30m/<63µm	321,46	75,01	246,45	279,22	<63µm	88,26373469
13,30m/ 63µm	102,32	94,26	8,06		63µm	2,886612707
13,30m/125µm	62,85	61,85	1		125µm	0,358140534
13,30m/250µm	111,58	111	0,58		250µm	0,20772151
13,30m/0,5mm	88,23	87,42	0,81		0,5mm	0,290093833
13,30m/1mm	65,24	62,57	2,67		1mm	0,956235227
13,30m¨/2mm	130,93	111,28	19,65		2mm	7,0374615
Grain size distribution						
Name and size	Total weight (g)	Weight bowl (g)	Grain weight (g)	Total sample weight (g)		Grain weight (%)
13,68m/<63µm	98,97	86,44	12,53	78,7	<63µm	15,92121982
13,68m/63µm	71,66	55,47	16,19		63µm	20,57179161
13,68m/125µm	81,52	61,27	20,25		125µm	25,73062262
13,68m/250µm	69,38	59,89	9,49		250µm	12,05844981
13,68m/0,5mm	58,22	53,2	5,02		0,5mm	6,378653113

13,68m/1mm	64,29	59,22	5,07	C	1mm	6,442185515
13,68m/2mm	86,5	76,35	10,15	C	2mm	12,89707751
13,75m/<63µm	104,88	1,85	103,03	276,24	<63µm	37,29727773
13,75m/63µm	145,45	1,85	143,6		63µm	51,98378222
13,75m/125µm	21,9	1,85	20,05		125µm	7,258181292
13,75m/250µm	8,14	1,85	6,29		250µm	2,277005502
13,75m/0,5mm	5,12	1,85	3,27		0,5mm	1,183753258
13,75m/1mm			0		1mm	0
13,75m/2mm			0		2mm	0
13,86m/<63µm	58,68	1,89	56,79	111,04	<63µm	51,14373199
13,86m/63µm	46,1	1,83	44,27		63µm	39,86851585
13,86m/125µm	7,27	1,83	5,44		125µm	4,899135447
13,86m/250µm	3,62	1,83	1,79		250µm	1,6120317
13,86m/0,5mm	3,51	1,82	1,69		0,5mm	1,521974063
13,86m/1mm	2,88	1,82	1,06		1mm	0,954610951
13,86m/2mm			0		2mm	0
14,29m/<63µm	173,87	96,64	77,23	97,05	<63µm	79,57753735
14,29m/63µm	98,23	81,99	16,24		63µm	16,73364245
14,29m/125µm	86,11	84,16	1,95		125µm	2,00927357
14,29m/250µm	55,78	55,22	0,56		250µm	0,577022154
14,29m/0,5mm	57,55	57,06	0,49		0,5mm	0,504894384
14,29m/1mm	61,9	61,32	0,58		1mm	0,597630088
14,29m/2mm	0	0	0		2mm	0
14,67m/ <63µm	89,31	62,17	27,14	298,01	<63µm	9,107076944
14,67m / 63µm	109,05	84,02	25,03		63µm	8,399047012
14,67m/125µm	77,08	60,51	16,57		125µm	5,5602161
14,67m/250µm	78,6	60,87	17,73		250µm	5,949464783
14,67m/0,5mm	104,35	84,58	19,77		0,5mm	6,63400557
14,67m/1mm	82,28	59,23	23,05		1mm	7,734639777
14,67m/2mm	225,75	57,03	168,72		2mm	56,61554981
Grain size distribution						
Name and size	Total weight (g)	Weight bowl (g)	Grain weight (g)	Total sample weight (g)		Grain weight (%)
15,05m/<63µm	82,54	62,15	20,39	225,06	<63µm	9,059806274
15,05m/63µm	95,24	59,21	36,03		63µm	16,00906425
15,05m/125µm	122,96	61,44	61,52		125µm	27,33493291
15,05m/250µm	112,61	83,22	29,39		250µm	13,05873989
15,05m/0,5mm	67,16	56,7	10,46		0,5mm	4,647649516
15,05m/1mm	70,33	61,33	9		1mm	3,998933618
15,05m/2mm	140,73	82,46	58,27		2mm	25,89087354

15,45m/<63µm	30,76	1,74	29,02	150,53	<63µm	19,27854913
15,45m/63µm	16,82	1,8	15,02		63µm	9,97807746
15,45m/125µm	11,37	1,76	9,61		125µm	6,38410948
15,45m/250µm	7,75	1,78	5,97		250µm	3,965986846
15,45m/0,5mm	7,12	1,77	5,35		0,5mm	3,554108816
15,45m/1mm	8,79	1,79	7		1mm	4,650235833
15,45m/2mm	80,35	1,79	78,56		2mm	52,18893244
15,60m/<63µm	83,01	75,59	7,42	373,09	<63µm	1,988796269
15,60m/63µm	139,38	104,19	35,19		63µm	9,432040526
15,60m/125µm	288,93	102,63	186,3		125µm	49,9343322
15,60m/250µm	184,63	53,65	130,98		250µm	35,10681069
15,60/0,5mm	65,57	53,09	12,48		0,5mm	3,34503739
15,60m/1mm	75,17	74,75	0,42		1mm	0,112573374
15,60m/2mm	48,18	47,88	0,3		2mm	0,080409553
16,05m/ <63µm	164,35	107,39	56,96	1034,38	<63µm	5,50668033
16,05m / 63µm	167,33	96,11	71,22		63µm	6,885283938
16,05m/125µm	192,33	108,55	83,78		125µm	8,099537887
16,05m/250µm	225,98	110,25	115,73		250µm	11,18834471
16,05m/0,5mm	263,12	114,52	148,6		0,5mm	14,3660937
16,05m/1mm	254,97	111,54	143,43		1mm	13,86627738
16,05m/2mm	668,95	254,29	414,66		2mm	40,08778205
16,56m/<63µm	12,81	1,28	11,53	687,71	<63µm	1,67657879
16,56m/63µm	15,27	1,75	13,52		63µm	1,965944948
16,56m/125µm	48,97	1,75	47,22		125µm	6,866266304
16,56m/250µm	98,49	1,75	96,74		250µm	14,06697591
16,56m/0,5mm	101,9	1,72	100,18		0,5mm	14,56718675
16,56m/1mm	107,83	4,14	103,69		1mm	15,0775763
16,56m/2mm	318,96	4,13	314,83		2mm	45,779471
Grain size distribution						
Name and size	Total weight (g)	Weight bowl (g)	Grain weight (g)	Total sample weight (g)		Grain weight (%)
18,09m/<63µm	185,85	65,2	120,65	198,95	<63µm	60,64337773
18,09m/63µm	119,07	63,7	55,37		63µm	27,83111335
18,09m/125µm	69,45	61,29	8,16		125µm	4,101533049
18,09m/250µm	78,95	74,95	4		250µm	2,010555416
18,09m/0,5mm	90,12	86,4	3,72		0,5mm	1,869816537
18,09m/1mm	114,61	111,52	3,09		1mm	1,553154059
18,09m/2mm	64,73	60,77	3,96	C	2mm	1,990449862

18,92m/<63µm	134,76	1,28	133,48	2099,85	<63µm	6,356644522
18,92m/63µm	111,44	1,33	110,11		63µm	5,243707884
18,92m/125µm	163,25	1,31	161,94		125µm	7,711979427
18,92m/250µm	129,83	1,3	128,53		250µm	6,120913399
18,92m/0,5mm	117,26	1,75	115,51		0,5mm	5,50086911
18,92m/1mm	208,2	1,78	206,42		1mm	9,830225969
18,92m/2mm	1247,95	4,09	1243,86	C	2mm	59,23565969
21,12m/<63µm	41,14	1,18	39,96	645,46	<63µm	6,190933598
21,12m/63µm	226,95	1,85	225,1		63µm	34,87435317
21,12m/125µm	332,38	1,86	330,52		125µm	51,20689121
21,12m/250µm	44,45	1,3	43,15		250µm	6,685154773
21,12m/0,5mm	1,6	0,69	0,91		0,5mm	0,140984724
21,12m/1mm	0,77	0,67	0,1		1mm	0,015492827
21,12m/2mm	6,37	0,65	5,72		2mm	0,886189694
21,19m/ <63µm	74,35	57,07	17,28	1233,94	<63µm	1,400392239
21,19m / 63µm	183,47	86,29	97,18		63µm	7,875585523
21,19m/125µm	563,34	140,58	422,76		125µm	34,26098514
21,19m/250µm	676,01	184,78	491,23		250µm	39,8098773
21,19m/0,5mm	252,54	58,9	193,64		0,5mm	15,69282137
21,19m/1mm	66,92	56,7	10,22		1mm	0,828241243
21,19m/2mm	63,77	62,14	1,63	C	2mm	0,132097185
21,68m/<63µm	28,19	1,29	26,9	738,52	<63µm	3,642419975
21,68m/63µm	152,58	1,84	150,74		63µm	20,41109246
21,68m/125µm	272,56	1,73	270,83		125µm	36,67199263
21,68m/250µm	196,94	1,7	195,24		250µm	26,4366571
21,68m/0,5mm	85,06	1,77	83,29		0,5mm	11,27796133
21,68m/1mm	7,29	0,68	6,61		1mm	0,89503331
21,68m/2mm	5,58	0,67	4,91	C	2mm	0,6648432
Grain size distribution						
Name and size	Total weight (g)	Weight bowl (g)	Grain weight (g)	Total sample weight (g)		Grain weight (%)
21,68m/<63µm	32,85	1,3	31,55	547,21	<63µm	5,765611009
21,68m/63µm	181,06	1,86	179,2		63µm	32,74793955
21,68m/125µm	282,51	1,86	280,65		125µm	51,28743992
21,68m/250µm	47,23	1,19	46,04		250µm	8,413588933
21,68m/0,5mm	2,81	0,67	2,14		0,5mm	0,391074725
21,68m/1mm	2,19	0,69	1,5		1mm	0,274117798
21,68m/2mm	7,31	1,18	6,13		2mm	1,120228066

21,75m/<63µm	12,94	1,72	11,22	939,04	<63µm	1,194837281
21,75m/63µm	73,16	4,19	68,97		63µm	7,344735049
21,75/125µm	321,24	4,17	317,07		125µm	33,76533481
21,75m/250µm	365,24	4,07	361,17		250µm	38,46162038
21,75m/0,5mm	163,14	4,13	159,01		0,5mm	16,93325098
21,75m/1mm	13,81	1,79	12,02		1mm	1,28003067
21,75m/2mm	10,88	1,3	9,58	C	2mm	1,020190833
22,26m/<63µm	6	1,25	4,75	322,7	<63µm	1,471955377
22,26m/63µm	25,6	1,28	24,32		63µm	7,536411528
22,26m/125µm	201,1	1,83	199,27		125µm	61,75085218
22,26m/250µm	92,77	1,24	91,53		250µm	28,36380539
22,26m/0,5mm	4,05	1,29	2,76		0,5mm	0,855283545
22,26m/1mm	1,33	1,27	0,06		1mm	0,018593121
22,26m/2mm	1,33	1,32	0,01		2mm	0,003098853
23,44m/<63µm	20,91	0,68	20,23	1504,67	<63µm	1,34448085
23,44m/63µm	70,01	0,7	69,31		63µm	4,60632564
23,44m/125µm	463,37	1,76	461,61		125µm	30,67848764
23,44m/250µm	695,63	1,76	693,87		250µm	46,11443041
23,44m/0,5mm	230	1,35	228,65		0,5mm	15,19602305
23,44m/1mm	18,64	0,69	17,95		1mm	1,192952608
23,44m/2mm	13,75	0,7	13,05	C	2mm	0,867299807
23,76m/<63µm	205,74	1,83	203,91	2857,55	<63µm	7,135833144
23,76m/63µm	516,23	4,81	511,42		63µm	17,89714966
23,76m/125µm	352,1	5,18	346,92		125µm	12,14046998
23,76m/250µm	58,11	1,86	56,25		250µm	1,968469493
23,76m/0,5mm	88,37	1,87	86,5		0,5mm	3,027068643
23,76m/1mm	141,6	1,86	139,74		1mm	4,890203146
23,76m/2mm	1516,95	4,14	1512,81		2mm	52,94080594
Grain size distribution						
Name and size	Total weight (g)	Weight bowl (g)	Grain weight (g)	Total sample weight (g)		Grain weight (%)
23,81m/<63µm	46,68	1,3	45,38	552,65	<63µm	8,211345336
23,81m/63µm	186,16	1,84	184,32		63µm	33,35203112
23,81m/125µm	235,15	1,86	233,29		125µm	42,21297385
23,81m/250µm	18,67	1,3	17,37		250µm	3,143038089
23,81m/0,5mm	4,2	0,7	3,5		0,5mm	0,633312223
23,81m/1mm	4,99	1,32	3,67		1mm	0,664073102
23,81m/2mm	66,39	1,27	65,12	C	2mm	11,78322627
24,33m/<63µm	12,83	1,26	11,57	918,03	<63µm	1,260307397

24,33m/63µm	62,58	1,29	61,29		63µm	6,67625241
24,33m/125µm	341,16	1,73	339,43		125µm	36,97373724
24,33m/250µm	366	1,82	364,18		250µm	39,66972757
24,33m/0,5mm	107,98	1,79	106,19		0,5mm	11,56716011
24,33m/1mm	19,39	1,27	18,12		1mm	1,973791706
24,33m/2mm	18,97	1,72	17,25		2mm	1,879023561
25m/<63µm	119,4	1,89	117,51	3978,42	<63µm	2,953685131
25m/63µm	126,58	1,88	124,7		63µm	3,134410143
25m/125µm	201,88	1,87	200,01		125µm	5,027372676
25m/250µm	194,6	1,86	192,74		250µm	4,844636816
25m/0,5mm	250,32	1,85	248,47		0,5mm	6,245444171
25m/1mm	316,69	1,85	314,84		1mm	7,913694381
25m/2mm	2789,03	8,88	2780,15		2mm	69,88075668
26,02m/<63µm	81,27	1,86	79,41	2430,67	<63µm	3,267000457
26,02m/63µm	101,48	1,84	99,64		63µm	4,099281268
26,02m/125µm	250,26	1,85	248,41		125µm	10,21981594
26,02m/250µm	455,48	1,86	453,62		250µm	18,66234413
26,02m/0,5mm	536,02	1,83	534,19		0,5mm	21,97706805
26,02m/1mm	447	4,84	442,16		1mm	18,19086918
26,02m/2mm	578	4,76	573,24		2mm	23,58362098
27,14m/<63µm	76,03	1,85	74,18	2420,77	<63µm	3,064314247
27,14m/63µm	66,1	1,19	64,91		63µm	2,681378239
27,14m/125µm	141,1	1,82	139,28		125µm	5,753541229
27,14m/250µm	230,47	1,83	228,64		250µm	9,44492868
27,14m/0,5mm	467,8	4,75	463,05		0,5mm	19,12821127
27,14m/1mm	557,77	4,8	552,97		1mm	22,84273186
27,14m/2mm	906,64	8,9	897,74		2mm	37,08489448
Grain size distribution						
Name and size	Total weight (g)	Weight bowl (g)	Grain weight (g)	Total sample weight (g)		Grain weight (%)
27,60m/<63µm	32,73	1,16	31,57	956,5	<63µm	3,300575013
27,60m/63µm	31,32	1,16	30,16		63µm	3,153162572
27,60m/125µm	82,34	1,15	81,19		125µm	8,488238369
27,60m/250µm	170,71	1,74	168,97		250µm	17,66544694
27,60m/0,5mm	213,57	1,72	211,85		0,5mm	22,14845792
27,60m/1mm	234,04	1,73	232,31		1mm	24,28750653
27,60m/2mm	202,19	1,74	200,45	C	2mm	20,95661265
28,17m/<63µm	42,38	1,75	40,63	832,65	<63µm	4,879601273
28,17m/63µm	102,3	4,12	98,18		63µm	11,79126884

28,17m/125µm	321,14	4,11	317,03		125µm	38,07482135
28,17m/250µm	261	4,13	256,87		250µm	30,84969675
28,17m/0,5mm	46,95	1,73	45,22		0,5mm	5,4308533
28,17m/1mm	21,49	1,74	19,75		1mm	2,371944995
28,17m/2mm	56,73	1,76	54,97		2mm	6,601813487
28,36m/<63µm	39,97	1,28	38,69	1019,97	<63µm	3,793248821
28,36m/63µm	18,04	1,27	16,77		63µm	1,644166005
28,36m/125µm	0	0	0		125µm	0
28,36m/250µm	180,65	1,28	179,37		250µm	17,58581135
28,36m/0,5mm	226,2	1,75	224,45		0,5mm	22,00554918
28,36m/1mm	204,28	1,84	202,44		1mm	19,84764258
28,36m/2mm	360,07	1,82	358,25		2mm	35,12358207
30,05m/<63µm	73,92	1,81	72,11	1275,8	<63µm	5,652139834
30,05m/63µm	38,92	1,82	37,1		63µm	2,907979307
30,05m/125µm	64,14	1,83	62,31		125µm	4,883994356
30,05m/250µm	35	1,32	33,68		250µm	2,639912212
30,05m/0,5mm	119,93	1,3	118,63		0,5mm	9,298479385
30,05m/1mm	387,81	4,74	383,07		1mm	30,02586612
30,05m/2mm	573,7	4,8	568,9		2mm	44,59162878
31,22m/<63µm	60,78	0	60,78	1865,71	<63µm	3,257741021
31,22m/63µm		0	0		63µm	0
31,22m/125µm			0		125µm	0
31,22m/250µm	53,45	1,74	51,71		250µm	2,771599016
31,22m/0,5mm	143,06	1,75	141,31		0,5mm	7,574060277
31,22m/1mm	417,54	4,12	413,42		1mm	22,15885641
31,22m/2mm	1202,6	4,11	1198,49		2mm	64,23774327
Grain size distribution						
Name and size	Total weight (g)	Weight bowl (g)	Grain weight (g)	Total sample weight (g)		Grain weight (%)
32,18m/<63µm			0	1293,24	<63µm	0
32,18m/63µm			0		63µm	0
32,18m/125µm			0		125µm	0
32,18m/250µm			0		250µm	0
32,18m/0,5mm	197,94	1,76	196,18		0,5mm	15,16965142
32,18m/1mm	454,44	4,82	449,62		1mm	34,76694194
32,18m/2mm	652,22	4,78	647,44		2mm	50,06340664
33,31m/<63µm		0	0	889,93	<63µm	0
33,31m/63µm		0	0		63µm	0
33,31m/125µm		0	0		125µm	0

33,31m/250µm		0	0		250µm	0
33,31m/0,5mm	105,53	1,31	104,22		0,5mm	11,71103345
33,31m/1mm	246,28	1,74	244,54		1mm	27,47856573
33,31m/2mm	542,9	1,73	541,17		2mm	60,81040082
34,01m/<63µm	65,43	0	65,43	749,25	<63µm	8,732732733
34,01m/63µm		0	0		63µm	0
34,01m/125µm		0	0		125µm	0
34,01m/250µm	53,29	1,29	52		250µm	6,940273607
34,01m/0,5mm		0	0		0,5mm	0
34,01m/1mm	324,33	1,73	322,6		1mm	43,05638972
34,01m/2mm	310,98	1,76	309,22		2mm	41,27060394
34,35m/<63µm	23,98	1,31	22,67	1019,995	<63µm	2,222559915
34,35m/63µm	33,34	1,32	32,02		63µm	3,139231075
35,35m/125µm	18,19	1,825	16,365		125µm	1,60441963
35,35m/250µm	38,64	1,85	36,79		250µm	3,606880426
34,35m/0,5mm	190,18	1,8	188,38		0,5mm	18,46871798
34,35m/1mm	386,36	4,92	381,44		1mm	37,39626175
34,35m/2mm	347,15	4,82	342,33		2mm	33,56192923
34,75m/<63µm	75,36	1,85	73,51	2239,28	<63µm	3,282751599
34,75m/63µm	79,09	1,86	77,23		63µm	3,448876425
34,75m/125µm	109,22	1,85	107,37		125µm	4,794844772
34,75m/250µm	63,09	1,84	61,25		250µm	2,735254189
34,75m/0,5mm	423,56	1,85	421,71		0,5mm	18,83239255
34,75m/1mm	728,16	4,85	723,31		1mm	32,30100747
34,75m/2mm	779,8	4,9	774,9		2mm	34,60487299